January 1996 • NREL/TP-442-7816

Effects of Grit Roughness and Pitch Oscillations on the S810 Airfoil

Airfoil Performance Report, Revised (12/99)

R. Reuss Ramsay
M. J. Hoffmann
G.M. Gregorek
The Ohio State University
Columbus, Ohio

National Renewable Energy Laboratory
1617 Cole Boulevard
Golden, Colorado 80401-3393
A national laboratory of the U.S. Department of Energy
Managed by Midwest Research Institute
for the U.S. Department of Energy
under contract No. DE-AC36-83CH10093

Foreword

Airfoils for wind turbines have been selected by comparing data from different wind tunnels, tested under different conditions, making it difficult to make accurate comparisons. Most wind tunnel data sets do not contain airfoil performance in stall commonly experienced by turbines operating in the field. Wind turbines commonly experience extreme roughness for which there is very little data. Finally, recent tests have shown that dynamic stall is a common occurrence for most wind turbines operating in yawed, stall or turbulent conditions. Very little dynamic stall data exists for the airfoils of interest to a wind turbine designer. In summary, very little airfoil performance data exists which is appropriate for wind turbine design.

Recognizing the need for a wind turbine airfoil performance data base, the National Renewable Energy Laboratory (NREL), funded by the U.S. Department of Energy, awarded a contract to Ohio State University (OSU) to conduct a wind tunnel test program. Under this program, OSU tested a series of popular wind turbine airfoils. A standard test matrix was developed to assure that each airfoil was tested under the same conditions. The test matrix was developed in partnership with industry and is intended to include all of the operating conditions experienced by wind turbines. These conditions include airfoil performance at high angles of attack, rough leading edge (bug simulation), steady and unsteady angles of attack.

Special care has been taken to report as much of the test conditions and raw data as practical so that designers can make their own comparisons and focus on details of the data relevant to their design goals. Some of the airfoil coordinates are proprietary to NREL or an industry partner. To protect the information which defines the exact shape of the airfoil, the coordinates have not been included in the report. Instructions on how to obtain these coordinates may be obtained by contacting C.P. (Sandy) Butterfield at NREL.

C. P. (Sandy) Butterfield
Wind Technology Division
National Renewable Energy Laboratory
1617 Cole Blvd.
Golden, Colorado, 80401 USA
Internet Address: Sandy_Butterfield@NREL.GOV
Phone 303-384-6902
FAX 303-384-6901

Preface

The Ohio State University Aeronautical and Astronautical Research Laboratory is conducting a series of steady state and unsteady wind tunnel tests on a set of airfoils that have been or will be used for horizontal-axis wind turbines. The purpose is to investigate the effect of pitch oscillations and leading edge grit roughness (LEGR) on airfoil performance. The study of pitch oscillation effects can help to understand the behavior of horizontal axis wind turbines in yaw. The results of these tests will aid in the development of new airfoil performance codes that account for unsteady behavior and also aid in the design of new airfoils for wind turbines. The application of LEGR simulates surface irregularities that occur on wind turbines. These irregularities on the blades are due to the accumulation of insect debris, ice, and the aging process and can significantly reduce the output of the horizontal axis wind turbines. The experimental results from the application of leading edge grit roughness will help the development of airfoils that are less sensitive to roughness.

This work was made possible by the efforts and financial support of the National Renewable Energy Laboratory who provided major funding and technical monitoring and the U.S. Department of Energy is credited for its funding of this document through the National Renewable Energy Laboratory under contract number DE-AC36-83CH10093. The staff of The Ohio State University Aeronautical and Astronautical Research Laboratory appreciate the contributions made by personnel from that organization. In addition, the authors would like to recognize the efforts of the following graduate and undergraduate student research assistants, Fernando Falasca, Jolanta M. Janiszewska, and Mònica Angelats i Coll.

Summary

An S810 airfoil model was tested in The Ohio State University Aeronautical and Astronautical Research Laboratory 3×5 subsonic wind tunnel under steady state and unsteady conditions. The test defined baseline conditions for steady state angles of attack from -20° to +40° and examined unsteady behavior by oscillating the model about its pitch axis for three mean angles, three frequencies, and two amplitudes. For all cases, Reynolds numbers of 0.75, 1, 1.25, and 1.5 million were used. In addition, the above conditions were repeated after the application of leading edge grit roughness (LEGR) to determine contamination effects on the airfoil performance.

Baseline steady state results of the S810 testing showed a maximum lift coefficient of 1.15 at 15.2° angle of attack. The application of LEGR reduced the maximum lift coefficient by 12% and increased the 0.0066 minimum drag coefficient value by 86%. The zero lift pitching moment of -0.0286 showed a 16% reduction in magnitude to -0.0241 with LEGR applied.

Data were also obtained for two pitch oscillation amplitudes: ±5.5° and ±10°. The larger amplitude consistently gave a higher maximum lift coefficient than the smaller amplitude and both sets of unsteady maximum lift coefficients were greater than the steady state values. Stall was delayed on the airfoil while the angle of attack was increasing, thereby causing an increase in maximum lift coefficient. A hysteresis behavior was exhibited for all the unsteady test cases. The hysteresis loops were larger for the higher reduced frequencies and for the larger amplitude oscillations. In addition to the hysteresis behavior, an unusual feature of these data were a sudden increase in the lift coefficient where the onset of stall was expected. As in the steady case, the effect of LEGR in the unsteady case was to reduce the lift coefficient at high angles of attack.

In general, the unsteady maximum lift coefficient was up to 97% higher than the steady state maximum lift coefficient. Variation in the quarter chord pitching moment coefficient magnitude was in some cases more than eight times larger than the steady state values at high angles of attack. These findings indicate the importance of considering the unsteady flow behavior occurring in wind turbine operation in order to obtain accurate load estimates.

Table of Contents Page

List of Figures Page

List of Tables Page

List of Symbols

AOA	Angle of attack
A/C, a.c.	Alternating current
c	Model chord length
C_d	Drag coefficient
C_{dmin}	Minimum drag coefficient
C_{dp}	Pressure drag coefficient
C_{dw}	Wake drag coefficient
C_{du}	Uncorrected drag coefficient
C_l	Lift coefficient
C_{lmax}	Maximum lift coefficient
$C_{l\ dec}$	Lift coefficient at angle of maximum lift, but with angle of attack decreasing
C_{lu}	Uncorrected lift coefficient
C_m, $C_{m¼}$	Pitching moment coefficient about the quarter chord
$C_{m\ dec}$	Pitching moment coefficient at angle of maximum lift, but with angle of attack decreasing
$C_{m\ inc}$	Pitching moment coefficient at angle of maximum lift, but with angle of attack increasing
C_{mo}	Pitching moment coefficient about the quarter chord, at zero lift
$C_{m¼u}$	Uncorrected pitching moment coefficient about the quarter chord
C_p	Pressure coefficient, $(p- p_\infty)/q_\infty$
C_{pmin}	Minimum pressure coefficient
f	Frequency
h	Wind tunnel test section height
hp, Hp, HP	Horsepower
Hz	Hertz
k	Grit particle size
k/c	Grit particle size divided by airfoil model chord length
p	Pressure
q	Dynamic pressure
q_u	Uncorrected dynamic pressure
q_w	Dynamic pressure through the model wake
q_∞	Free stream dynamic pressure
Re	Reynolds number
Re_u	Uncorrected Reynolds number
t	Time
U_∞	Corrected free stream velocity
V	Velocity
V_u	Uncorrected velocity
x	Axis parallel to model reference line
y	Axis perpendicular to model reference line

α	Angle of attack
α_{dec}	Decreasing angle of attack
α_{inc}	Increasing angle of attack
α_{m}	Median angle of attack
α_{mean}	Mean angle of attack
α_{u}	Uncorrected angle of attack
ϵ	Tunnel solid wall correction scalar
ϵ_{sb}	Solid blockage correction scalar
ϵ_{wb}	Wake blockage correction scalar
Λ	Body-shape factor (0.305 used)
π	3.1416
σ	Tunnel solid wall correction parameter
ω_{red}, $\omega_{reduced}$	Reduced frequency, $\pi fc/U_{\infty}$

Introduction

Horizontal axis wind turbine rotors experience unsteady aerodynamics due to wind shear when the rotor is yawed, when rotor blades pass through the support tower wake, and when the wind is gusting. An understanding of this unsteady behavior is necessary to assist in the calculations of rotor performance and loads. The rotors also experience performance degradation due to surface roughness. These surface irregularities are caused by the accumulation of insect debris, ice, and the aging process. Wind tunnel studies which examine both the steady and unsteady behavior of airfoils can help define pertinent flow phenomena, and the resultant data can be used to validate analytical computer codes.

An S810 airfoil model was tested in The Ohio State University Aeronautical and Astronautical Research Laboratory (OSU/AARL) 3×5 subsonic wind tunnel (3×5) under steady flow and stationary model conditions, as well as with the model undergoing pitch oscillations. To study the possible extent of performance loss due to surface roughness, a standard grit pattern (LEGR) was used to simulate leading edge contamination. After baseline cases were completed, the LEGR was applied for both steady state and model pitch oscillation cases. The Reynolds numbers for steady state conditions were 0.75, 1, 1.25, and 1.5 million, while the angle of attack ranged from -20° to +40°. With the model undergoing pitch oscillations, data were acquired at Reynolds numbers of 0.75, 1, 1.25, and 1.5 million, at frequencies of 0.6, 1.2, and 1.8 Hz. Two sine wave forcing functions were used, ±5.5° and ±10°, at mean angles of attack of 8°, 14°, and 20°. For purposes herein, any reference to unsteady conditions means the airfoil model was in pitch oscillation about the quarter chord.

Experimental Facility

Wind Tunnel

The OSU/AARL 3×5 was used to conduct tests on the S810 airfoil section. Schematics of the top and side views of the tunnel are shown in figures 1 and 2. This open circuit tunnel has a velocity range of 0 - 55 m/s (180 ft/sec) produced by a 2.4-m (8-ft) diameter, six-bladed fan. The fan is belt driven by a 93.2-kw (125-hp)

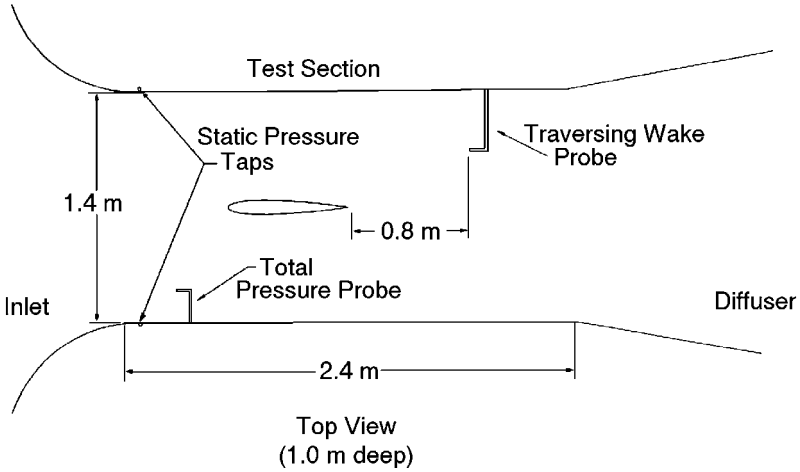

Figure 1. 3x5 subsonic wind tunnel, top view.

three phase a.c. motor connected to a variable frequency motor controller. Nominal test section dimensions are 1.0-m (39-inches) high by 1.4-m (55-inches) wide by 2.4 m (96 inch) long. The 457-mm (18-inches) chord airfoil model was mounted vertically in the test section. A steel tube through the quarter chord of the

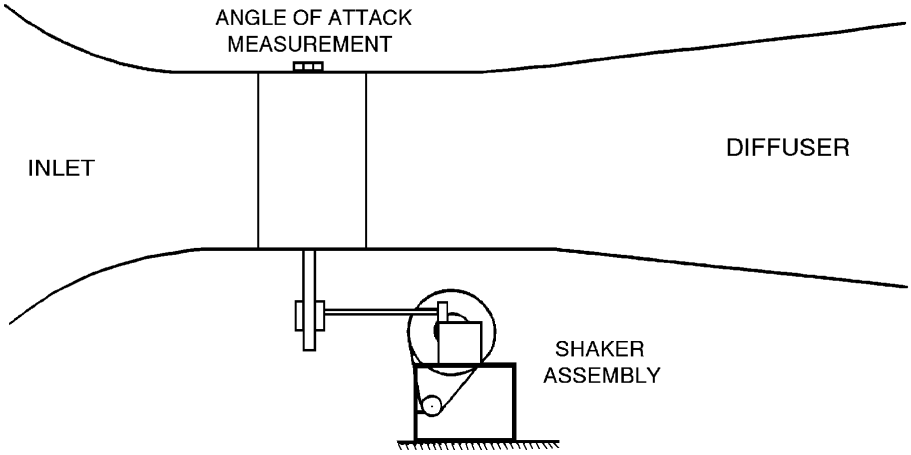

Figure 2. 3x5 subsonic wind tunnel, side view.

model attached the model to the tunnel during testing. An angle of attack potentiometer was fastened to the model at the top of the tunnel, as shown in figure 2. The steady state angle of attack was adjusted with a worm gear drive attached to the model strut below the tunnel floor.

Oscillation System

Portions of the airfoil model testing required the use of a reliable model pitch oscillation system. The OSU/AARL "shaker" system incorporated a face cam and follower arm attached to the model support tube below the wind tunnel floor, as shown in figure 3. The choice of cam governed the type and amplitude of the wave form produced. Sine wave forms with amplitudes of ±5.5° and ±10° were used for these tests. The wave form is defined by the equation

$$\alpha = \alpha_m + A\sin(2\pi ft)$$

where A is the respective amplitude. The shaker system was powered by a 5-hp a.c. motor with variable line frequency controller. The useable oscillating frequency range was 0.1 - 2.0 Hz, with three frequencies used for this test: 0.6, 1.2, and 1.8 Hz.

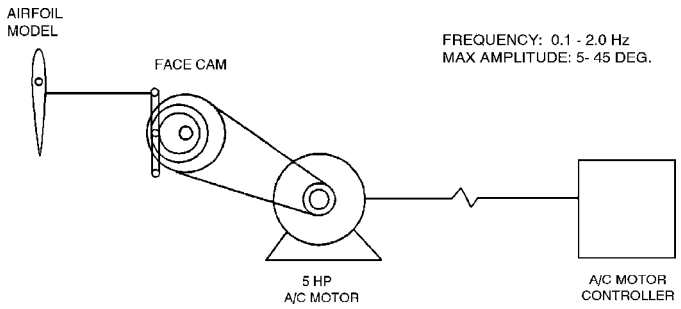

Figure 3. 3x5 wind tunnel oscillation system.

Model Details

A 457-mm (18-inch) constant chord S810 airfoil model was designed by OSU/AARL personnel and manufactured by others. Figure 4 shows the airfoil section. Due to their proprietary nature, model coordinates are not presented in tabular form. The trailing edge was thickened to 1.25 mm (0.05 inch) for

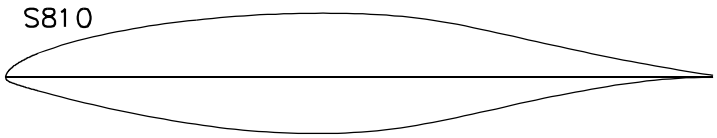

Figure 4. S810 airfoil section.

fabrication purposes. This thickness was added to the upper surface over the last 10% of the chord. The model was made of a nine-layer composite lay up of alternating fiberglass and carbon fiber over ribs. The main load bearing member was a 38-mm (1.5-inch) diameter steel tube which passed through the model quarter chord station. Ribs and end plates were used to transfer loads from the skin to the steel tube. The final surface was filled, painted and wet sanded to attain given coordinates within a requested tolerance of ±0.25-mm (±0.01-inch). The completed model was measured at three spanwise locations using a Sheffield-Cordax coordinate measurement machine. Measurements were made in English units and later converted to metric. Figure 5 shows the results of comparing measured-to-desired coordinates by calculating

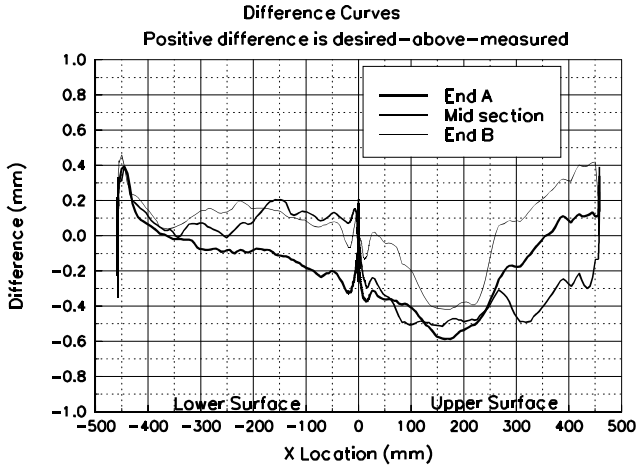

Figure 5. Comparison of desired to measured model coordinates.

differences normal to the profiled surface at three stations on the model. The "spikes" apparent near the trailing edge are due to the numerical methods used and are not real. Although not all the surface was within tolerance, this model was accepted because this discrepancy was not large and the overall model construction was excellent.

To minimize pressure response times, which is important for the unsteady testing, the surface pressure tap lead-out lines had to be as short as possible. Consequently, a compartment was built into the model so pressure scanning modules could be installed inside the model. This compartment was accessed through a panel door fitted flush with the model contour on the lower (pressure) surface.

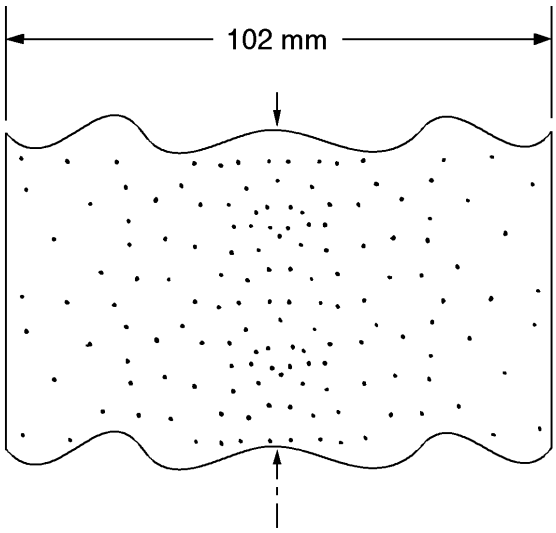

Figure 6. Roughness pattern.

For test cases involving LEGR, a standard, repeatable pattern with lapidary grit as roughness elements was desired. The roughness pattern used was jointly developed by OSU/AARL and KENETECH, Windpower personnel from a molded insect pattern taken from a wind turbine in the field by personnel at the University of Texas Permian Basin. The particle density was 5 particles per cm^2 (32 particles per square inch) in the middle of the pattern, thinning to 1.25 particles per cm^2 (8 particles per square inch) at the edge of the pattern. Figure 6 shows the pattern. To make a usable template, the pattern was repeatedly cut into a steel sheet 102-mm (4-inches) wide and 91-cm (3-ft) long with holes just large enough for one grain of grit. Based on average particle size from the field specimen, standard #40 lapidary grit was chosen for the roughness elements, giving k/c=0.0019 for a 457-mm (18-inch) chord model.

To use the template, 102-mm (4-inch) wide double-sided tape was applied to one side of the template and grit was poured and brushed from the opposite side. The tape was then removed from the template and transferred to the model. This method allowed the same roughness pattern to be replicated for any test.

Test Equipment and Procedures

Data Acquisition

Data were acquired and processed from 60 surface pressure taps, four individual tunnel pressure transducers, an angle of attack potentiometer, a wake probe position potentiometer, and a tunnel thermocouple. The data acquisition system included an IBM PC compatible 80486-based computer connected to a Pressure Systems Incorporated (PSI) data scanning system. The PSI system included a 780B Data Acquisition and Control Unit (DACU), 780B Pressure Calibration Unit (PCU), 81-IFC scanning module interface, two 2.5-psid pressure scanning modules (ESPs), one 20-inch water column range pressure scanning module, and a 30-channel Remotely Addressed Millivolt Module (RAMM-30). Figure 7 is a schematic of the data acquisition system.

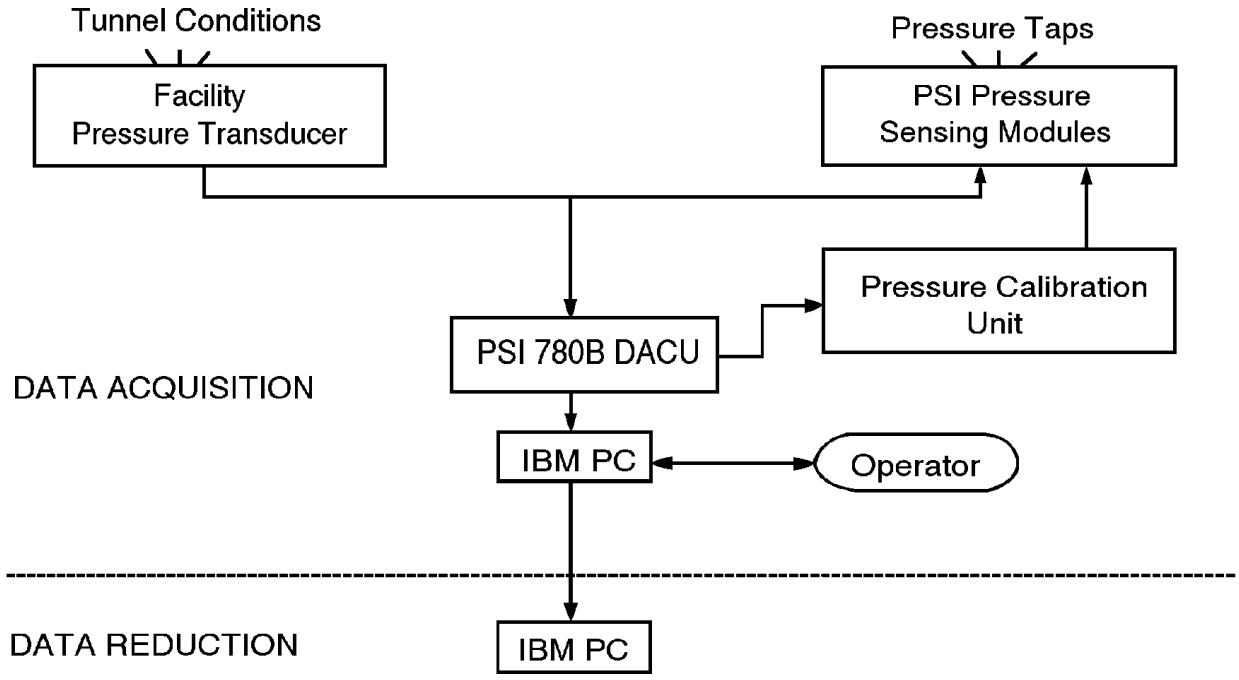

Figure 7. Data acquisition schematic.

Four individual pressure transducers read tunnel total pressure, tunnel north static pressure, tunnel south static pressure, and wake dynamic pressure. Before the test began, these transducers were bench calibrated using a water manometer to determine their sensitivities and offsets. Related values were entered into the data acquisition and reduction program so the transducers could be shunt resistor calibrated before each series of wind tunnel runs.

The rotary angle of attack potentiometer of 0.5% linearity was regularly calibrated during the tunnel pressure transducers shunt calibration. The angle of attack calibration was accomplished by taking voltage readings at known values of set angle of attack. This calibration method gave angle of attack readings within ±0.25° over the entire angle range. The wake probe position potentiometer was a linear potentiometer and it was regularly calibrated during the shunt calibration of the tunnel pressure transducers.

Calibration of the three ESPs was done simultaneously using the DACU and PCU. At operator request, the DACU commanded the PCU to apply known regulated pressures to the ESPs and read the output voltages from each integrated pressure sensor. From these values, the DACU calculated the calibration coefficients and stored them internally until the coefficients were requested by the controlling computer. This calibration

was done several times during a run set because the ESPs were installed inside the model and their outputs tended to drift with temperature changes during a test sequence. Frequent on-line calibrations minimized the effect.

For steady state cases, the model was set to angle of attack and the tunnel conditions were adjusted. At operator request, pressure measurements from the airfoil surface taps and all other channels of information were acquired and stored by the DACU and subsequently passed to the controlling computer for final processing. The angles of attack were always set in the same progression, from 0° to -20° and then from 0° to +40°.

For model oscillating cases, the tunnel conditions were set while the model was stationary at the desired mean angle of attack. The "shaker" was started, a timed wait of approximately 10 seconds imposed, and then model surface pressure and tunnel condition data were acquired. Generally, 120 data scans were acquired over three model oscillation cycles. Since surface pressures were scanned sequentially, the data rate was set so the model rotated through less than 0.50° during any data burst. Finally, due to the unsteady and complex nature of the pitch oscillation cases, model wake surveys (for drag) were not conducted.

Data Reduction

The data reduction routine was included as a section of the data acquisition program. This combination of data acquisition and reduction routines allowed data to be reduced on-line during a test. By quickly reducing selected runs, integrity checks could be made to ensure the equipment was working properly and to allow timely decisions about the test matrix.

The ambient pressure was manually input into the computer and updated regularly. This value, along with measurements from the tunnel pressure transducers and the tunnel thermocouple, were used to calculate tunnel airspeed. As a continuous check of readings, the tunnel total and static pressures were read by both the tunnel individual pressure transducers and the 20-inch water column ESP.

A typical steady state datum point was derived by acquiring ten data scans of all channels over a 10-second window at each angle of attack and tunnel condition. The reduction portion of the program processed each data scan to coefficient forms (C_p, C_l, $C_{m¼}$, and C_{dp}) using the measured surface pressure voltages, calibration coefficients, tap locations and wind tunnel conditions. All scan sets for a given condition were then ensemble averaged to provide one data set and that data set was corrected for the effects of solid tunnel walls. All data were saved in electronic form.

Corrections due to solid tunnel sidewalls were applied to the wind tunnel data. As described by Pope and Harper (1966), tunnel conditions are represented by the following equations:

$$q = q_u(1 + 2\epsilon)$$

$$V = V_u(1 + \epsilon)$$

$$R_e = R_{e_u}(1 + \epsilon)$$

Airfoil aerodynamic characteristics are corrected by:

$$\alpha = \alpha_u + \frac{57.3\sigma}{2\pi}(C_{l_u} + 4C_{m\frac{1}{4}_u})$$

$$C_l = C_{l_u}(1 - \sigma - 2\epsilon)$$

$$C_{m_{\frac{1}{4}}} = C_{m_{\frac{1}{4}_u}}(1 - 2\epsilon) + \frac{\sigma\, C_l}{4}$$

$$C_d = C_{d_u}(1 - 3\epsilon_{sb} - 2\epsilon_{wb})$$

where

$$\sigma = \frac{\pi^2}{48}\left(\frac{c}{h}\right)^2$$

$$\epsilon = \epsilon_{sb} + \epsilon_{wb}$$

$$\epsilon_{sb} = \Lambda\sigma$$

$$\epsilon_{wb} = \frac{c}{h4} C_{d_u}$$

Model wake data were taken for steady state cases when the wake could be completely traversed. Pressures were acquired from a pitot-static probe which was connected to measure incompressible dynamic pressure through the wake. These pressure measurements were used to calculate drag coefficient using a form of the Jones equation derived from Schlichting (1979).

$$C_{dw} = \frac{2}{c}\int \sqrt{\frac{q_w}{q_\infty}}\left(1 - \sqrt{\frac{q_w}{q_\infty}}\right) dy$$

This equation assumes that static pressure at the measurement site is the free-stream value. The integration was done automatically except the computer operator chose the end points of the integration from a plot of the wake survey displayed on the computer screen.

For pitch oscillation cases, model surface pressures were reduced to pressure coefficient form with subsequent integrations and angle of attack considerations giving lift, moment, and pressure drag coefficients. The wind tunnel was not calibrated for unsteady model pitch conditions; therefore, the unsteady pressure data were not corrected for any possible effects due to time dependent pitching or solid tunnel walls. Also, for these cases, the wind tunnel contraction pressures (used for steady state cases) could not be used to calculate instantaneous freestream conditions due to slow response. The tunnel conditions were obtained from a total pressure probe and the average of opposing static taps in the test section entrance, thereby giving near instantaneous flow pressure conditions for the pitching frequencies used.

Test Matrix

The test was designed to study steady state and unsteady pitch oscillation data. Steady state data were acquired at Reynolds numbers of 0.75, 1, 1.25, and 1.5 million with and without LEGR. Refer to the tabular data in Appendix B for the actual Reynolds number for each steady state angle of attack. The angle of attack increment was two degrees for $-20° < \alpha < +10°$ or $+20° < \alpha < +40°$ and one degree for $+10° < \alpha < +20°$. Wake surveys were conducted to find total airfoil drag over an approximate angle of attack range of -10° to +10°. Unsteady data were taken for Reynolds numbers of 0.75, 1, 1.25, and 1.5 million. Sine wave cams with amplitudes ±5.5° and ±10° were used for pitch oscillations, and the mean angles for both of these amplitudes

were 8°, 14°, and 20°. For all these conditions, the frequencies were varied to 0.6, 1.2, and 1.8 Hz. All data points for the unsteady cases were acquired for both clean and LEGR cases.

Results and Discussion

The S810 airfoil model was tested under steady state and pitch oscillation conditions. A brief discussion of the results follows, beginning with a comparison of experimental data and computational predictions.

Comparison With Theory

Present wind tunnel steady state data were compared with computed predictions made using the North Carolina State Airfoil Analysis Code. This analysis code has proven to be accurate for moderate angles of attack. The analysis was made with specifications set to allow free transition from laminar to turbulent flow, and the pressure distribution comparisons were matched to the same angle of attack as the wind tunnel cases. Figure 8 shows the lift coefficient versus angle of attack for the 1 million Reynolds number case. For

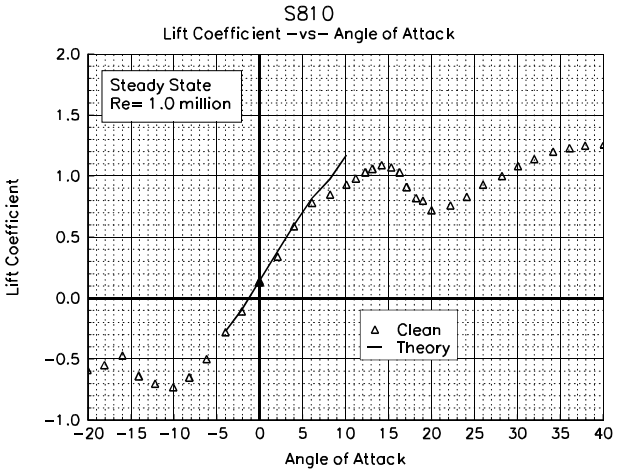

Figure 8. Comparison with theory, C_l vs α.

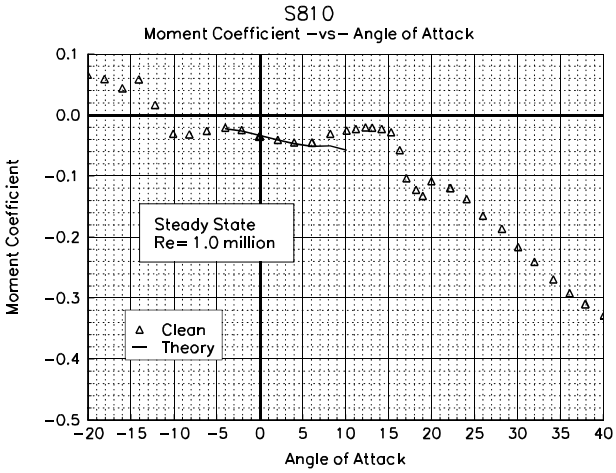

Figure 9. Comparison with theory, C_m vs α.

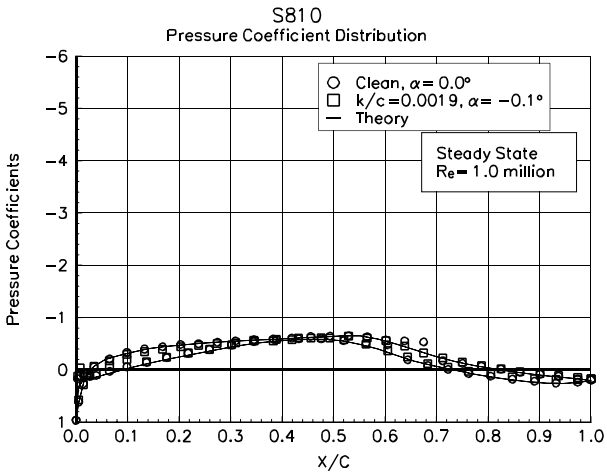

Figure 10. Comparison with theory, C_p vs x/c, α=0.0°.

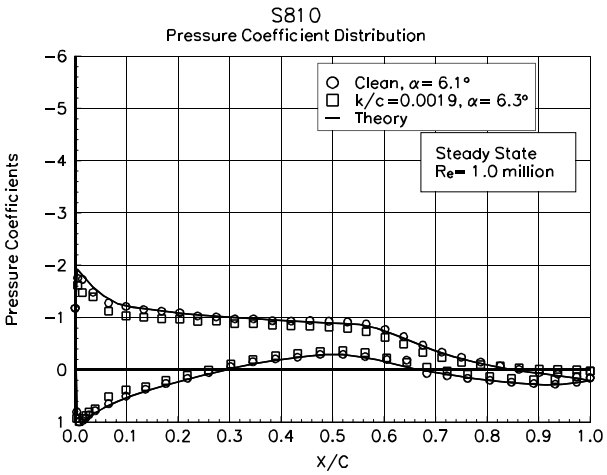

Figure 11. Comparison with theory, C_p vs x/c, α=6.1°.

moderate angles of attack, where the analysis code is valid, the comparison shows good agreement. The pitching moment about the quarter chord, shown in figure 9, also shows good agreement for angles of attack from -5° to +5°. The pressure distributions shown in figures 10 and 11 are for angles of attack of 0° and 6.1°, respectively, and include clean and LEGR wind tunnel data as compared to computed, free transition pressure

distributions. For both angles of attack, there is reasonable correlation between the experimental and predicted values.

Steady State Data

The S810 airfoil model was tested at four Reynolds numbers at nominal angles of attack from -20° to +40°. Figures 12 and 13 show lift coefficients for all tested Reynolds numbers both for a clean model and with LEGR applied, respectively. The maximum positive lift coefficient for Reynolds number of 1.5 million for the clean cases is 1.15 and 1.01 for the LEGR cases, a 12% reduction. Both clean and LEGR cases have positive stall slightly beyond 14° angle of attack. In comparison, the clean data show a deeper stall than the LEGR data. Finally, the average lift curve slope for clean data is about 0.104 and slightly lower for the LEGR case at 0.098. The associated average lift coefficients at zero angle of attack are 0.13 for the clean case and 0.092 for the LEGR case.

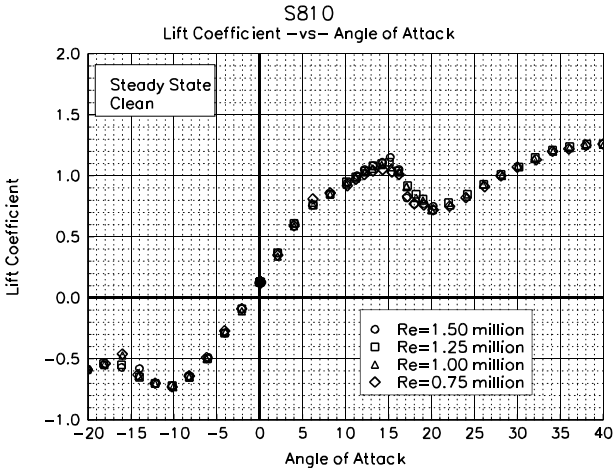

Figure 12. C_l vs α, clean.

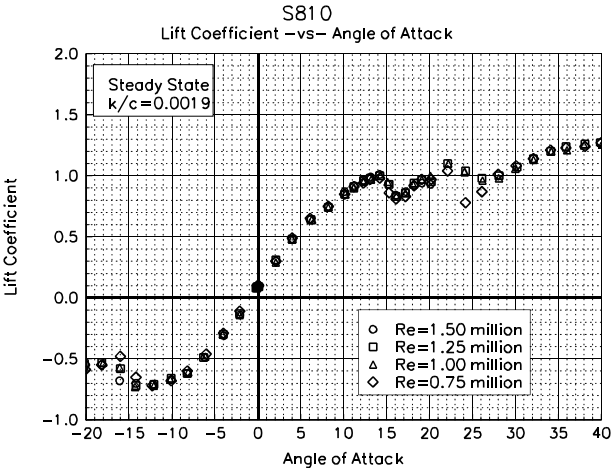

Figure 13. C_l vs α, LEGR, k/c=0.0019.

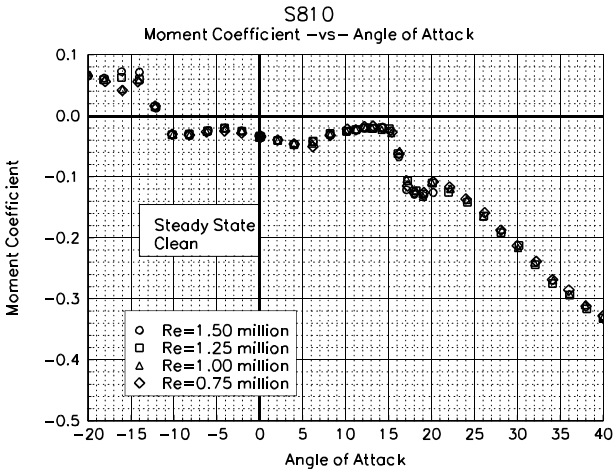

Figure 14. C_m vs α, clean.

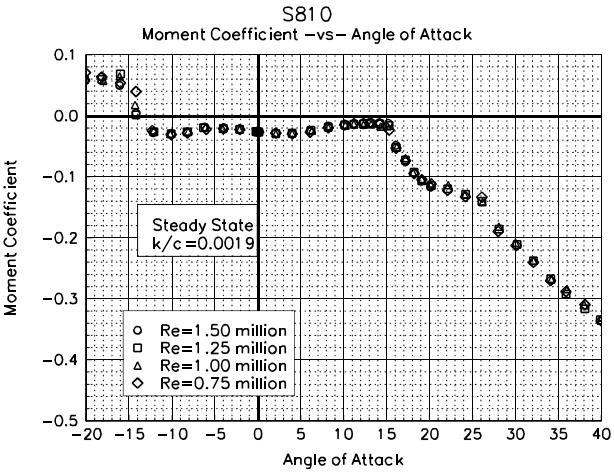

Figure 15. C_m vs α, LEGR, k/c=0.0019.

Figure 14 shows the pitching moment about the quarter chord for the clean cases and figure 15 shows the same for the LEGR cases. The clean data show an abrupt increase in the magnitude of the pitching moment, which corresponds to the angle of attack where stall occurs. The LEGR cases do not show as abrupt a magnitude increase through stall angles as do the clean cases. Through low angles of attack, -10° through

+15°, the LEGR curve is flatter than for the clean case. The zero lift pitching moment coefficient about the quarter chord for the 1.25 million Reynolds number, clean case, is -0.0294 and -0.0248 for the LEGR case.

Total wake drag data were obtained for the steady state cases over an angle of attack range of -10° to +10°. A pitot-static probe was used to describe the wake profile. This method is reliable when there is relatively low turbulence in the wake flow; therefore, only moderate angles of attack have reliable total drag coefficient data. At angles of attack other than those indicated above, surface pressure data was integrated to give C_{dp} and are shown in the drag polars as small symbols. The model clean drag data is shown in figure 16 and the LEGR data are shown in figure 17. At 1 million Reynolds number, the minimum drag coefficient for the clean cases was measured as 0.0081, and 0.0133 for LEGR, a 64% increase.

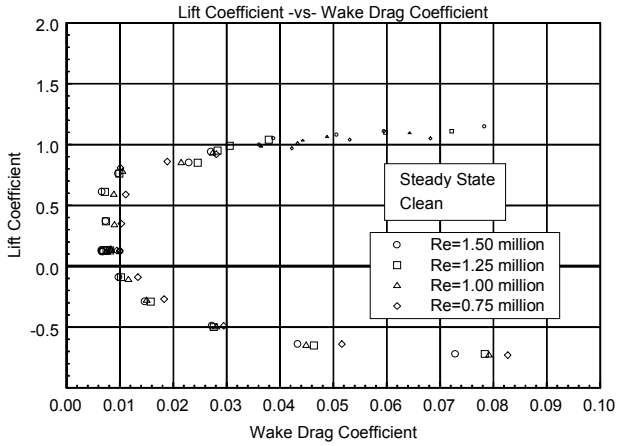

Figure 16. Clean, drag polar.

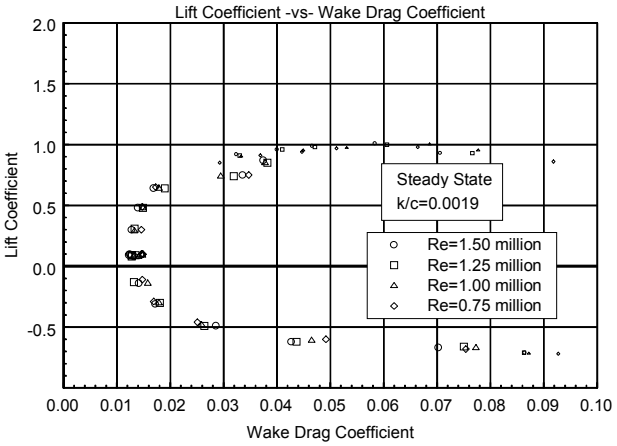

Figure 17. LEGR, drag polar.

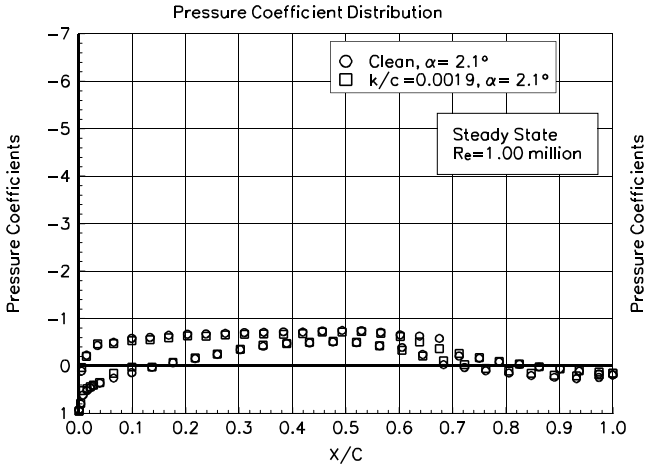

Figure 18. Pressure distribution, α=2.1°.

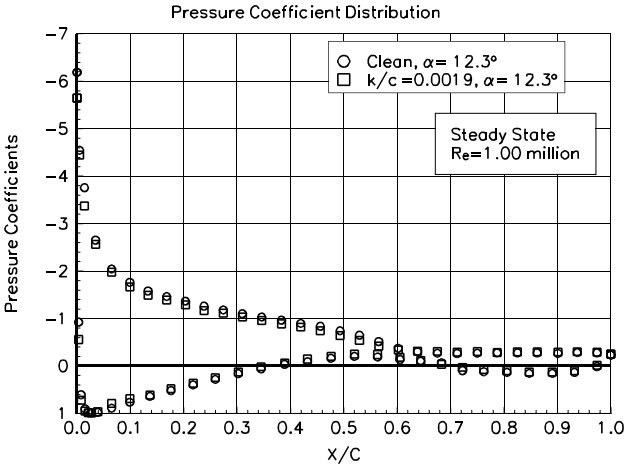

Figure 19. Pressure distribution, α=12.3°.

Two examples of the surface pressure distributions are shown in figures 18 and 19 for 2.1° and 12.3°, respectively, for 1 million Reynolds number. At the angles of attack close to zero degrees, LEGR does not appear to significantly change the pressure distribution compared to the clean case; however, an effect is apparent in the lift coefficient with values of 0.29 for the LEGR case and 0.34 for the clean case. For the higher angle of attack case, figure 19, the effect of LEGR is to reduce the magnitude of the pressure peak from -6.2 to -5.6 and to slightly increase the pressures on the upper (suction) surface over the forward 60% of the chord. On the lower (pressure) surface, the LEGR and the clean cases are very similar except for a

small region just down stream of the stagnation point. The net effect is an 8% reduction in lift coefficient, from 1.03 to 0.95.

Unsteady Data

Unsteady experimental data were obtained for the S810 airfoil model undergoing sinusoidal pitch oscillations. As mentioned earlier, no attempt was made to calibrate the wind tunnel for the unsteady oscillating model conditions; the steady state tunnel calibration was used to set the flow conditions while the model was stationary at its mean angle of attack. The use of the unsteady data should be limited to comparisons with other models tested in this same facility and can be used to detect possible trends. A comprehensive set of test conditions was used to describe unsteady behavior of the S810 airfoil, including two angle of attack amplitudes, ±5.5° and ±10°; four Reynolds numbers, 0.75, 1, 1.25, and 1.5 million; three pitch oscillation frequencies, 0.6, 1.2, and 1.8; and three mean angles of attack, 8°, 14°, and 20°.

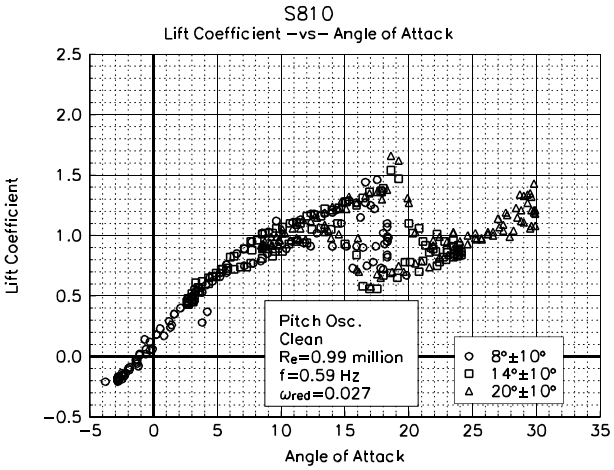

Figure 20. Clean, C_l vs α, ω_{red}=0.027, ±10°.

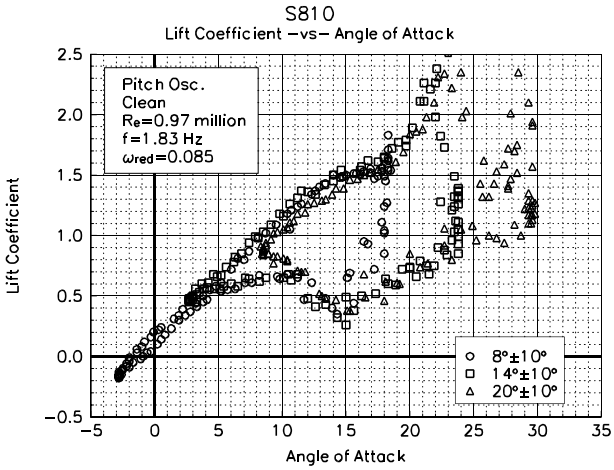

Figure 21. Clean, C_l vs α, ω_{red}=0.085, ±10°.

Figures 20 and 21 show the lift coefficient versus angle of attack for the ±10° amplitude model, clean case, at reduced frequency of 0.027 and 0.085 and 1 million Reynolds number. Note that all three mean angles of attack are plotted on the same figure. Hysteresis behavior was apparent for all unsteady cases. When the model is traveling through increasing angle of attack, the air flow tends to stay attached and, therefore, stall is delayed. In contrast, when the model is traveling through decreasing angles of attack, the stall recovery is delayed and the lift coefficient is lower than what the steady state behavior predicts. In addition to hysteresis effects, an unusual feature of the S810 airfoil model was the sudden increase in the lift coefficient where the onset of stall was expected. This phenomenon was observed in all the clean unsteady data and in some of the LEGR data. It is important to note that this event occurs for both the ±10° and the ±5.5° amplitude cases even though the model is oscillating at a lower speed for the lower amplitude case, indicating that the spike may be attributed to the model configuration.

Some preliminary analysis has been conducted to discover the cause of this spike. The four following figures show several individual unsteady pressure distributions over time intervals concurrent with the pressure peak. Looking at the figures in order, a slow moving wave appears to travel down the surface of the airfoil model

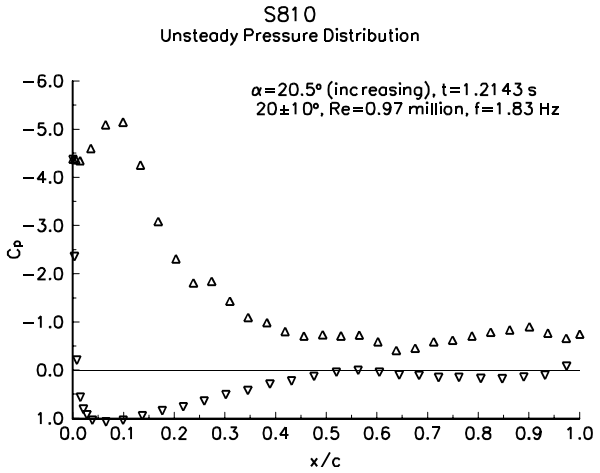

Figure 22. Unsteady pressure dist., α=20.5°.

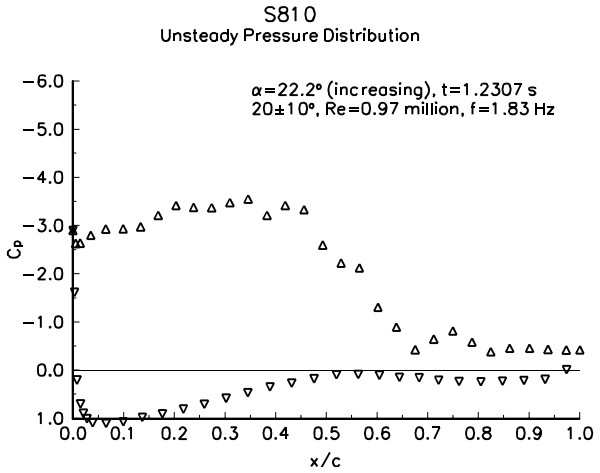

Figure 23. Unsteady pressure dist., α=22.2°.

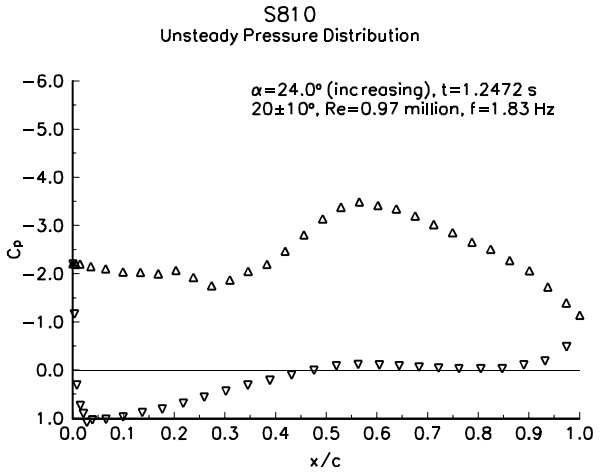

Figure 24. Unsteady pressure dist., α=24.0°.

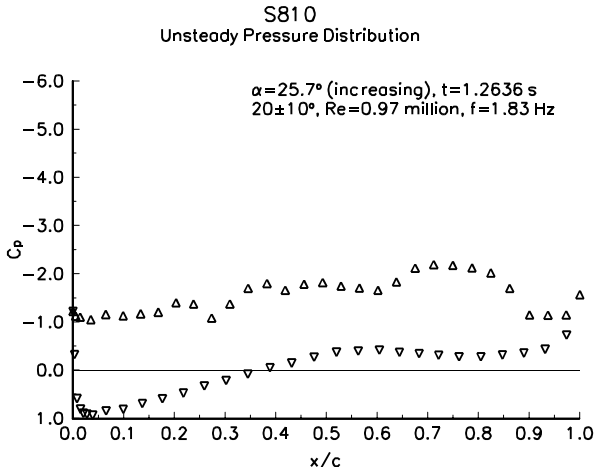

Figure 25. Unsteady pressure dist., α=25.7°.

at a speed approximately one-third of the free stream velocity. This cannot be caused by vortex shedding, which would move near the free stream velocity. Rather, it is related to the viscous forces on the model surface. One possibility is that a laminar separation bubble forms near the leading edge and that the separation (stall) then expands downstream. This airfoil has a very small leading edge radius and, therefore, might be susceptible to this behavior. A further possibility is that, as the separated zone expands, it creates (impulsively) a low pressure region as evident in the pressure distributions thus accounting for the momentarily high lift.

Figure 26 shows a surface plot of the unsteady pressure coefficient from which the previous four individual pressure distributions were taken. For plotting clarity, the model pressures were "unwrapped" about the trailing edge. The upper surface pressures are depicted on the right side of the surface plot; lower surface values are on the left. The trailing edge is at the midpoint of the x-axis with the leading edge at each extreme. For clarification of the irregularities in the pressure distribution, an equally spaced grid was used. The pressure coefficients were linearly interpolated to the specified number of evenly spaced x positions. The time scale corresponds to angle of attack. The slow moving wave is shown in figure 26 times, which corresponding to instances where the model experiences the lift coefficient spike.

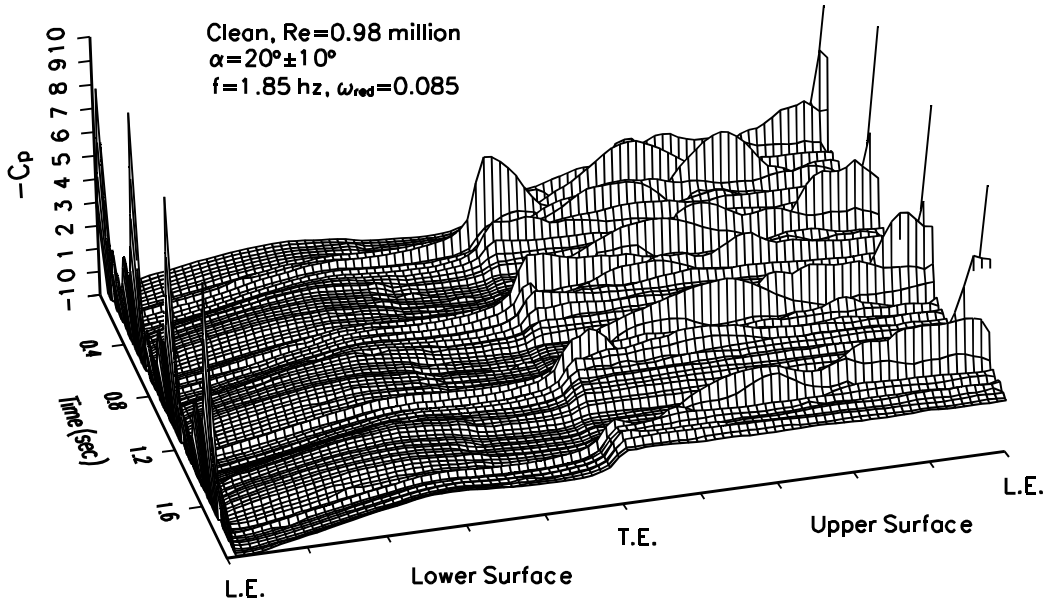

Figure 26. Unsteady pressure distribution, clean, ω_{red}=0.085, 20±10°.

Although this data spike is notable phenomenon and should be the basis for further study, for comparison purposes, maximum lift coefficient values will be taken at a value prior to the lift coefficient spike. This approach is justified when the short time interval in which this event occurs and the inertia of a wind turbine system is considered. Again considering figure 20, where the reduced frequency is 0.027 for a Reynolds number of 1 million, the clean, maximum, pre-stall lift coefficient is near 1.39 and occurs at 18° angle of attack. The lift coefficient on the "return" portion of the curve, at the angle of attack where maximum lift coefficient occurs, can be used to obtain some measure of the hysteresis behavior. For the case discussed here, the hysteresis lift coefficient is 0.67, a 44% decrease from the 1.39 unsteady maximum value. By comparison, the steady state maximum lift coefficient is 1.09. At a higher reduced frequency of 0.085, shown previously in figure 21, the hysteresis behavior is more pronounced. In addition to greater hysteresis, the maximum lift coefficient is increased to about 1.57, a 52% increase over the steady state value. The corresponding hysteresis lift coefficient is 0.62. This difference between steady state behavior and unsteady hysteresis behavior is a main reason why unsteady testing should be required for airfoils used in wind turbine applications.

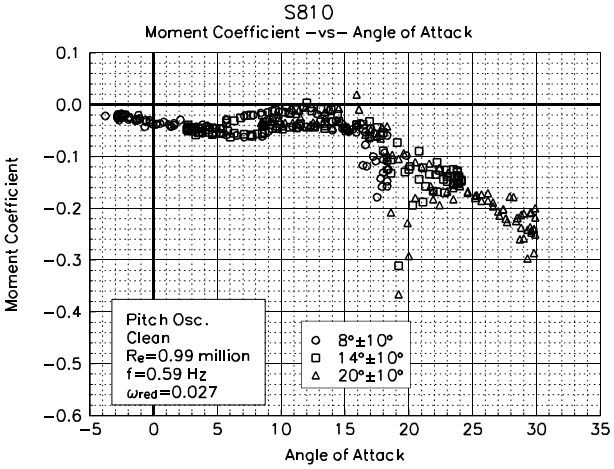

Figure 27. Clean, C_m vs α, ω_{red}=0.027, ±10°.

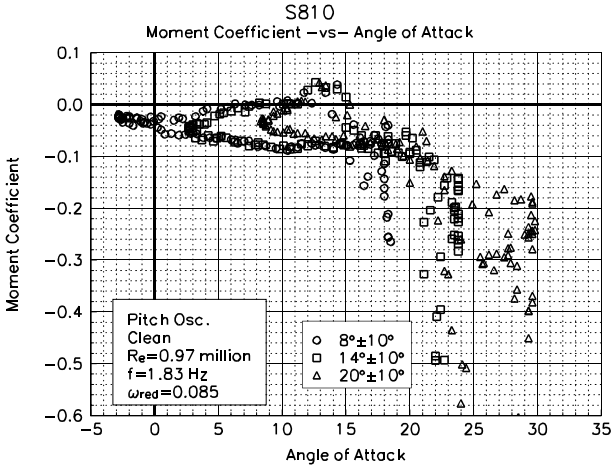

Figure 28. Clean, C_m vs α, ω_{red}=0.085, ±10°.

The pitching moments in figures 27 and 28 correspond to the same conditions as the two lift coefficient plots discussed above. Hysteresis behavior is indicated, but it is not as apparent as in the lift coefficient plots. The higher reduced frequency case, however, does show hysteresis more than the lower reduced frequency case. In addition, a spike in the data can be observed over an angle of attack range consistent with the lift coefficient spike. For reference, the steady state maximum lift occurs near 14° angle of attack, and the steady state pitching moment at this maximum lift point is -0.0228. In comparison, when the airfoil is undergoing pitch oscillation at the lower frequency, pitching moment varies from -0.0543 to -0.0889 (at the angle of attack where maximum lift occurs), a 138% to 290% increase in magnitude from the steady state value. Note the angle of attack where the maximum lift coefficient occurs does not necessarily show the "greatest" hysteresis behavior, but it does give a relative indication of the effect.

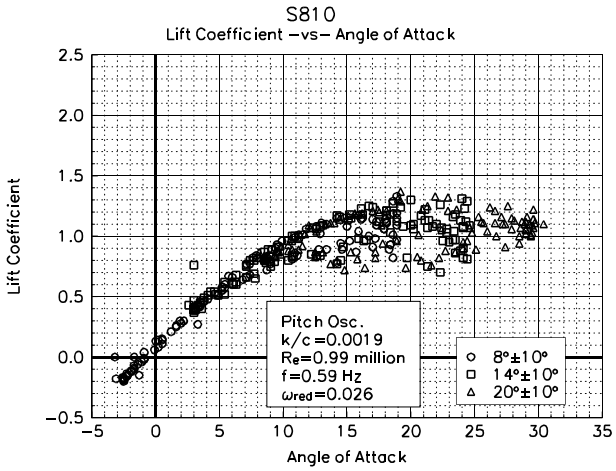

Figure 29. LEGR, C_l vs α, ω_{red}=0.026, ±10°.

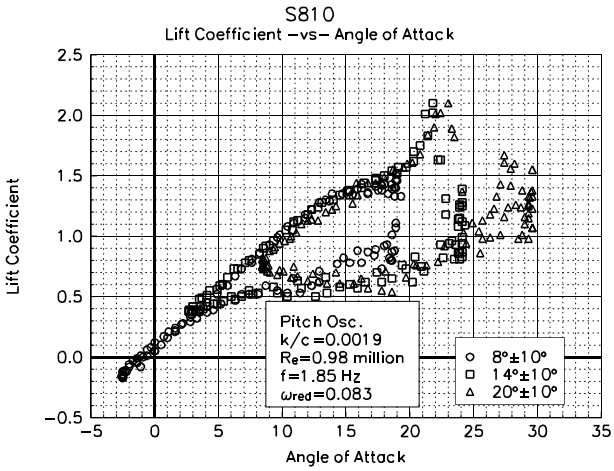

Figure 30. LEGR, C_l vs α, ω_{red}=0.083, ±10°.

Compared to the clean data, the application of LEGR reduces the maximum lift coefficient in the pitch oscillation cases. Lift coefficient versus angle of attack with LEGR applied is shown in figure 29 for the 0.026 reduced frequency case. The 0.083 reduced frequency case is shown in figure 30. Both cases correspond to the same run conditions described earlier for the clean cases. For the lower reduced frequency, the maximum unsteady lift coefficient is reduced to 1.25 from the corresponding clean case of 1.39, a 10% decrease. Hysteresis behavior is apparent at this frequency but is slightly less than the clean case; the corresponding hysteresis lift coefficient is 0.97 when LEGR is applied. The higher frequency LEGR case has a maximum lift coefficient of 1.54 while the model is increasing in angle of attack and the corresponding decreasing angle of attack lift coefficient is 0.65. In this case, the application of LEGR reduced the hysteresis loop behavior through the stall region compared to with the clean case at the same run conditions. Note that a spike in the lift coefficient does develop for these high frequency conditions even with LEGR applied.

The pitching moment coefficient shown in figure 31 is for 0.026 reduced frequency with LEGR applied. At the angle of unsteady maximum lift, the pitching moment ranges from -0.0444 to -0.0678; the steady state LEGR pitching moment is -0.0173 at the steady state maximum lift angle of attack (14.3°). The higher reduced frequency of 0.083 with LEGR applied is shown in figure 32. As was seen with the lift coefficient, pitching moment hysteresis is also more apparent at higher reduced frequency than in the corresponding lower reduced frequency case. Unsteady maximum lift angle of attack for this reduced frequency occurs at 18.6°, and the pitching moment ranges from -0.0743 to -0.0587 at that angle. Throughout the higher angle of attack range, the magnitude of the unsteady pitching moment can be very different from the steady state clean case (steady state pitching moment at maximum lift is -0.0228). It seems these differences can have an impact on the fatigue life predictions of a wind turbine system.

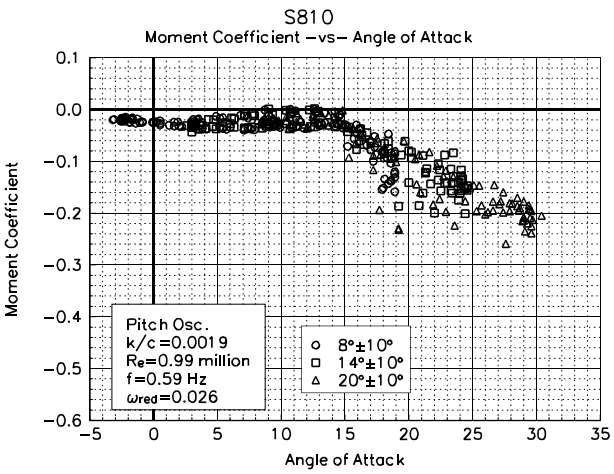

Figure 31. LEGR, C_m vs α, ω_{red}=0.026, ±10°.

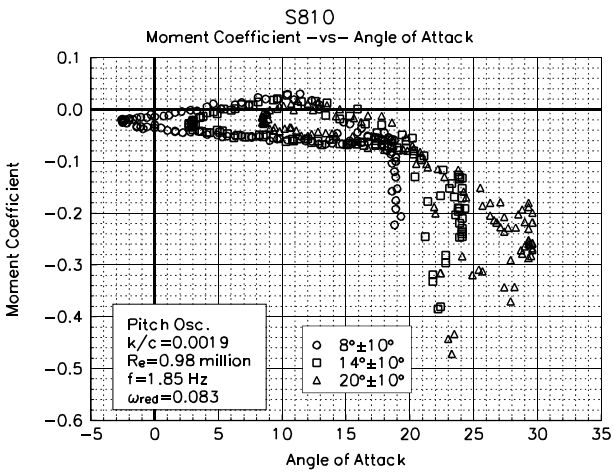

Figure 32. LEGR, C_m vs α, ω_{red}=0.083, ±10°.

Figure 33 shows a surface pressure distribution for the 14°±10° LEGR case at 0.085 reduced frequency and 1 million Reynolds number, the same as the case above . These data show indications of a traveling wave as did the clean case in figure 26. The mean angle of attack was 14°, indicating that the flow recovered from stall. This can be observed as the stable flow region between the occurrences of the traveling waves.

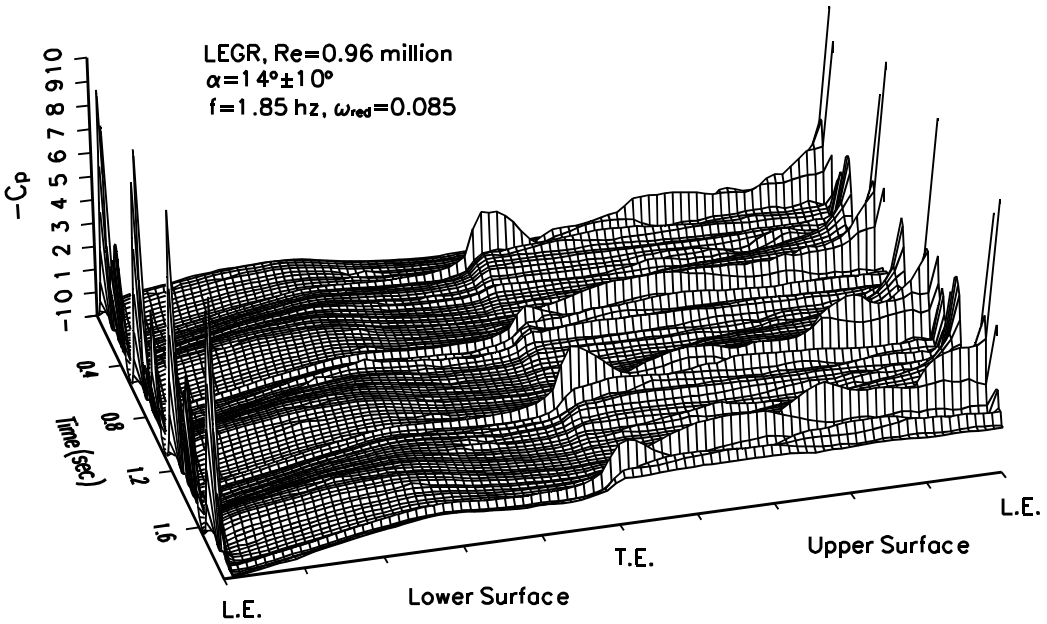

Figure 33. Unsteady pressure distribution, LEGR, ω_{red}=0.085, 14±10°.

In addition to the ±10° unsteady experimental data, ±5.5° unsteady data were obtained with and without LEGR. The data used were taken at 1 million Reynolds number using the same mean angles and frequencies as the 10° amplitude cases. Figures 34 and 35 show the ±5.5°, unsteady, clean lift coefficient for the reduced frequencies of 0.028 and 0.086, respectively. The maximum lift coefficient for the lower frequency is 1.32 and occurs, as expected, when the airfoil is traveling through increasing angle of attack. The hysteresis lift coefficient (at 16.7°) is 0.87. At the higher reduced frequency, the lift coefficient spike becomes apparent. The maximum lift coefficient prior to the data spike occurs at 17.8° and is 1.48. The corresponding

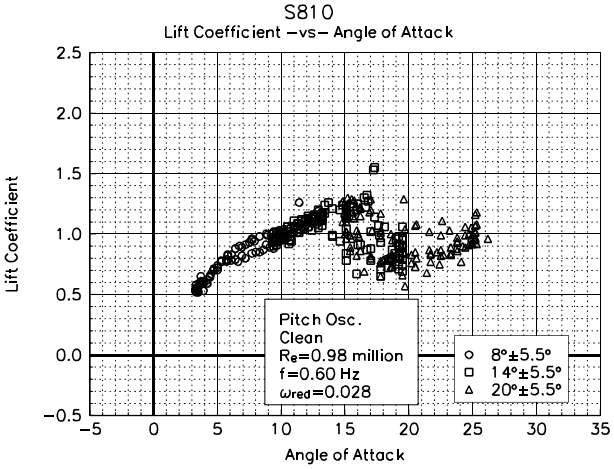

Figure 34. Clean, C_l vs α, ω_{red}=0.028, ±5.5°.

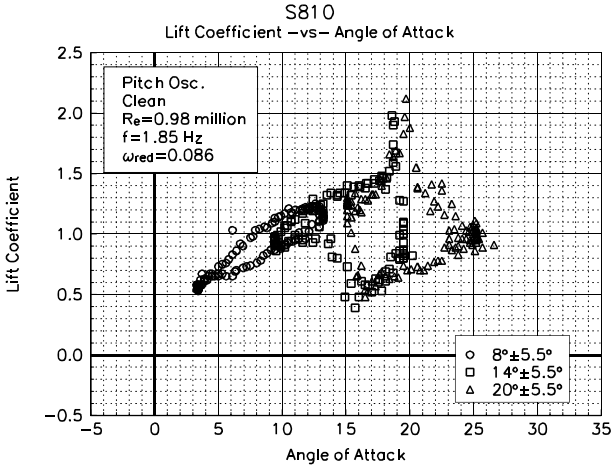

Figure 35. Clean, C_l vs α, ω_{red}=0.086, ±5.5°.

hysteresis lift coefficient is 0.53. The difference between the maximum lift coefficient and the hysteresis lift coefficient indicates a much greater hysteresis response than experienced for the lower reduced frequency. The steady state, clean, maximum lift coefficient is 1.09; therefore, the unsteady behavior created lift coefficients more than 36% higher than the steady state conditions.

The quarter chord pitching moments with the same reduced frequencies as the lift coefficient cases are shown in figures 36 and 37. The hysteresis behavior observed in the lift coefficient plots is also reflected in this pitching moment data. Near the maximum lift angle, 16.7° for the lower frequency, the pitching moment coefficient ranges from -0.0111 to -0.1415. The 0.086 reduced frequency case has maximum lift near 17.8° and pitching moment ranges from -0.0713 to -0.0509. In comparison, the steady state pitching moment is -0.0228 near the steady state maximum lift coefficient angle of attack of 14°. The higher reduced frequency again shows large hysteresis loops for all three mean angles of attack.

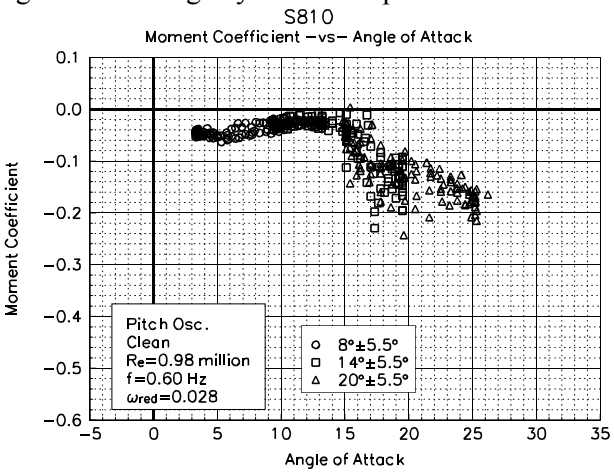

Figure 36. Clean, C_m vs α, ω_{red}=0.028, ±5.5°.

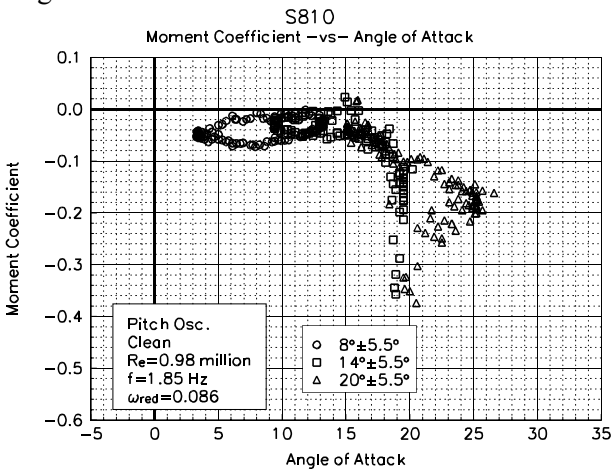

Figure 37. Clean, C_m vs α, ω_{red}=0.086, ±5.5°.

Figures 38 and 39 compare the effect of mean angle of attack on the surface pressure distributions for conditions corresponding to the 0.085 reduced frequency case described above. For an angle of attack range of 8°±5.5°, figure 38, the model does not exceed the stall angle of attack of 14.7°; therefore, the pressure distributions are well behaved, reflecting the increase and decrease in angle of attack. On the other hand,

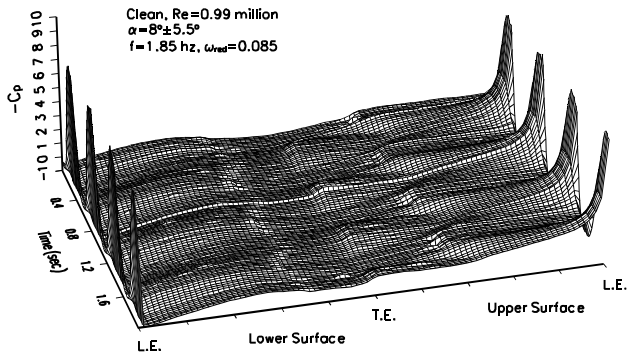

Figure 38. Unsteady pressure distribution, clean, ω_{red}=0.085, 8±5.5°.

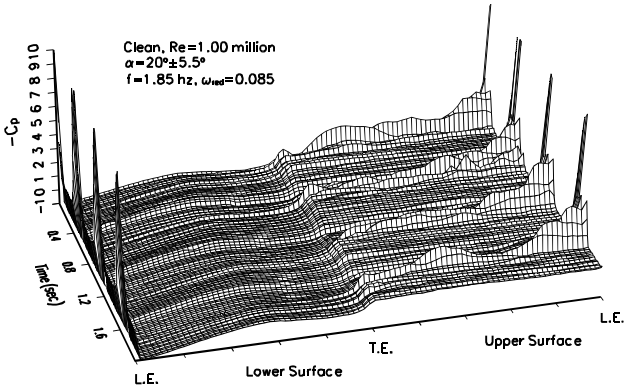

Figure 39. Unsteady pressure distribution, clean, ω_{red}=0.085, 20±5.5°.

for an angle of attack range of 20°±5.5° the model does not have the opportunity to fully recover from stall and a large portion of the upper surface appears to be stalled. In addition, traveling waves are observed because the model is oscillating through a range of angles including the angles at which the lift coefficient spike occurs.

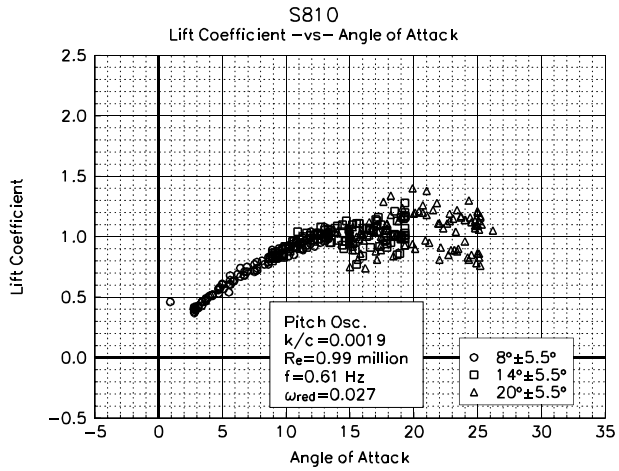

Figure 40. LEGR, C_l vs α, ω_{red}=0.027, ±5.5°.

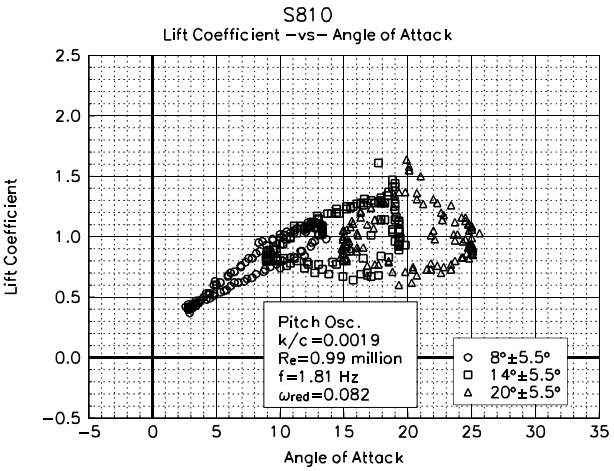

Figure 41. LEGR, C_l vs α, ω_{red}=0.082, ±5.5°.

The application of LEGR degrades the lift performance of the airfoil, as would be expected from the results discussed previously. The LEGR lift coefficient data for reduced frequencies of 0.027 and 0.082 are shown in figures 40 and 41, respectively. The maximum lift coefficient is reduced to 1.13 from 1.32 for the low frequency clean case. Although there is a reduction, this value is still significantly higher than the LEGR steady state case which has a maximum lift coefficient of 1.00 at 14.3° angle of attack. The higher reduced frequency has a maximum lift coefficient of 1.37, which occurs near 18.5° angle of attack. The corresponding lift coefficient at 18.5° for the airfoil traveling with decreasing angle of attack is 0.83, a 39% reduction from the unsteady maximum.

Figures 42 and 43 show the corresponding pitching moment coefficients for the LEGR cases at reduced frequencies of 0.027 and 0.082. For the 0.027 reduced frequency case, the pitching moment varies from -0.0445 to -0.0661 at 14.7° (where the maximum lift occurs). The hysteresis behavior is more pronounced for the higher reduced frequency case, where the range of pitching moments at the maximum lift angle of 18.5° were from -0.1429 to -0.0917. The comparable values for steady state LEGR is -0.0173.

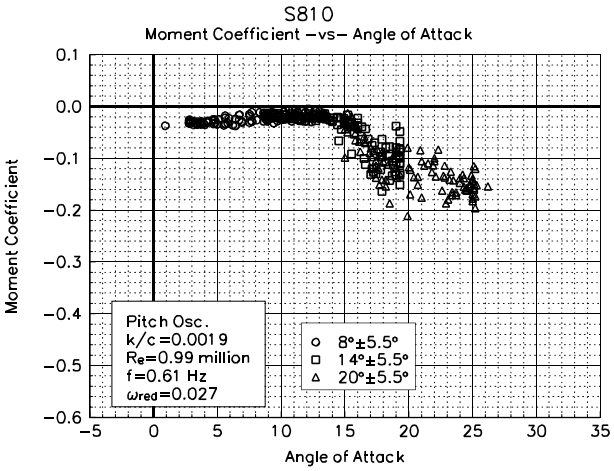

Figure 42. LEGR, C_m vs α, ω_{red}=0.027, ±5.5°.

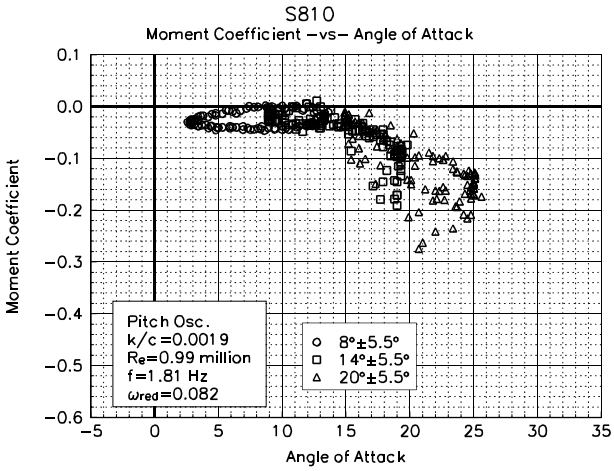

Figure 43. LEGR, C_m vs α, ω_{red}=0.082, ±5.5°.

Although all the unsteady data have not been discussed here, the previous discussion included typical examples of the wind tunnel data. The remaining data for ±5.5° and ±10° pitch oscillations for all the Reynolds numbers are included in Appendix C.

Summary of Results

An S810 airfoil model was tested under steady state and pitch oscillation conditions. Baseline tests were made while the model was clean, and then corresponding tests were conducted with LEGR applied.

A summary of the steady state aerodynamic parameters is shown in Table 1. As observed, the application of LEGR reduced the maximum lift of the airfoil up to 12% and the minimum drag coefficient increased up to 86%. LEGR also affects the zero lift pitching moment coefficient, reducing the magnitude by more than 15% in some cases.

Table 1. S810 Steady State Parameters Summary

Grit Pattern	Re x 10^{-6}	C_{lmax}	C_{dmin}	C_{mo}
Clean	0.75	1.05 @ 14.3°	0.0094	-0.0312
k/c=0.0019	0.75	0.98 @ 14.2°	0.0146	-0.0246
Clean	1.00	1.09 @ 14.2°	0.0081	-0.0295
k/c=0.0019	1.00	1.00 @ 14.3°	0.0133	-0.0250
Clean	1.25	1.11 @ 15.1°	0.0069	-0.0294
k/c=0.0019	1.25	1.00 @ 14.2°	0.0128	-0.0248
Clean	1.50	1.15 @ 15.2°	0.0066	-0.0286
k/c=0.0019	1.50	1.01 @ 14.2°	0.0123	-0.0241

Table 2. S810, Unsteady, Clean, ±5.5°

ω_{red}	Re x 10^{-6}	f	C_{lmax}	α_{max}	$C_{l\,dec}$	$C_{m\,inc}$	$C_{m\,dec}$
0.038	0.74	0.61	1.34	16.0	0.64	-0.0527	-0.0570
0.074	0.74	1.18	1.44	16.5	0.57	-0.0586	-0.0733
0.112	0.73	1.79	1.61	18.1	0.69	-0.0461	-0.1044
0.028	0.98	0.60	1.32	16.7	0.87	-0.0111	-0.1415
0.055	0.98	1.18	1.40	17.3	0.59	-0.0734	-0.0579
0.086	0.98	1.85	1.48	17.8	0.53	-0.0713	-0.0509
0.022	1.24	0.60	1.34	17.3	0.67	-0.2086	-0.0850
0.045	1.23	1.22	1.35	17.0	0.71	-0.0330	-0.0934
0.069	1.23	1.85	1.45	17.3	0.62	-0.0658	-0.0553
0.018	1.48	0.59	1.35	16.8	0.93	-0.1890	-0.0168
0.037	1.47	1.19	1.37	17.4	0.71	-0.0650	-0.1443
0.057	1.47	1.85	1.44	17.3	0.71	-0.0492	-0.1228

The pitch oscillation data can be divided into two groups, the ±5.5° amplitude and ±10° amplitude oscillations, which show similar trends. For both ±5.5° and ±10°, the unsteady test conditions and some parameters are listed in Tables 2, 3, 4, and 5. As the reduced frequency, which takes oscillation and tunnel speed into account, is increased, the maximum lift coefficient also increases. In addition, the hysteresis behavior becomes increasingly apparent with increased reduced frequency.

Table 3. S810, Unsteady, LEGR, ±5.5°

ω_{red}	Re x 10^{-6}	f	C_{lmax}	α_{max}	$C_{l\,dec}$	$C_{m\,inc}$	$C_{m\,dec}$
0.036	0.75	0.61	1.24	16.9	1.06	-0.1344	-0.0544
0.073	0.75	1.21	1.34	18.2	0.83	-0.1144	-0.0739
0.110	0.75	1.83	1.50	19.0	0.96	-0.1698	-0.0887
0.027	0.99	0.61	1.13	14.7	0.90	-0.0445	-0.0661
0.054	0.99	1.19	1.22	15.7	0.77	-0.0392	-0.0372
0.082	0.99	1.81	1.37	18.5	0.83	-0.1429	-0.0917
0.022	1.24	0.60	1.15	14.6	0.82	-0.0260	-0.0221
0.044	1.24	1.21	1.22	16.3	0.79	-0.0523	-0.0729
0.066	1.24	1.85	1.29	17.1	0.77	-0.0485	-0.0819
0.018	1.47	0.61	1.11	14.4	0.89	-0.0268	-0.0024
0.036	1.47	1.21	1.22	18.5	0.82	-0.1576	-0.0914
0.055	1.47	1.83	1.27	18.2	0.82	-0.1723	-0.1112

Table 4. S810, Unsteady, Clean, ±10°

ω_{red}	Re x 10^{-6}	f	C_{lmax}	α_{max}	$C_{l\,dec}$	$C_{m\,inc}$	$C_{m\,dec}$
0.038	0.74	0.62	1.33	16.7	0.50	-0.0710	-0.0637
0.073	0.73	1.18	1.58	16.7	0.40	-0.0789	-0.0309
0.114	0.73	1.83	1.91	18.9	0.78	-0.0811	-0.1659
0.027	0.99	0.59	1.39	18.00	0.67	-0.0543	-0.0889
0.055	0.98	1.19	1.45	17.2	0.55	-0.0633	-0.0478
0.085	0.97	1.83	1.57	19.7	0.62	-0.0741	-0.0556
0.022	1.23	0.60	1.36	17.5	0.76	-0.0650	-0.0629
0.044	1.23	1.19	1.38	15.9	0.68	-0.0470	-0.0502
0.068	1.22	1.85	1.61	18.6	0.65	-0.0796	-0.0955
0.018	1.45	0.60	1.35	17.8	0.75	-0.0460	-0.1443
0.036	1.44	1.18	1.48	18.4	0.70	-0.0617	-0.0672
0.056	1.44	1.79	1.67	19.7	0.69	-0.0828	-0.0889

As expected, the application of LEGR reduces the aerodynamic performance of the airfoil. The maximum lift coefficient is reduced up to 18% for the ±5.5° case and up to 16% for the ±10° case. In addition to following the same trends as the clean, unsteady data discussed previously, the LEGR causes hysteresis behavior to persist into lower angles of attack than in the clean cases. Overall, the unsteady wind tunnel data show hysteresis behavior that becomes more apparent with increased reduced frequency. The maximum unsteady lift coefficient can be up to 97% higher than the steady state maximum lift coefficient. Variation in the quarter chord pitching moment coefficient can be more than eight times greater than that indicated by steady state results. These findings indicate that it is very important to consider the unsteady loading that will occur in wind turbine operation because steady state results can greatly underestimate the forces.

Table 5. S810, Unsteady, LEGR, ±10°

ω_{red}	Re x 10^{-6}	f	C_{lmax}	α_{max}	$C_{l\,dec}$	$C_{m\,inc}$	$C_{m\,dec}$
0.036	0.74	0.61	1.27	16.0	0.86	-0.0608	-0.1003
0.073	0.73	1.22	1.47	18.1	0.58	-0.0747	-0.0279
0.112	0.72	1.85	1.93	21.9	0.63	-0.1485	-0.1180
0.026	0.99	0.59	1.25	16.7	0.97	-0.0444	-0.0678
0.053	0.98	1.19	1.41	18.5	0.72	-0.0523	-0.0754
0.083	0.98	1.85	1.54	18.6	0.65	-0.0743	-0.0587
0.021	1.23	0.60	1.20	19.5	0.76	-0.1270	-0.0954
0.043	1.23	1.21	1.37	19.2	0.84	-0.0661	-0.1052
0.066	1.22	1.85	1.51	18.9	0.69	-0.0651	-0.0438
0.018	1.45	0.60	1.18	15.9	0.77	-0.0437	-0.0168
0.037	1.45	1.22	1.28	18.1	0.65	-0.0576	-0.0743
0.055	1.44	1.83	1.41	19.2	0.68	-0.0604	-0.0701

References

Pope, A.; Harper, J.J. 1966. *Low Speed Wind Tunnel Testing*. New York, NY: John Wiley & Sons, Inc.

Schlichting, H. 1979. *Boundary Layer Theory*. New York, NY: McGraw-Hill Inc.

Smetana, F., Summey, D., et-al. 1975. *Light Aircraft Lift, Drag, Moment Prediction - a Review and Analysis*. North Carolina State University. NASA CR-2523.

Appendix A: Surface Pressure Tap Coordinates

List of Tables Page

Table A1. S810 Surface Pressure Taps, Non-Dimensional Coordinates		
Tap Number	Chord Station	Ordinate
1	1.0004	--
2	0.9741	--
3	0.9315	--
4	0.8898	--
5	0.8474	--
6	0.8052	--
7	0.7619	--
8	0.7217	--
9	0.6833	--
10	0.6440	--
11	0.6048	--
12	0.5630	--
13	0.5200	--
14	0.4759	--
15	0.4318	--
16	0.3888	--
17	0.3452	--
18	0.3021	--
19	0.2594	--
20	0.2179	--
21	0.1764	--
22	0.1369	--
23	0.0993	--
24	0.0654	--
25	0.0388	--
26	0.0275	--
27	0.0207	--
28	0.0147	--
29	0.0078	--
30	0.0029	--
31	0.0000	--
32	0.0054	--
33	0.0140	--
34	0.0354	--

Table A1. S810 Surface Pressure Taps, Non-Dimensional Coordinates		
Tap Number	Chord Station	Ordinate
35	0.0645	--
36	0.0990	--
37	0.1333	--
38	0.1684	--
39	0.2033	--
40	0.2382	--
41	0.2739	--
42	0.3098	--
43	0.3458	--
44	0.3827	--
45	0.4189	--
46	0.4559	--
47	0.4929	--
48	0.5289	--
49	0.5652	--
50	0.6019	--
51	0.6383	--
52	0.6754	--
53	0.7121	--
54	0.7496	--
55	0.7874	--
56	0.8245	--
57	0.8619	--
58	0.9010	--
59	0.9374	--
60	0.9735	--
End of Table A1		

Appendix B: Steady State Data
Integrated Coefficients and Pressure Distributions

List of Tables Page

List of Figures Page

Table B1. S810, Clean, Re = 0.75 x 10^6						
RUN	AOA	C_l	C_{dp}	$C_{m¼}$	Re x10^{-6}	C_{dw}
49	-20.1	-0.59	0.3169	0.0652	0.75	--
48	-18.0	-0.54	0.2702	0.0559	0.75	--
47	-16.0	-0.46	0.2191	0.0413	0.76	--
46	-14.2	-0.63	0.2111	0.0556	0.76	--
45	-12.2	-0.70	0.1441	0.0158	0.75	--
44	-10.2	-0.73	0.0642	-0.0303	0.75	0.0827
43	-8.2	-0.64	0.0335	-0.0316	0.75	0.0516
42	-6.2	-0.49	0.0147	-0.0267	0.74	0.0295
41	-4.1	-0.27	0.0049	-0.0250	0.75	0.0183
40	-2.1	-0.09	0.0022	-0.0285	0.74	0.0134
39	0.1	0.13	0.0047	-0.0352	0.75	0.0094
50	0.1	0.13	0.0042	-0.0343	0.75	0.0100
76	0.1	0.12	0.0044	-0.0335	0.75	0.0100
51	2.1	0.35	0.0083	-0.0398	0.75	0.0103
52	4.0	0.59	0.0123	-0.0464	0.75	0.0111
53	6.2	0.81	0.0167	-0.0507	0.74	0.0101
54	8.2	0.86	0.0244	-0.0325	0.75	0.0189
55	10.2	0.92	0.0319	-0.0219	0.75	0.0281
56	11.2	0.97	0.0422	-0.0232	0.75	--
57	12.2	1.01	0.0433	-0.0178	0.75	--
58	13.2	1.04	0.0531	-0.0169	0.74	--
59	14.3	1.05	0.0682	-0.0205	0.74	--
60	15.4	1.03	0.1166	-0.0269	0.75	--
61	16.2	1.01	0.1986	-0.0625	0.76	--
62	17.2	0.83	0.2889	-0.1150	0.76	--
63	18.0	0.77	0.3131	-0.1260	0.76	--
64	19.1	0.76	0.3311	-0.1260	0.77	--
65	20.2	0.72	0.3288	-0.1082	0.76	--

Table B1. S810, Clean, Re = 0.75 x 10^6						
RUN	AOA	C_l	C_{dp}	$C_{m¼}$	Re x10^{-6}	C_{dw}
66	22.1	0.75	0.3766	-0.1169	0.76	--
67	24.0	0.82	0.4439	-0.1364	0.75	--
68	26.2	0.91	0.5260	-0.1592	0.75	--
69	28.1	1.00	0.6199	-0.1877	0.75	--
70	30.0	1.07	0.7061	-0.2130	0.75	--
71	32.2	1.13	0.8003	-0.2388	0.75	--
72	34.1	1.20	0.9041	-0.2687	0.74	--
73	36.0	1.22	0.9764	-0.2858	0.73	--
74	38.0	1.25	1.0738	-0.3122	0.74	--
75	40.0	1.26	1.1510	-0.3280	0.74	--
End of Table B1						

Table B2. S810, Clean, Re = 1 x 10^6						
RUN	AOA	C_l	C_{dp}	$C_{m¼}$	Re x10^{-6}	C_{dw}
11	-20.1	-0.59	0.3156	0.0665	1.00	--
10	-18.1	-0.55	0.2739	0.0592	1.01	--
9	-16.0	-0.47	0.2213	0.0436	1.00	--
8	-14.1	-0.64	0.2125	0.0584	1.01	--
7	-12.2	-0.70	0.1433	0.0163	1.00	--
6	-10.1	-0.73	0.0632	-0.0309	1.00	0.0792
5	-8.2	-0.65	0.0333	-0.0317	1.00	0.0449
4	-6.2	-0.50	0.0152	-0.0258	1.00	0.0281
3	-4.0	-0.28	0.0034	-0.0209	1.00	0.0150
2	-2.1	-0.11	0.0018	-0.0246	1.00	0.0116
1	-0.1	0.13	0.0026	-0.0353	1.01	0.0084
12	0.0	0.14	0.0030	-0.0357	1.00	0.0083
38	0.0	0.13	0.0041	-0.0341	1.00	0.0081
13	2.1	0.34	0.0083	-0.0407	1.00	0.0090
14	4.0	0.59	0.0095	-0.0449	1.00	0.0089
15	6.1	0.78	0.0140	-0.0451	1.00	0.0105
16	8.2	0.85	0.0215	-0.0308	1.00	0.0215
17	10.1	0.93	0.0311	-0.0254	1.00	0.0274
18	11.2	0.98	0.0365	-0.0227	1.00	--
19	12.3	1.03	0.0443	-0.0201	1.00	--
20	13.1	1.06	0.0488	-0.0205	1.00	--
21	14.2	1.09	0.0643	-0.0228	1.00	--
22	15.3	1.07	0.1071	-0.0279	1.00	--
23	16.3	1.03	0.1818	-0.0573	0.99	--
24	17.1	0.91	0.2782	-0.1038	1.01	--
25	18.2	0.82	0.3148	-0.1224	1.01	--
26	19.0	0.80	0.3417	-0.1323	1.01	--
27	20.0	0.72	0.3288	-0.1083	1.02	--

Table B2. S810, Clean, Re = 1 x 10^6						
RUN	AOA	C_l	C_{dp}	$C_{m¼}$	Re x10^{-6}	C_{dw}
28	22.2	0.76	0.3841	-0.1195	1.01	--
29	24.1	0.83	0.4502	-0.1378	1.01	--
30	26.0	0.93	0.5335	-0.1649	1.00	--
31	28.2	1.00	0.6172	-0.1863	1.00	--
32	30.1	1.08	0.7146	-0.2162	1.00	--
33	32.0	1.14	0.8015	-0.2406	1.00	--
34	34.2	1.20	0.9048	-0.2691	0.99	--
35	36.1	1.23	0.9932	-0.2921	0.99	--
36	37.9	1.25	1.0683	-0.3101	0.99	--
37	40.1	1.26	1.1540	-0.3277	0.99	--
End of Table B2						

Table B3. S810, Clean, Re = 1.25 x 10^6						
RUN	AOA	C_l	C_{dp}	$C_{m¼}$	Re x10^{-6}	C_{dw}
337	-20.2	-0.59	0.3146	0.0663	1.26	--
336	-18.2	-0.54	0.2724	0.0588	1.26	--
335	-16.1	-0.55	0.2420	0.0628	1.27	--
334	-14.0	-0.65	0.2105	0.0595	1.26	--
333	-12.2	-0.70	0.1403	0.0146	1.26	--
332	-10.2	-0.72	0.0631	-0.0311	1.26	0.0784
331	-8.2	-0.65	0.0328	-0.0303	1.25	0.0464
330	-6.1	-0.50	0.0139	-0.0247	1.25	0.0276
329	-4.1	-0.29	0.0029	-0.0200	1.25	0.0158
328	-2.1	-0.09	0.0026	-0.0256	1.25	0.0102
327	0.0	0.13	0.0026	-0.0350	1.26	0.0075
364	0.0	0.13	0.0035	-0.0332	1.24	0.0082
338	0.1	0.13	0.0029	-0.0345	1.25	0.0069
339	2.1	0.37	0.0051	-0.0407	1.25	0.0074
340	4.0	0.61	0.0076	-0.0471	1.26	0.0072
341	6.2	0.76	0.0148	-0.0420	1.25	0.0099
342	8.2	0.85	0.0176	-0.0290	1.25	0.0246
343	10.1	0.95	0.0285	-0.0252	1.25	0.0283
344	11.2	0.99	0.0357	-0.0230	1.25	0.0306
345	12.3	1.04	0.0410	-0.0196	1.25	0.0379
346	13.2	1.08	0.0469	-0.0206	1.26	--
347	14.2	1.10	0.0598	-0.0195	1.25	--
348	15.1	1.11	0.0722	-0.0215	1.24	--
349	16.1	1.04	0.1932	-0.0623	1.26	--
350	17.2	0.92	0.2743	-0.1068	1.27	--
351	18.2	0.85	0.3153	-0.1229	1.28	--
352	19.0	0.81	0.3379	-0.1279	1.28	--
353	20.1	0.72	0.3307	-0.1105	1.28	--

Table B3. S810, Clean, Re = 1.25 x 10^6						
RUN	AOA	C_l	C_{dp}	$C_{m¼}$	Re x10^{-6}	C_{dw}
354	22.0	0.78	0.3904	-0.1252	1.25	--
355	24.2	0.85	0.4580	-0.1419	1.25	--
356	26.1	0.93	0.5340	-0.1643	1.25	--
357	28.1	1.01	0.6243	-0.1917	1.24	--
358	30.2	1.07	0.7112	-0.2126	1.24	--
359	32.1	1.15	0.8111	-0.2441	1.23	--
360	34.1	1.21	0.9146	-0.2749	1.24	--
361	36.1	1.24	0.9993	-0.2943	1.24	--
362	38.1	1.26	1.0884	-0.3166	1.23	--
363	40.0	1.26	1.1577	-0.3318	1.23	--
End of Table B3						

Table B4. S810, Clean, Re = 1.5 x 10^6						
RUN	AOA	C_l	C_{dp}	$C_{m¼}$	Re x10^{-6}	C_{dw}
411	-20.0	-0.59	0.3115	0.0656	1.48	--
410	-18.1	-0.55	0.2754	0.0618	1.49	--
409	-16.1	-0.57	0.2510	0.0724	1.50	--
408	-14.0	-0.58	0.2170	0.0714	1.51	--
407	-12.1	-0.70	0.1340	0.0123	1.51	--
406	-10.2	-0.72	0.0644	-0.0309	1.51	0.0729
405	-8.3	-0.64	0.0331	-0.0302	1.50	0.0434
404	-6.0	-0.49	0.0135	-0.0244	1.50	0.0273
403	-4.1	-0.29	0.0022	-0.0201	1.51	0.0147
402	-2.1	-0.09	0.0023	-0.0251	1.50	0.0098
401	-0.1	0.12	0.0020	-0.0333	1.50	0.0069
412	0.1	0.12	0.0026	-0.0331	1.50	0.0067
428	0.1	0.13	0.0026	-0.0330	1.50	0.0066
413	2.1	0.37	0.0053	-0.0407	1.50	0.0074
414	4.1	0.61	0.0077	-0.0470	1.50	0.0067
415	6.2	0.76	0.0153	-0.0425	1.50	0.0097
416	8.2	0.85	0.0208	-0.0300	1.50	0.0230
417	10.2	0.94	0.0308	-0.0260	1.50	0.0271
418	11.3	1.00	0.0361	-0.0235	1.50	--
419	12.2	1.05	0.0388	-0.0203	1.50	--
420	13.2	1.08	0.0506	-0.0209	1.51	--
421	14.3	1.11	0.0595	-0.0189	1.50	--
422	15.2	1.15	0.0783	-0.0251	1.50	--
423	16.2	1.05	0.1861	-0.0673	1.53	--
424	17.1	0.82	0.2915	-0.1215	1.51	--
425	18.0	0.77	0.3142	-0.1284	1.49	--
426	19.1	0.77	0.3357	-0.1307	1.47	--
427	20.2	0.75	0.3483	-0.1259	1.48	--
End of Table B4						

Table B5. S810, LEGR, Re = 0.75 x 10^6						
RUN	AOA	C_l	C_{dp}	$C_{m¼}$	Re x10^{-6}	C_{dw}
87	-20.1	-0.59	0.3226	0.0708	0.76	--
86	-18.2	-0.55	0.2810	0.0636	0.74	--
85	-16.0	-0.48	0.2315	0.0536	0.75	--
84	-14.2	-0.65	0.1955	0.0397	0.75	--
83	-12.3	-0.72	0.0927	-0.0246	0.75	--
82	-10.1	-0.68	0.0483	-0.0308	0.75	0.0754
81	-8.2	-0.60	0.0245	-0.0286	0.76	0.0492
80	-6.0	-0.46	0.0099	-0.0223	0.75	0.0251
79	-4.0	-0.29	0.0058	-0.0213	0.75	0.0169
78	-2.1	-0.11	0.0037	-0.0227	0.75	0.0148
77	0.0	0.10	0.0037	-0.0264	0.75	0.0148
88	0.0	0.10	0.0030	-0.0262	0.75	0.0149
114	0.1	0.10	0.0038	-0.0271	0.75	0.0146
89	2.1	0.30	0.0074	-0.0285	0.75	0.0146
90	4.0	0.49	0.0112	-0.0297	0.75	0.0148
91	6.1	0.65	0.0159	-0.0271	0.75	0.0173
92	8.2	0.75	0.0218	-0.0199	0.74	0.0347
93	10.1	0.85	0.0293	-0.0150	0.75	--
94	11.2	0.91	0.0369	-0.0129	0.74	--
95	12.3	0.94	0.0447	-0.0130	0.75	--
96	13.1	0.97	0.0512	-0.0111	0.74	--
97	14.2	0.98	0.0664	-0.0138	0.76	--
98	15.3	0.86	0.0918	-0.0238	0.75	--
99	16.1	0.81	0.1464	-0.0534	0.76	--
100	17.2	0.83	0.1948	-0.0738	0.75	--
101	18.2	0.92	0.2475	-0.0946	0.76	--
102	19.1	0.97	0.2886	-0.1047	0.75	--
103	20.2	0.97	0.3231	-0.1119	0.76	--

Table B5. S810, LEGR, Re = 0.75 x 10^6						
RUN	AOA	C_l	C_{dp}	$C_{m¼}$	Re x10^{-6}	C_{dw}
104	22.1	1.04	0.3882	-0.1221	0.76	--
105	24.2	0.78	0.4300	-0.1328	0.75	--
106	26.1	0.87	0.4786	-0.1335	0.74	--
107	28.0	1.01	0.6198	-0.1898	0.74	--
108	30.1	1.08	0.7060	-0.2127	0.74	--
109	32.1	1.14	0.8010	-0.2405	0.73	--
110	34.1	1.21	0.9061	-0.2702	0.73	--
111	35.9	1.23	0.9809	-0.2883	0.73	--
112	38.1	1.24	1.0666	-0.3094	0.72	--
113	40.0	1.27	1.1611	-0.3358	0.70	--
End of Table B5						

Table B6. S810, LEGR, Re = 1 x 10^6						
RUN	AOA	C_l	C_{dp}	$C_{m¼}$	Re x10^{-6}	C_{dw}
125	-20.2	-0.56	0.3109	0.0661	1.00	--
124	-18.0	-0.53	0.2671	0.0574	1.01	--
123	-16.1	-0.57	0.2341	0.0648	1.00	--
122	-14.3	-0.73	0.1657	0.0173	1.00	--
121	-12.1	-0.72	0.0872	-0.0237	1.00	--
120	-10.2	-0.67	0.0483	-0.0299	1.00	0.0773
119	-8.1	-0.61	0.0214	-0.0262	0.99	0.0465
118	-6.1	-0.48	0.0087	-0.0188	1.01	0.0259
117	-4.1	-0.30	0.0042	-0.0213	1.01	0.0179
116	-2.1	-0.14	0.0023	-0.0223	1.01	0.0158
126	-0.1	0.08	0.0017	-0.0265	0.99	0.0141
115	0.0	0.09	0.0022	-0.0262	1.01	0.0134
152	0.0	0.09	0.0024	-0.0260	1.00	0.0148
127	2.1	0.29	0.0059	-0.0297	1.01	0.0133
128	4.0	0.48	0.0086	-0.0294	1.00	0.0149
129	6.3	0.64	0.0136	-0.0243	1.00	0.0179
130	8.2	0.74	0.0196	-0.0191	1.01	0.0295
131	10.2	0.85	0.0302	-0.0159	1.00	0.0378
132	11.2	0.90	0.0333	-0.0134	1.00	--
133	12.3	0.95	0.0449	-0.0145	1.00	--
134	13.2	0.97	0.0531	-0.0139	1.00	--
135	14.3	1.00	0.0686	-0.0173	0.99	--
136	15.1	0.95	0.0777	-0.0171	1.00	--
137	16.2	0.84	0.1400	-0.0512	1.01	--
138	17.2	0.86	0.1859	-0.0694	0.99	--
139	18.1	0.93	0.2383	-0.0931	1.01	--
140	19.1	0.97	0.2806	-0.1037	1.00	--
141	20.1	1.00	0.3195	-0.1111	1.01	--

Table B6. S810, LEGR, Re = 1 x 10^6						
RUN	AOA	C_l	C_{dp}	$C_{m¼}$	Re x10^{-6}	C_{dw}
142	22.2	1.10	0.3882	-0.1135	1.00	--
143	24.1	1.03	0.4550	-0.1292	1.01	--
144	26.2	0.96	0.5062	-0.1413	1.01	--
145	28.1	0.98	0.6030	-0.1817	1.00	--
146	30.0	1.06	0.6946	-0.2080	1.00	--
147	32.1	1.13	0.7946	-0.2372	0.98	--
148	34.2	1.20	0.9006	-0.2680	0.98	--
149	36.0	1.21	0.9726	-0.2841	0.98	--
150	38.0	1.25	1.0666	-0.3099	0.99	--
151	40.1	1.26	1.1546	-0.3308	0.97	--
End of Table B6						

Table B7. S810, LEGR, Re = 1.25 x 10^6						
RUN	AOA	C_l	C_{dp}	$C_{m¼}$	Re x10^{-6}	C_{dw}
163	-20.2	-0.54	0.3010	0.0590	1.26	--
162	-18.2	-0.53	0.2734	0.0596	1.26	--
161	-16.0	-0.58	0.2334	0.0685	1.26	--
160	-14.2	-0.72	0.1469	0.0016	1.26	--
159	-12.1	-0.71	0.0863	-0.0265	1.26	--
158	-10.1	-0.66	0.0489	-0.0298	1.25	0.0750
157	-8.2	-0.62	0.0232	-0.0263	1.25	0.0437
156	-6.3	-0.49	0.0075	-0.0199	1.25	0.0264
155	-4.0	-0.30	0.0035	-0.0208	1.26	0.0181
154	-2.1	-0.13	0.0016	-0.0225	1.25	0.0132
190	-0.2	0.08	0.0022	-0.0262	1.25	0.0128
164	-0.1	0.09	0.0020	-0.0262	1.25	0.0135
153	0.1	0.09	0.0027	-0.0272	1.25	0.0128
165	2.1	0.31	0.0045	-0.0293	1.25	0.0133
166	4.0	0.48	0.0071	-0.0284	1.25	0.0149
167	6.2	0.64	0.0117	-0.0241	1.26	0.0190
168	8.2	0.74	0.0180	-0.0185	1.26	0.0319
169	10.1	0.85	0.0264	-0.0149	1.25	0.0382
170	11.2	0.91	0.0330	-0.0136	1.25	--
171	12.3	0.96	0.0410	-0.0133	1.25	--
172	13.1	0.98	0.0471	-0.0123	1.25	--
173	14.2	1.00	0.0606	-0.0132	1.25	--
174	15.3	0.93	0.0766	-0.0158	1.25	--
175	16.1	0.83	0.1416	-0.0521	1.25	--
176	17.2	0.86	0.1913	-0.0727	1.26	--
177	18.2	0.94	0.2401	-0.0930	1.27	--
178	19.1	0.97	0.2828	-0.1068	1.27	--
179	20.2	0.95	0.3199	-0.1146	1.28	--

Table B7. S810, LEGR, Re = 1.25 x 10^6						
RUN	AOA	C_l	C_{dp}	$C_{m¼}$	Re x10^{-6}	C_{dw}
180	22.1	1.10	0.3881	-0.1198	1.26	--
181	24.2	1.04	0.4538	-0.1286	1.25	--
182	26.1	0.98	0.5072	-0.1404	1.25	--
183	28.1	1.00	0.6076	-0.1858	1.25	--
184	30.2	1.07	0.7016	-0.2112	1.25	--
185	32.1	1.14	0.7969	-0.2378	1.25	--
186	34.1	1.20	0.8981	-0.2673	1.23	--
187	35.9	1.24	0.9879	-0.2927	1.22	--
188	38.1	1.26	1.0821	-0.3165	1.21	--
189	39.9	1.27	1.1554	-0.3345	1.19	--
End of Table B7						

Table B8. S810, LEGR, Re = 1.5 x 10^6						
RUN	AOA	C_l	C_{dp}	$C_{m¼}$	Re x10^{-6}	C_{dw}
201	-20.1	-0.55	0.3039	0.0580	1.43	--
200	-18.2	-0.55	0.2773	0.0631	1.45	--
199	-16.1	-0.68	0.2321	0.0494	1.46	--
198	-14.2	-0.70	0.1514	0.0041	1.48	--
197	-12.2	-0.71	0.0864	-0.0281	1.50	--
196	-10.1	-0.67	0.0498	-0.0309	1.51	0.0703
195	-8.2	-0.62	0.0255	-0.0271	1.51	0.0427
194	-6.2	-0.49	0.0068	-0.0185	1.50	0.0286
193	-4.0	-0.31	0.0031	-0.0197	1.51	0.0172
192	-2.1	-0.14	0.0022	-0.0216	1.50	0.0142
218	0.0	0.09	0.0030	-0.0257	1.50	0.0127
191	0.1	0.09	0.0038	-0.0252	1.50	0.0123
202	0.1	0.10	0.0031	-0.0267	1.50	0.0124
203	2.1	0.30	0.0059	-0.0286	1.50	0.0128
204	4.0	0.48	0.0081	-0.0290	1.50	0.0140
205	6.1	0.64	0.0110	-0.0245	1.51	0.0169
206	8.2	0.75	0.0169	-0.0170	1.50	0.0336
207	10.1	0.87	0.0259	-0.0150	1.50	0.0375
208	11.2	0.92	0.0324	-0.0133	1.50	--
209	12.3	0.96	0.0400	-0.0117	1.50	--
210	13.1	0.99	0.0466	-0.0122	1.49	--
211	14.2	1.01	0.0583	-0.0114	1.51	--
212	15.2	0.93	0.0706	-0.0123	1.51	--
213	16.1	0.84	0.1361	-0.0486	1.50	--
214	17.2	0.87	0.1973	-0.0753	1.48	--
215	18.2	0.92	0.2457	-0.0943	1.46	--
216	19.1	0.94	0.2823	-0.1065	1.45	--
217	20.1	0.93	0.3210	-0.1170	1.44	--
End of Table B8						

S810

Pressure Distributions, Steady State, Re = 0.75 million

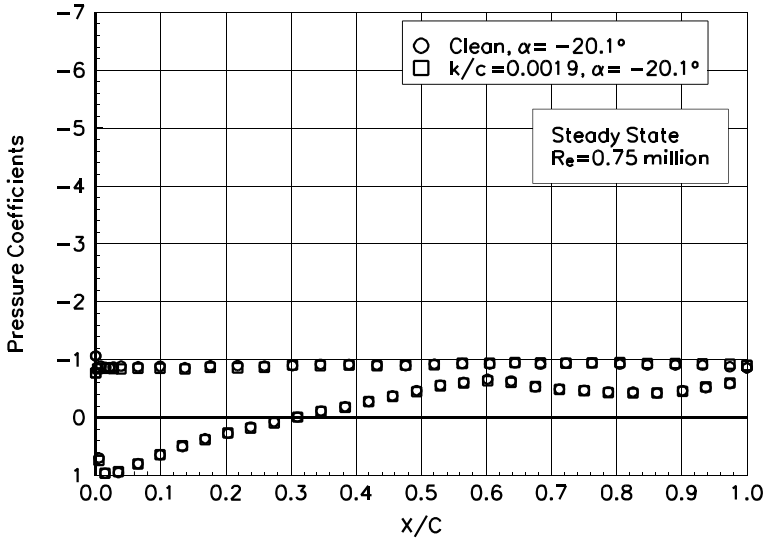

Figure 1. α = -20.1°

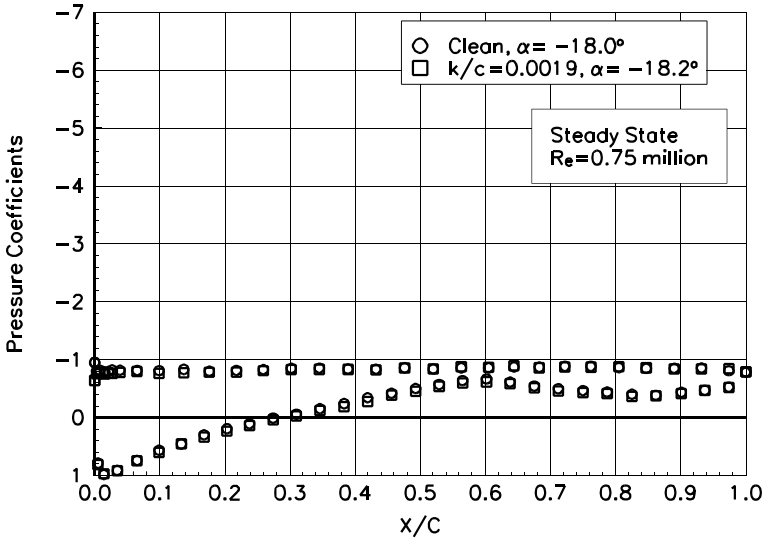

Figure 2. α = -18.0°

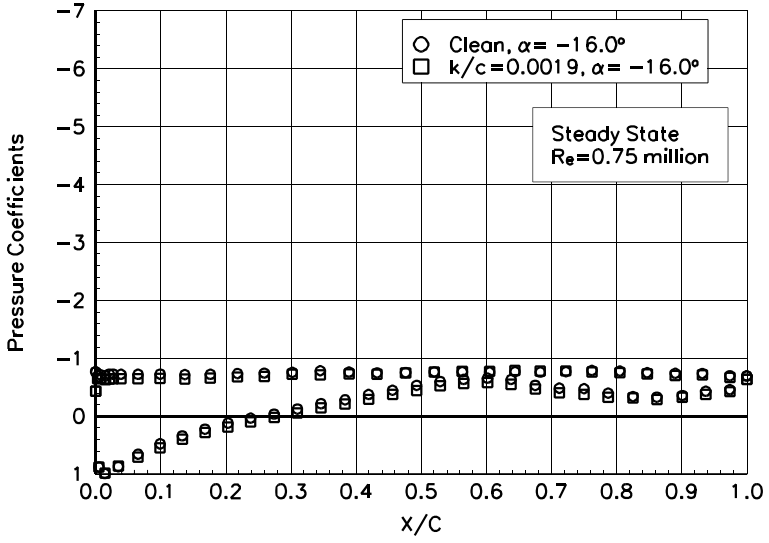

Figure 3. α = -16.0°

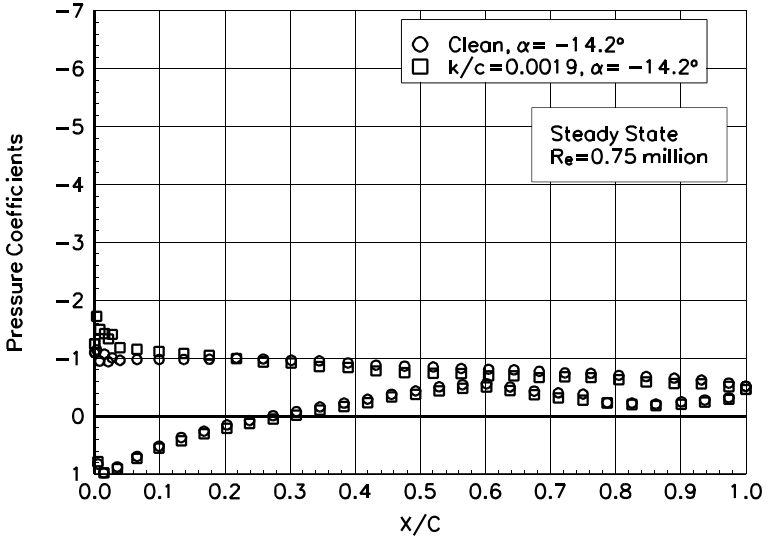

Figure 4. α = -14.2°

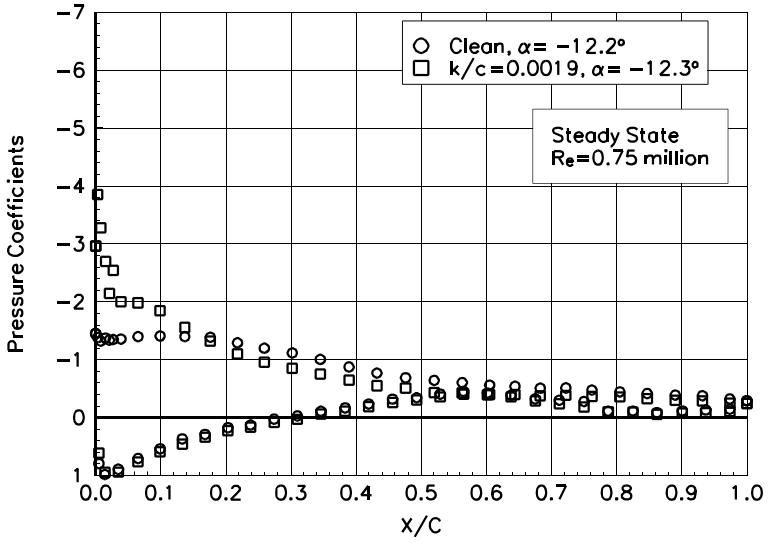

Figure 5. α = -12.2°

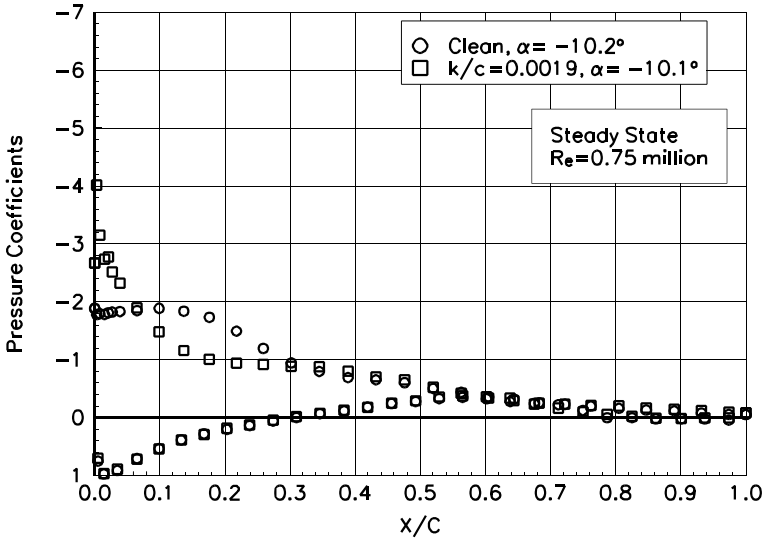

Figure 6. α = -10.2°

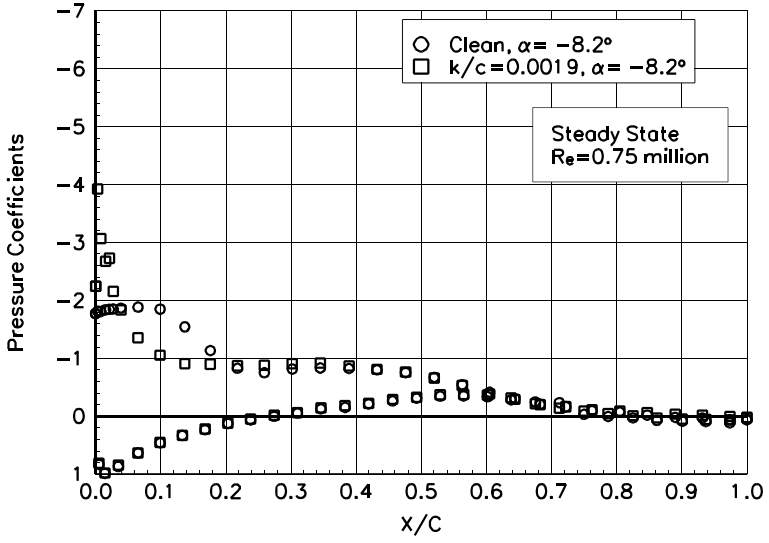

Figure 7. α = -8.2°

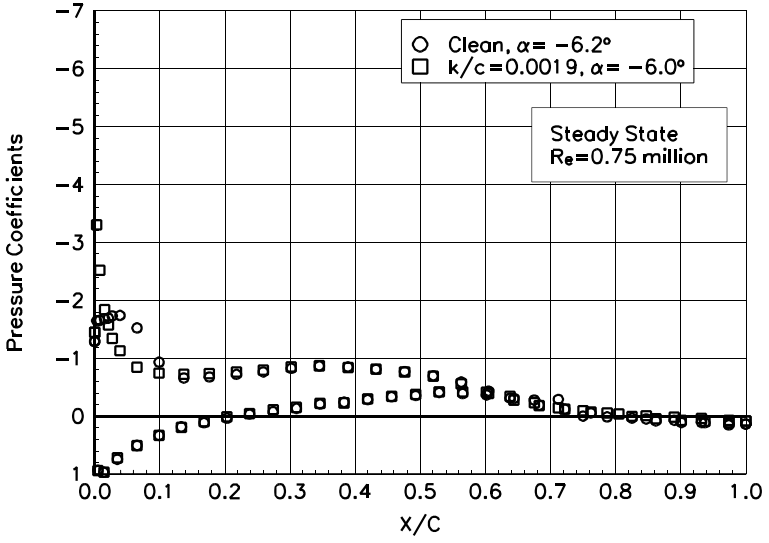

Figure 8. α = -6.2°

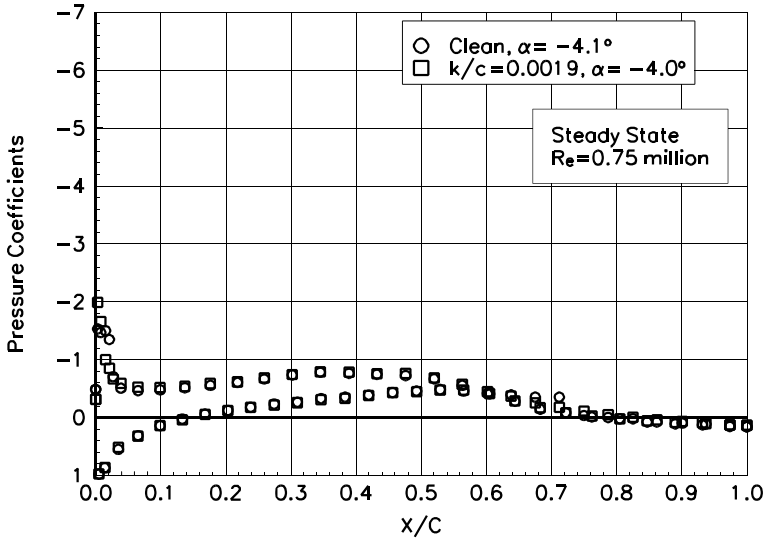

Figure 9. α = -4.1°

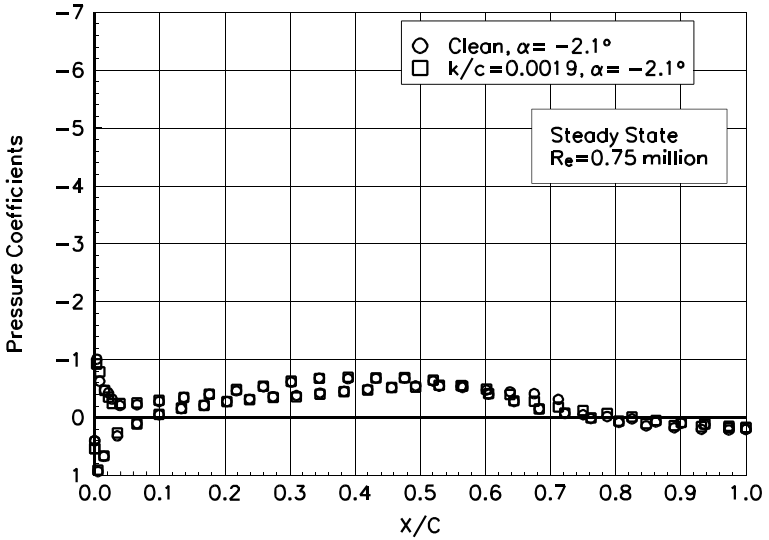

Figure 10. α = -2.1°

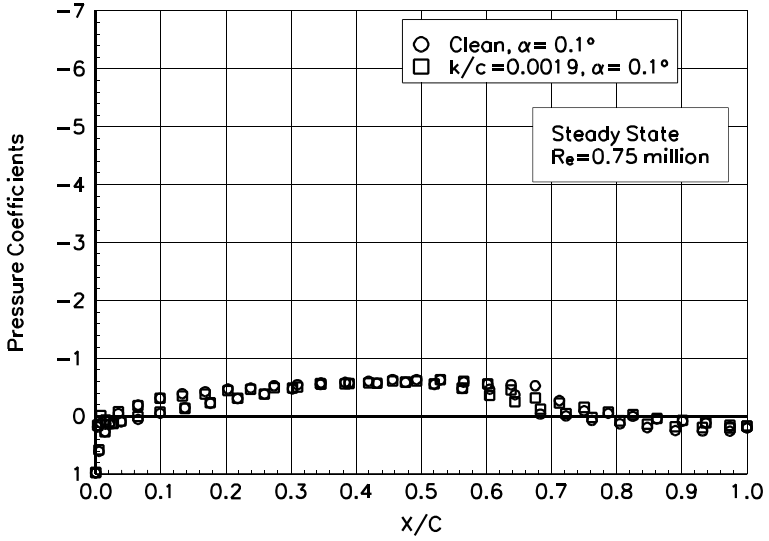

Figure 11. α = 0.1°

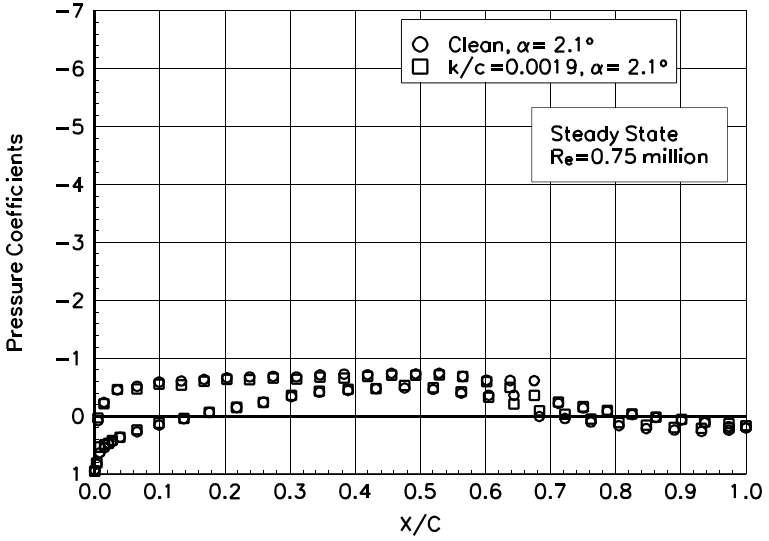

Figure 12. α = 2.1°

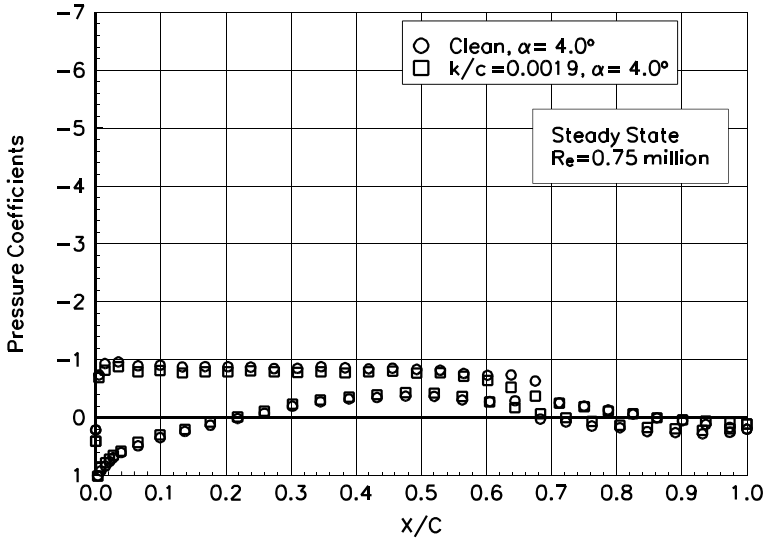

Figure 13. α = 4.0°

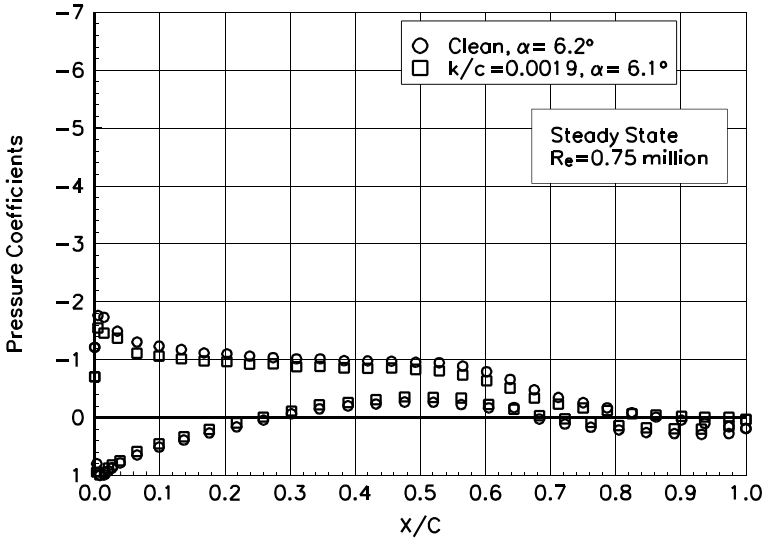

Figure 14. α = 6.2°

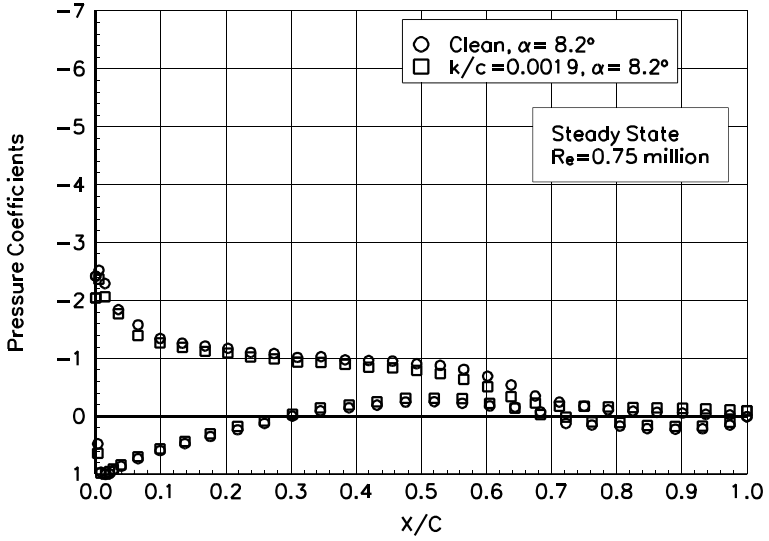

Figure 15. α = 8.2°

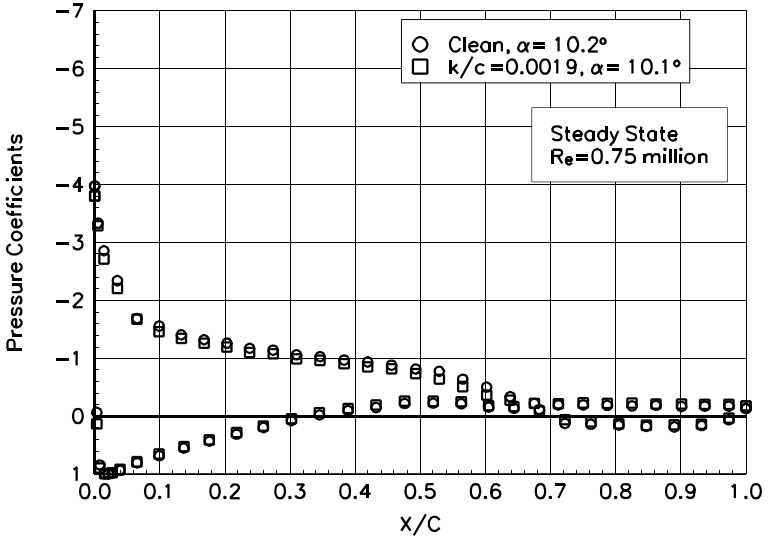

Figure 16. α = 10.2°

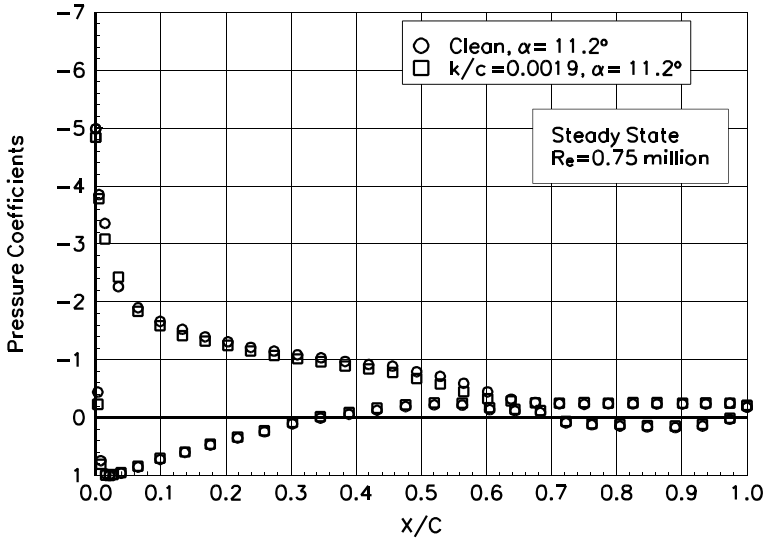

Figure 17. α = 11.2°

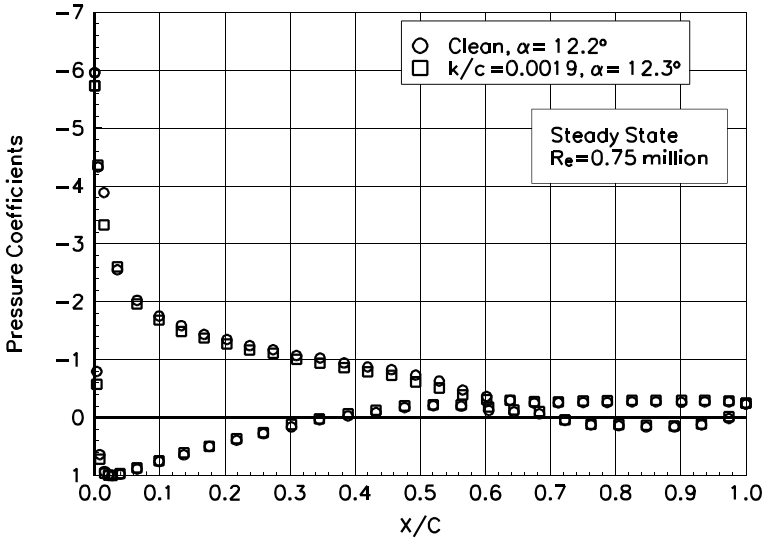

Figure 18. α = 12.2°

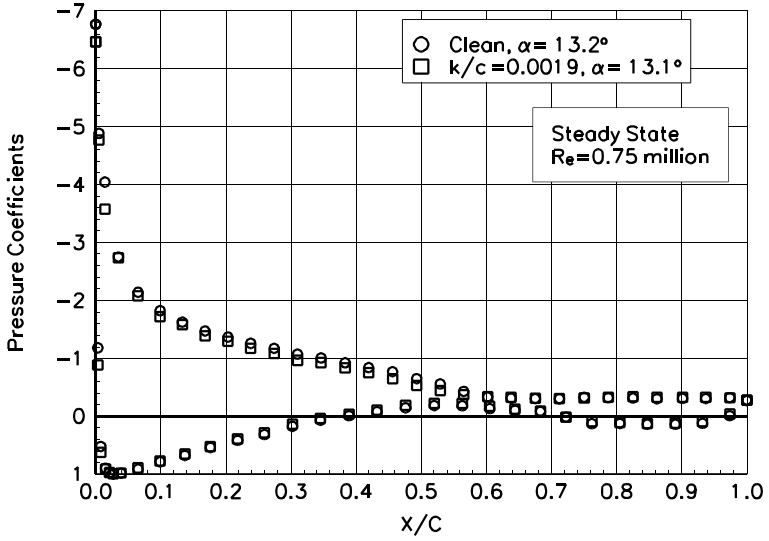

Figure 19. α = 13.2°

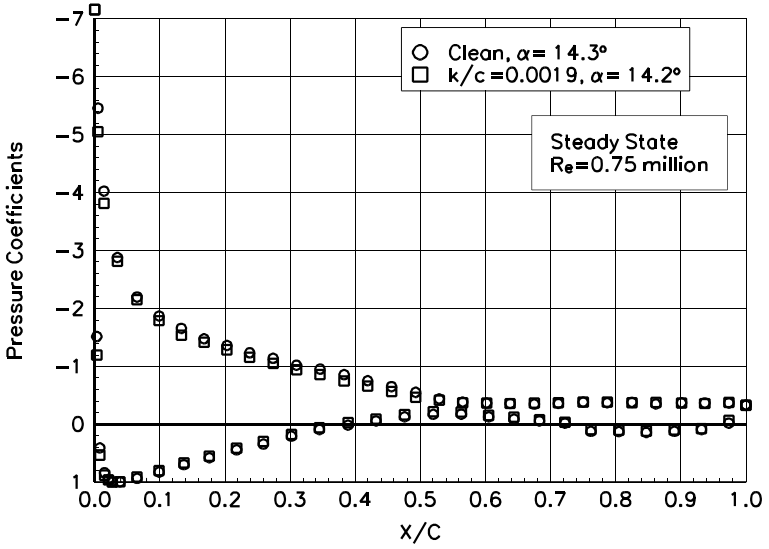

Figure 20. α = 14.3°

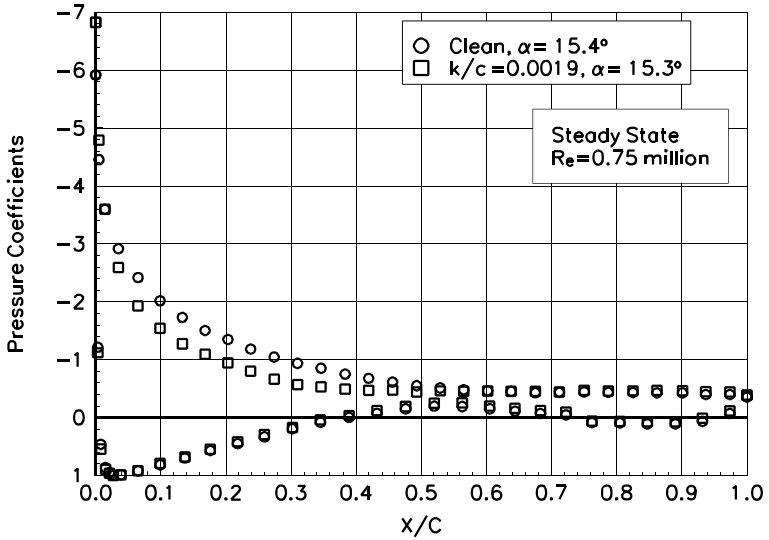

Figure 21. α = 15.4°

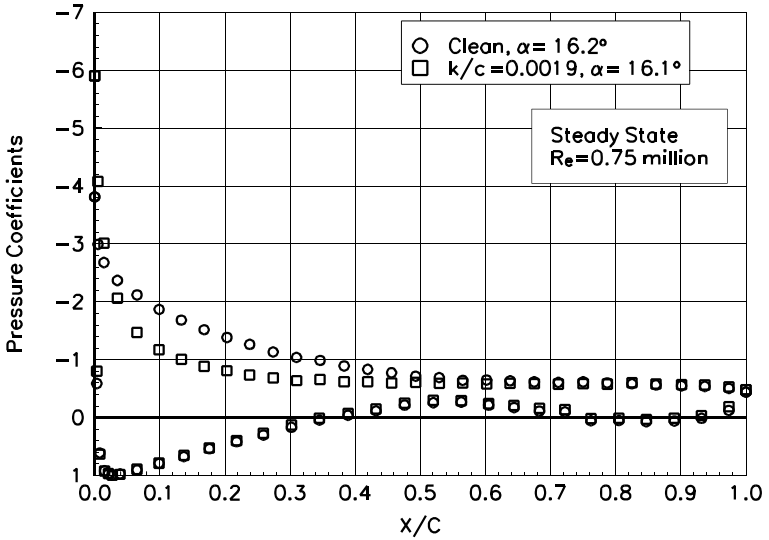

Figure 22. α = 16.2°

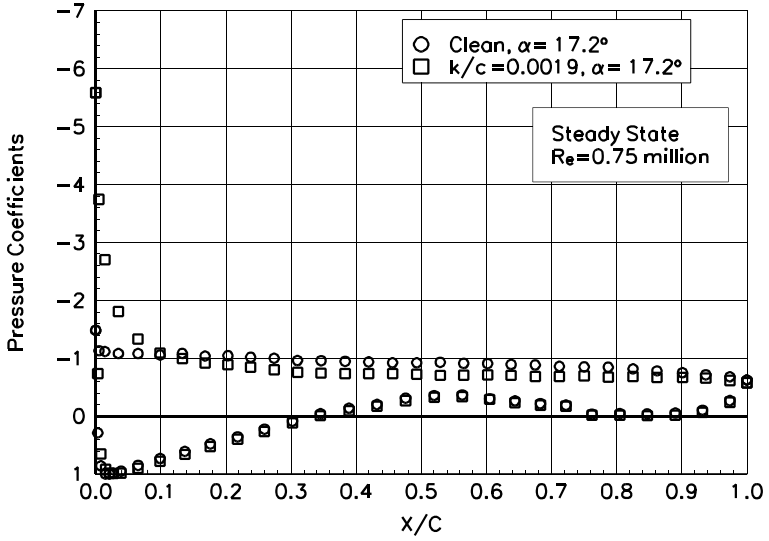

Figure 23. α = 17.2°

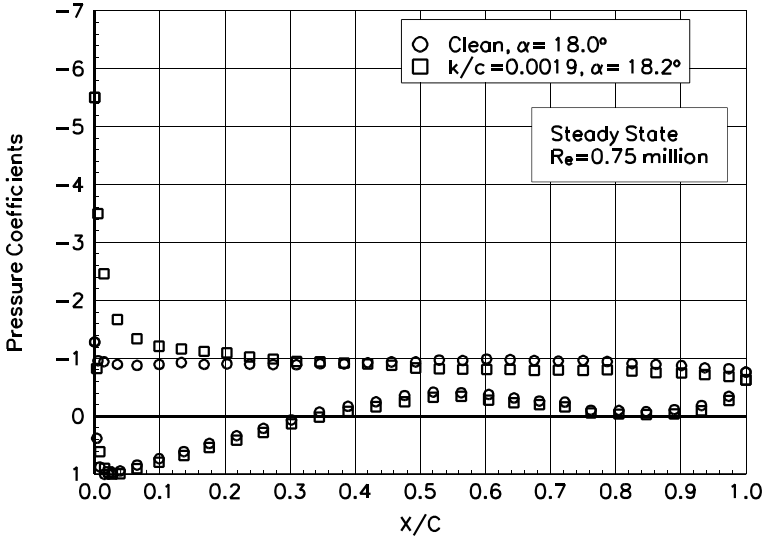

Figure 24. α = 18.0°

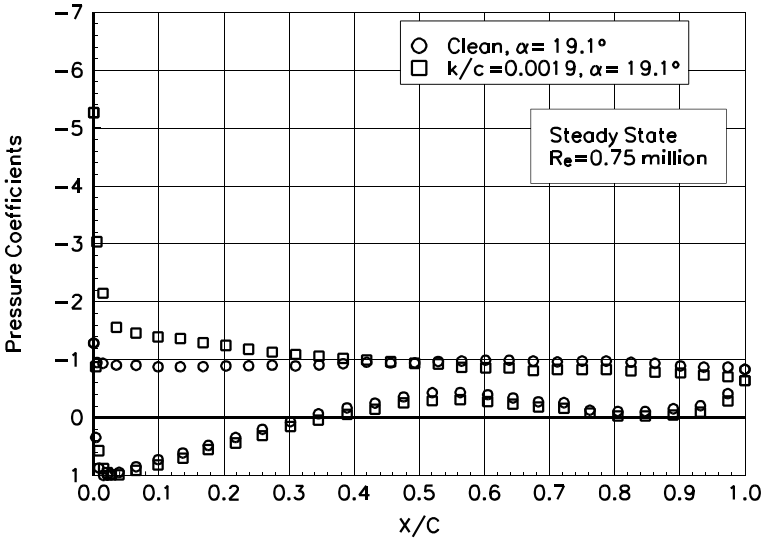

Figure 25. α = 19.1°

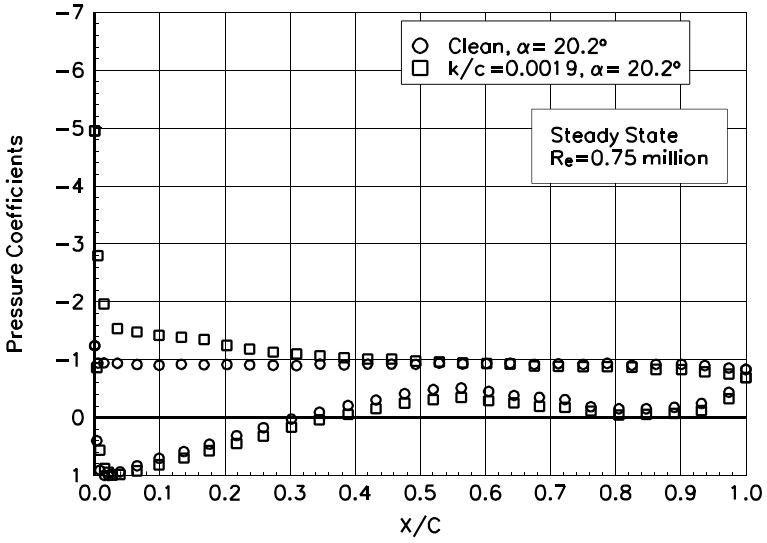

Figure 26. α = 20.2°

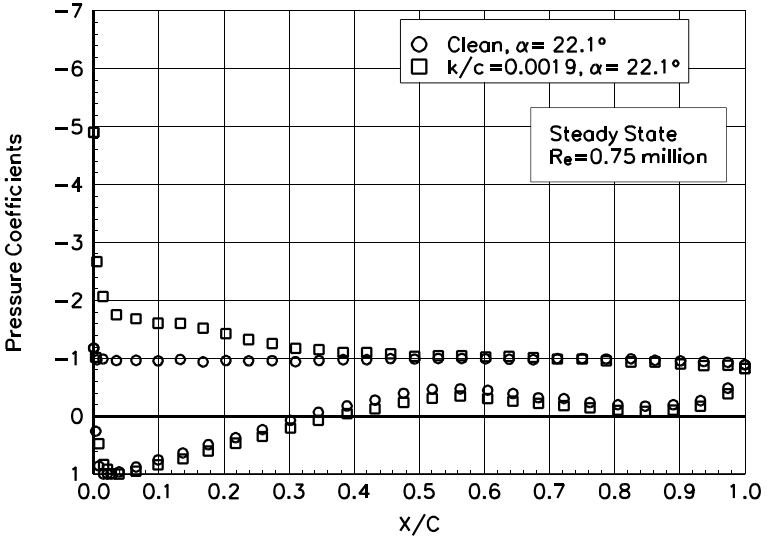

Figure 27. α = 22.1°

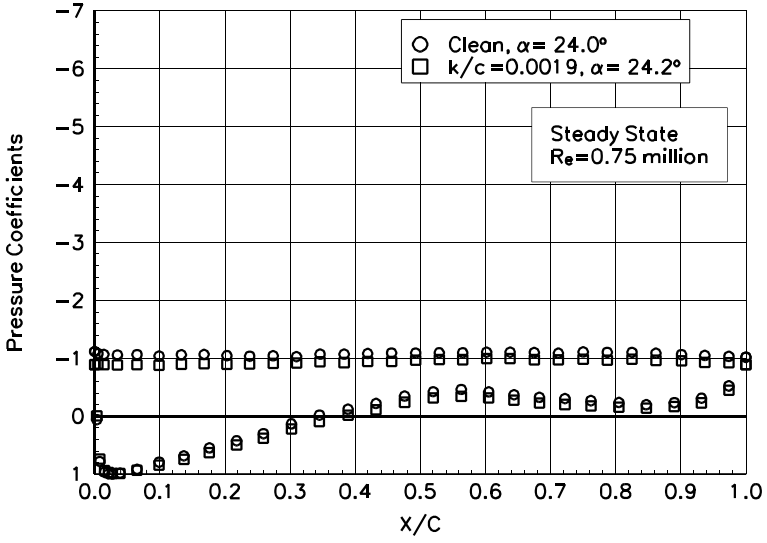

Figure 28. α = 24.0°

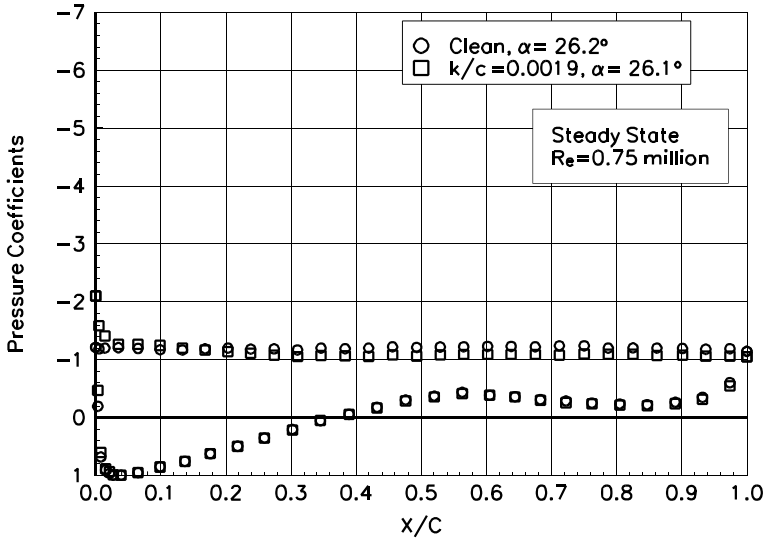

Figure 29. α = 26.2°

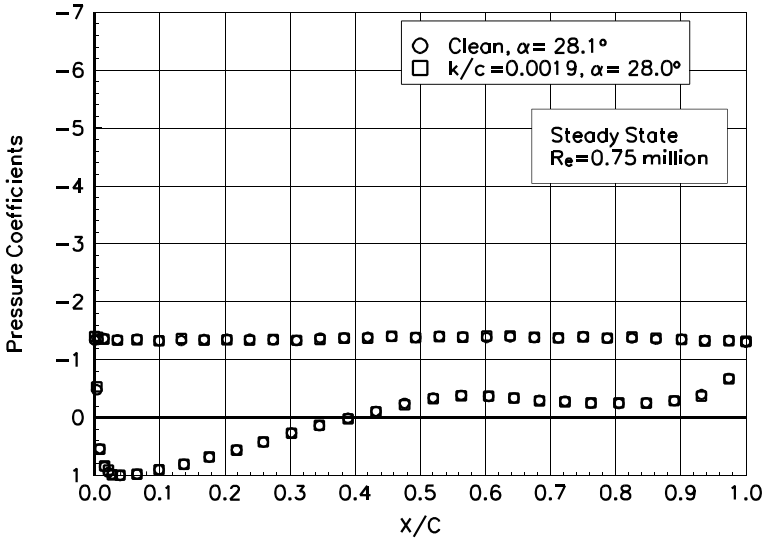

Figure 30. α = 28.1°

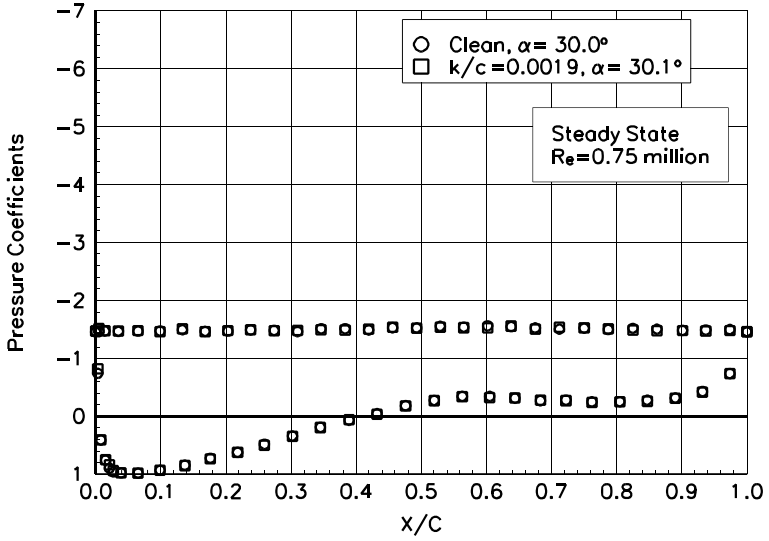

Figure 31. α = 30.0°

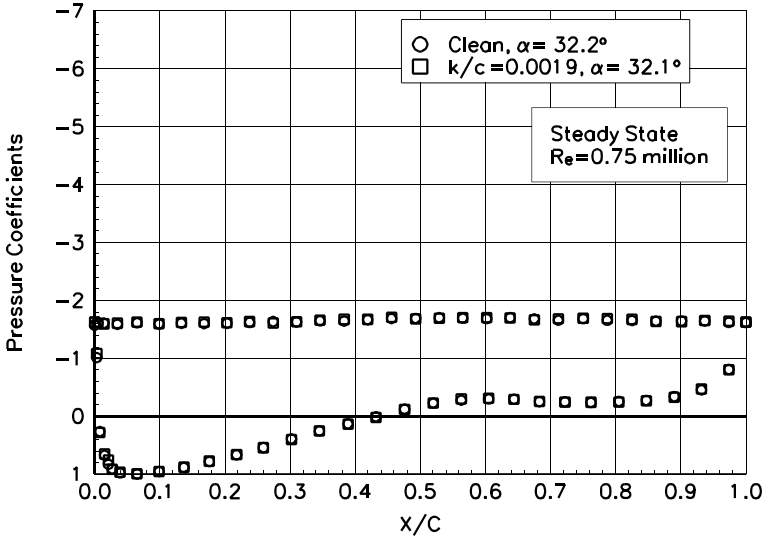

Figure 32. α = 32.2°

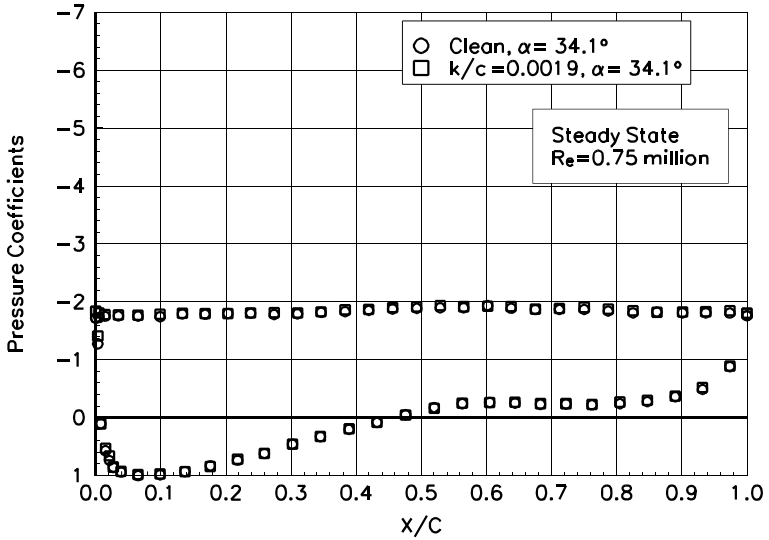

Figure 33. α = 34.1°

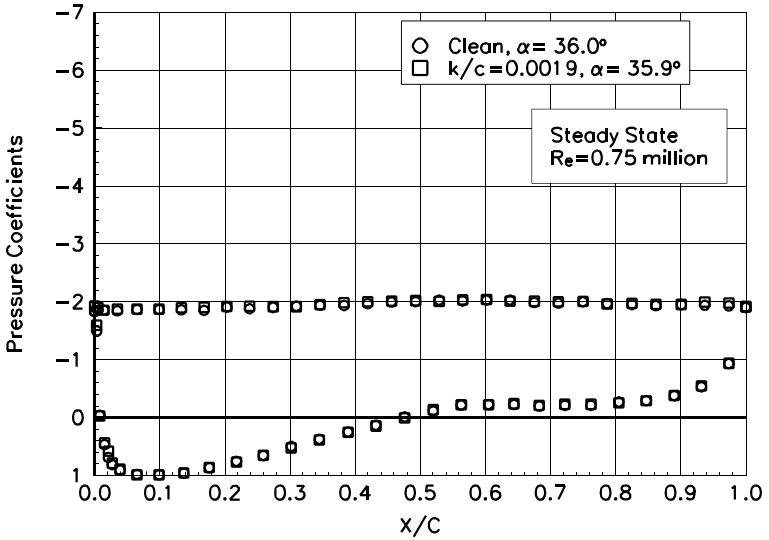

Figure 34. α = 36.0°

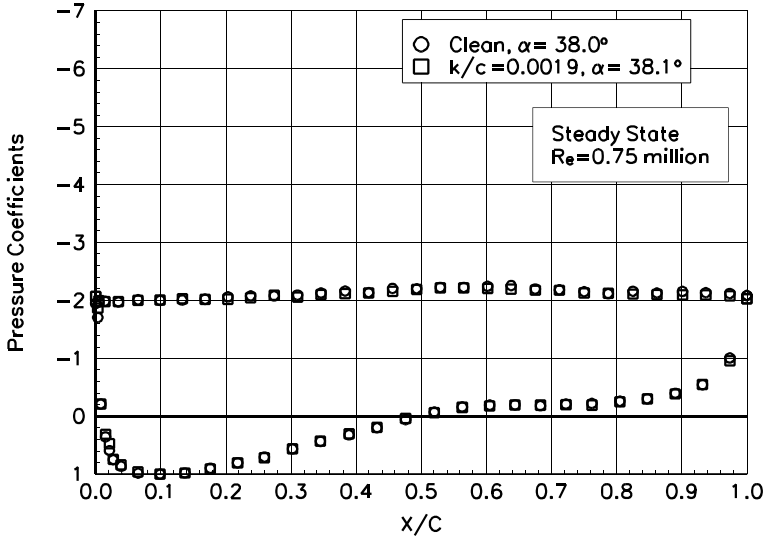

Figure 35. α = 38.0°

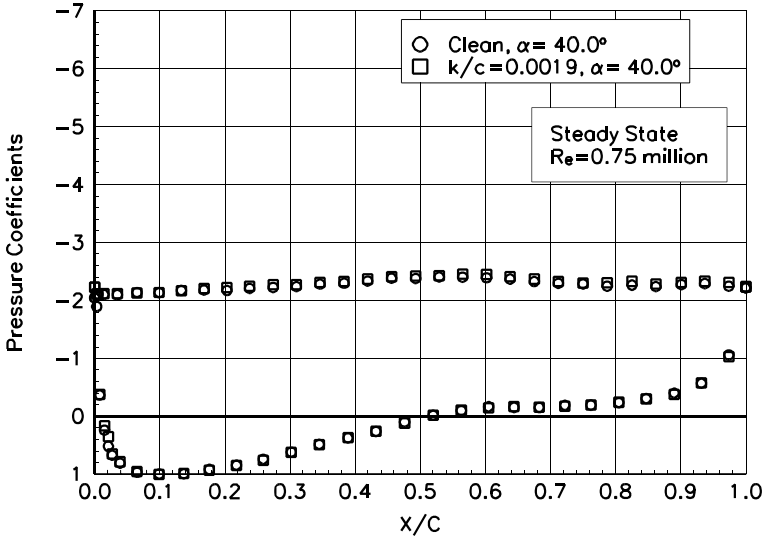

Figure 36. α = 40.0°

S810

Pressure Distributions, Steady State, Re = 1 million

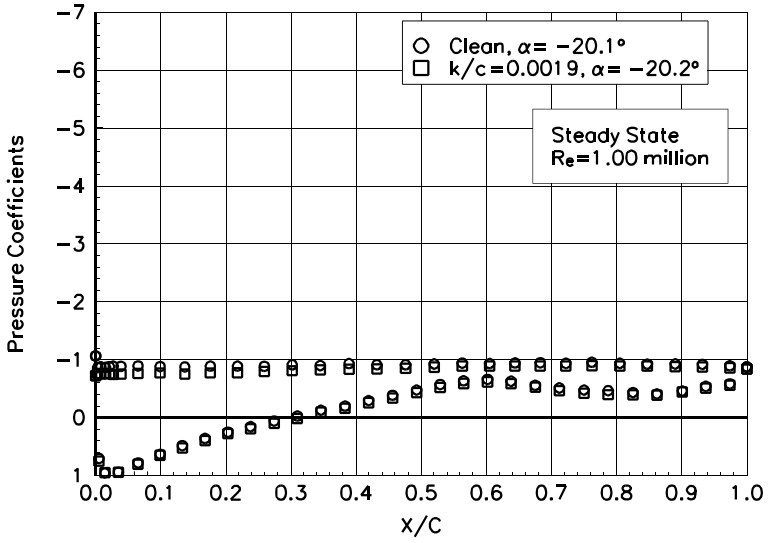

Figure 37. α = -20.1°

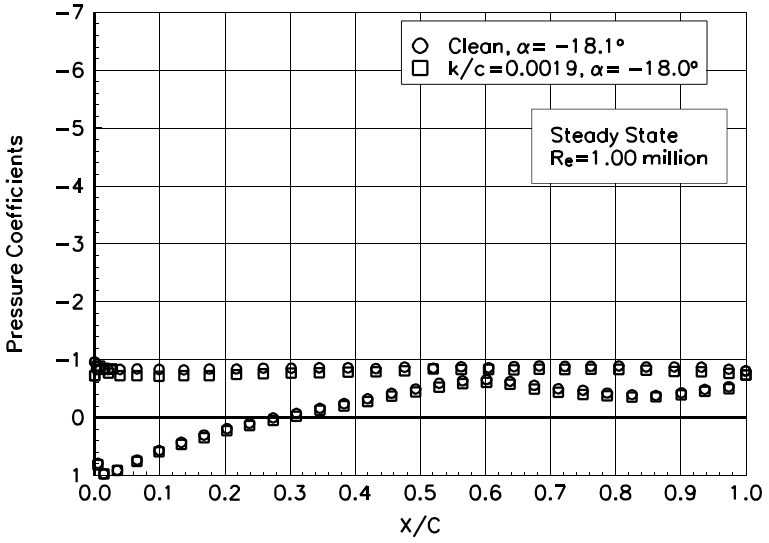

Figure 38. α = -18.1°

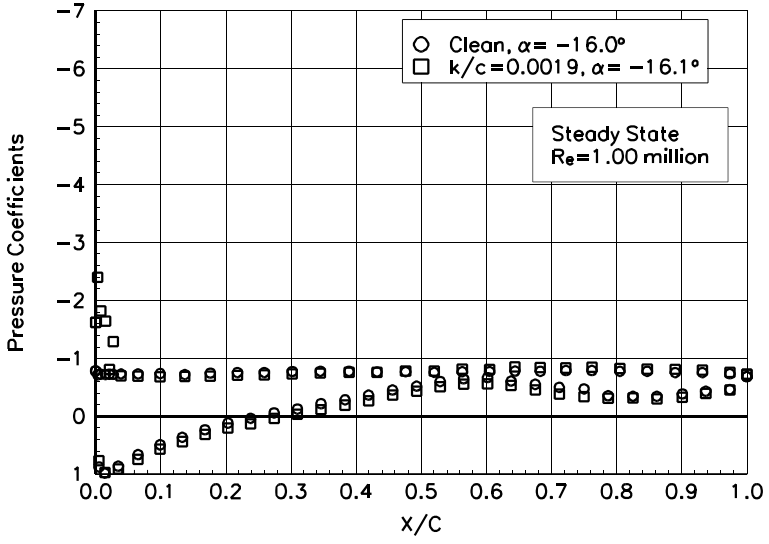

Figure 39. α = -16.0°

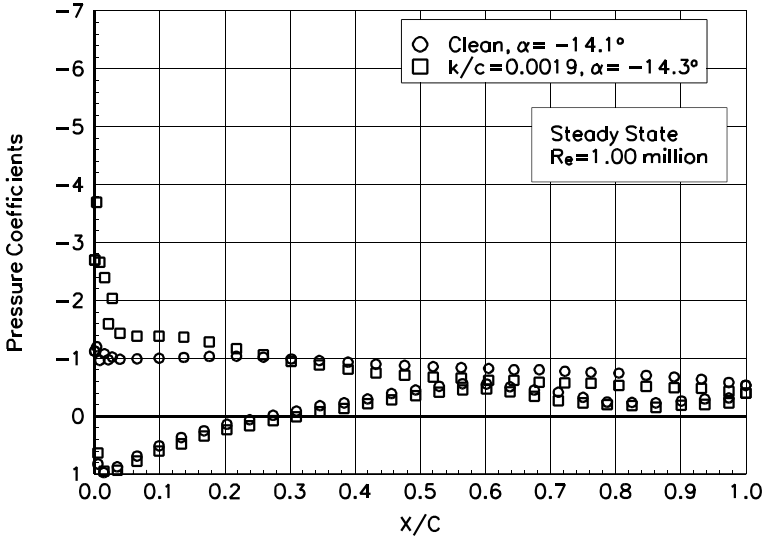

Figure 40. α = -14.1°

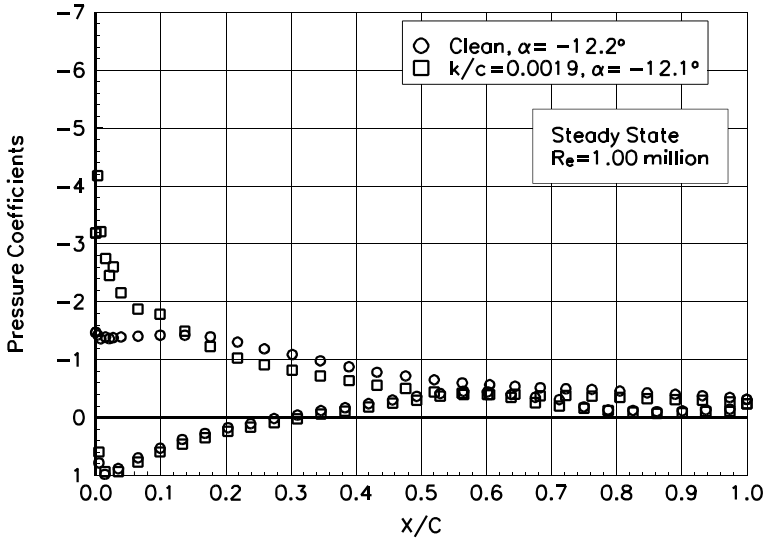

Figure 41. α = -12.2°

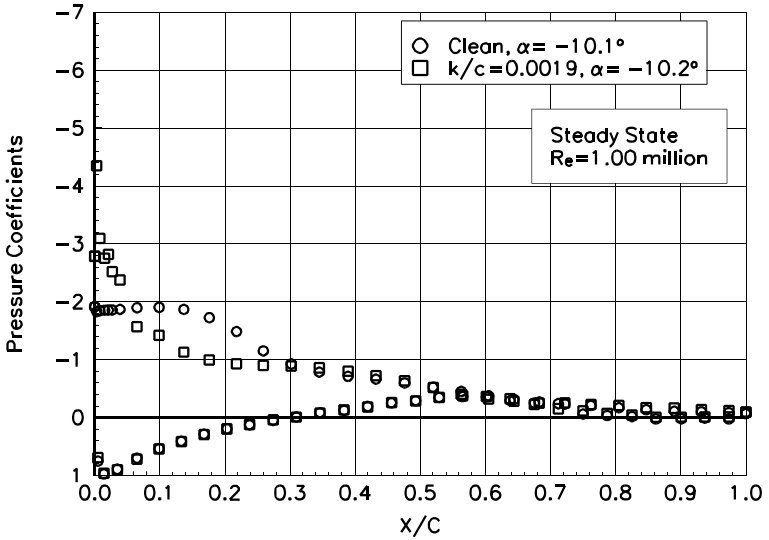

Figure 42. α = -10.1°

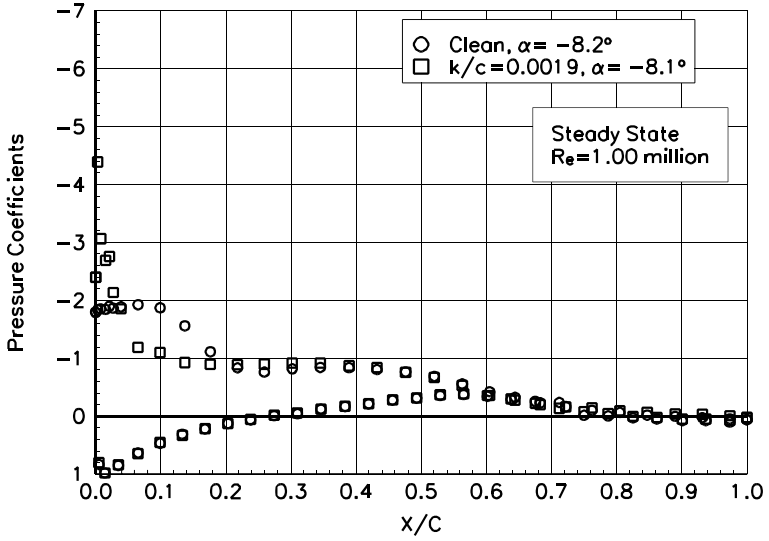

Figure 43. α = -8.2°

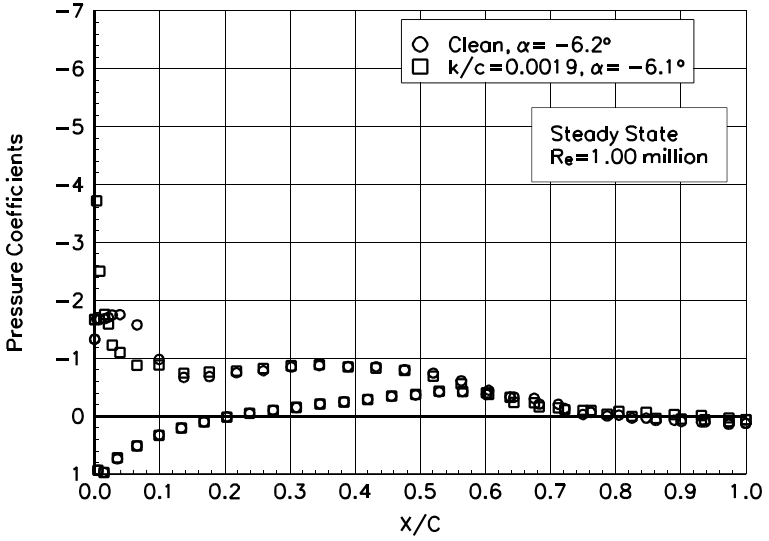

Figure 44. α = -6.2°

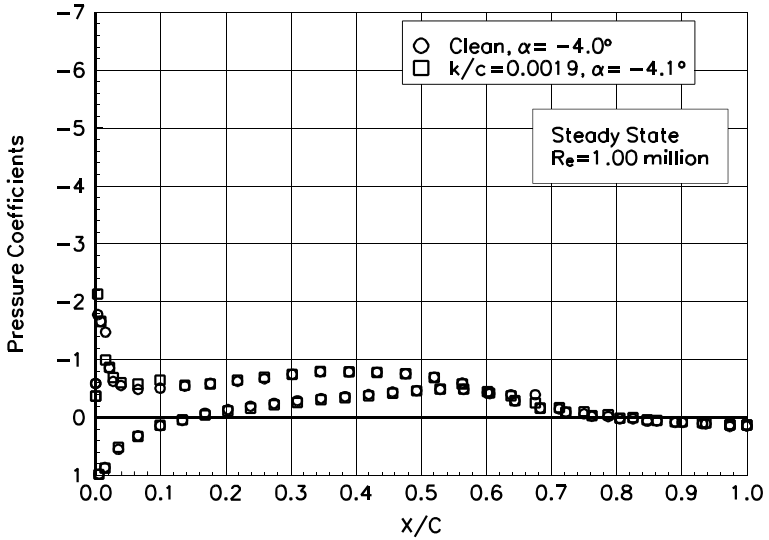

Figure 45. α = -4.0°

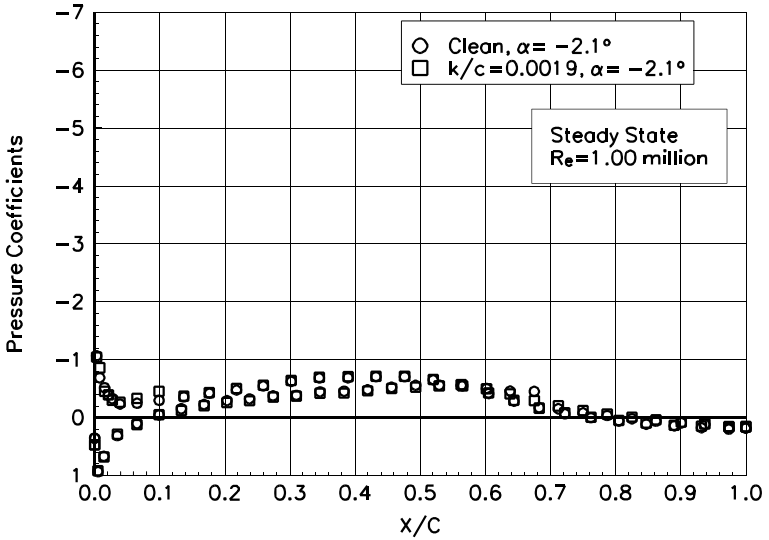

Figure 46. α = -2.1°

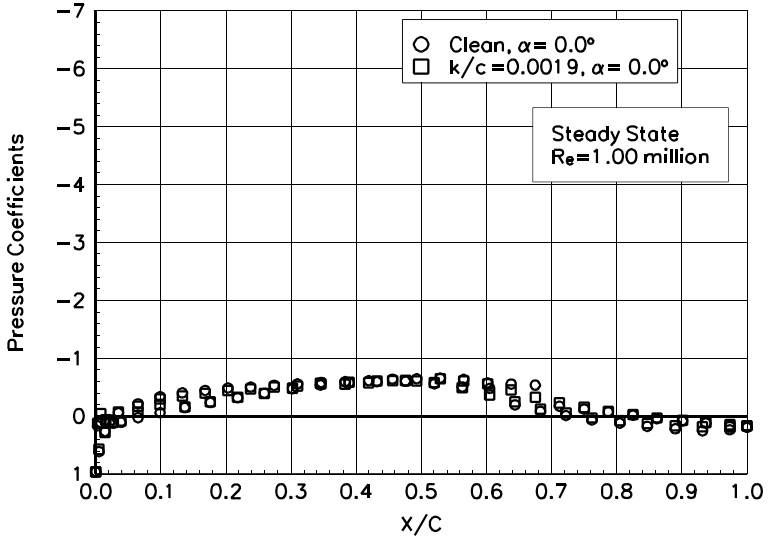

Figure 47. α = 0.0°

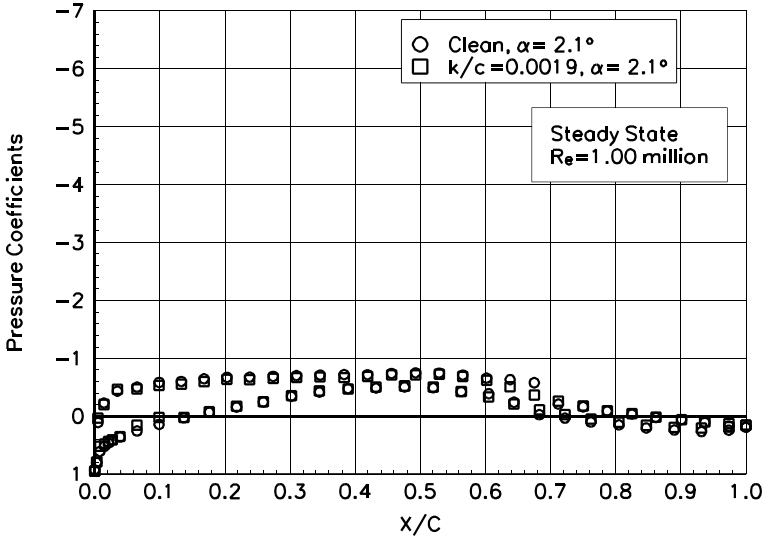

Figure 48. α = 2.1°

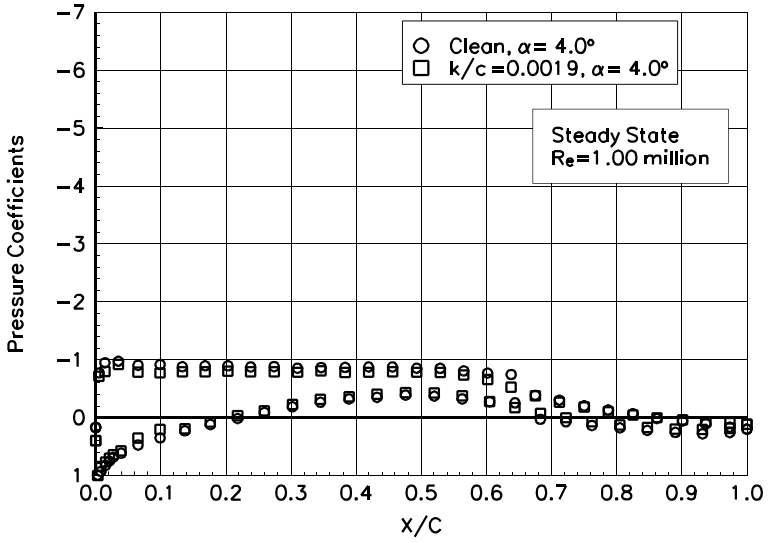

Figure 49. α = 4.0°

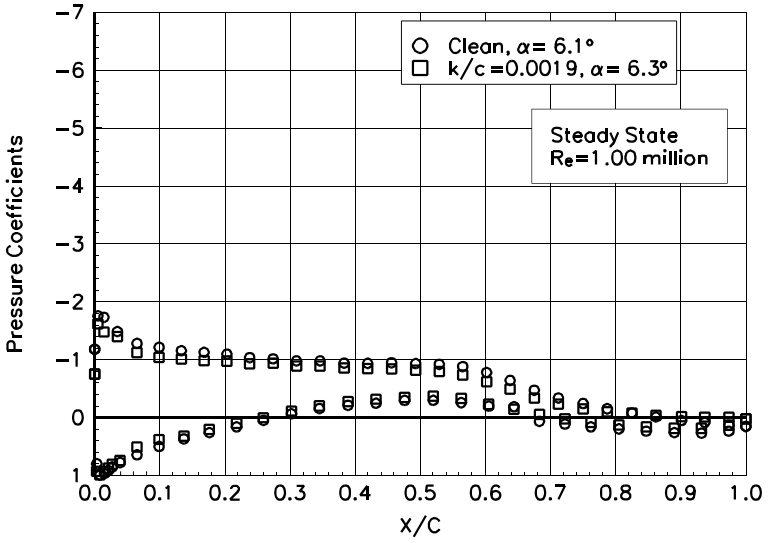

Figure 50. α = 6.1°

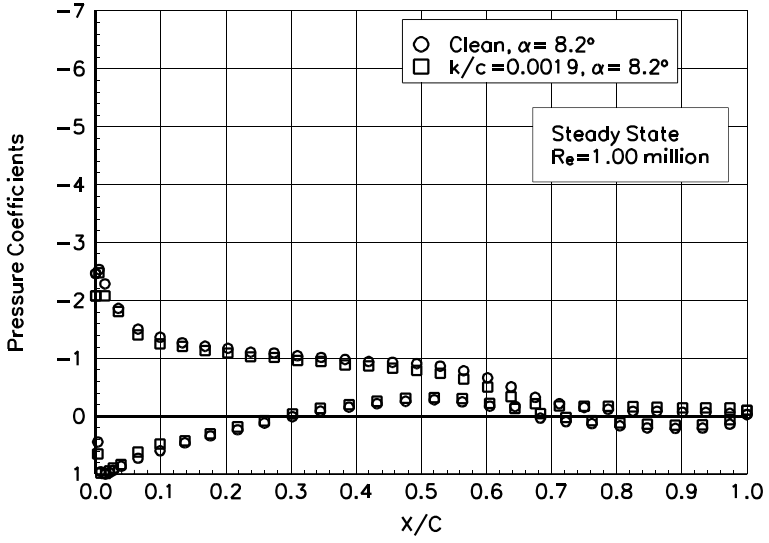

Figure 51. α = 8.2°

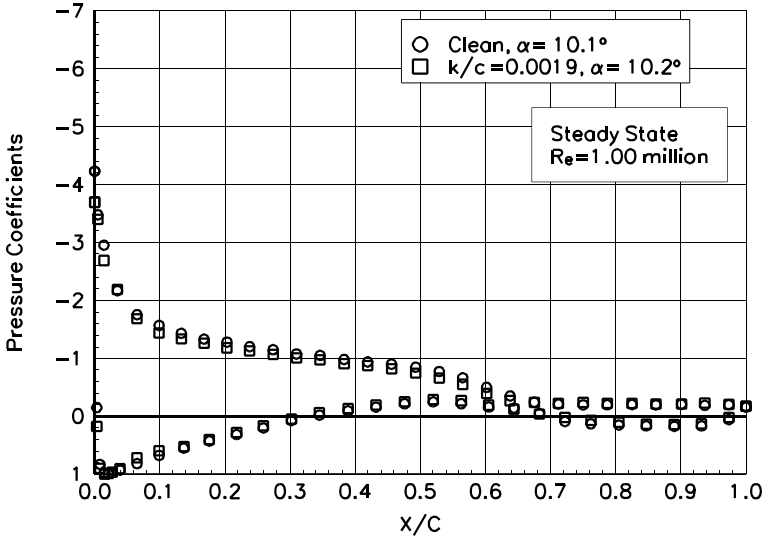

Figure 52. α = 10.1°

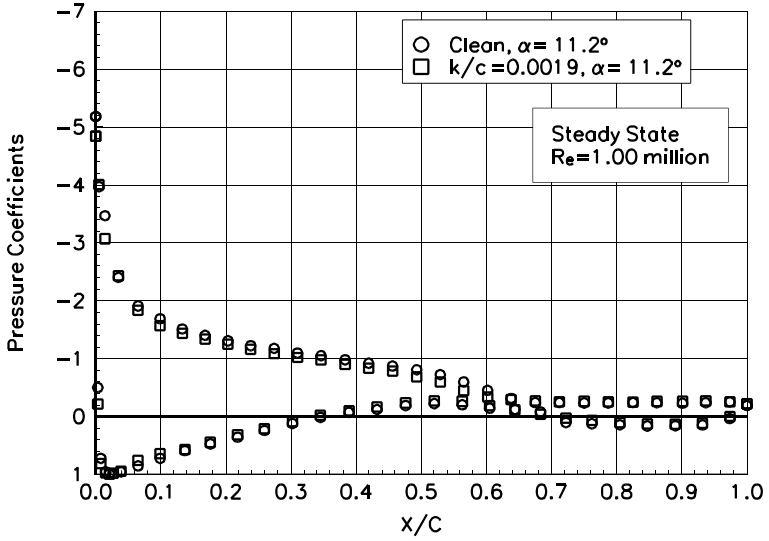

Figure 53. α = 11.2°

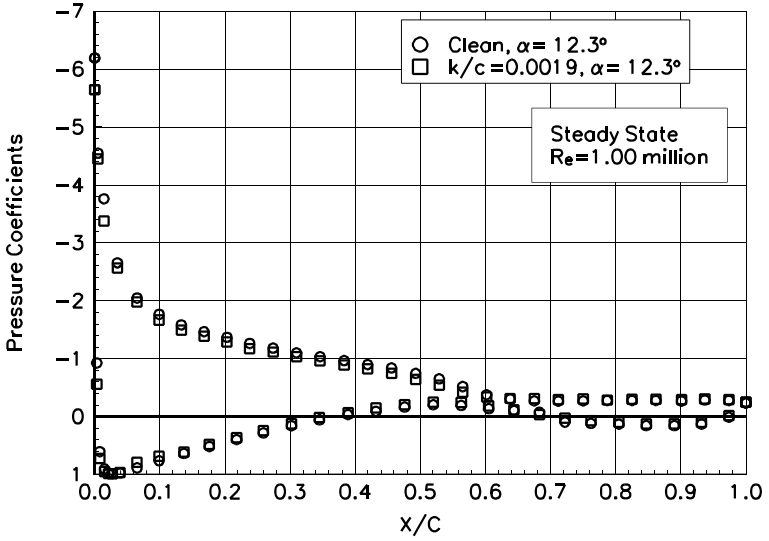

Figure 54. α = 12.3°

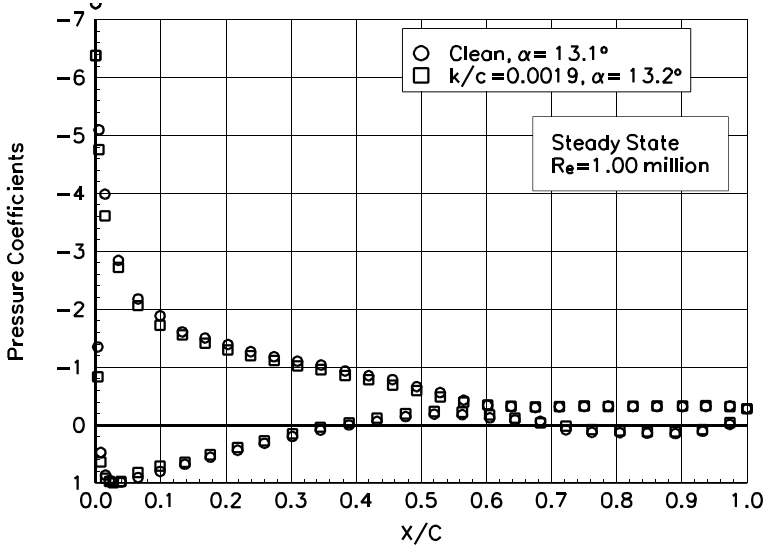

Figure 55. α = 13.1°

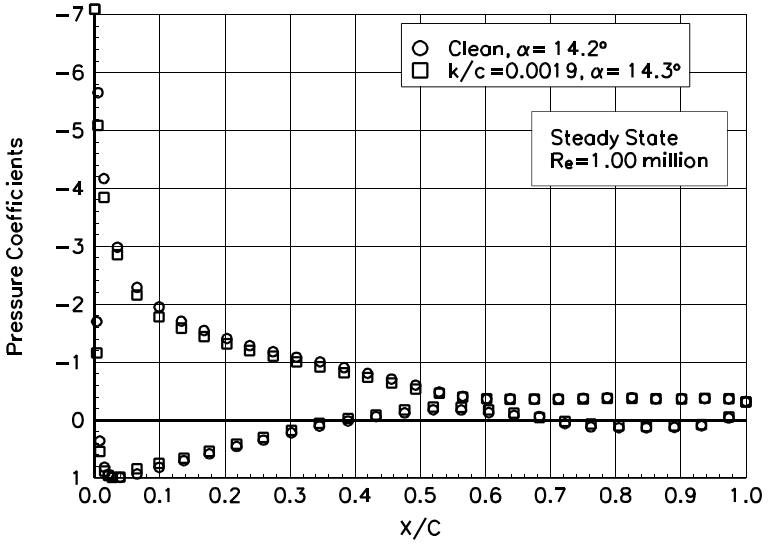

Figure 56. α = 14.2°

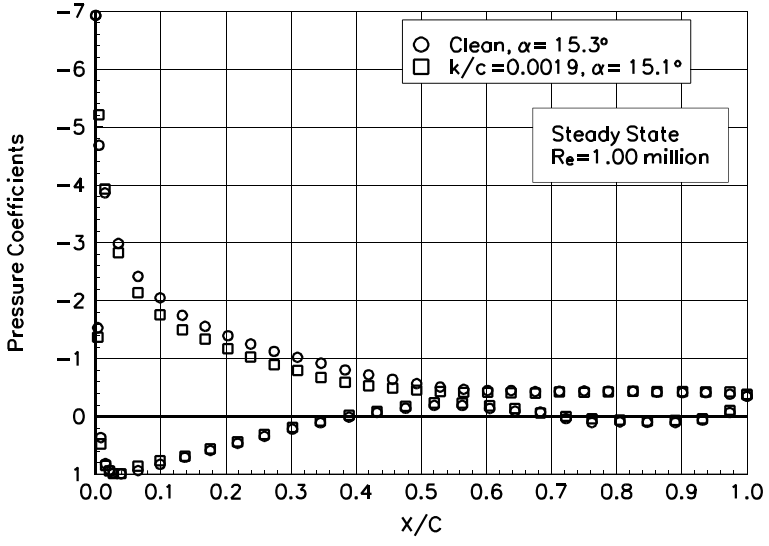

Figure 57. α = 15.3°

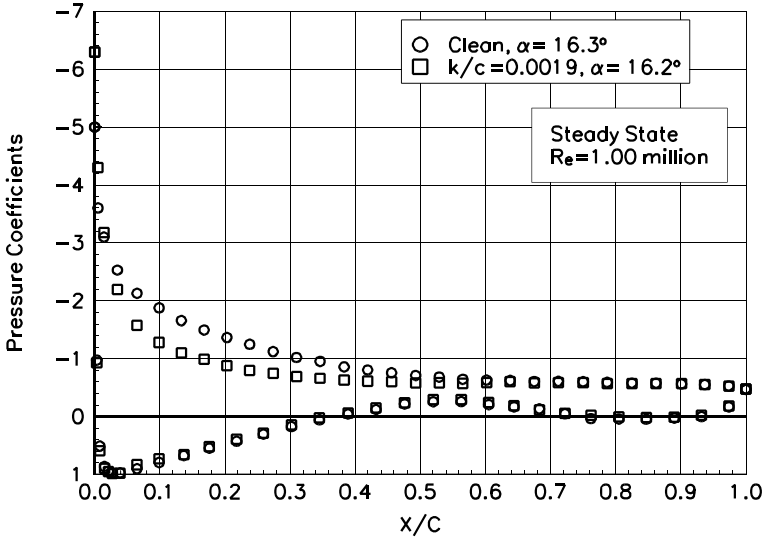

Figure 58. α = 16.3°

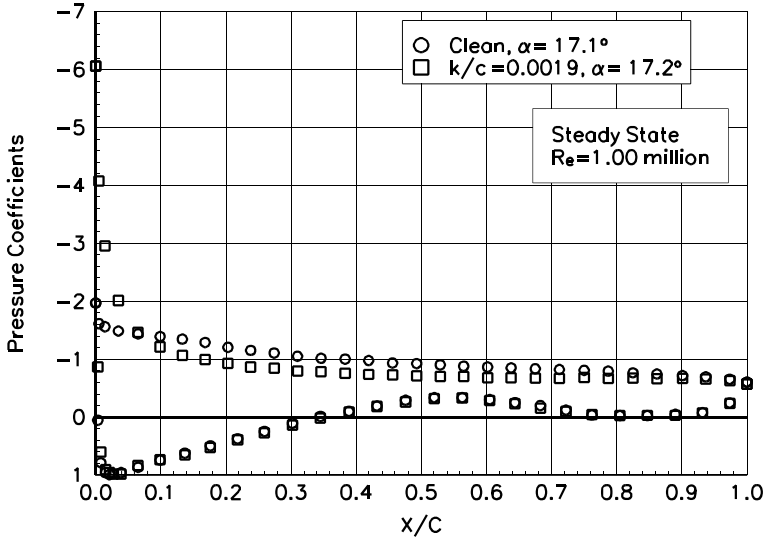

Figure 59. α = 17.1°

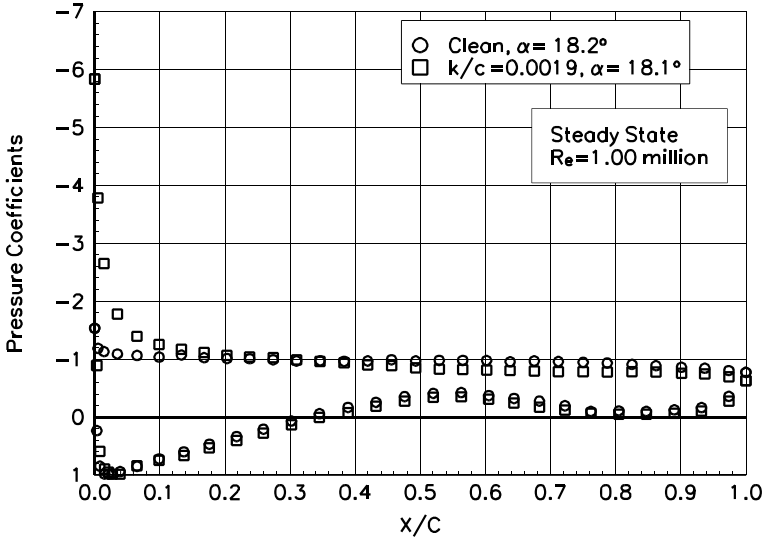

Figure 60. α = 18.2°

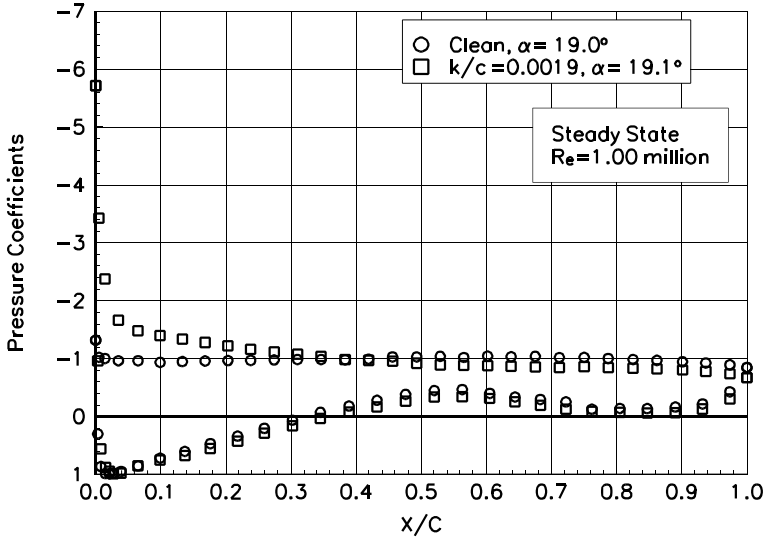

Figure 61. α = 19.0°

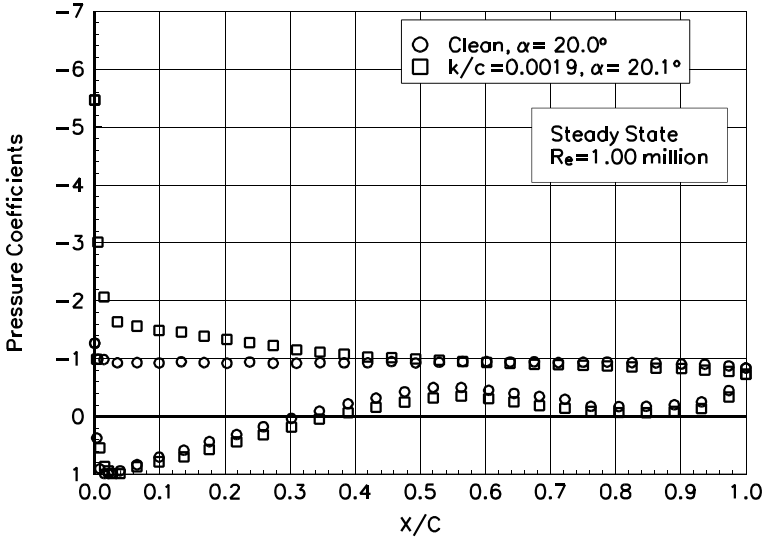

Figure 62. α = 20.0°

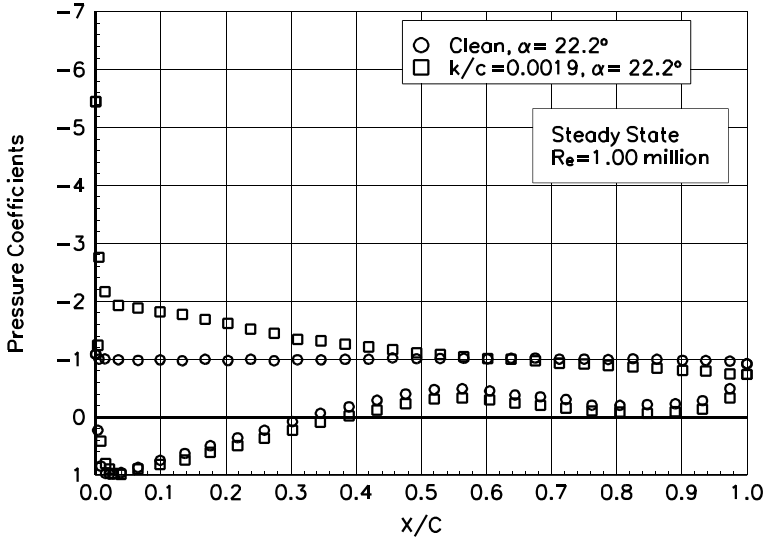

Figure 63. α = 22.2°

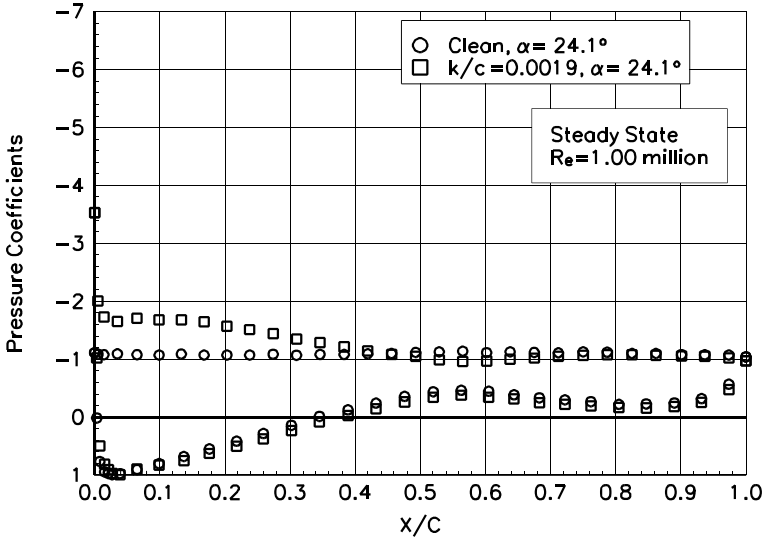

Figure 64. α = 24.1°

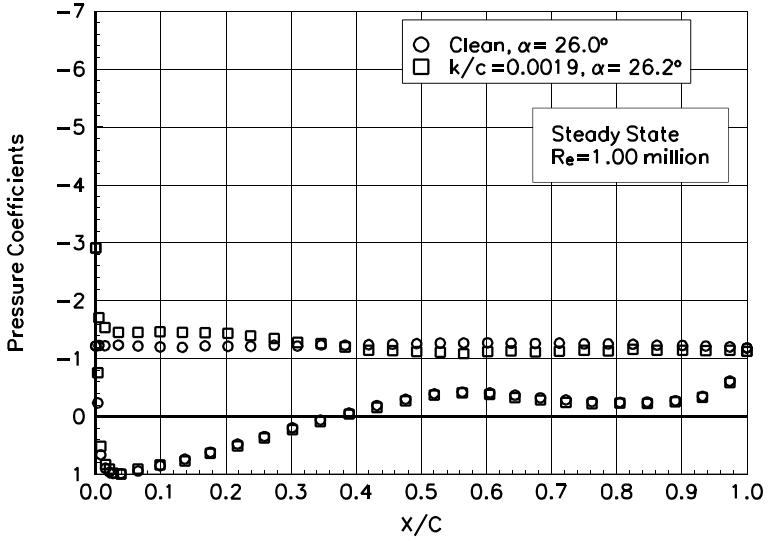

Figure 65. α = 26.0°

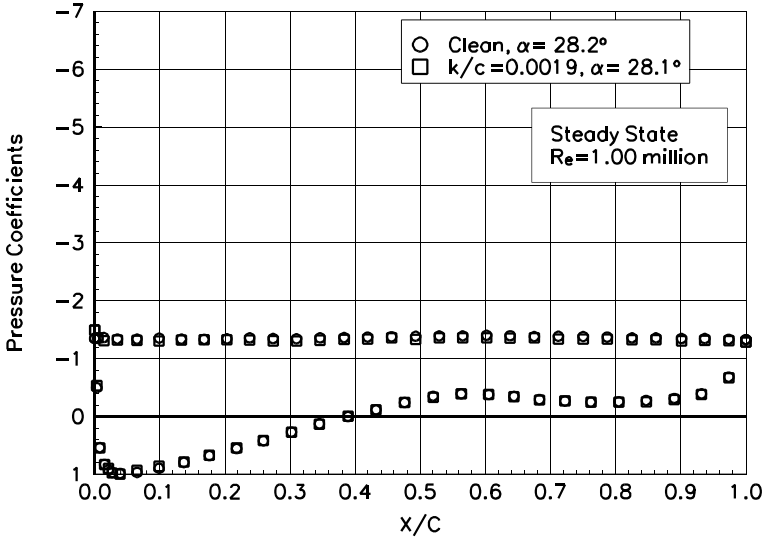

Figure 66. α = 28.2°

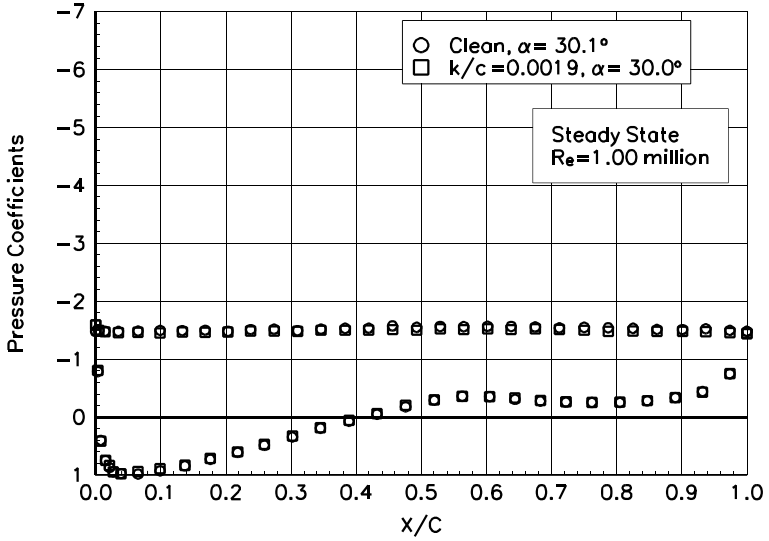

Figure 67. α = 30.1°

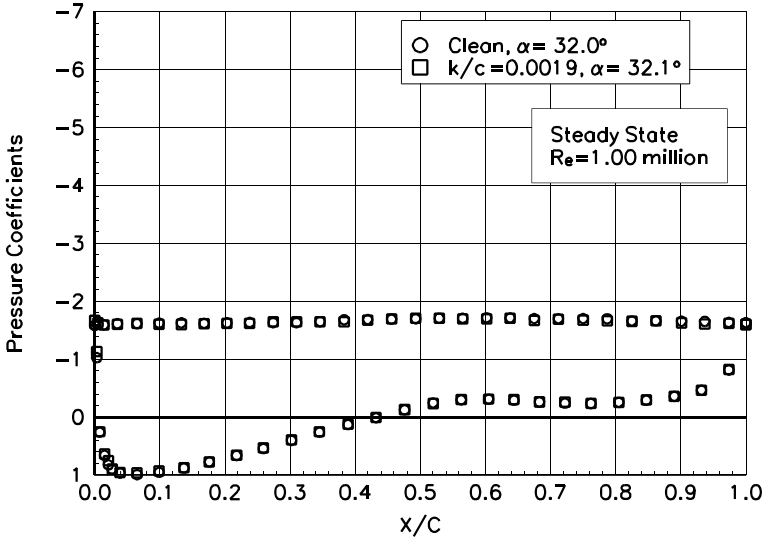

Figure 68. α = 32.0°

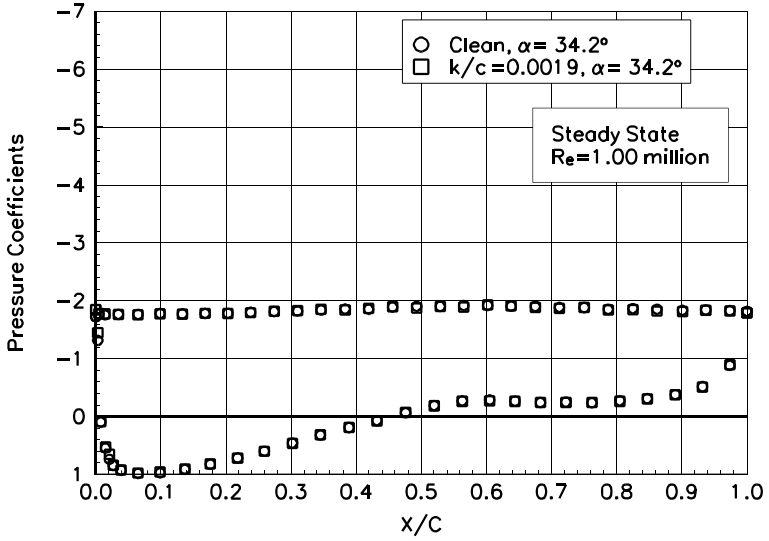

Figure 69. α = 34.2°

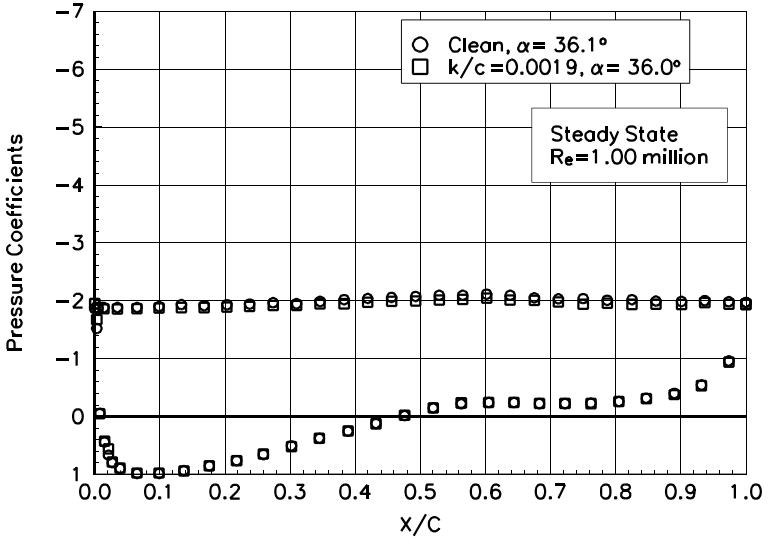

Figure 70. α = 36.1°

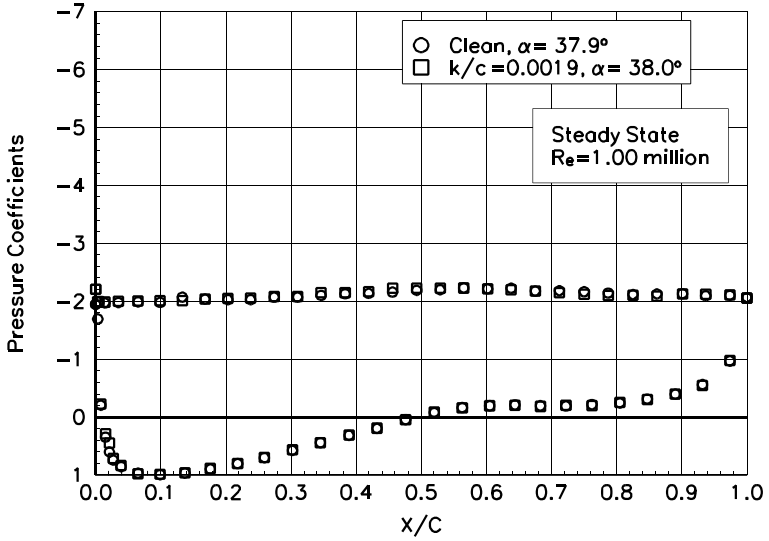

Figure 71. α = 37.9°

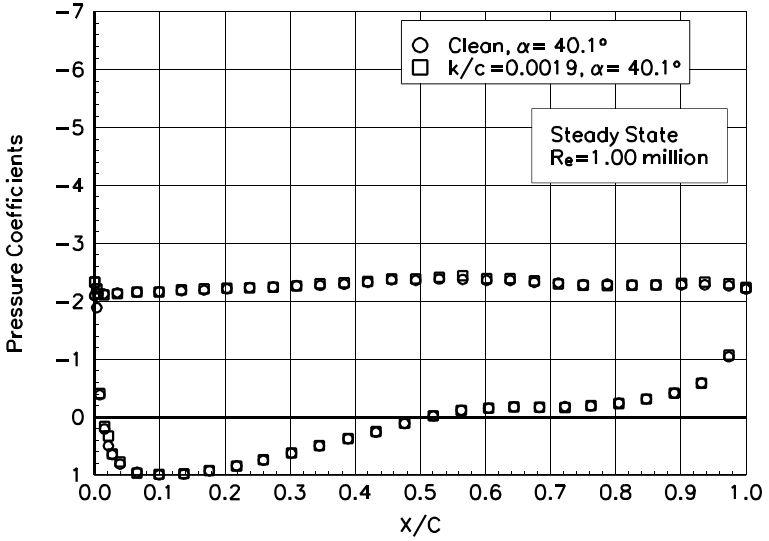

Figure 72. α = 40.1°

S810

Pressure Distributions, Steady State, Re = 1.25 million

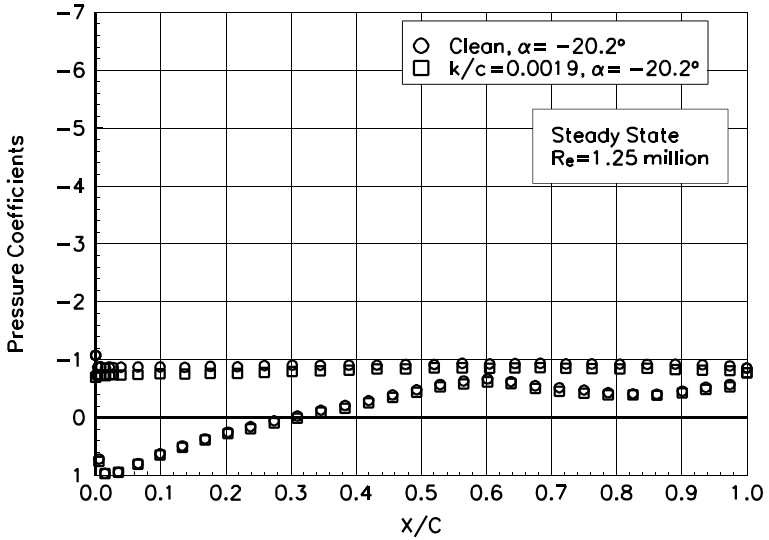

Figure 73. α = -20.2°

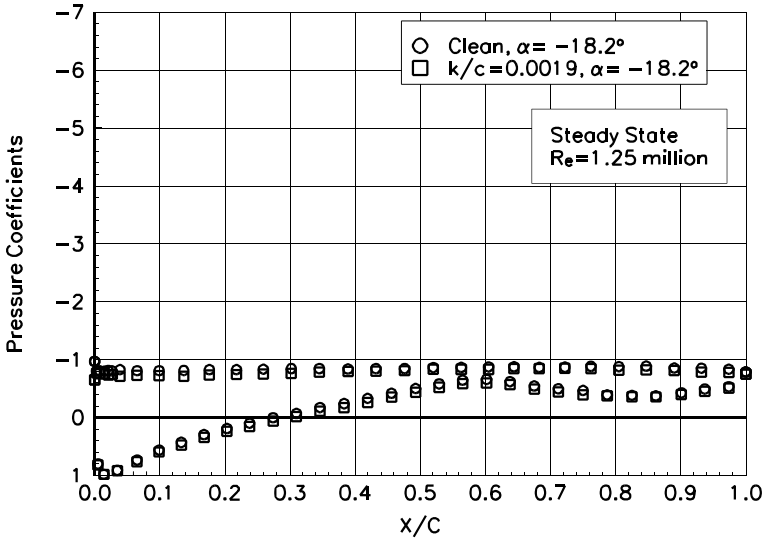

Figure 74. α = -18.2°

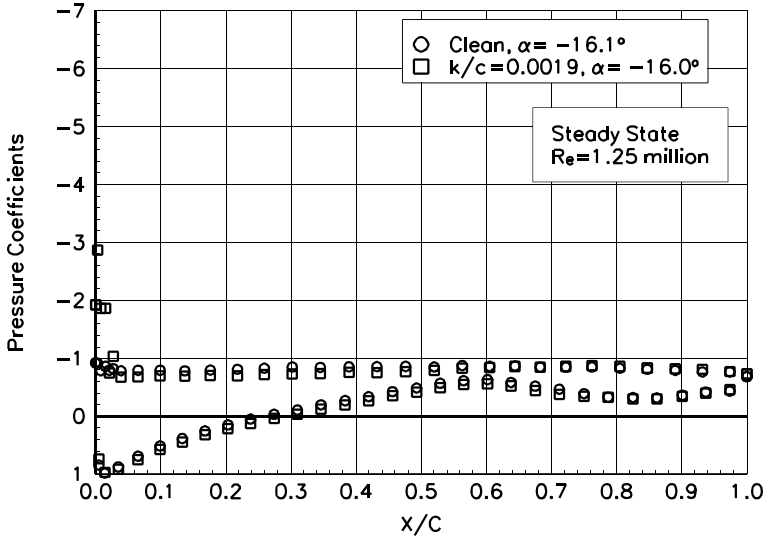

Figure 75. α = -16.1°

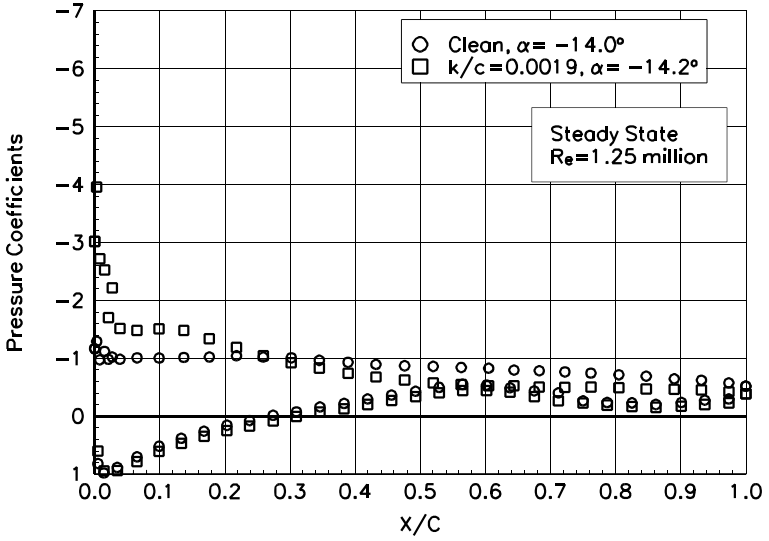

Figure 76. α = -14.0°

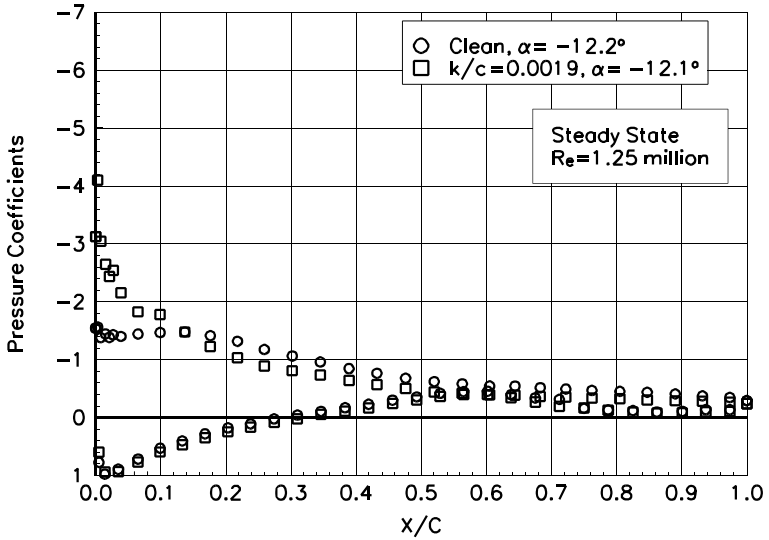

Figure 77. α = -12.2°

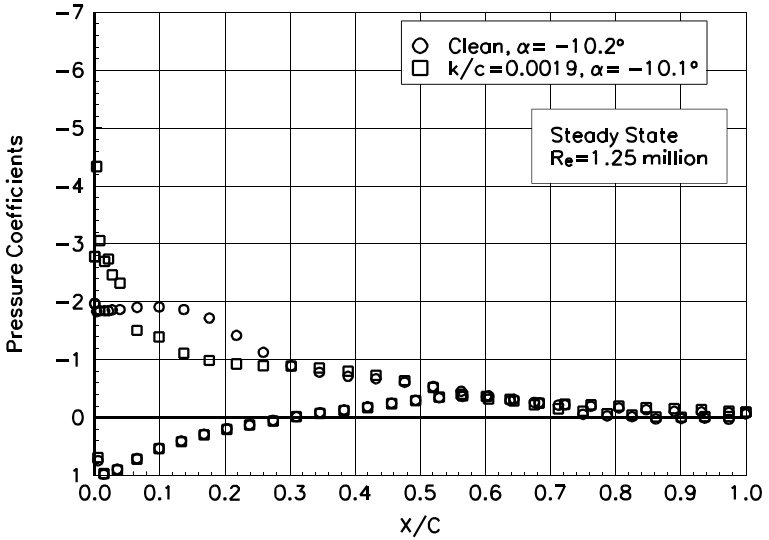

Figure 78. α = -10.2°

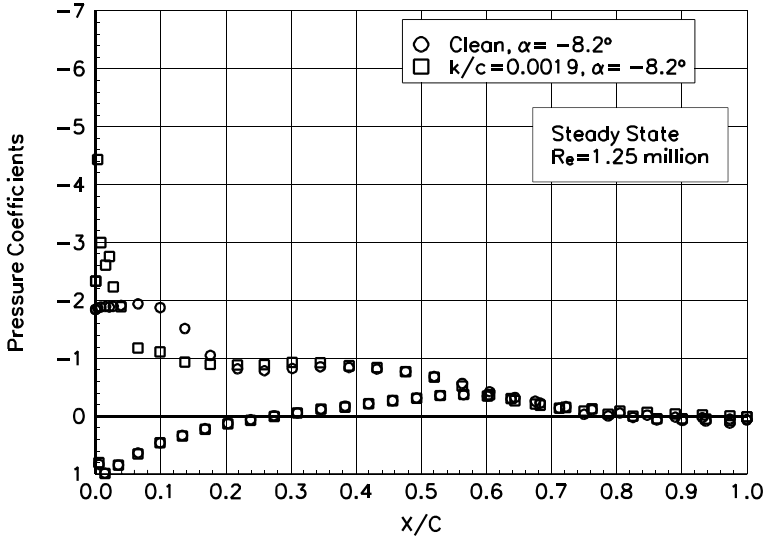

Figure 79. α = -8.2°

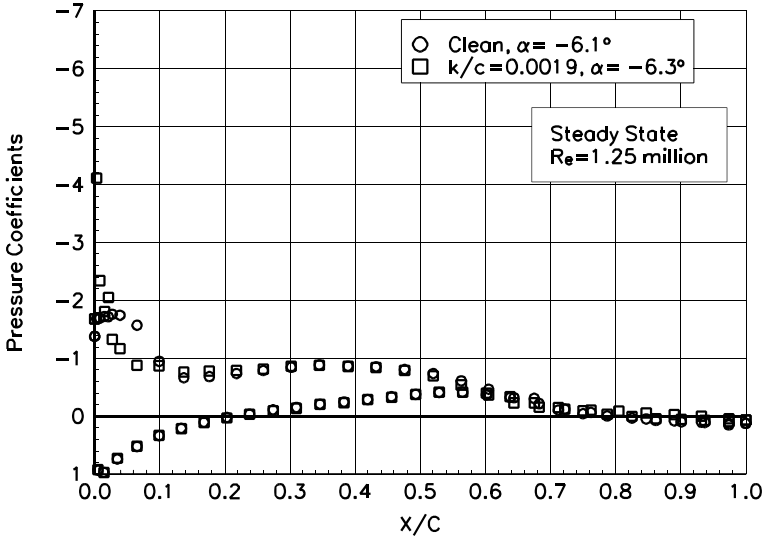

Figure 80. α = -6.1°

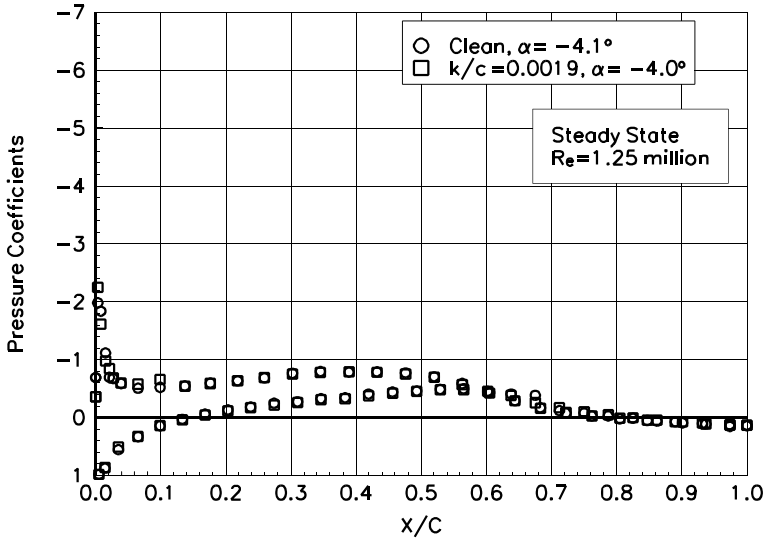

Figure 81. α = -4.1°

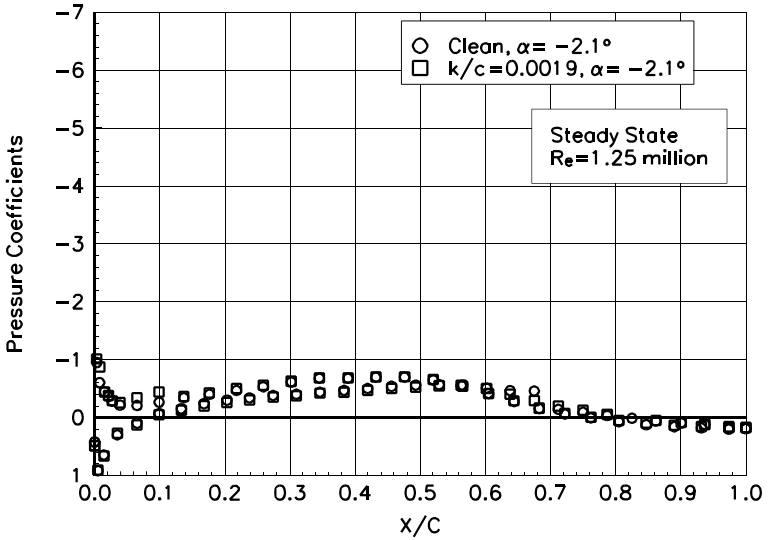

Figure 82. α = -2.1°

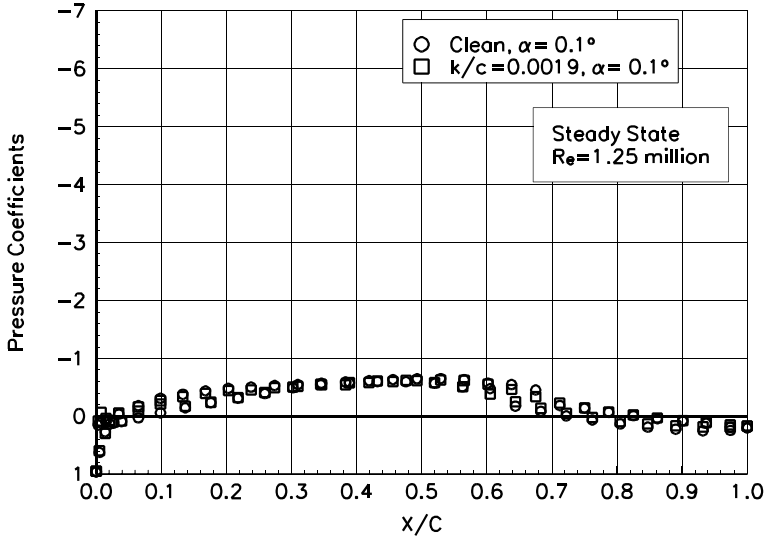

Figure 83. α = 0.1°

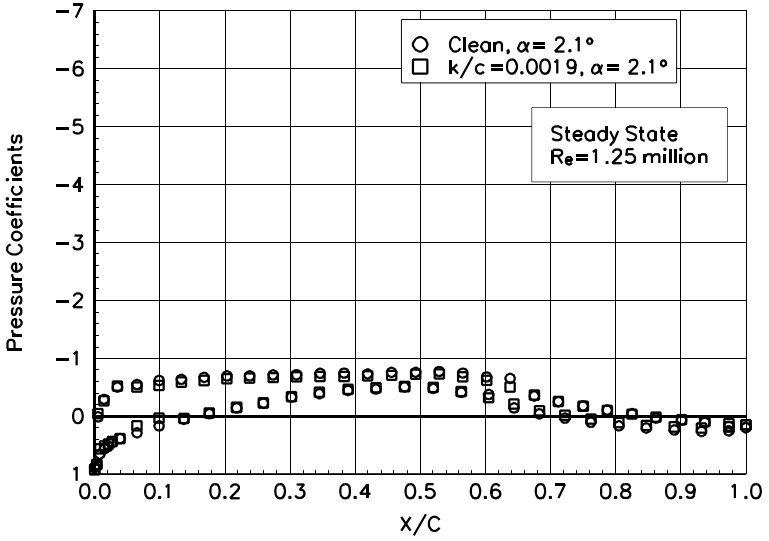

Figure 84. α = 2.1°

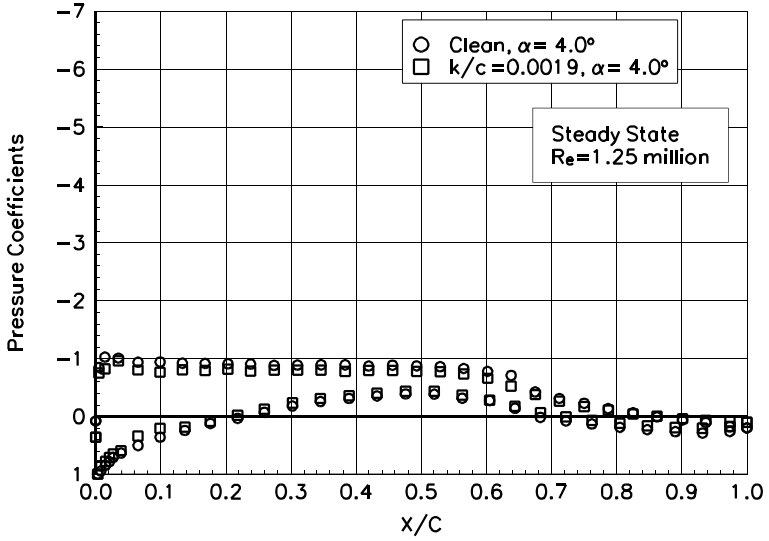

Figure 85. α = 4.0°

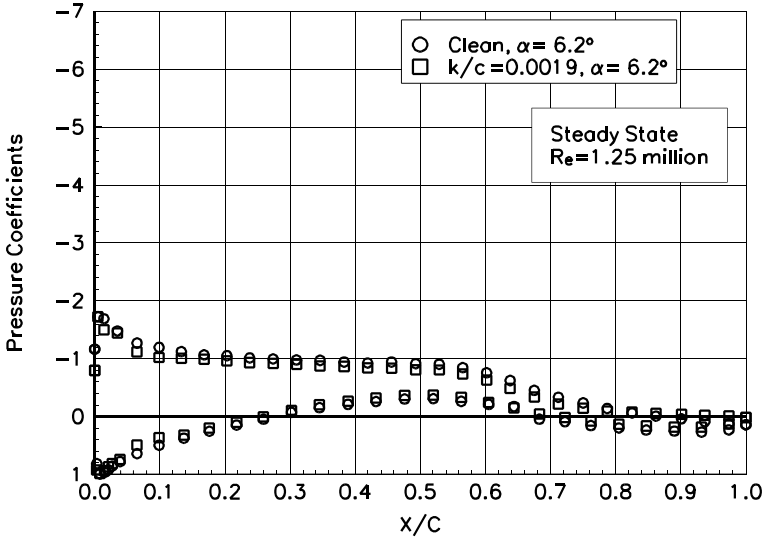

Figure 86. α = 6.2°

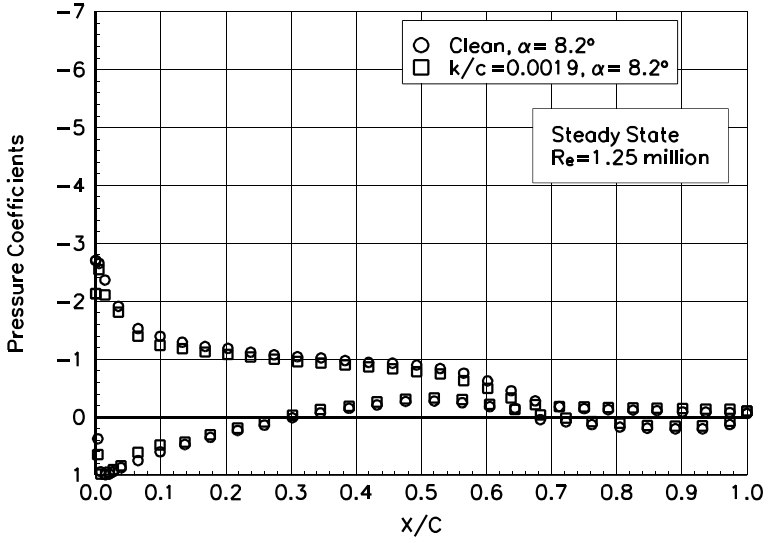

Figure 87. α = 8.2°

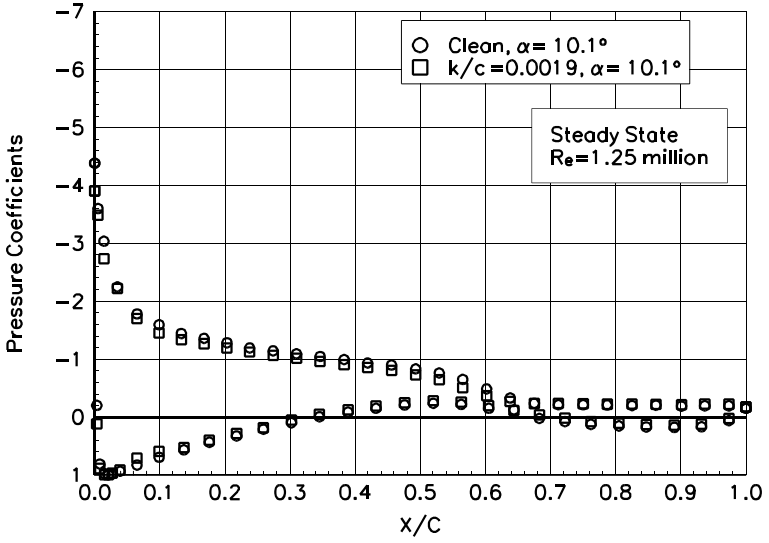

Figure 88. α = 10.1°

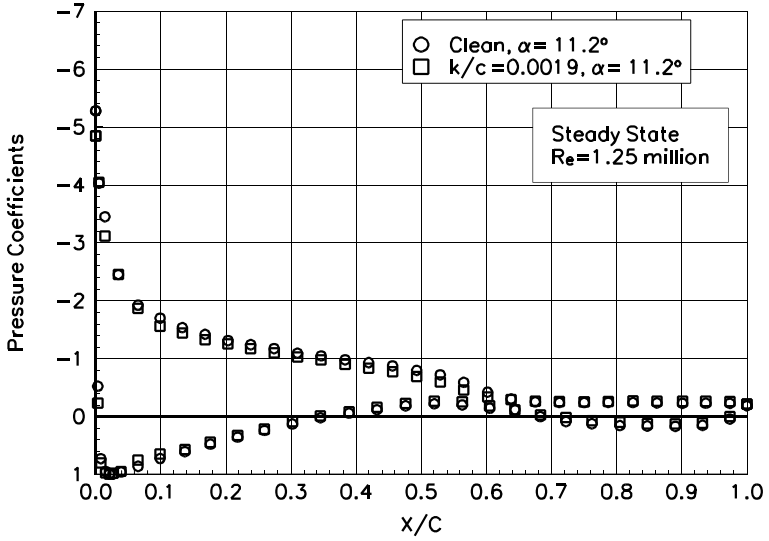

Figure 89. α = 11.2°

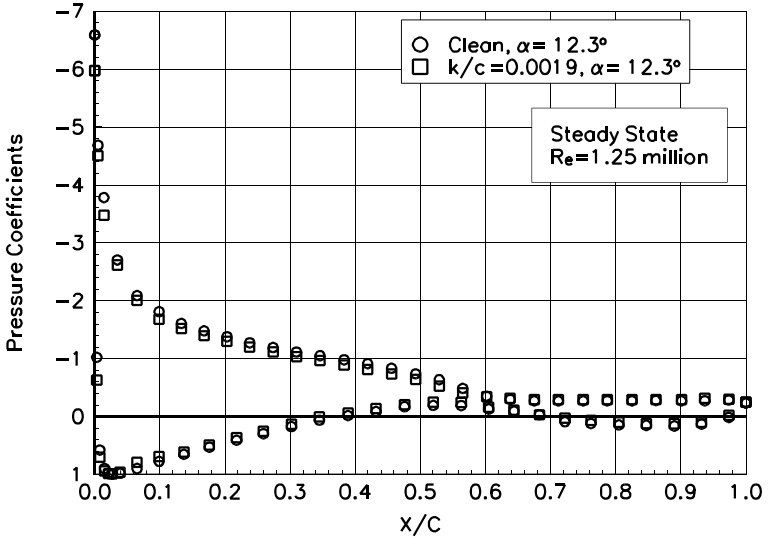

Figure 90. α = 12.3°

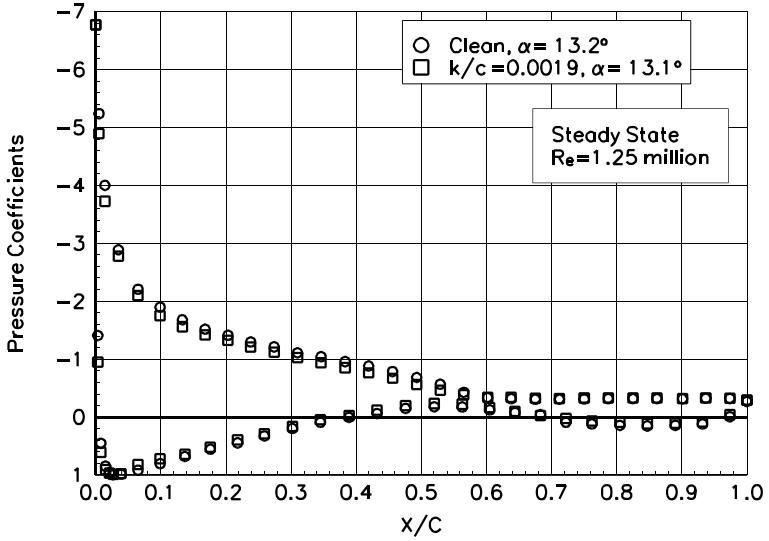

Figure 91. α = 13.2°

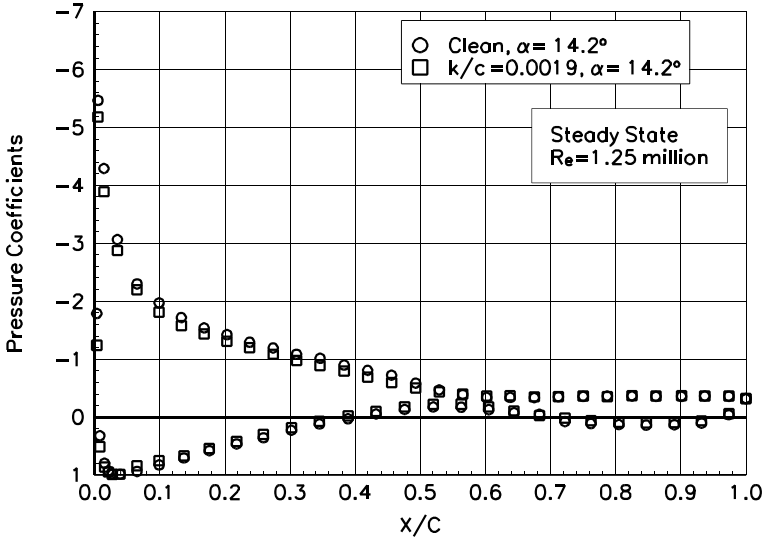

Figure 92. α = 14.2°

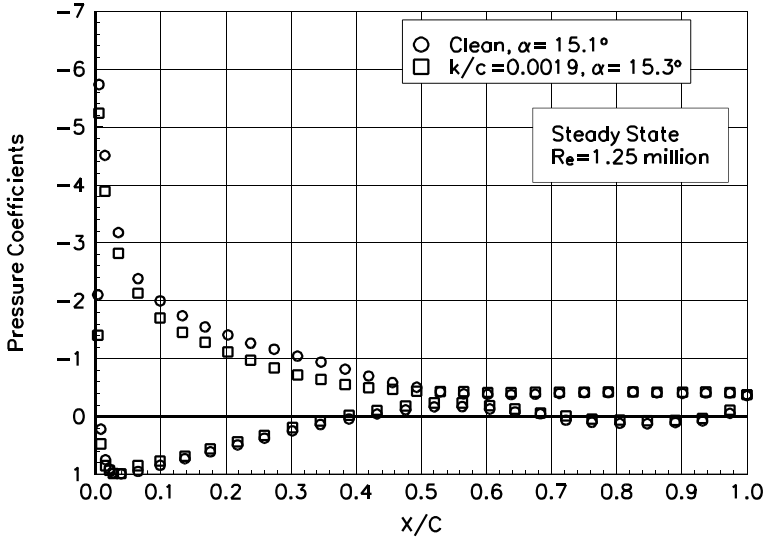

Figure 93. α = 15.1°

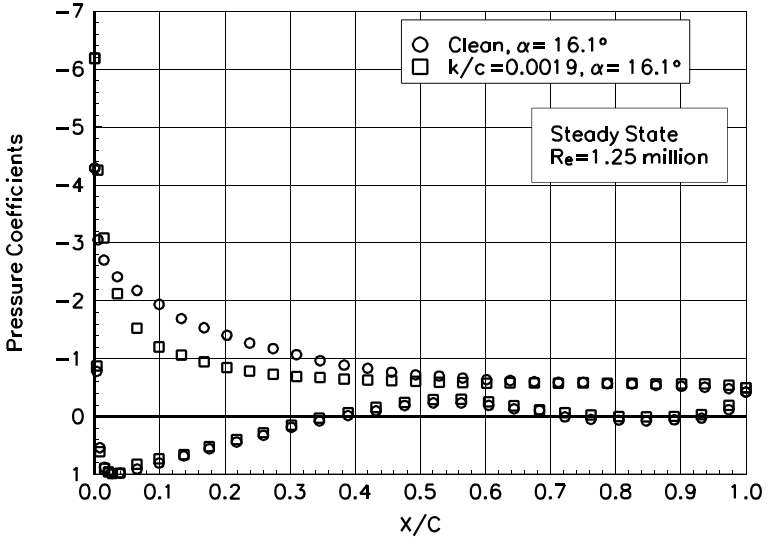

Figure 94. α = 16.1°

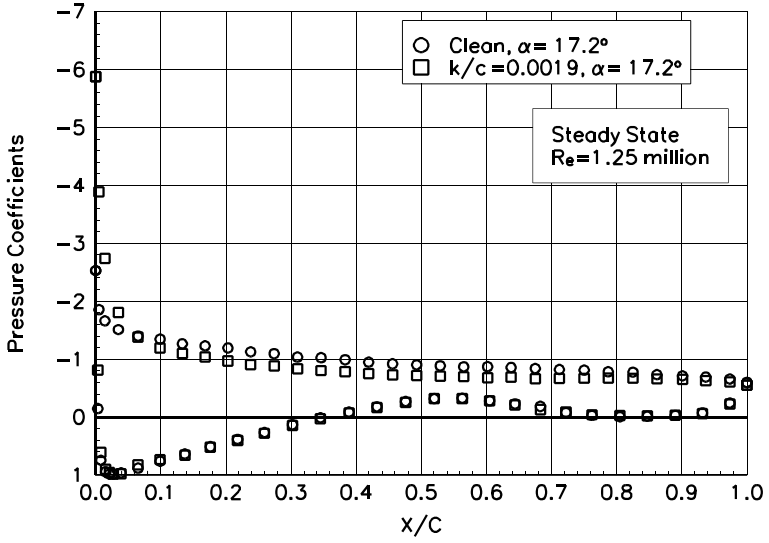

Figure 95. α = 17.2°

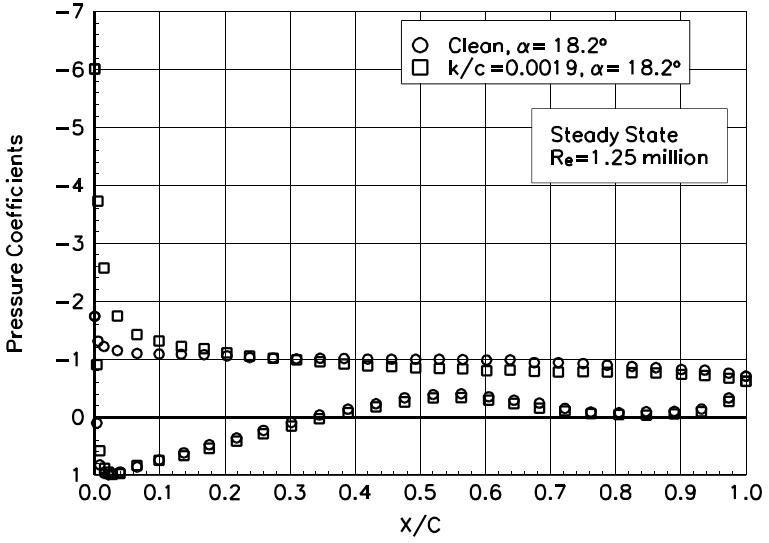

Figure 96. α = 18.2°

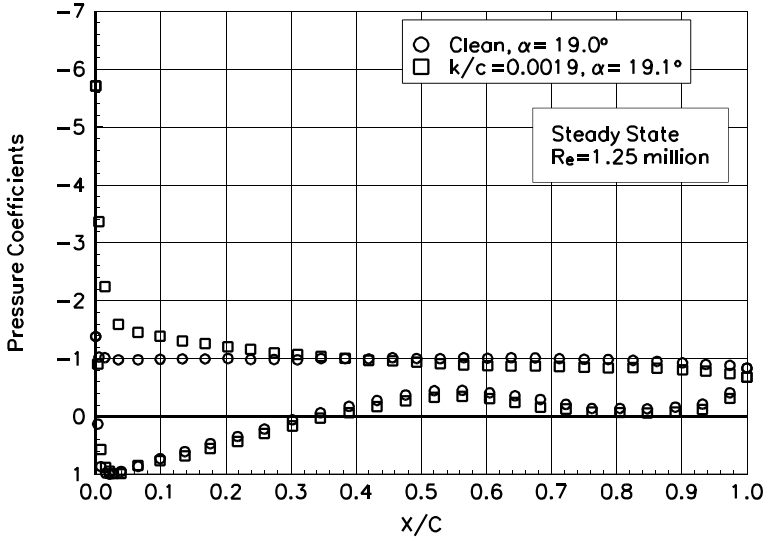

Figure 97. α = 19.0°

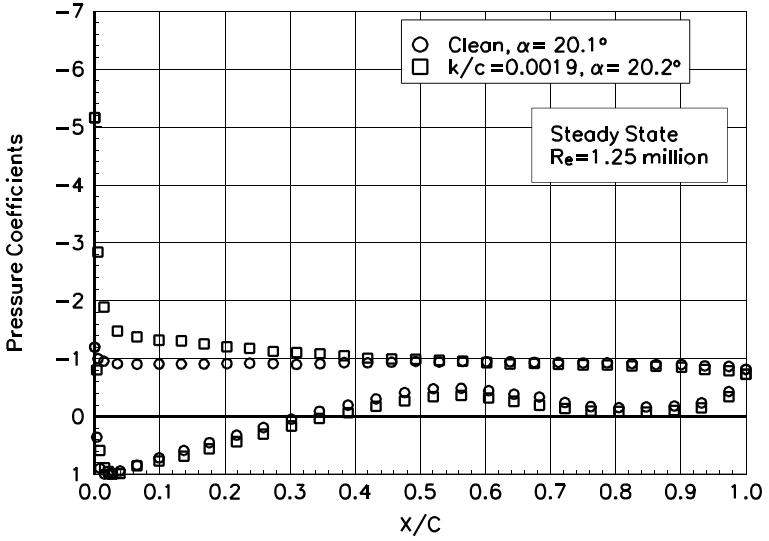

Figure 98. α = 20.1°

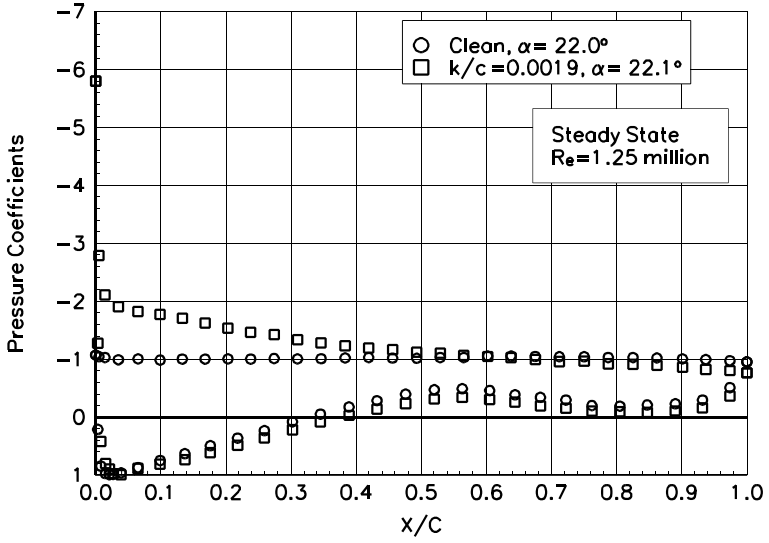

Figure 99. α = 22.0°

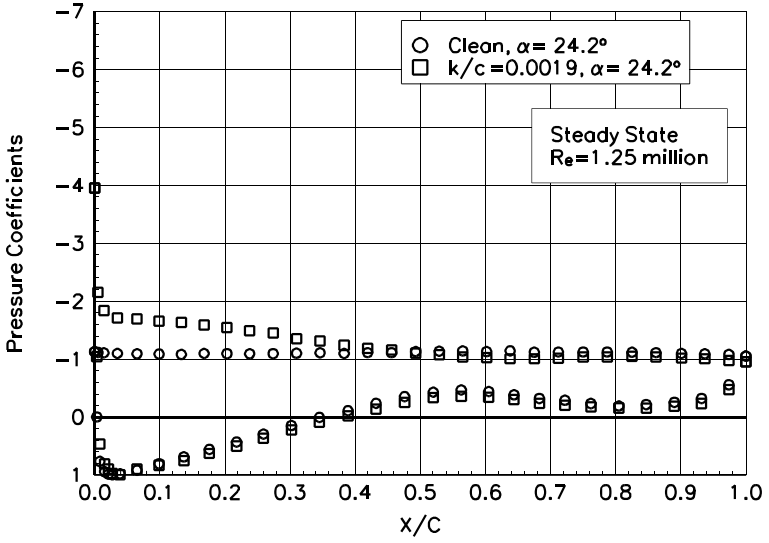

Figure 100. α = 24.2°

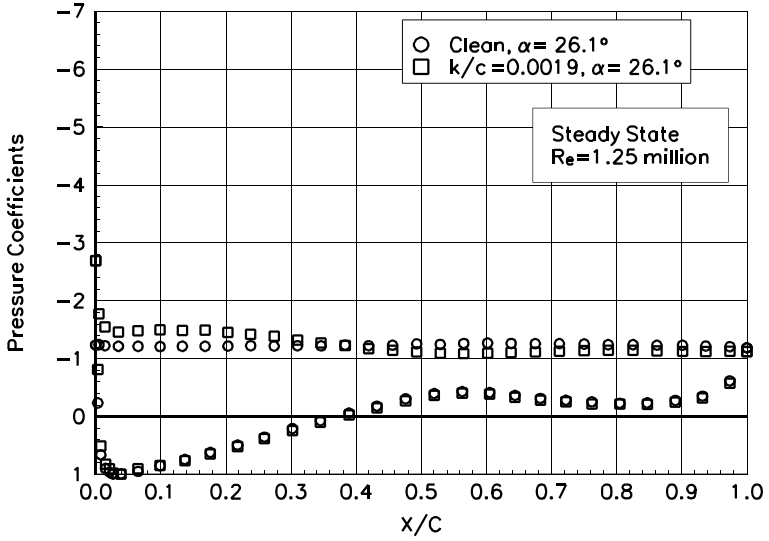

Figure 101. α = 26.1°

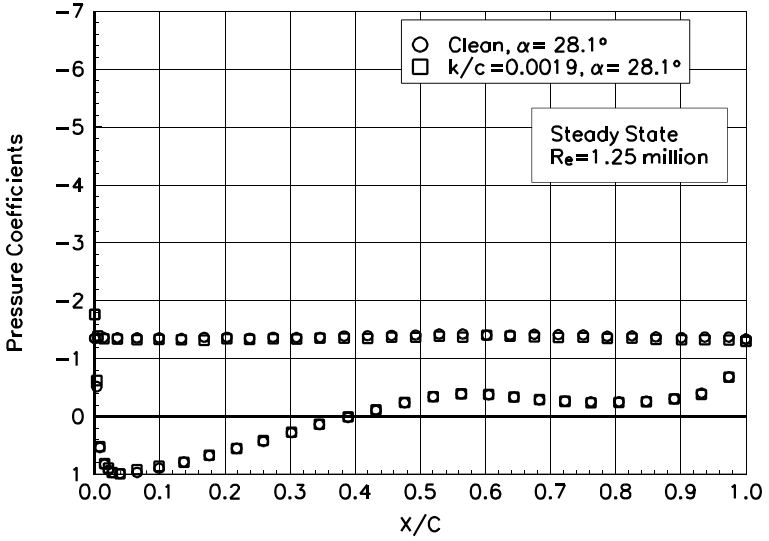

Figure 102. α = 28.1°

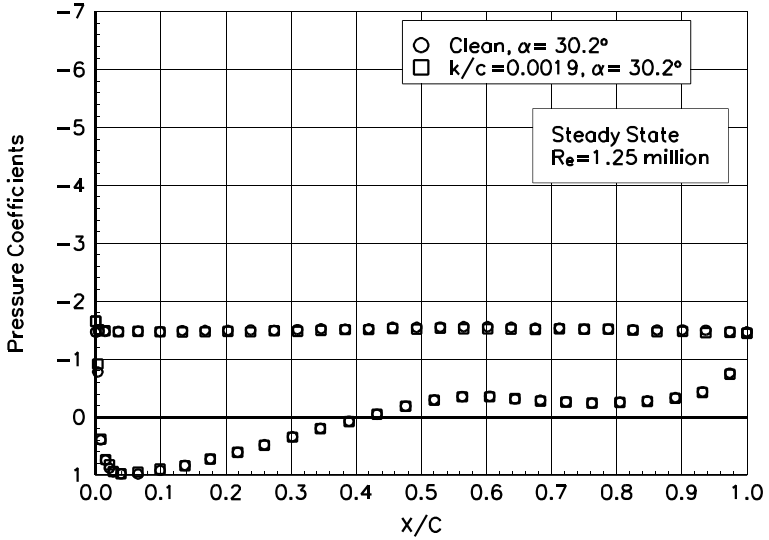

Figure 103. α = 30.2°

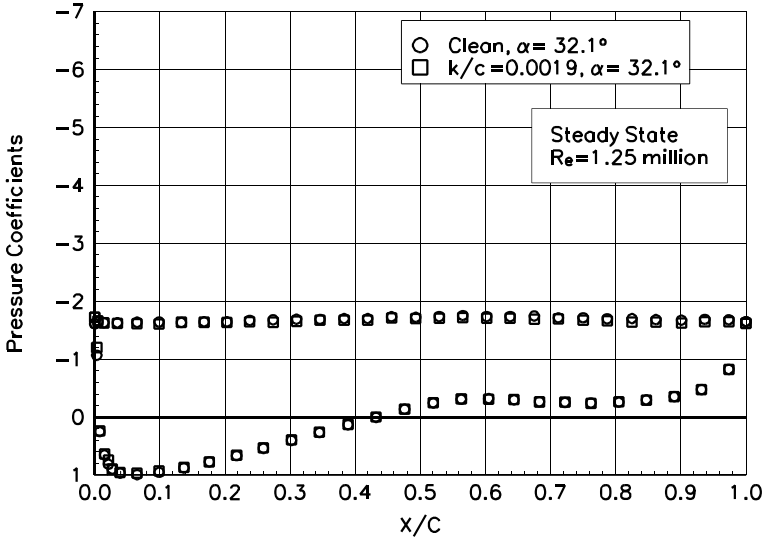

Figure 104. α = 32.1°

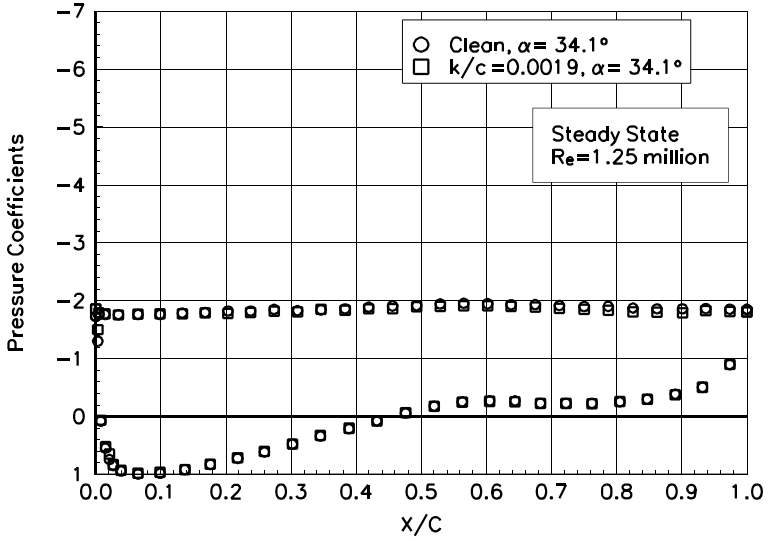

Figure 105. α = 34.1°

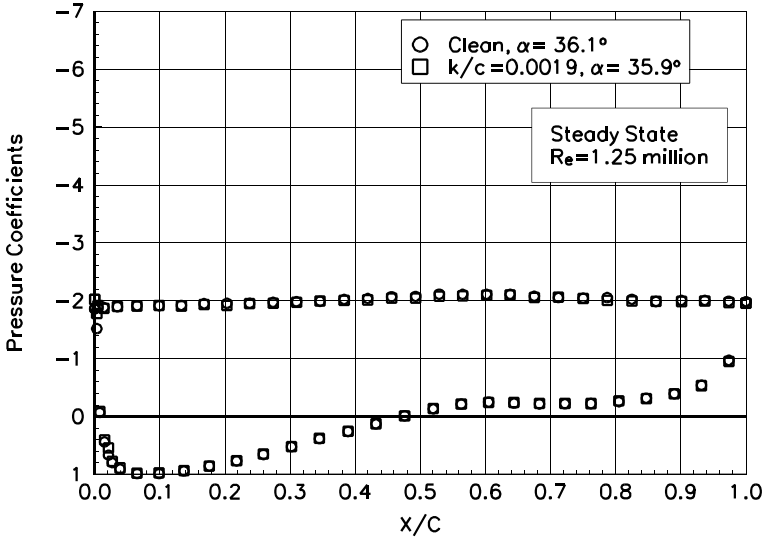

Figure 106. α = 36.1°

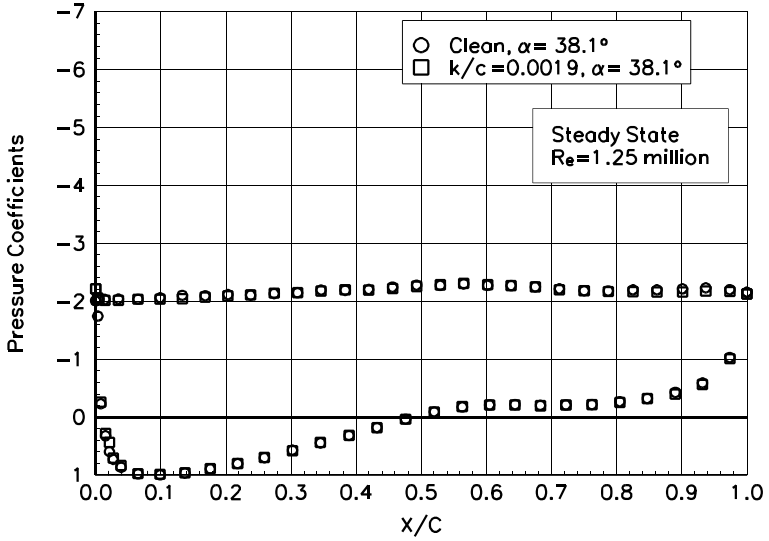

Figure 107. α = 38.1°

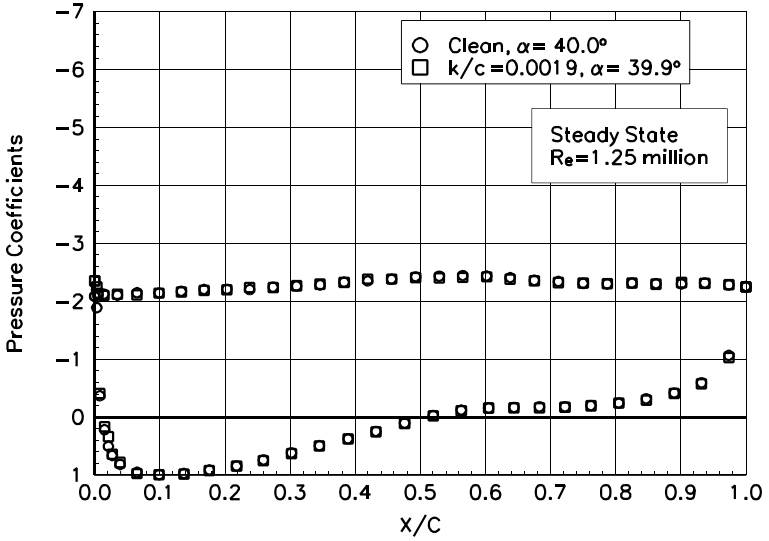

Figure 108. α = 40.0°

S810

Pressure Distributions, Steady State, Re = 1.5 million

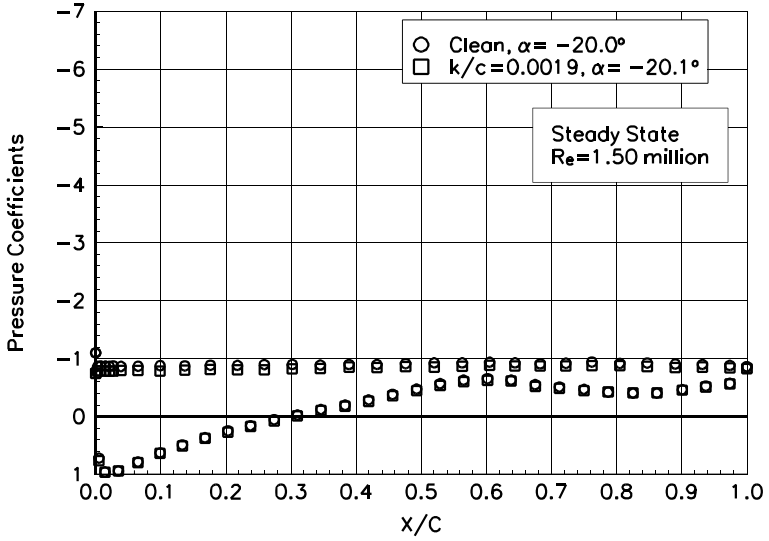

Figure 109. α = -20.0°

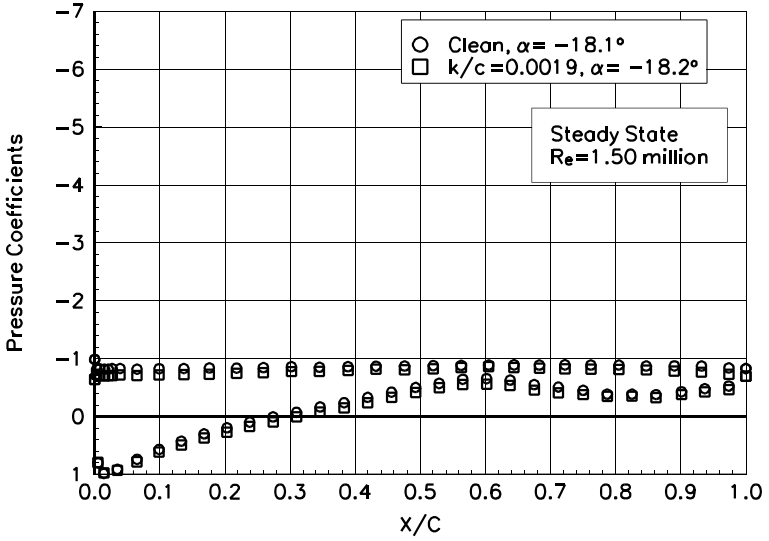

Figure 110. α = -18.1°

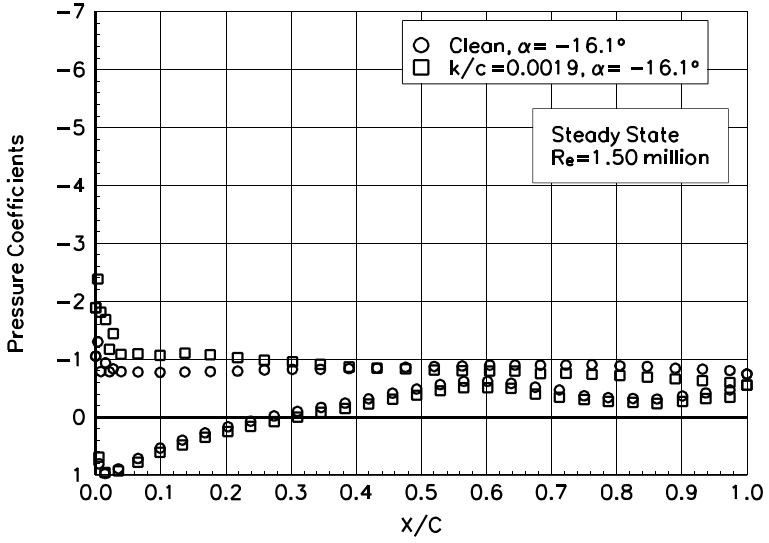

Figure 111. α = -16.1°

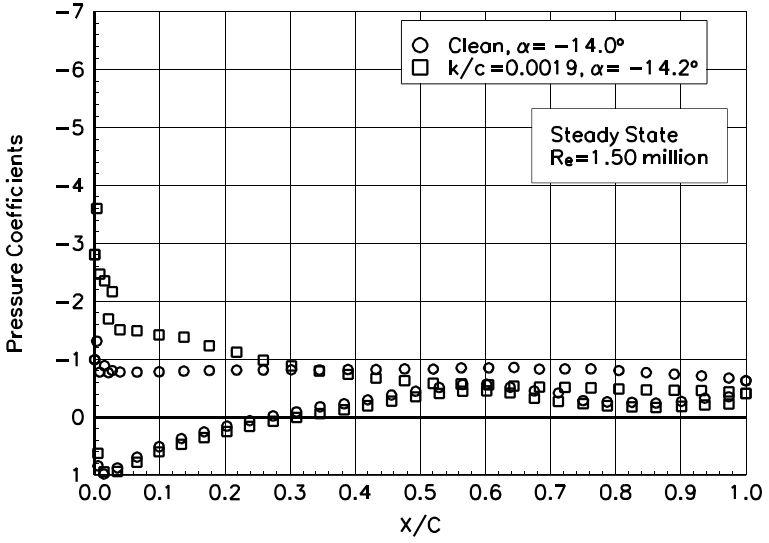

Figure 112. α = -14.0°

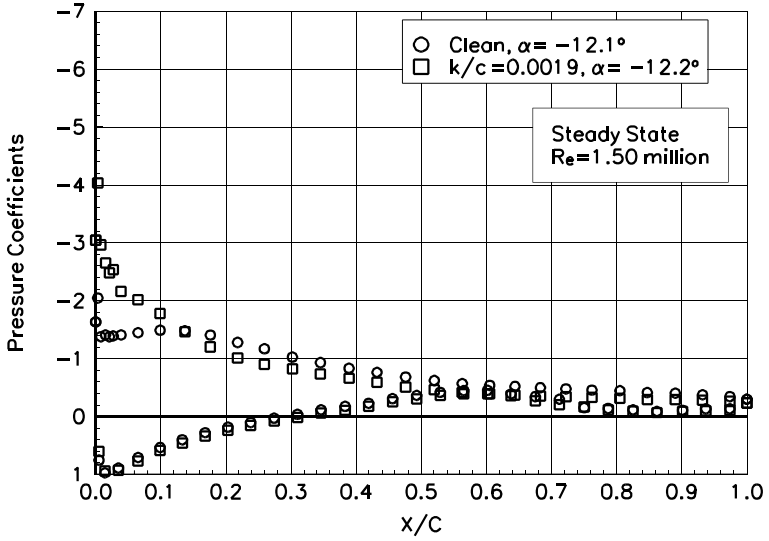

Figure 113. α = -12.1°

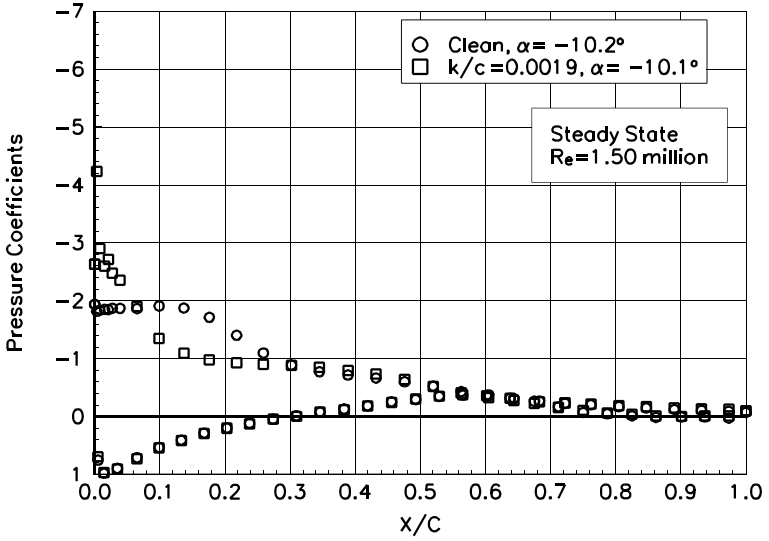

Figure 114. α = -10.2°

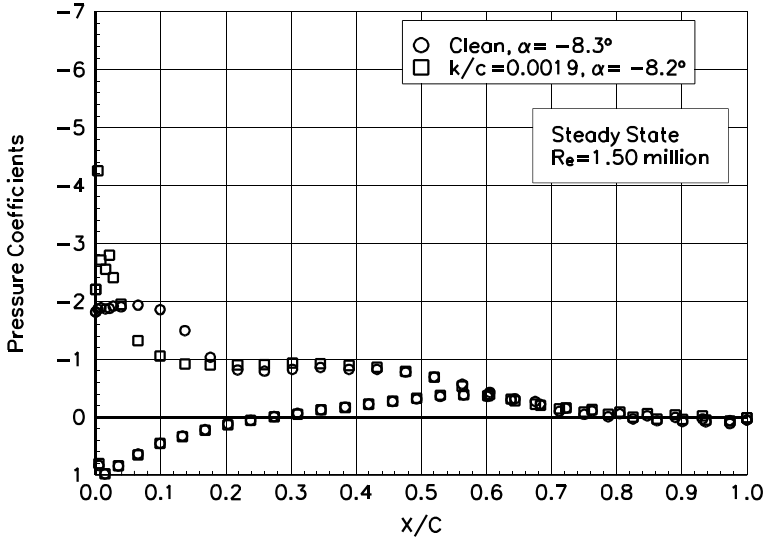

Figure 115. α = -8.3°

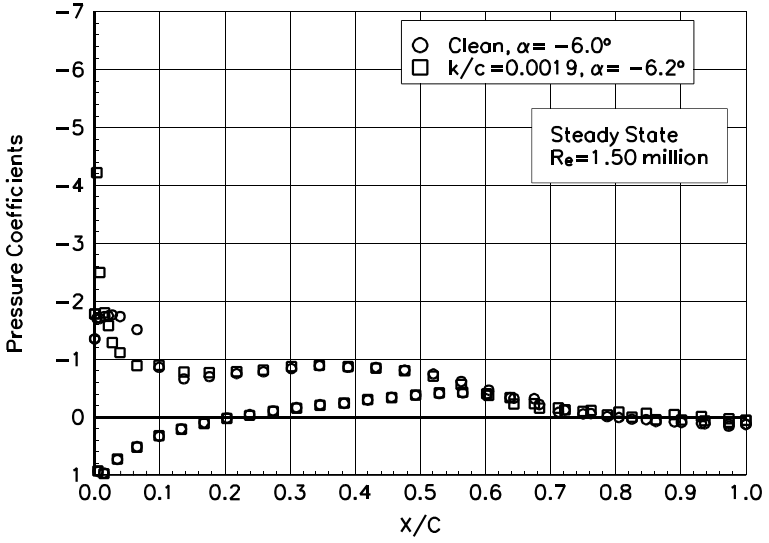

Figure 116. α = -6.0°

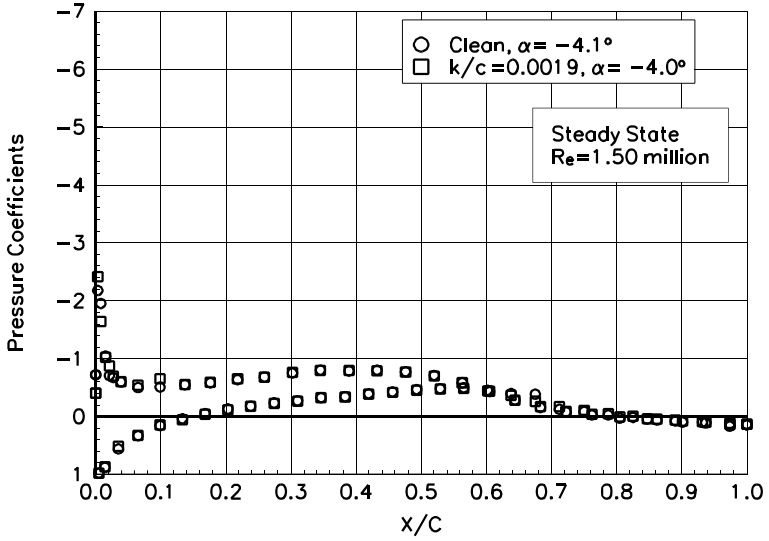

Figure 117. α = -4.1°

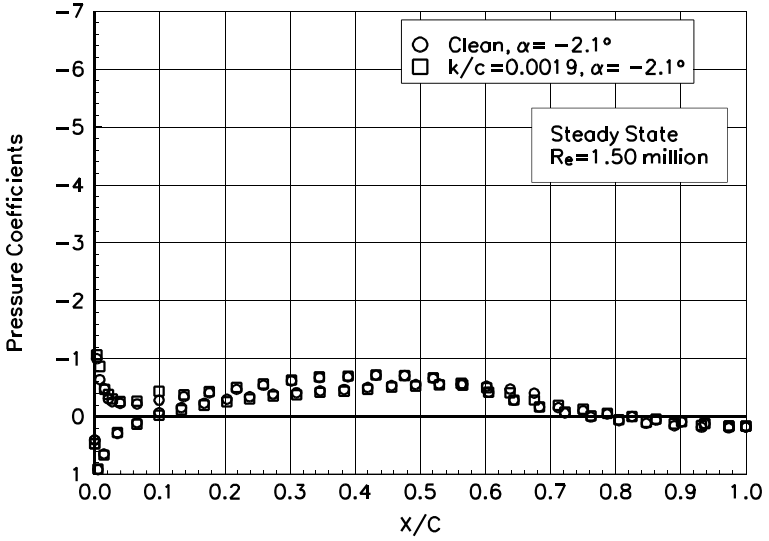

Figure 118. α = -2.1°

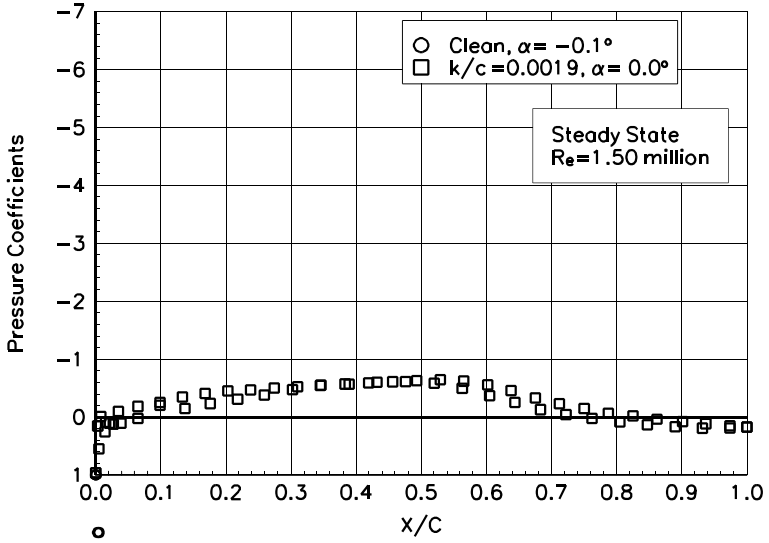

Figure 119. α = -0.1°

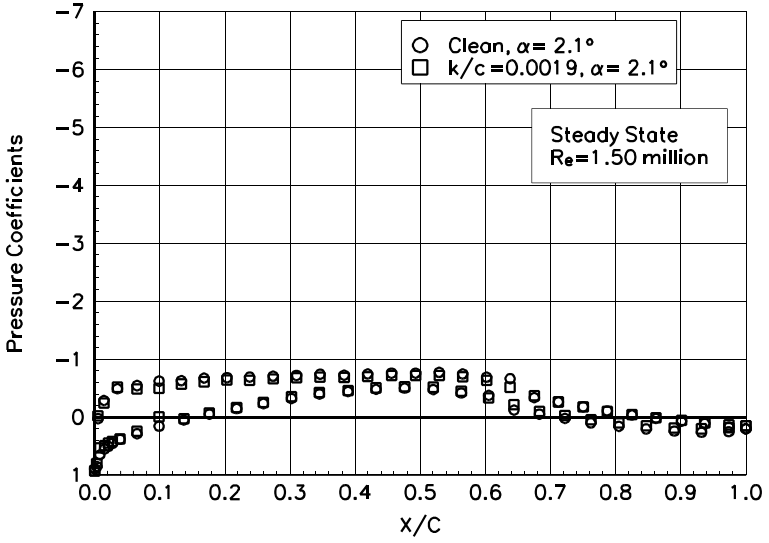

Figure 120. α = 2.1°

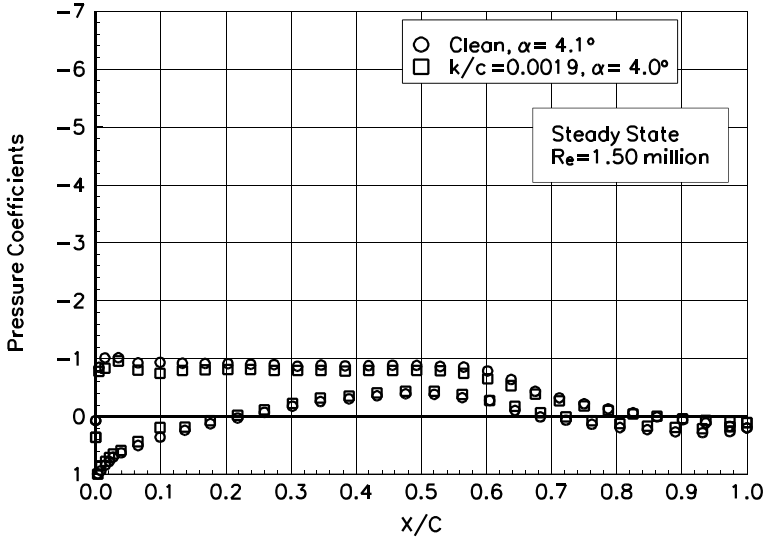

Figure 121. α = 4.1°

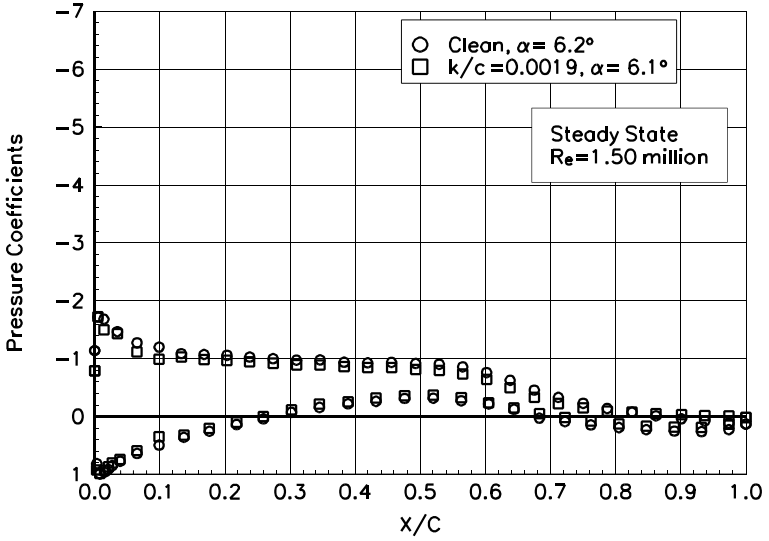

Figure 122. α = 6.2°

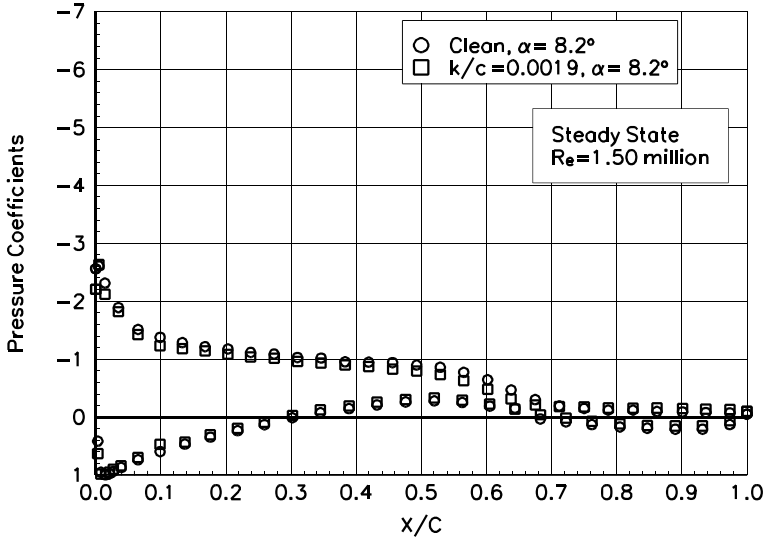

Figure 123. α = 8.2°

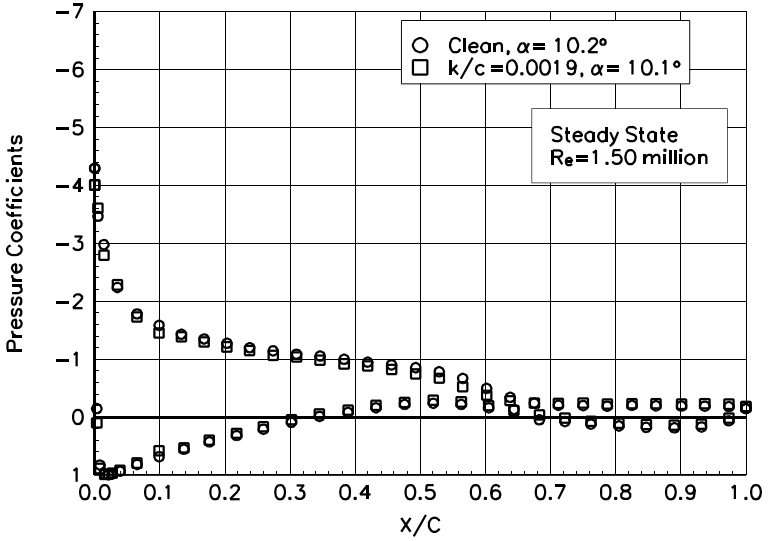

Figure 124. α = 10.2°

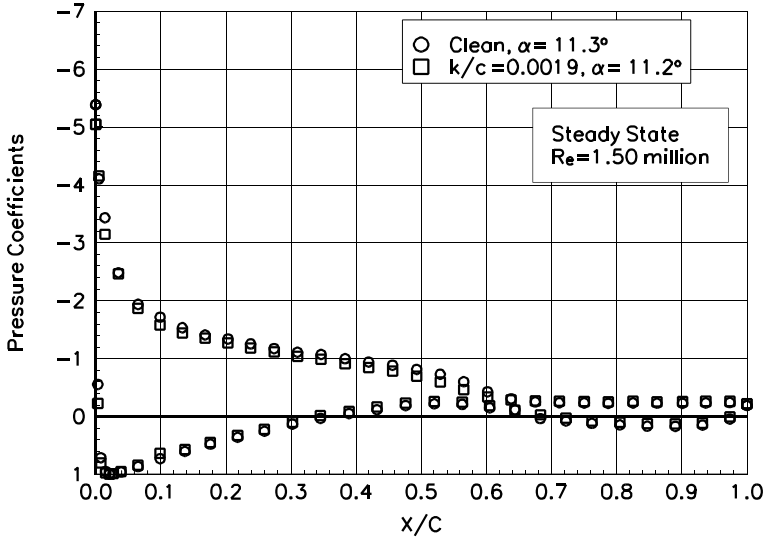

Figure 125. α = 11.3°

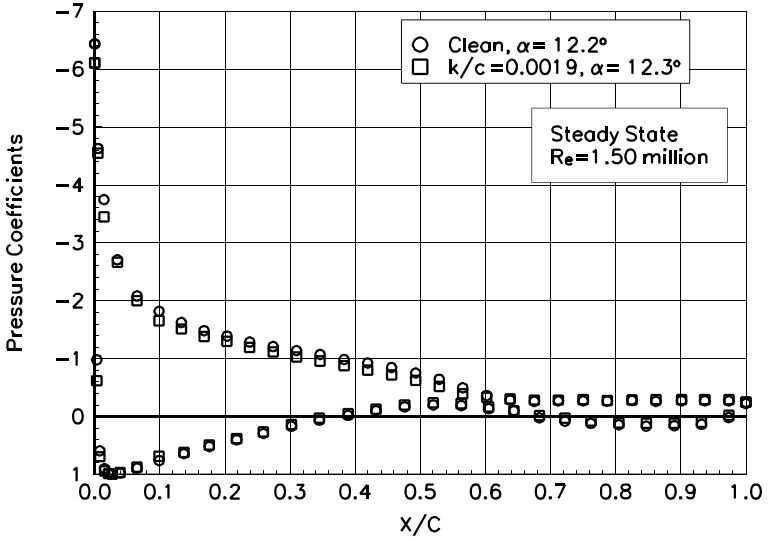

Figure 126. α = 12.2°

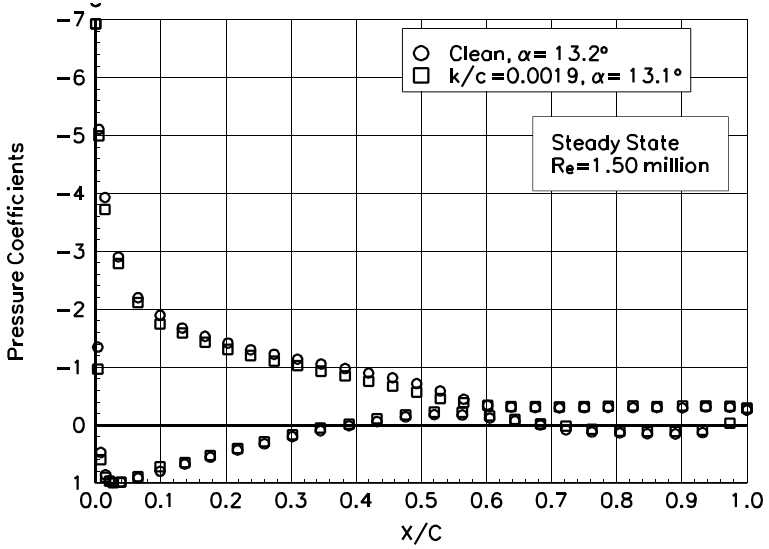

Figure 127. α = 13.2°

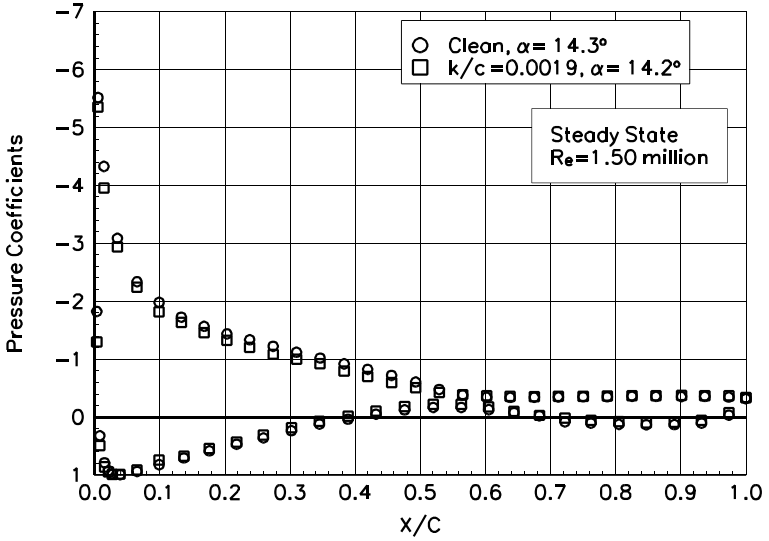

Figure 128. α = 14.3°

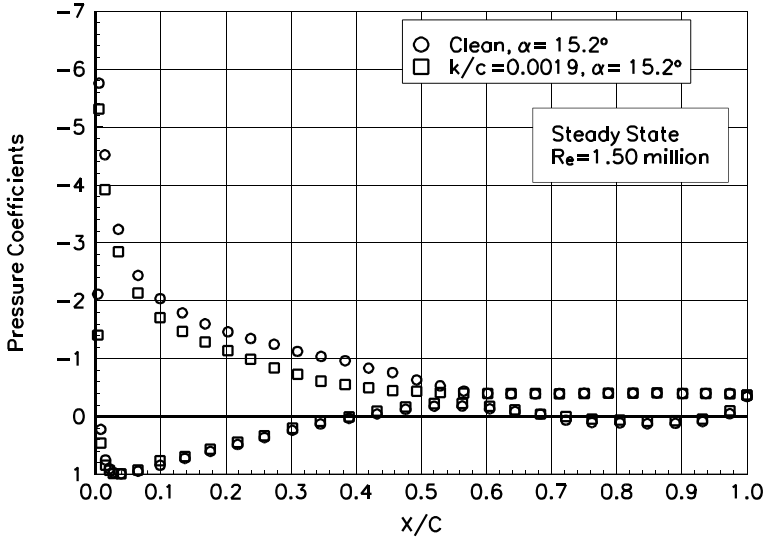

Figure 129. α = 15.2°

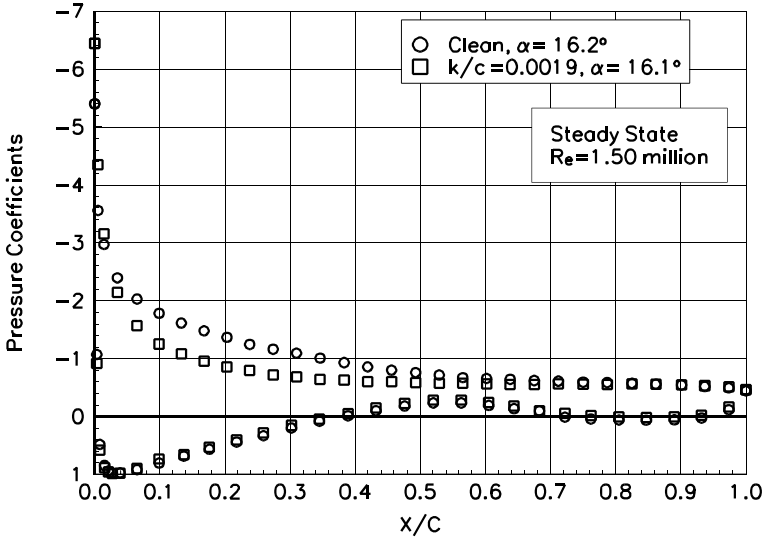

Figure 130. α = 16.2°

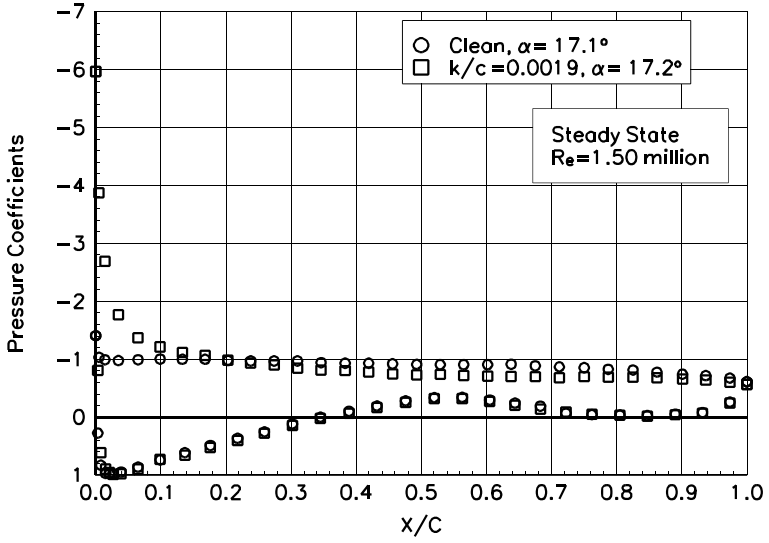

Figure 131. α = 17.1°

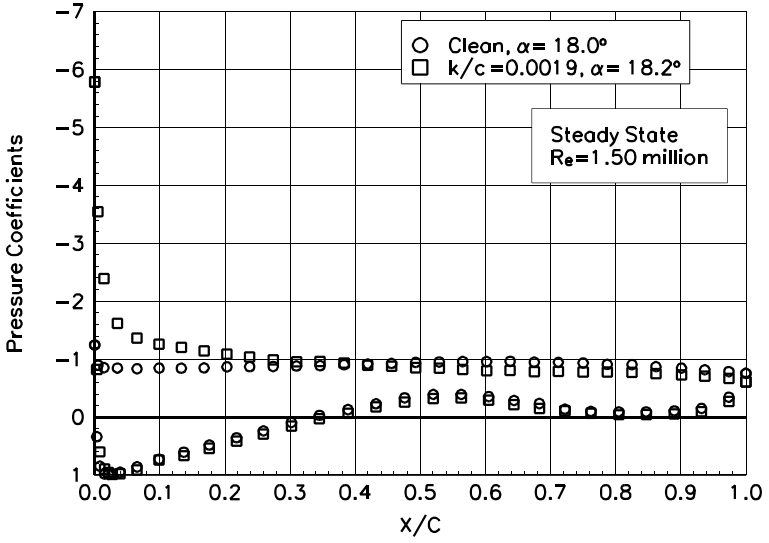

Figure 132. α = 18.0°

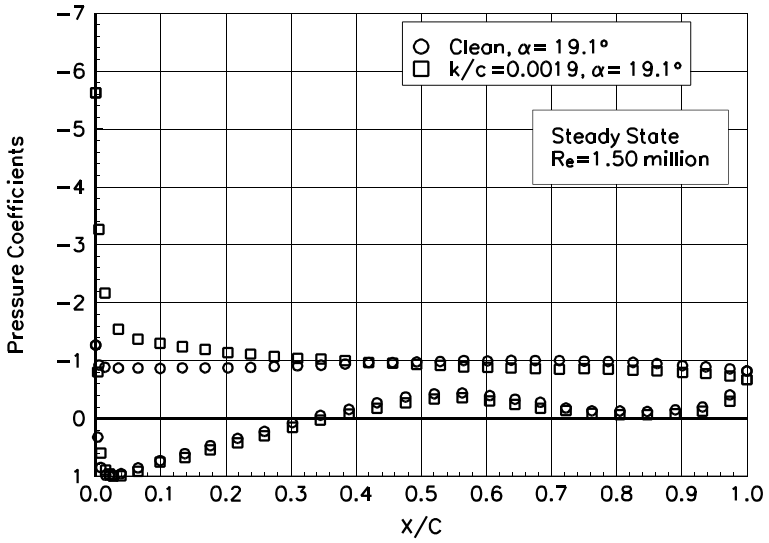

Figure 133. α = 19.1°

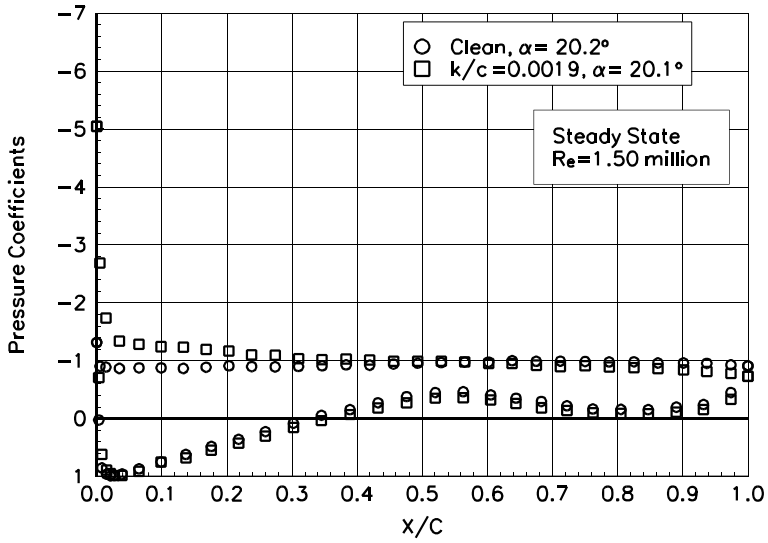

Figure 134. α = 20.2°

Appendix C: Unsteady Integrated Coefficients

List of Figures Page

Unsteady Airfoil Characteristics

±5.5° Sine, Re = 0.75 million

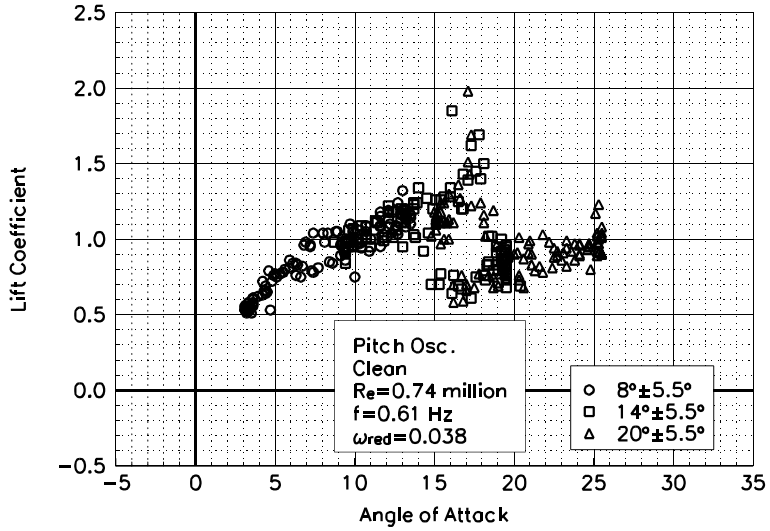

S810
Clean
Re=0.74 million
$\omega_{reduced}$=0.038

Figure C1. Lift coefficient vs α.

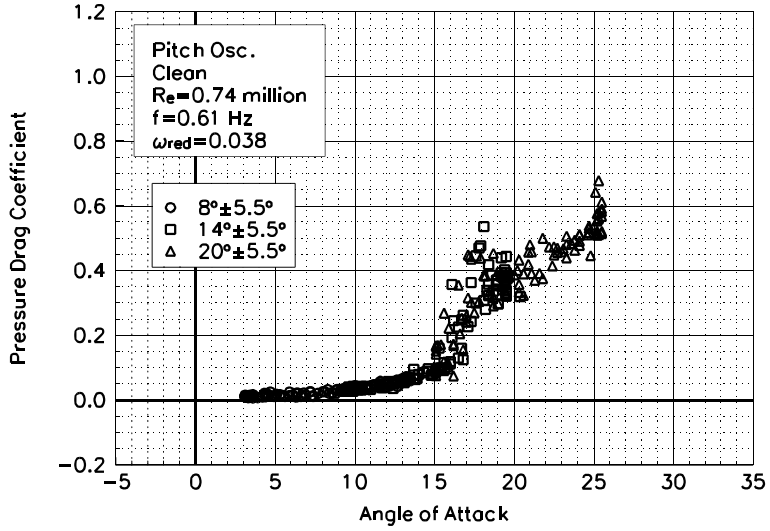

Figure C2. Pressure drag coefficient vs α.

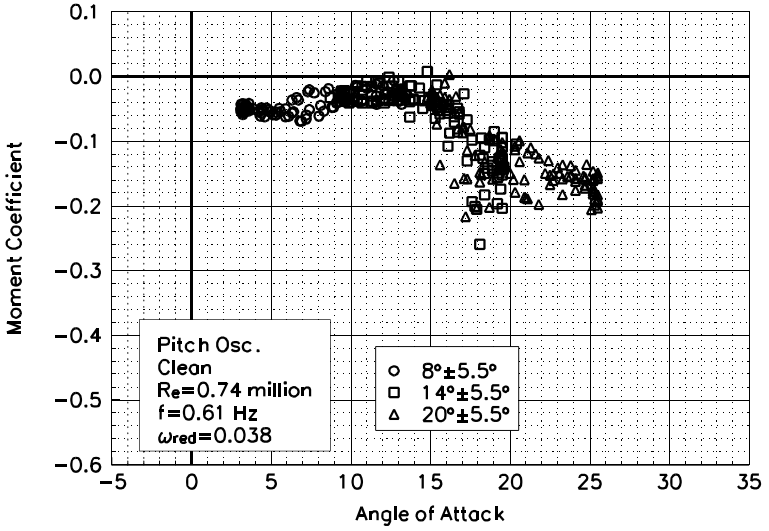

Figure C3. Moment coefficient vs α.

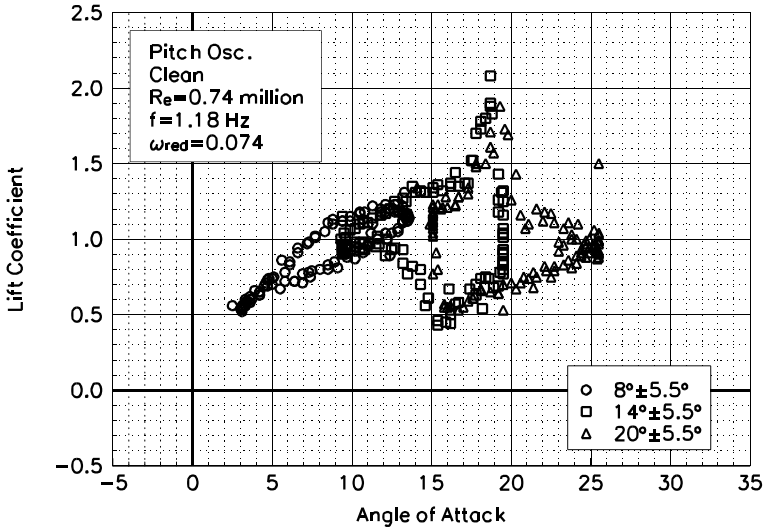

Figure C4. Lift coefficient vs α.

S810
Clean
Re=0.74 million
$\omega_{reduced}$=0.074

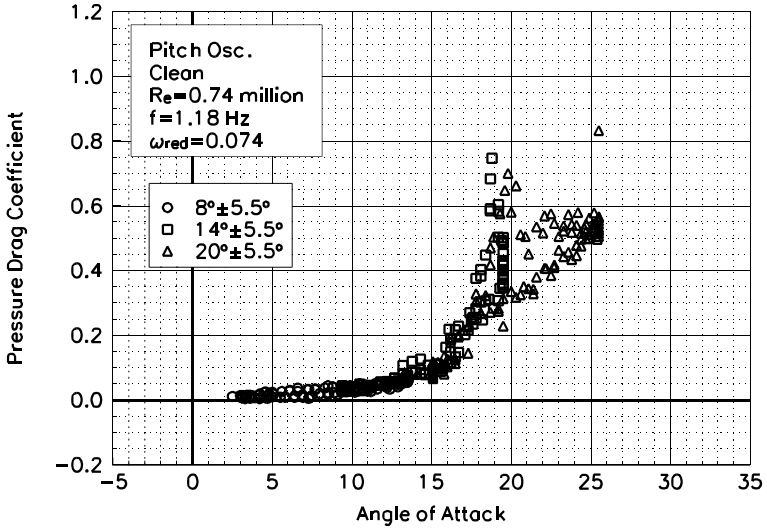

Figure C5. Pressure drag coefficient vs α.

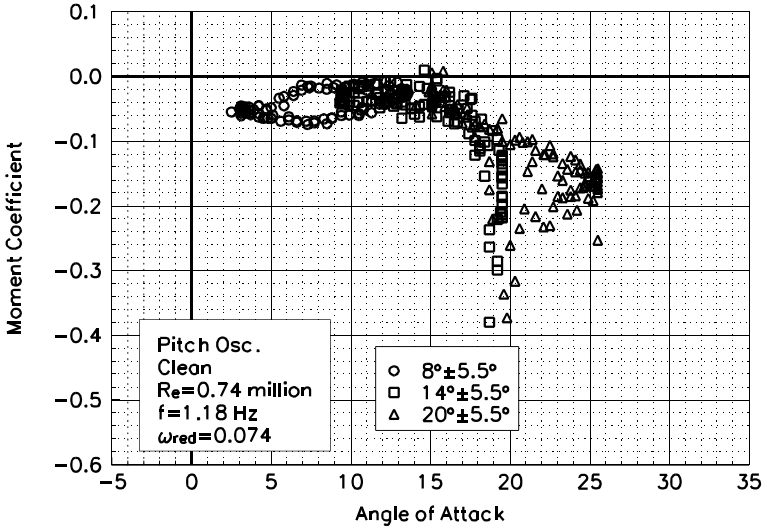

Figure C6. Moment coefficient vs α.

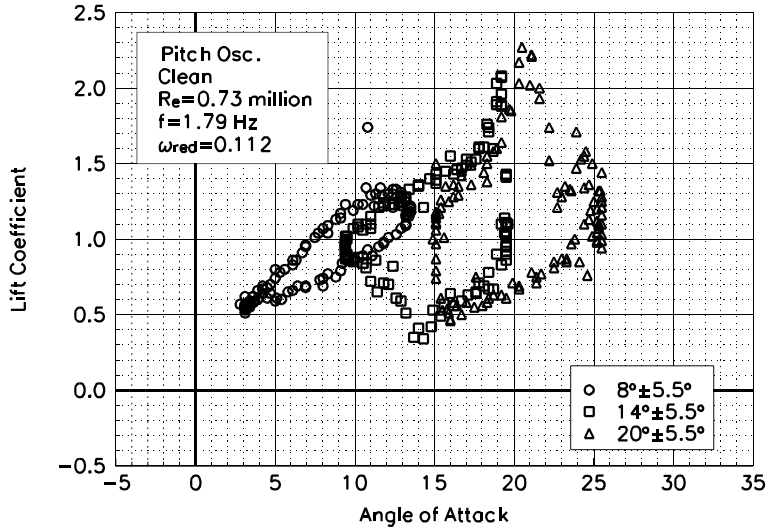

Figure C7. Lift coefficient vs α.

S810
Clean
Re=0.73 million
$\omega_{reduced}$=0.112

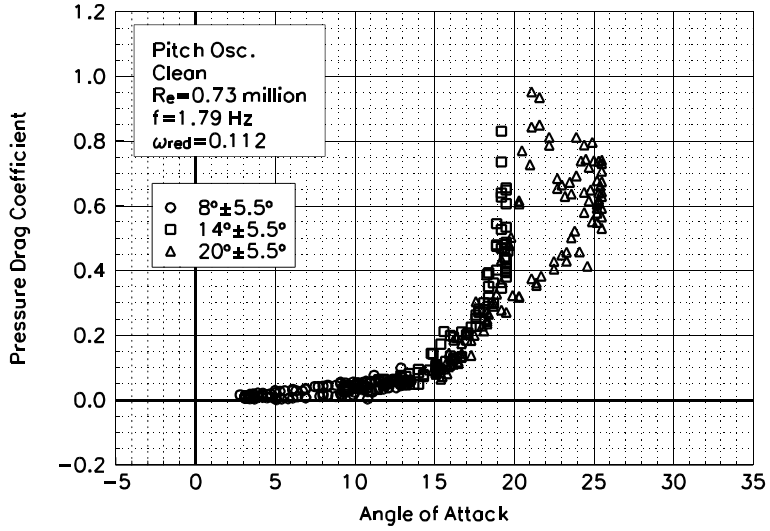

Figure C8. Pressure drag coefficient vs α.

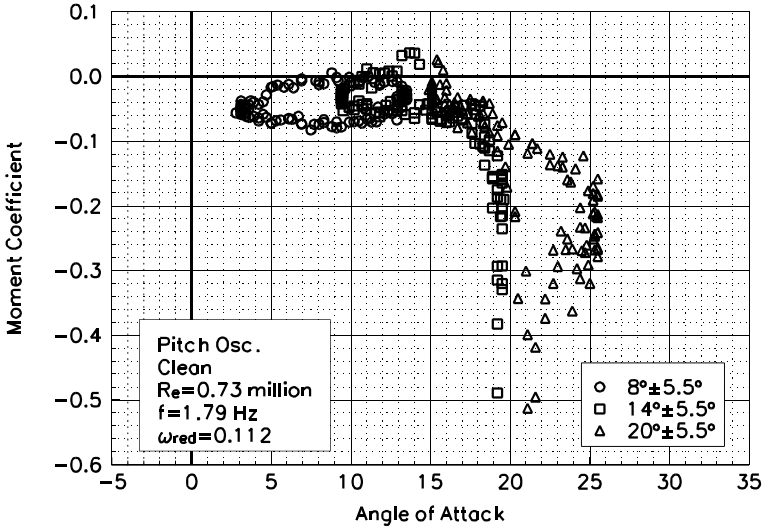

Figure C9. Moment coefficient vs α.

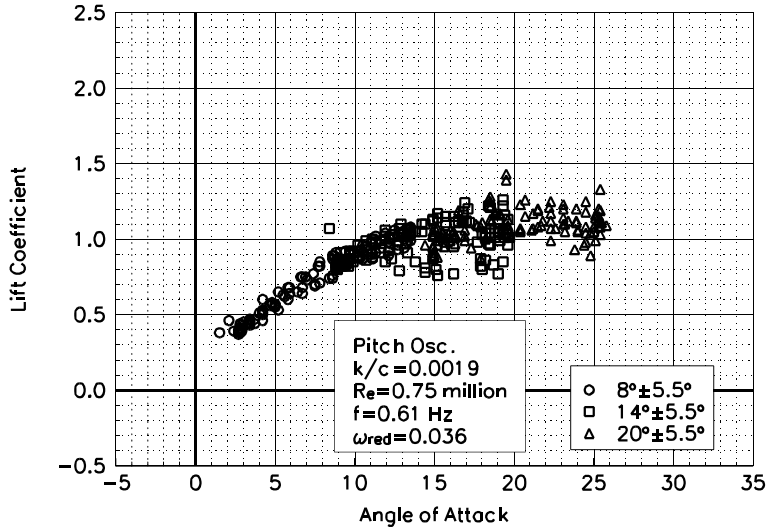

Figure C10. Lift coefficient vs α.

S810
LEGR
Re=0.75 million
$\omega_{reduced}$=0.036

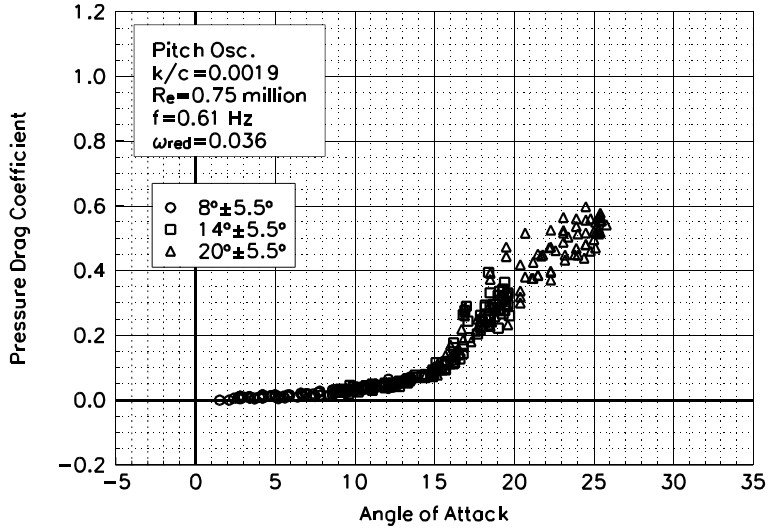

Figure C11. Pressure drag coefficient vs α.

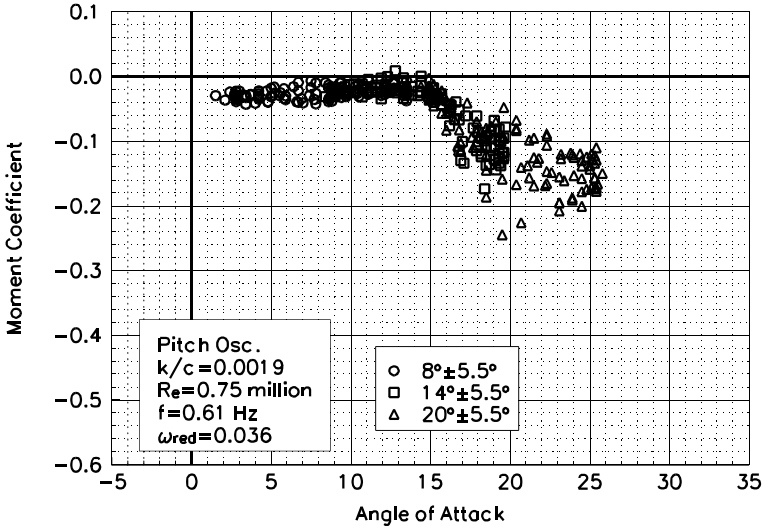

Figure C12. Moment coefficient vs α.

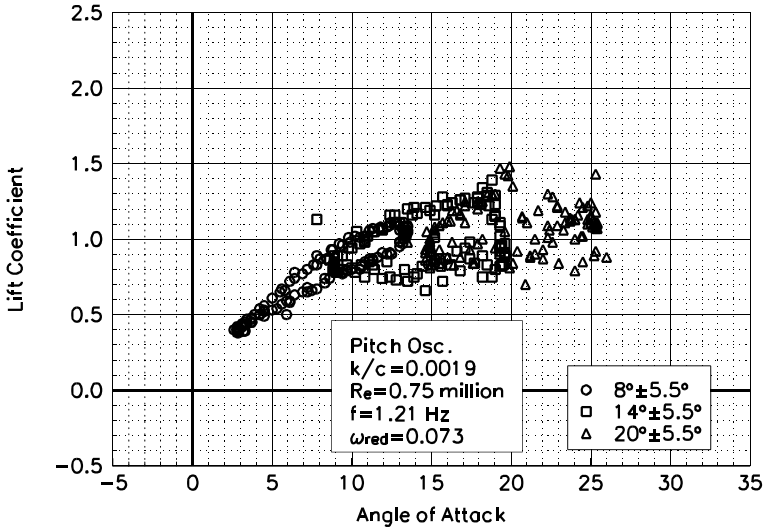

Figure C13. Lift coefficient vs α.

S810
LEGR
Re=0.75 million
$\omega_{reduced}$=0.073

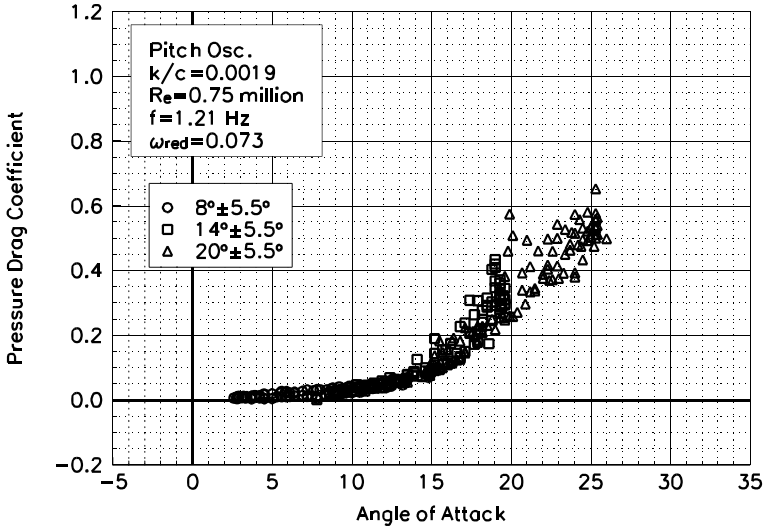

Figure C14. Pressure drag coefficient vs α.

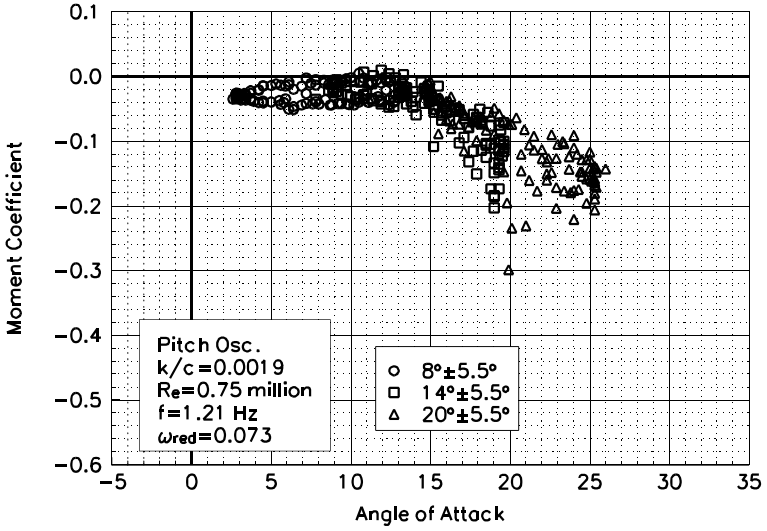

Figure C15. Moment coefficient vs α.

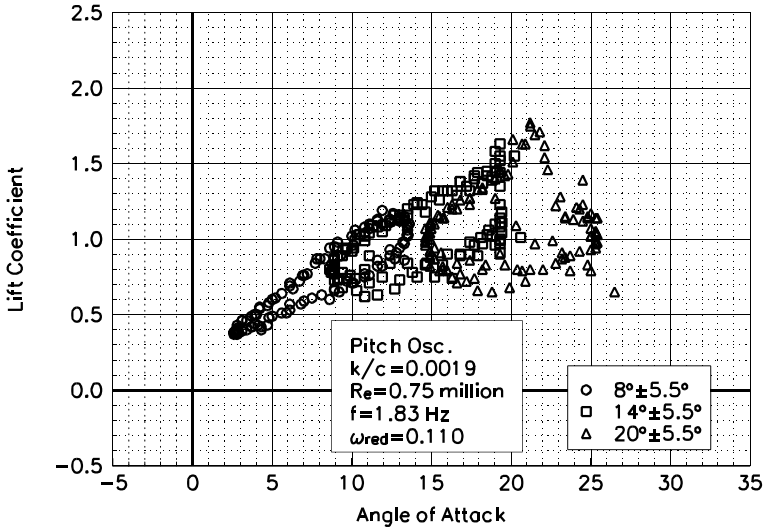

S810
LEGR
Re=0.75 million
$\omega_{reduced}$=0.110

Figure C16. Lift coefficient vs α.

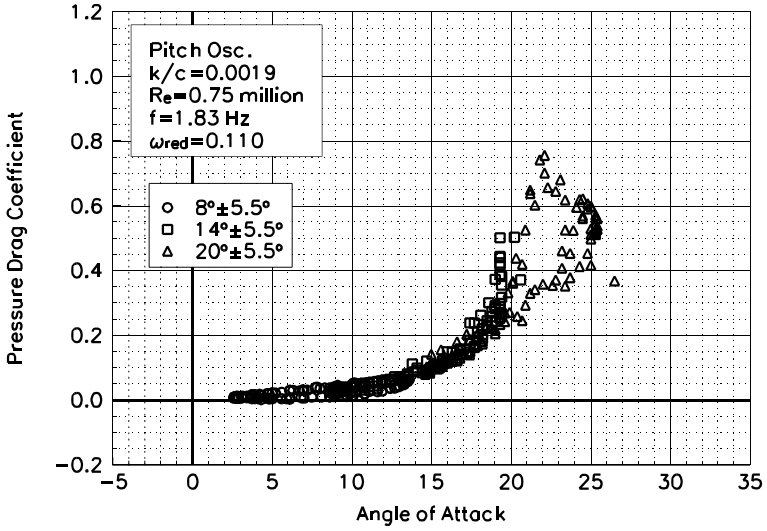

Figure C17. Pressure drag coefficient vs α.

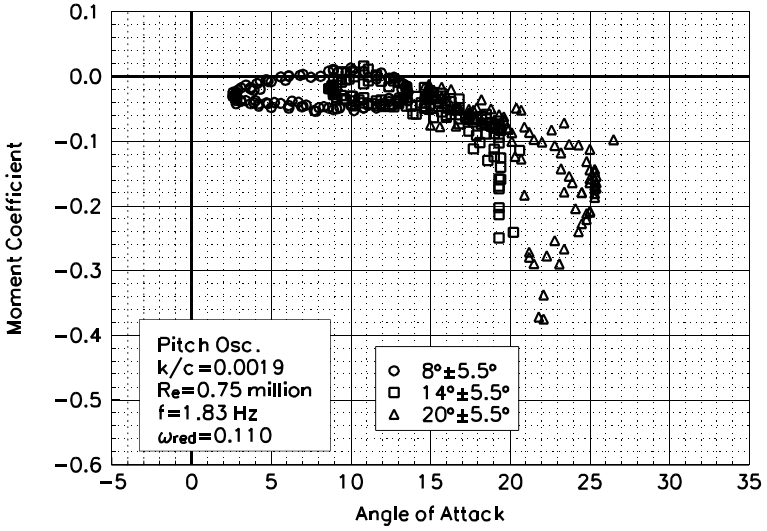

Figure C18. Moment coefficient vs α.

Unsteady Airfoil Characteristics

±5.5° Sine, Re = 1 million

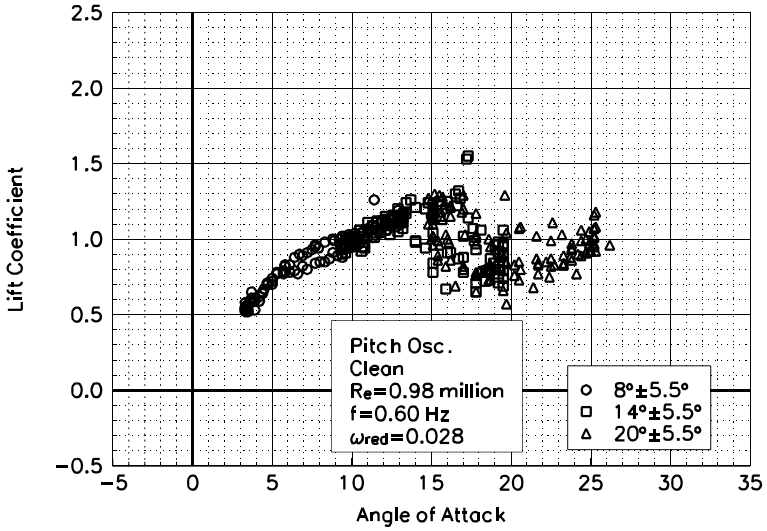

Figure C19. Lift coefficient vs α.

S810
Clean
Re=0.98 million
$\omega_{reduced}$=0.028

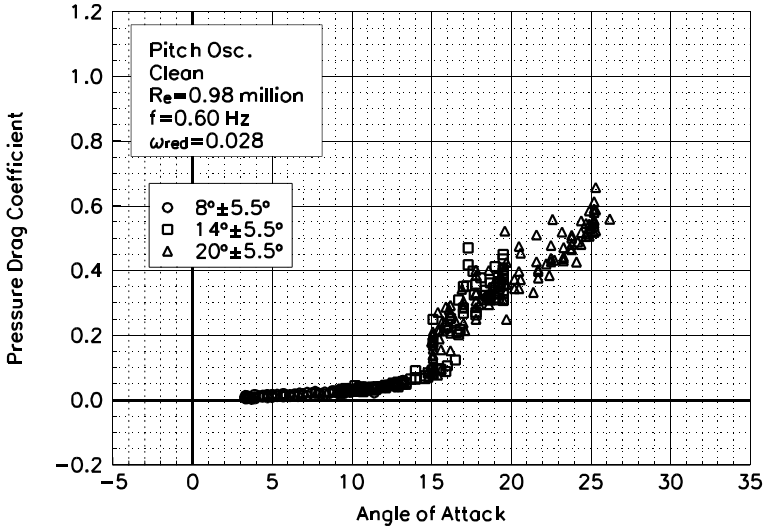

Figure C20. Pressure drag coefficient vs α.

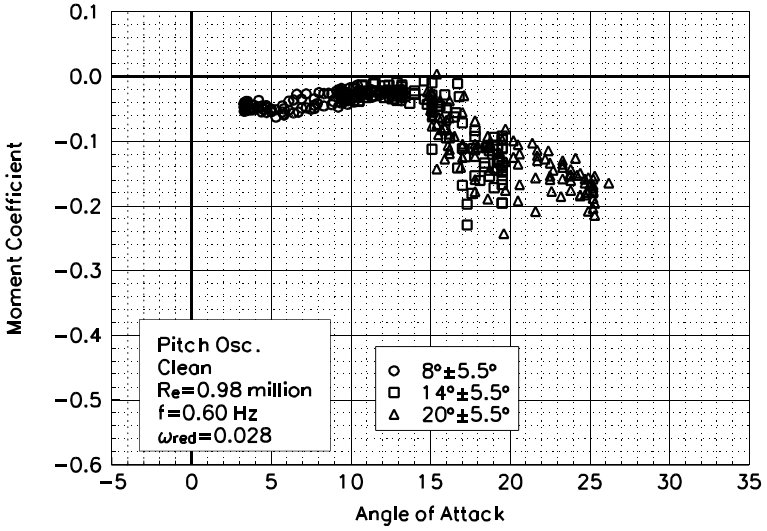

Figure C21. Moment coefficient vs α.

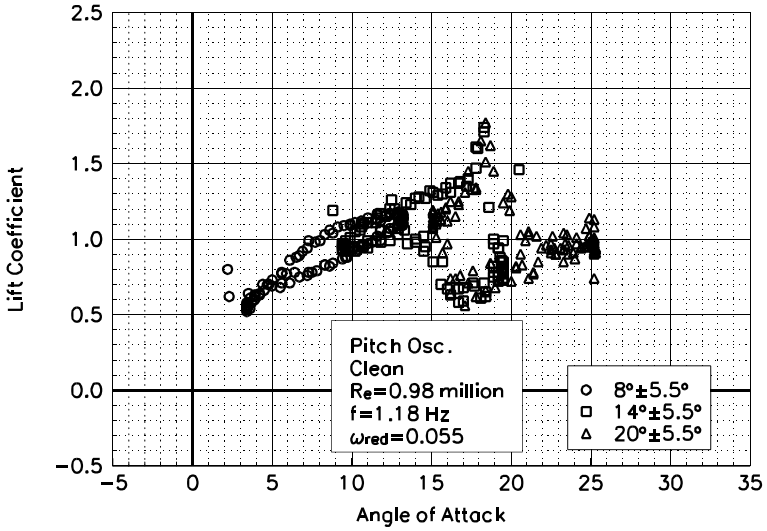

Figure C22. Lift coefficient vs α.

S810
Clean
Re=0.98 million
$\omega_{reduced}$=0.055

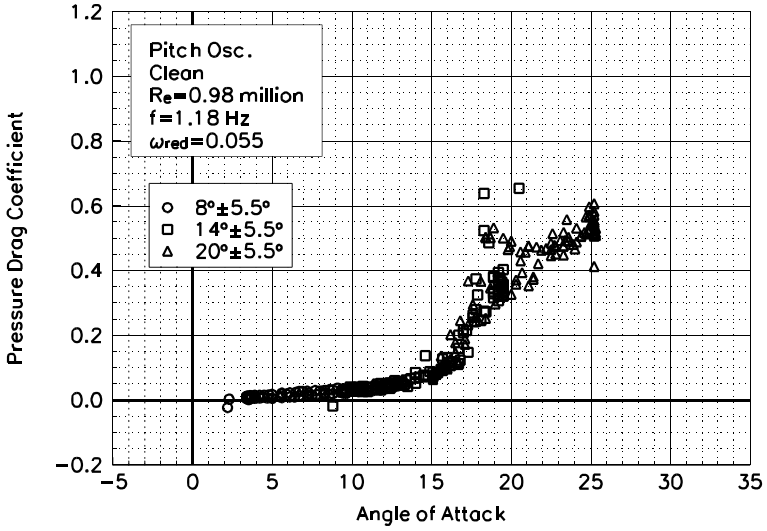

Figure C23. Pressure drag coefficient vs α.

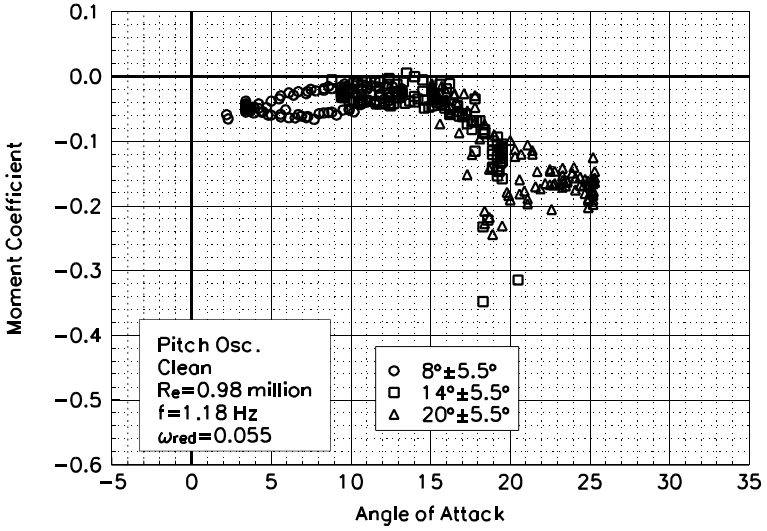

Figure C24. Moment coefficient vs α.

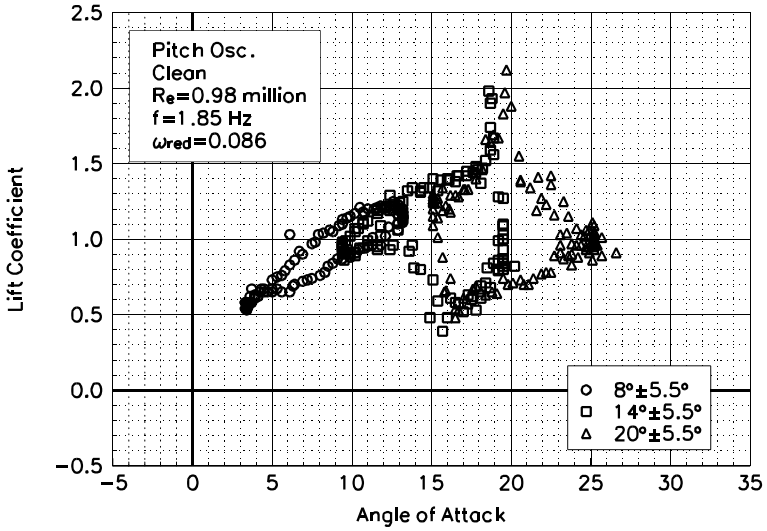

Figure C25. Lift coefficient vs α.

S810
Clean
Re=0.98 million
$\omega_{reduced}$=0.086

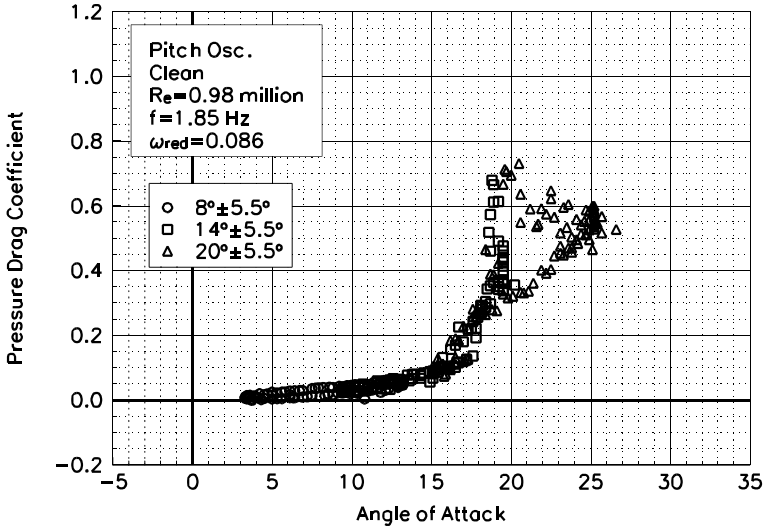

Figure C26. Pressure drag coefficient vs α.

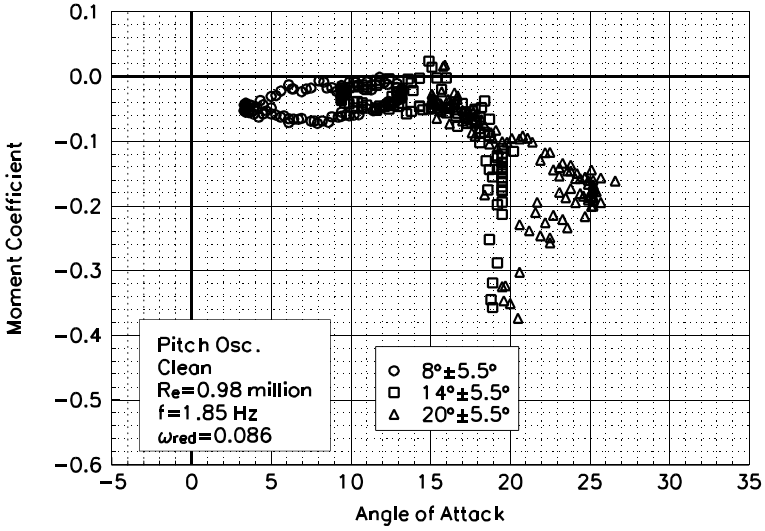

Figure C27. Moment coefficient vs α.

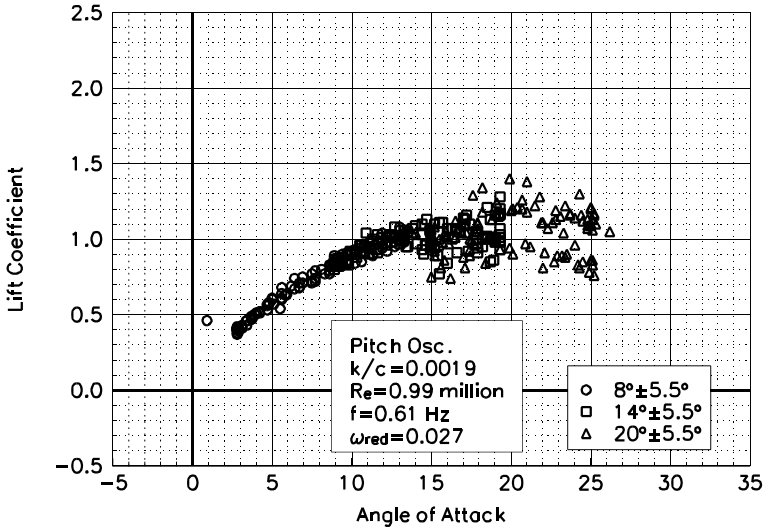

Figure C28. Lift coefficient vs α.

S810
LEGR
Re=0.99 million
$\omega_{reduced}$=0.027

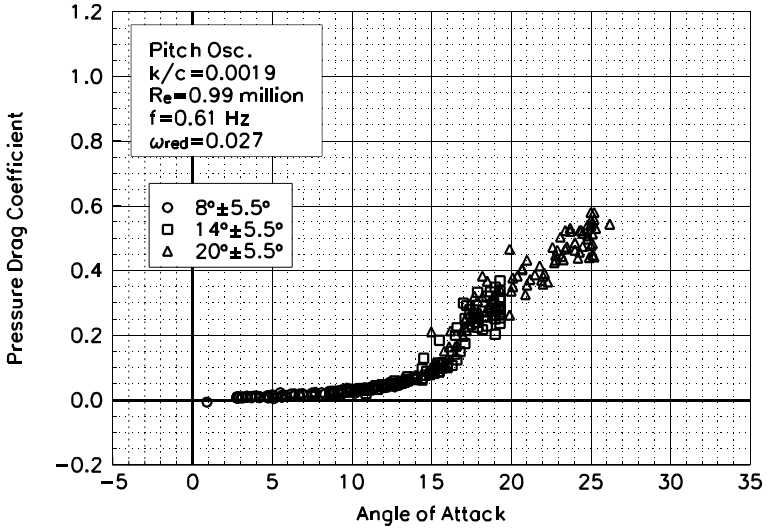

Figure C29. Pressure drag coefficient vs α.

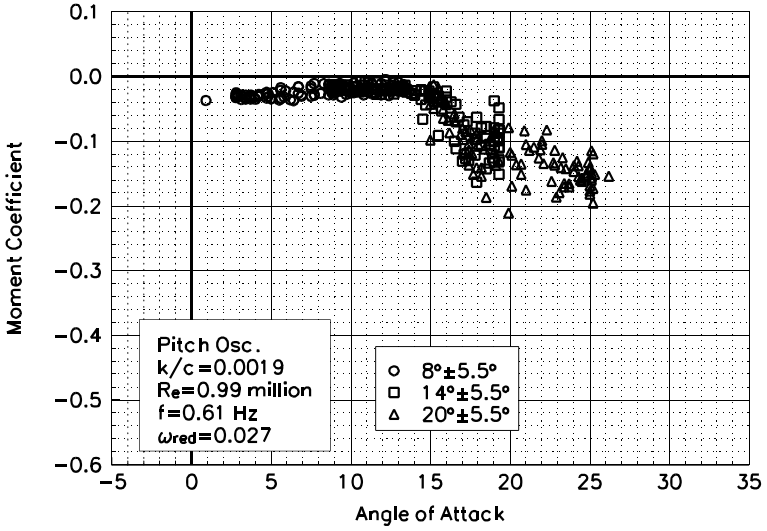

Figure C30. Moment coefficient vs α.

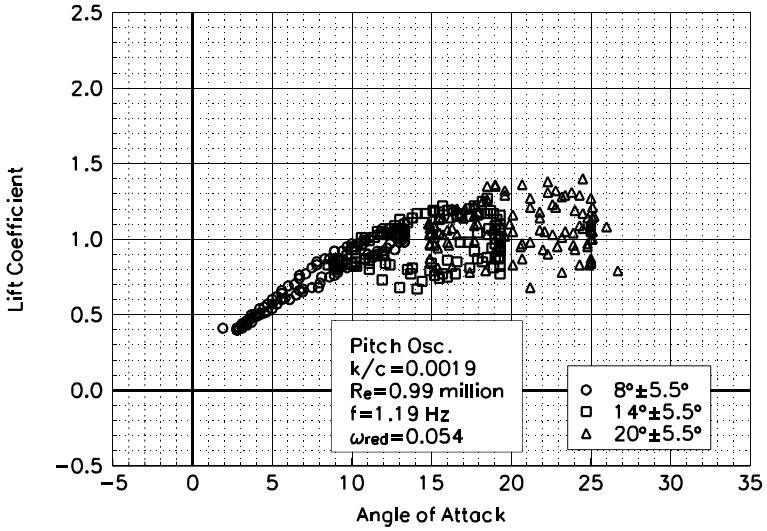

Figure C31. Lift coefficient vs α.

S810
LEGR
Re=0.99 million
$\omega_{reduced}$=0.054

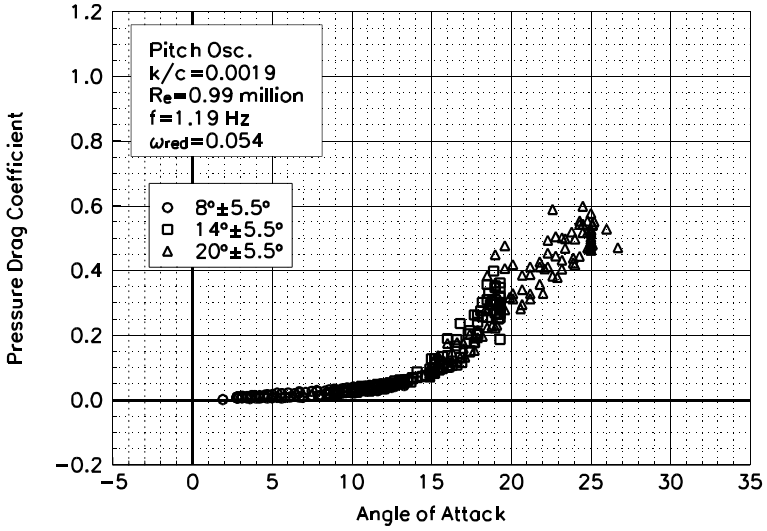

Figure C32. Pressure drag coefficient vs α.

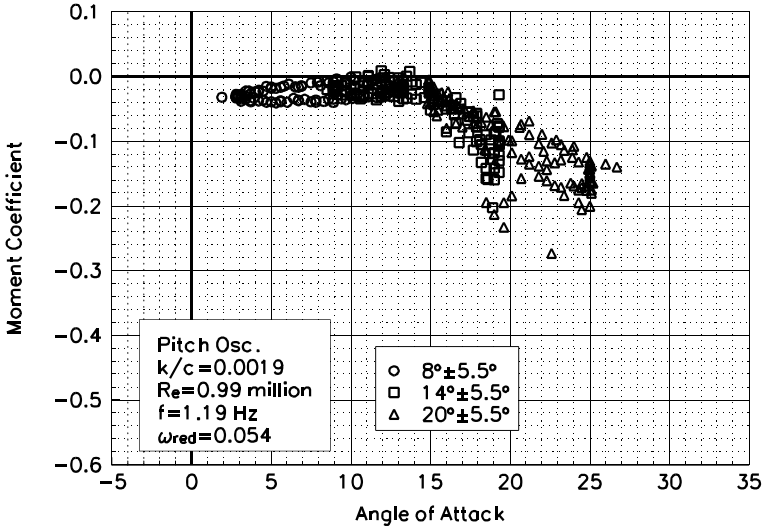

Figure C33. Moment coefficient vs α.

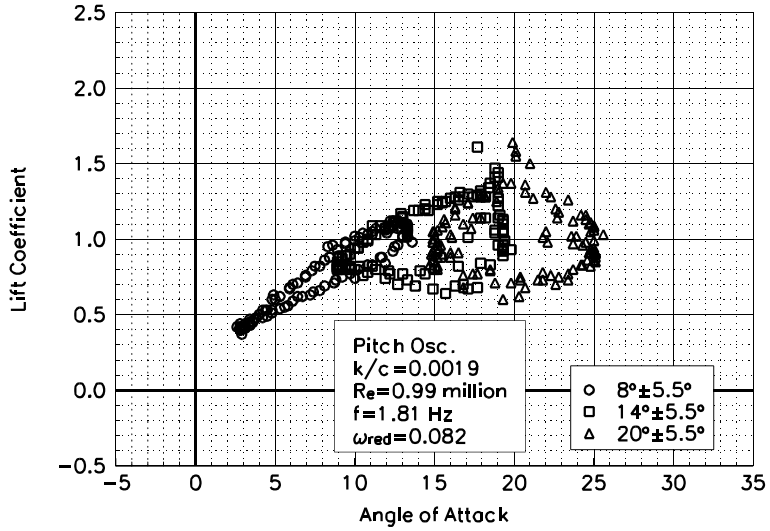

Figure C34. Lift coefficient vs α.

S810
LEGR
Re=0.99 million
$\omega_{reduced}$=0.082

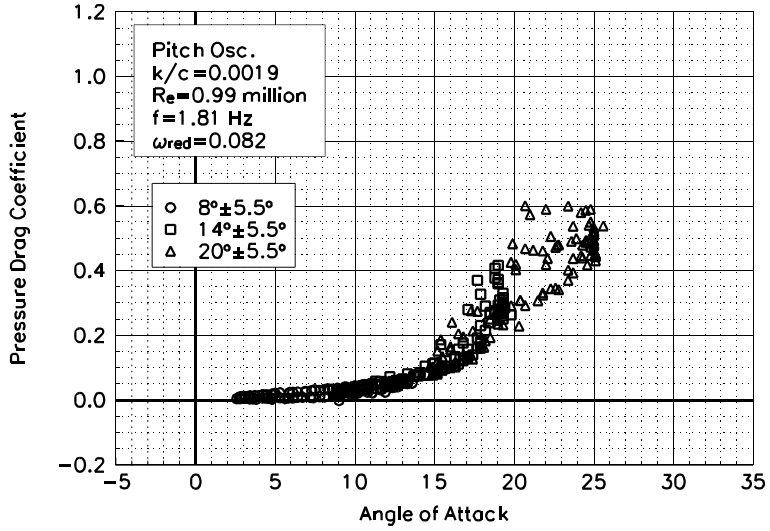

Figure C35. Pressure drag coefficient vs α.

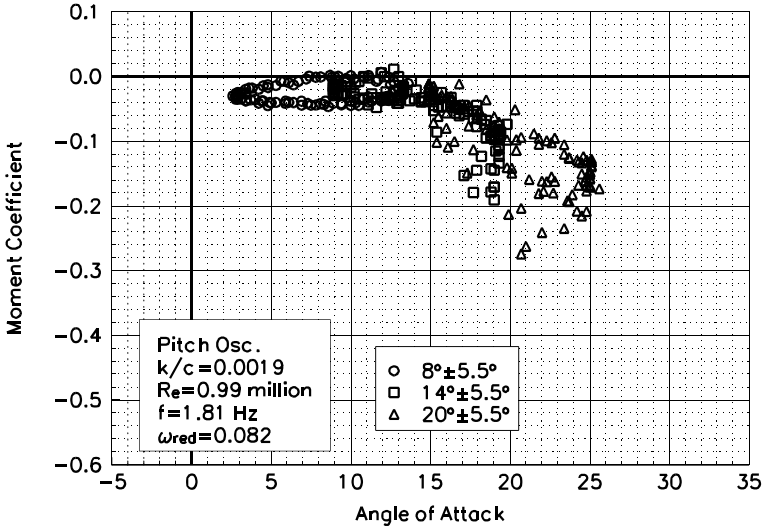

Figure C36. Moment coefficient vs α.

Unsteady Airfoil Characteristics

±5.5° Sine, Re= 1.25 million

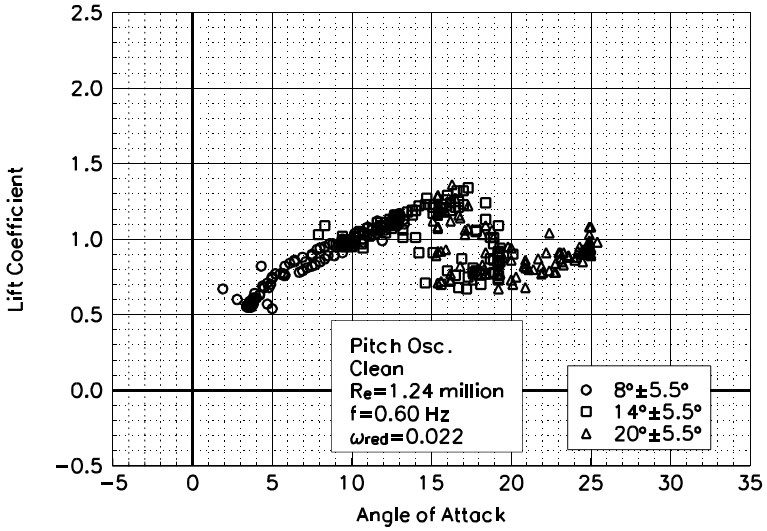

Figure C37. Lift coefficient vs α.

S810
Clean
Re=1.24 million
$\omega_{reduced}$=0.022

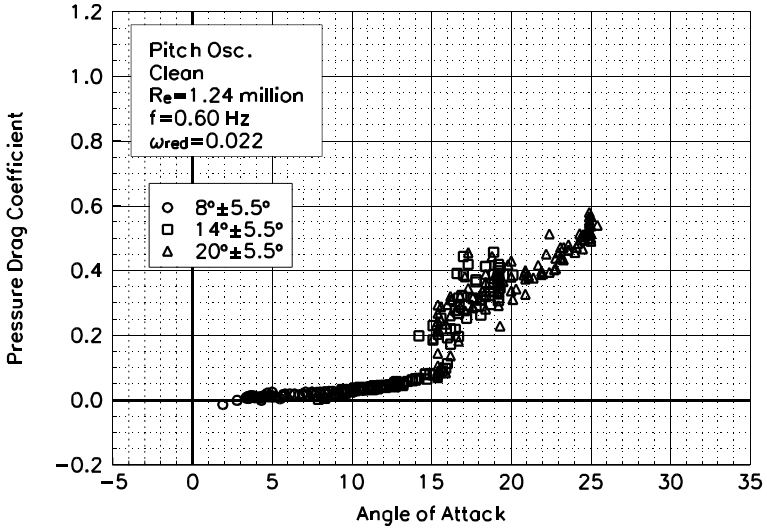

Figure C38. Pressure drag coefficient vs α.

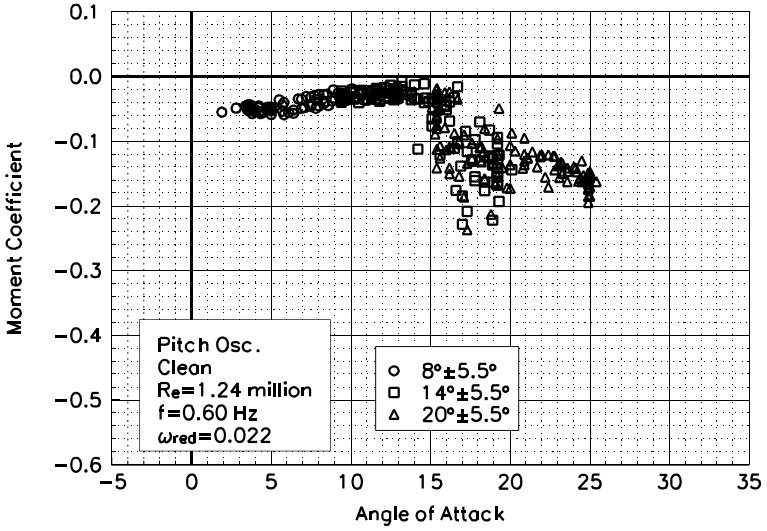

Figure C39. Moment coefficient vs α.

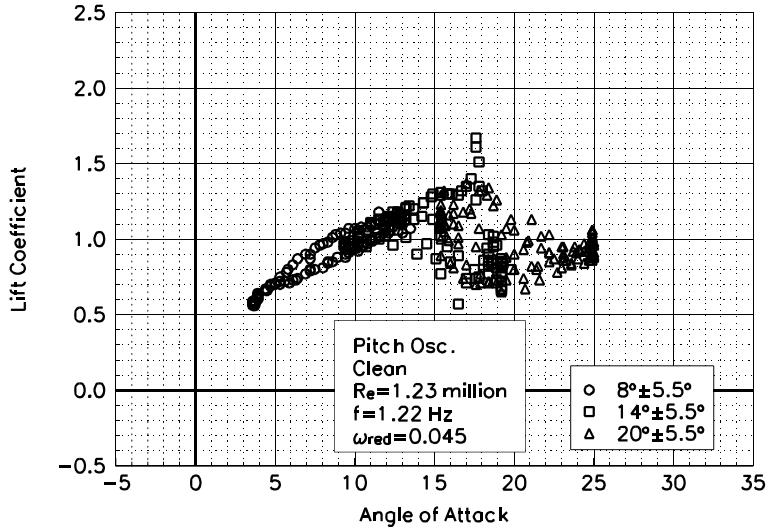

Figure C40. Lift coefficient vs α.

S810
Clean
Re=1.23 million
$\omega_{reduced}$=0.045

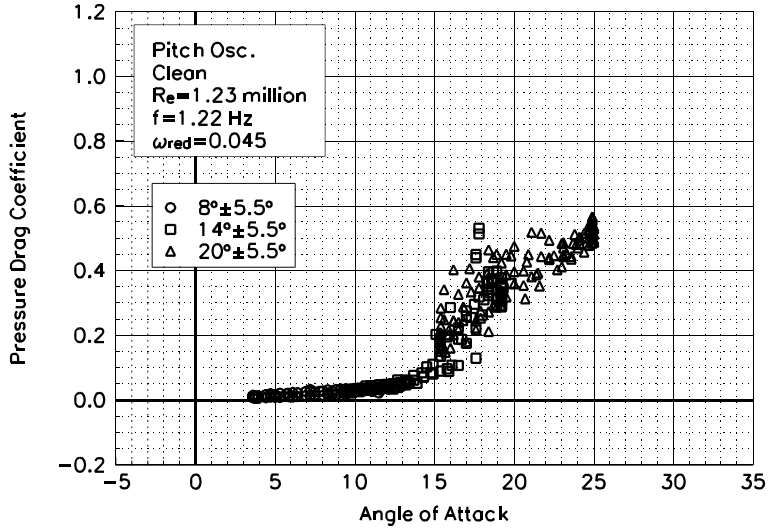

Figure C41. Pressure drag coefficient vs α.

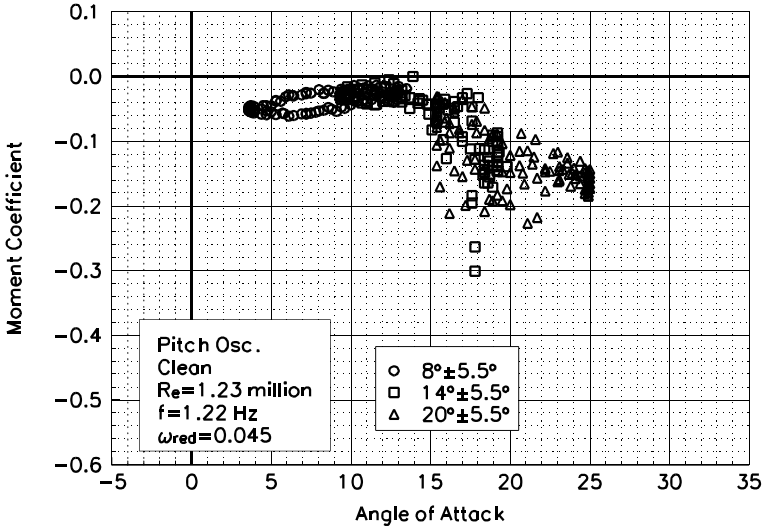

Figure C42. Moment coefficient vs α.

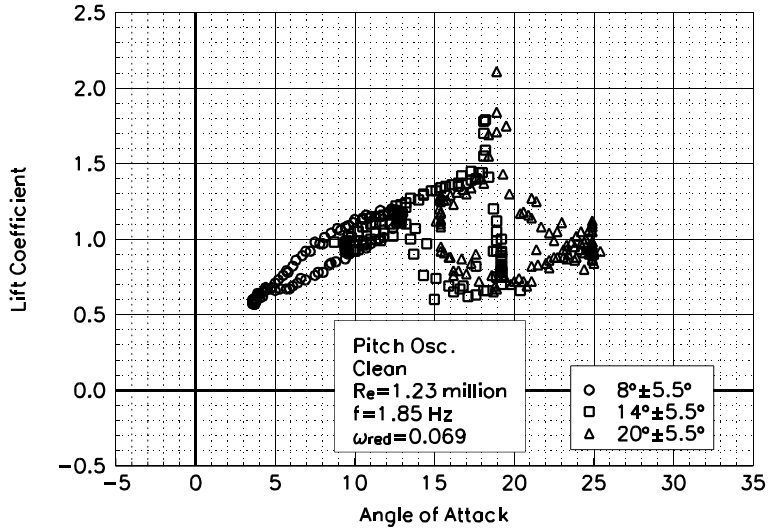

S810
Clean
Re=1.23 million
$\omega_{reduced}$=0.069

Figure C43. Lift coefficient vs α.

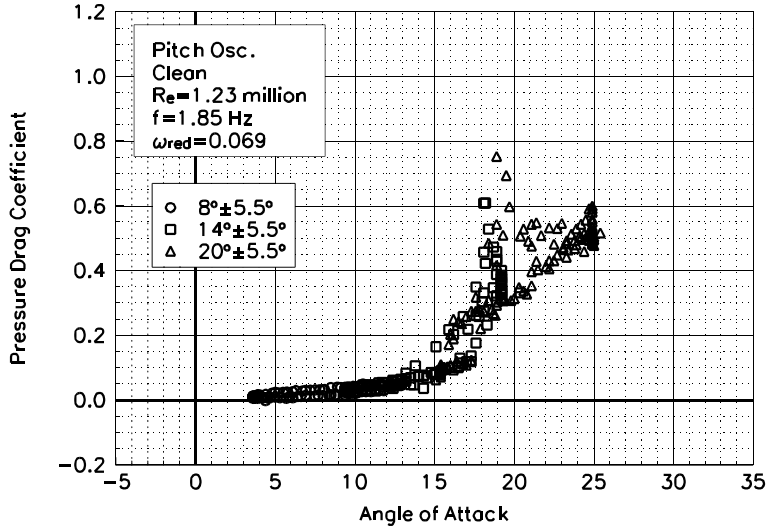

Figure C44. Pressure drag coefficient vs α.

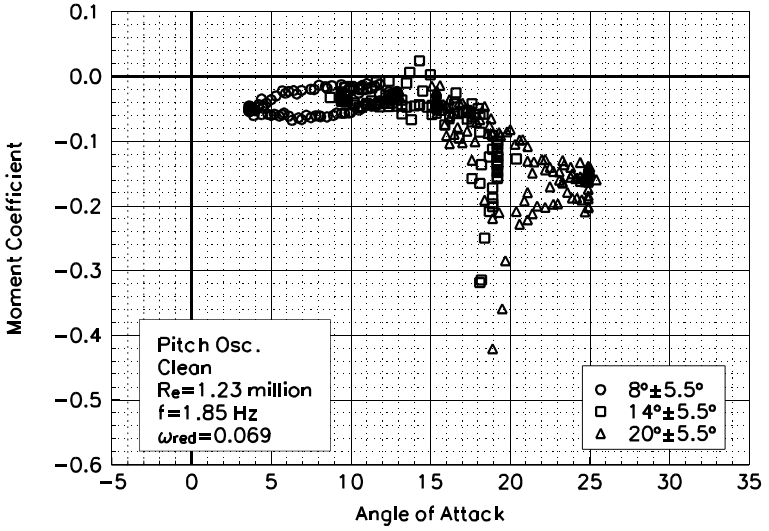

Figure C45. Moment coefficient vs α.

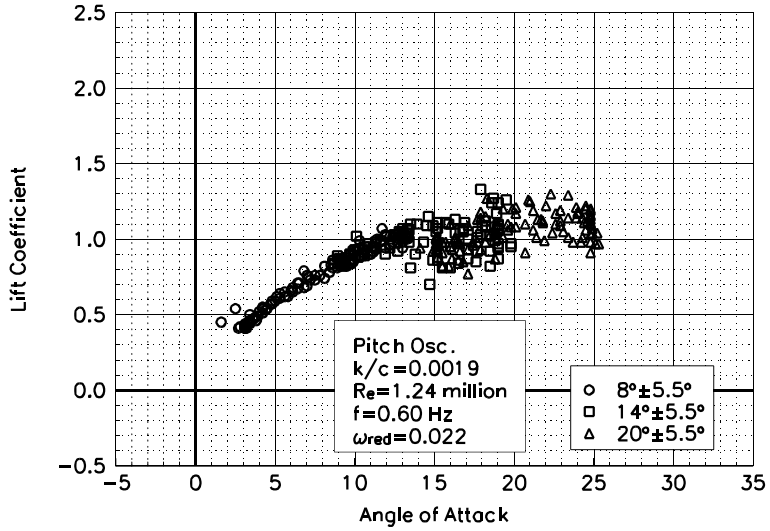

Figure C46. Lift coefficient vs α.

S810
LEGR
Re=1.24 million
$\omega_{reduced}$=0.022

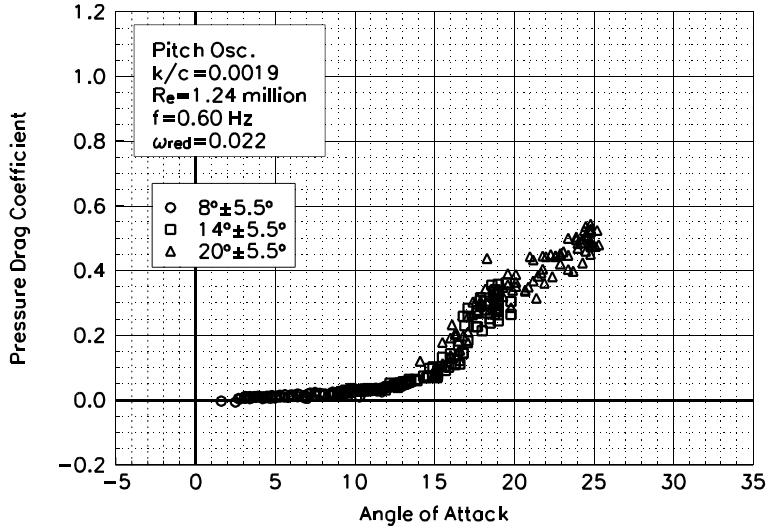

Figure C47. Pressure drag coefficient vs α.

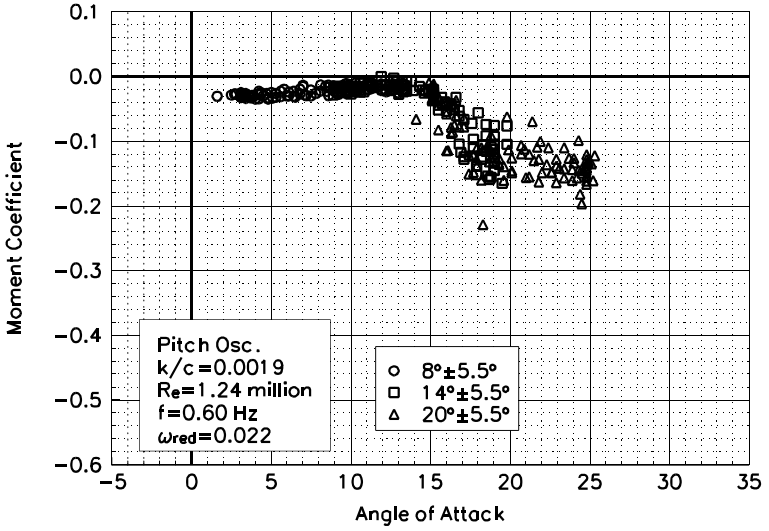

Figure C48. Moment coefficient vs α.

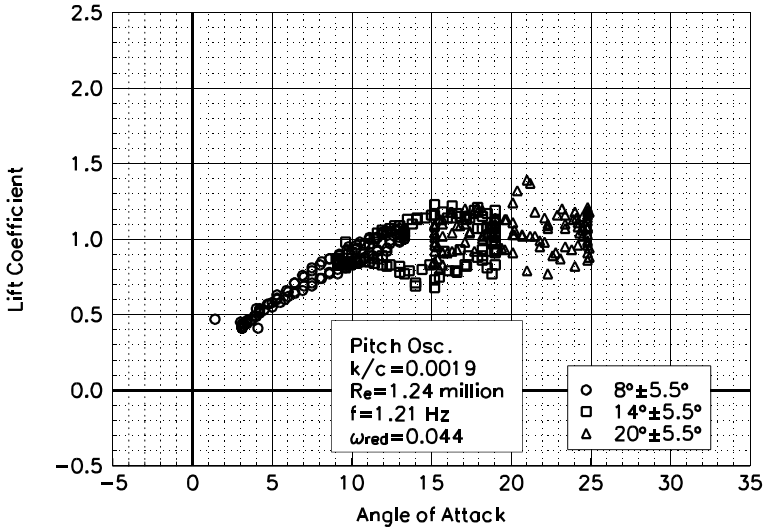

Figure C49. Lift coefficient vs α.

S810
LEGR
Re=1.24 million
$\omega_{reduced}$=0.044

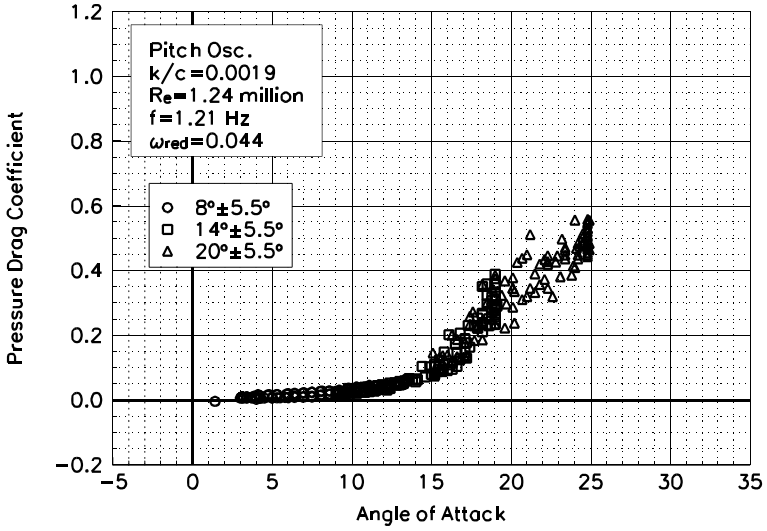

Figure C50. Pressure drag coefficient vs α.

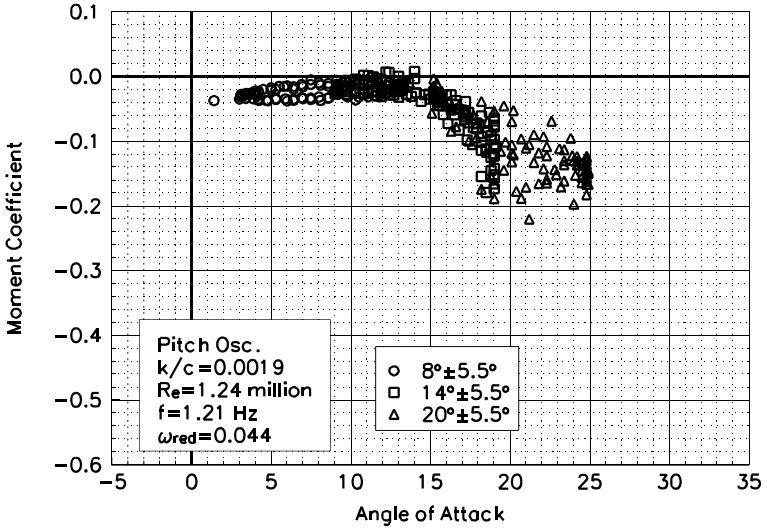

Figure C51. Moment coefficient vs α.

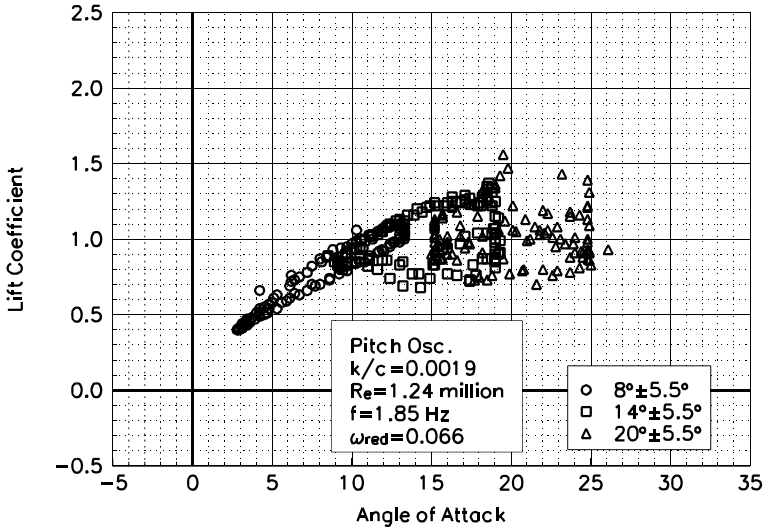

Figure C52. Lift coefficient vs α.

S810
LEGR
Re=1.24 million
$\omega_{reduced}$=0.066

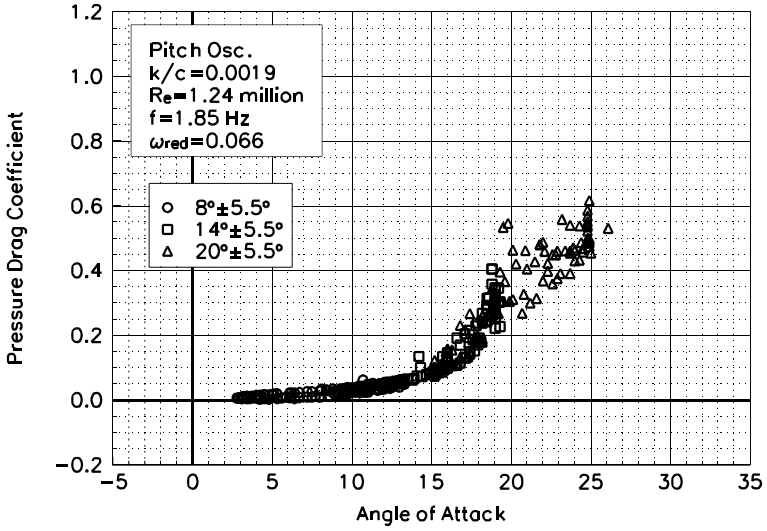

Figure C53. Pressure drag coefficient vs α.

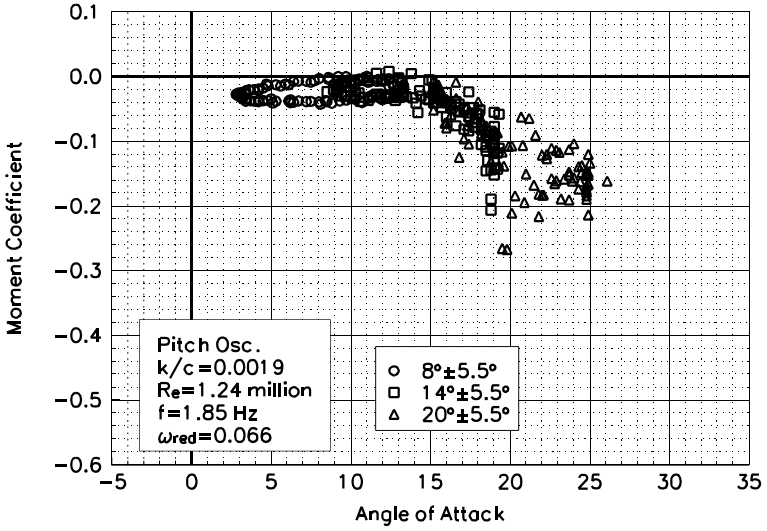

Figure C54. Moment coefficient vs α.

Unsteady Airfoil Characteristics

±5.5° Sine, Re = 1.5 million

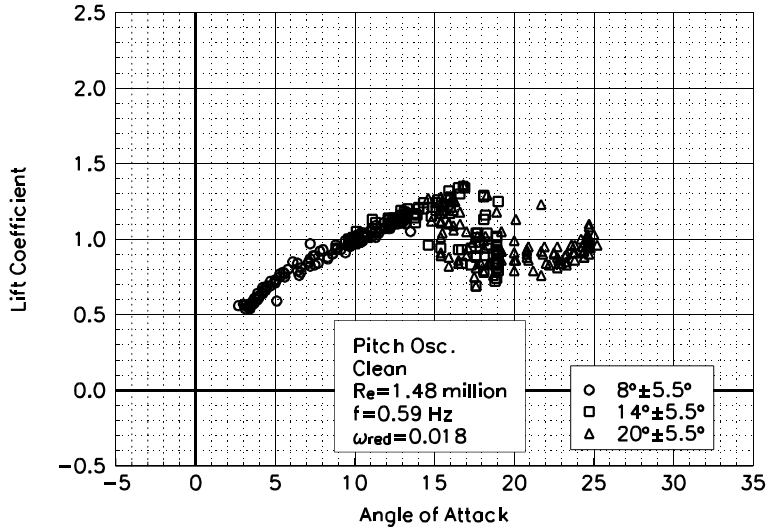

Figure C55. Lift coefficient vs α.

S810
Clean
Re=1.48 million
$\omega_{reduced}$=0.018

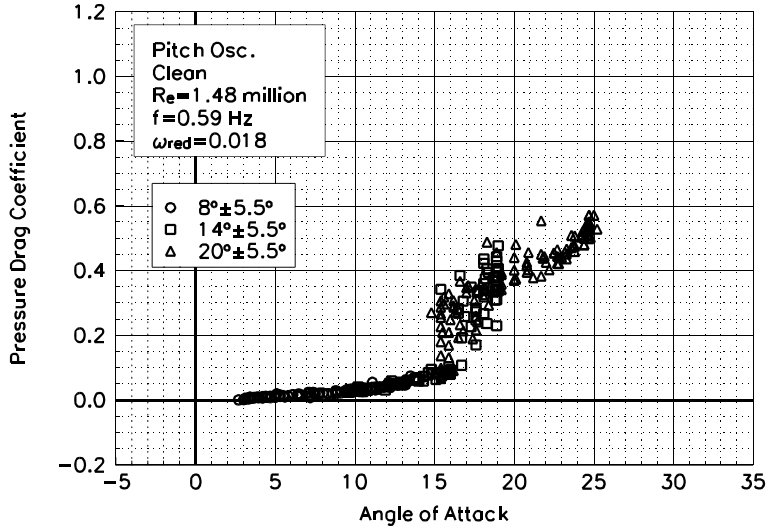

Figure C56. Pressure drag coefficient vs α.

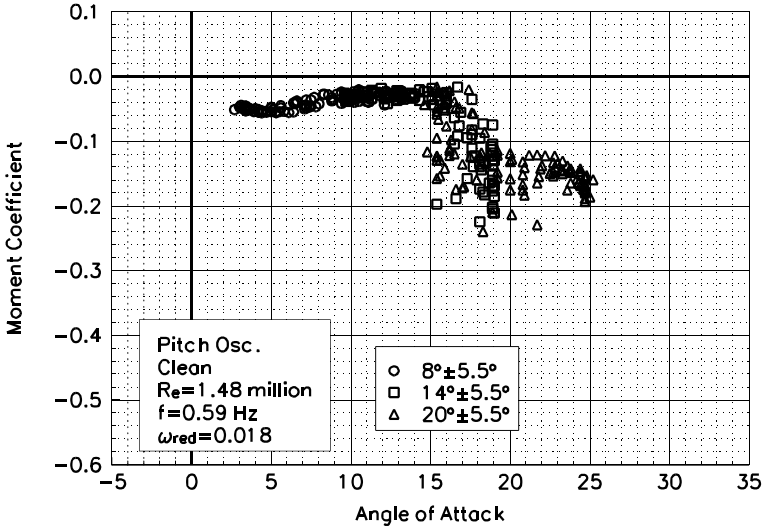

Figure C57. Moment coefficient vs α.

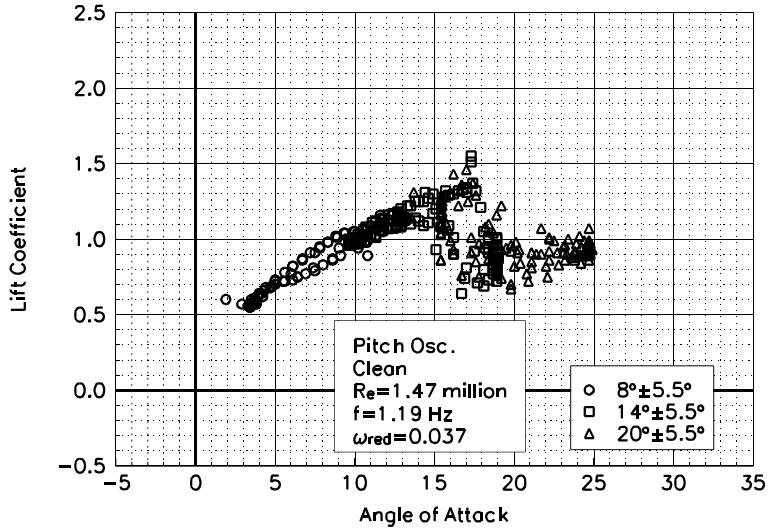

Figure C58. Lift coefficient vs α.

S810
Clean
Re=1.47 million
$\omega_{reduced}$=0.037

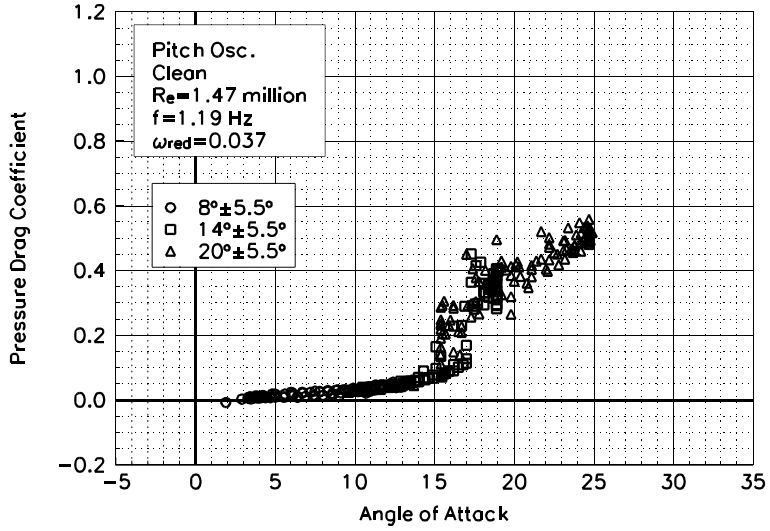

Figure C59. Pressure drag coefficient vs α.

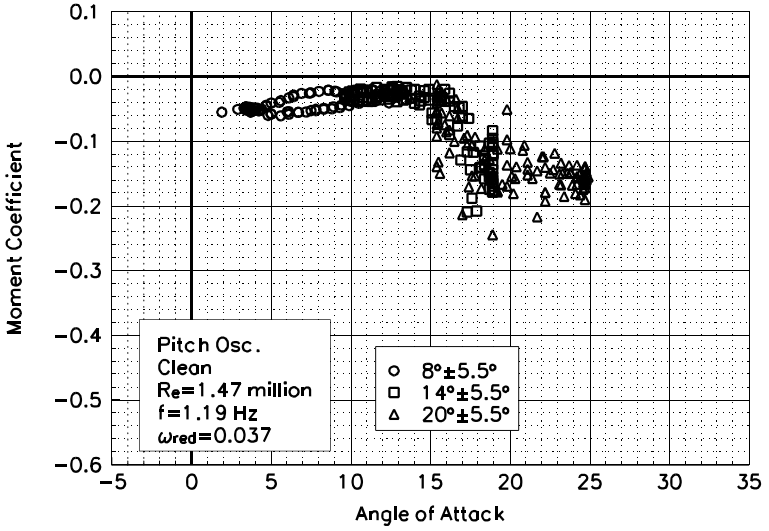

Figure C60. Moment coefficient vs α.

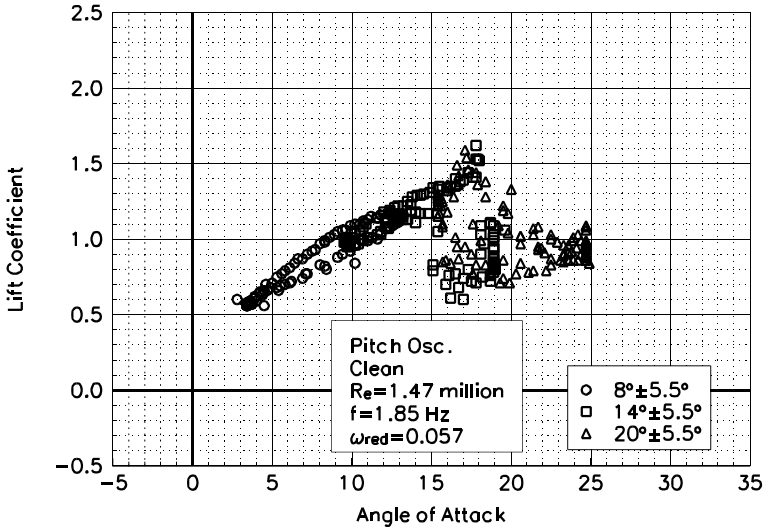

Figure C61. Lift coefficient vs α.

S810
Clean
Re=1.47 million
$\omega_{reduced}$=0.057

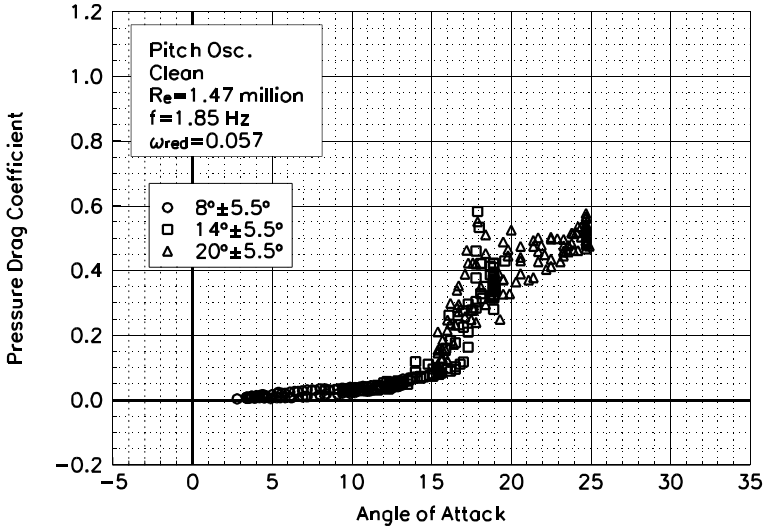

Figure C62. Pressure drag coefficient vs α.

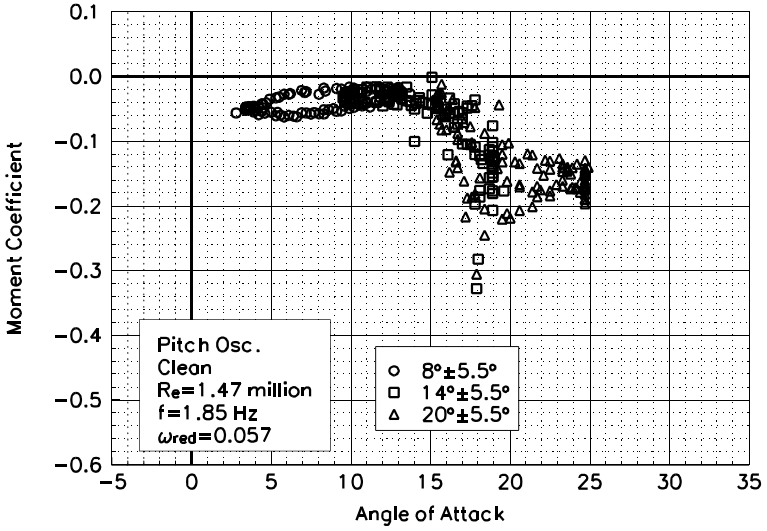

Figure C63. Moment coefficient vs α.

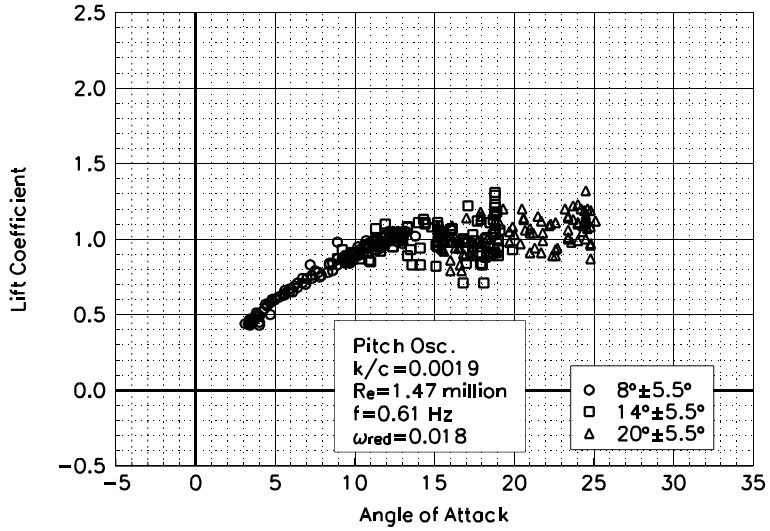

Figure C64. Lift coefficient vs α.

S810
LEGR
Re=1.47 million
$\omega_{reduced}$=0.018

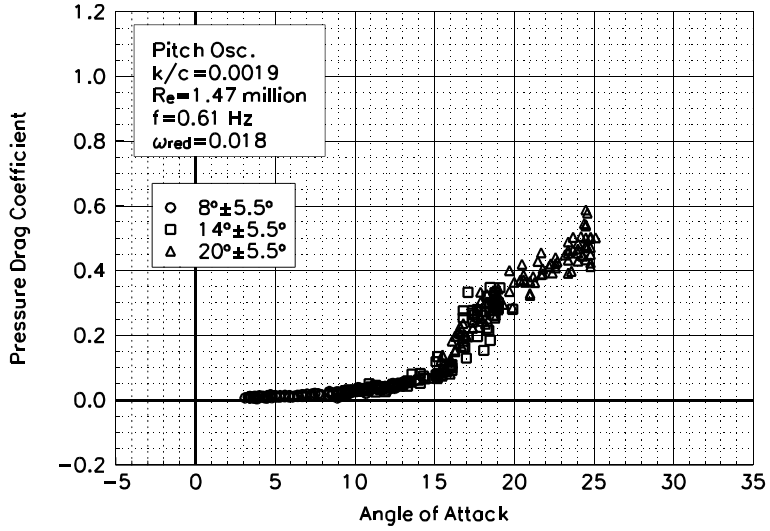

Figure C65. Pressure drag coefficient vs α.

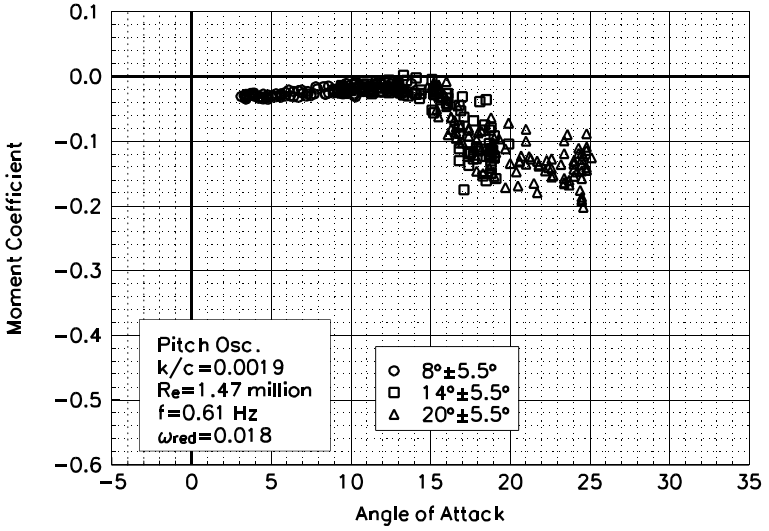

Figure C66. Moment coefficient vs α.

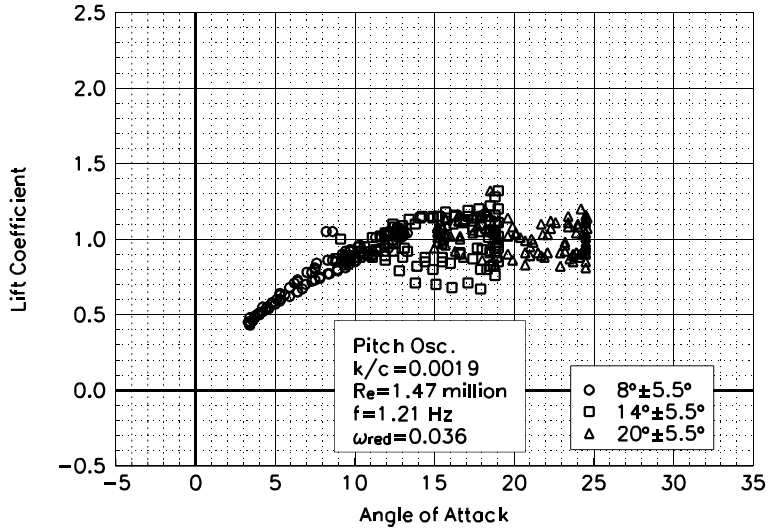

S810
LEGR
Re=1.47 million
$\omega_{reduced}$=0.036

Figure C67. Lift coefficient vs α.

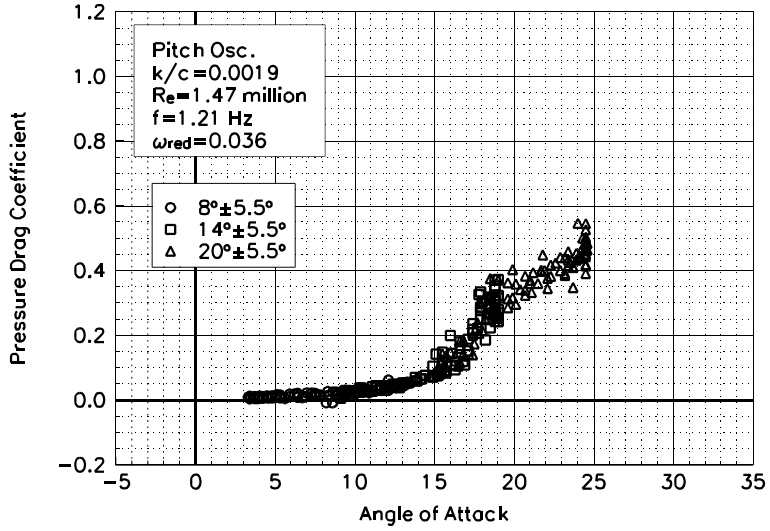

Figure C68. Pressure drag coefficient vs α.

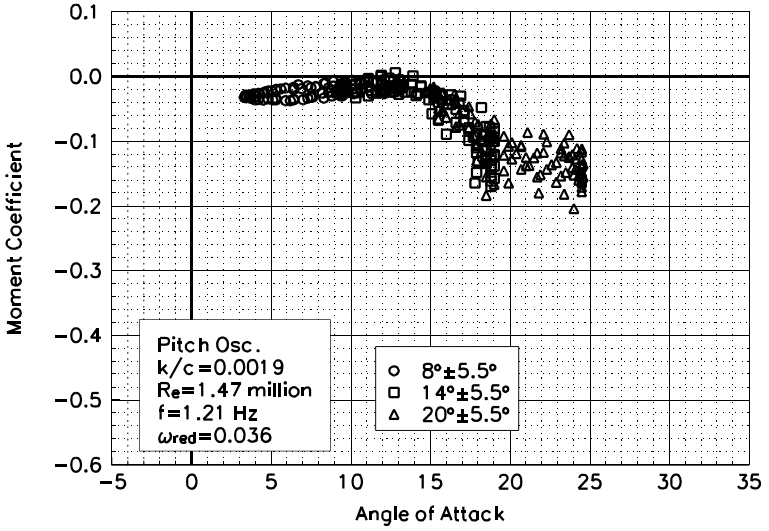

Figure C69. Moment coefficient vs α.

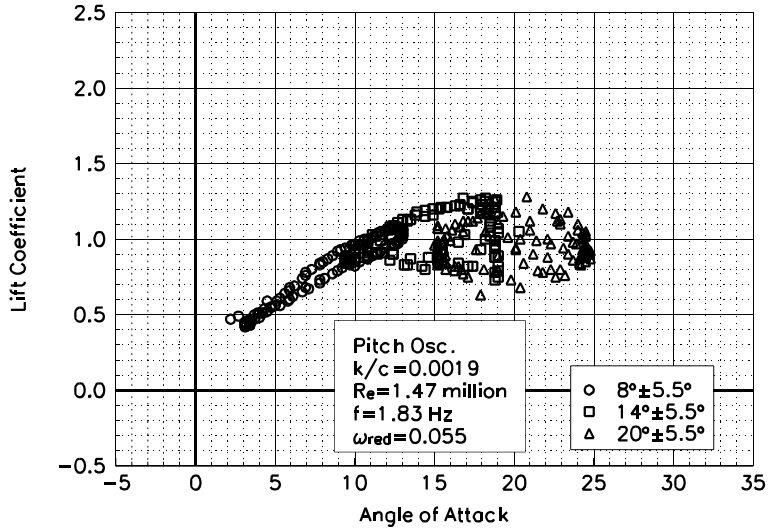

Figure C70. Lift coefficient vs α.

S810
LEGR
Re=1.47 million
$\omega_{reduced}$=0.055

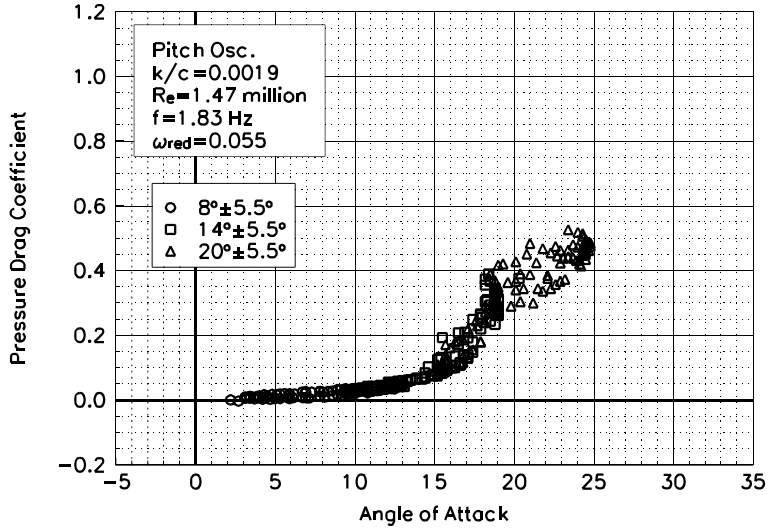

Figure C71. Pressure drag coefficient vs α.

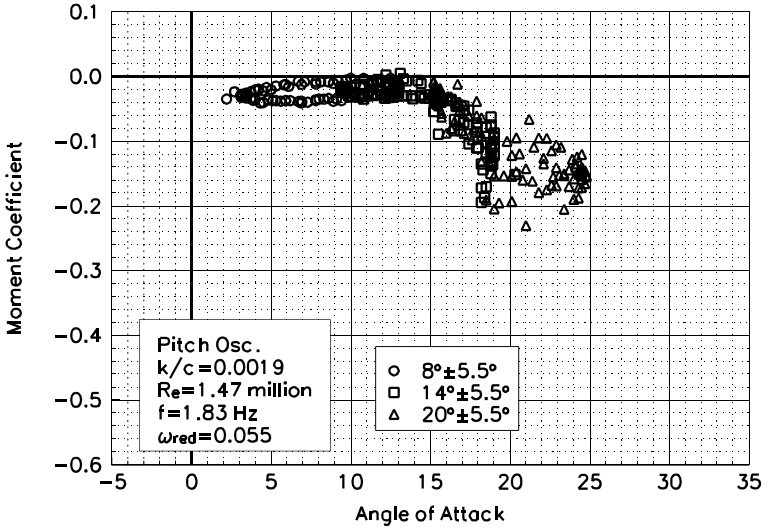

Figure C72. Moment coefficient vs α.

Unsteady Airfoil Characteristics

±10° Sine, Re = 0.75 million

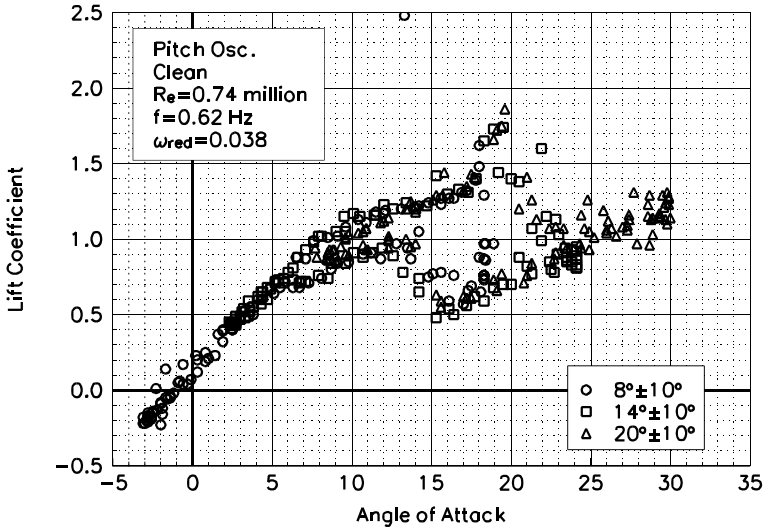

Figure C73. Lift coefficient vs α.

S810
Clean
Re=0.74 million
$\omega_{reduced}$=0.038

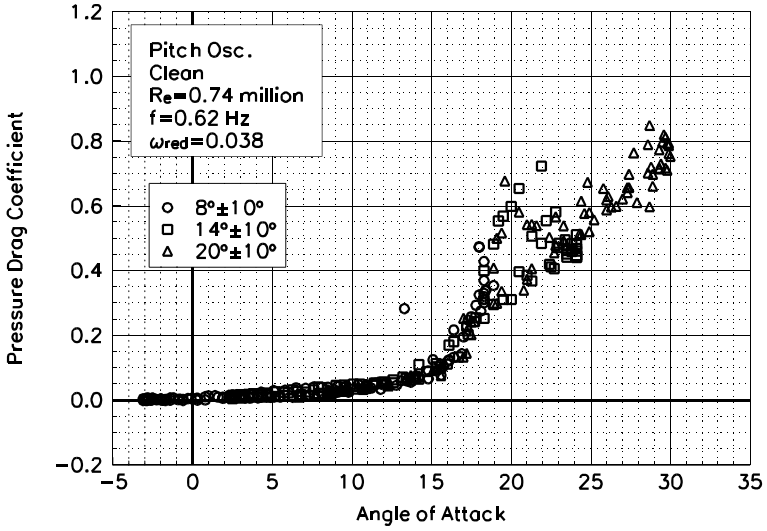

Figure C74. Pressure drag coefficient vs α.

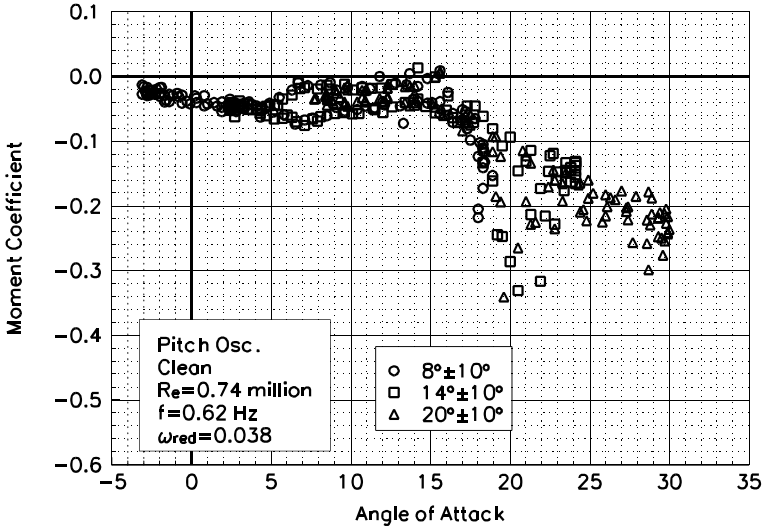

Figure C75. Moment coefficient vs α.

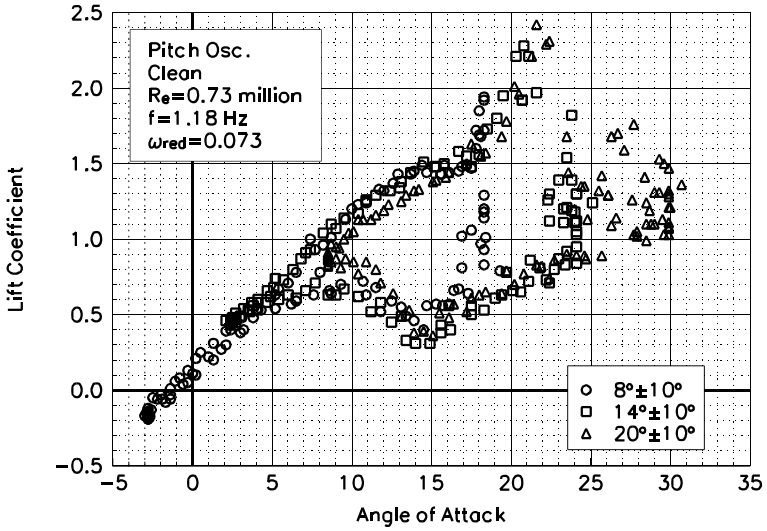

Figure C76. Lift coefficient vs α.

S810
Clean
Re=0.73 million
$\omega_{reduced}$=0.073

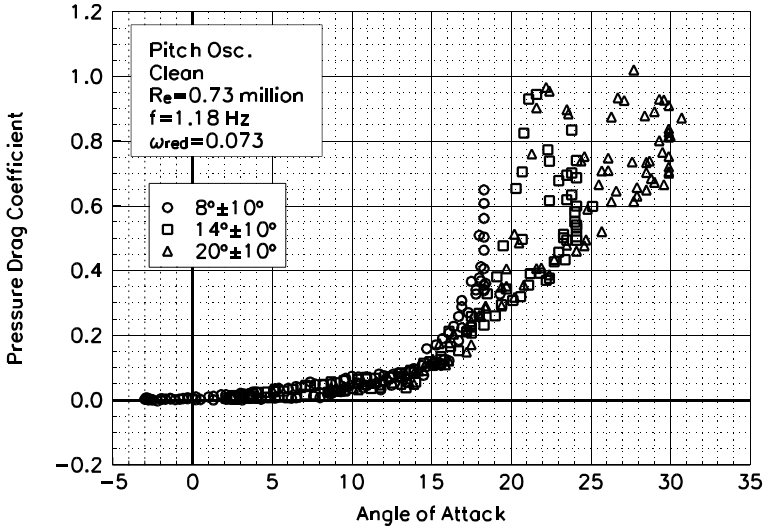

Figure C77. Pressure drag coefficient vs α.

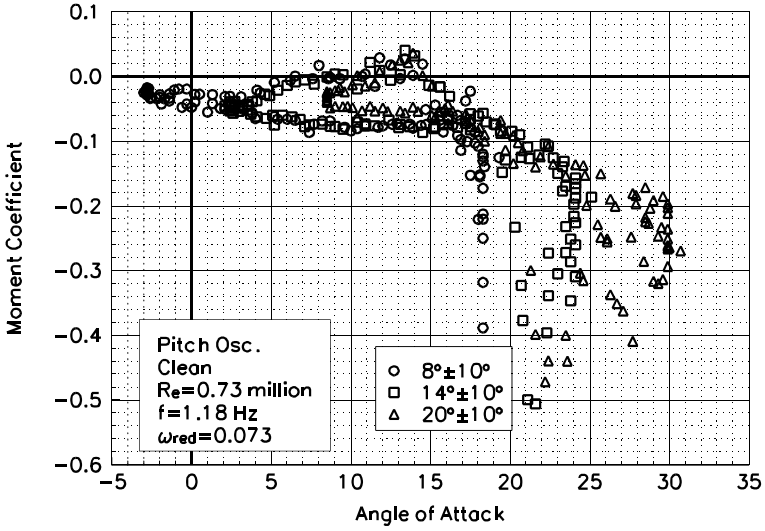

Figure C78. Moment coefficient vs α.

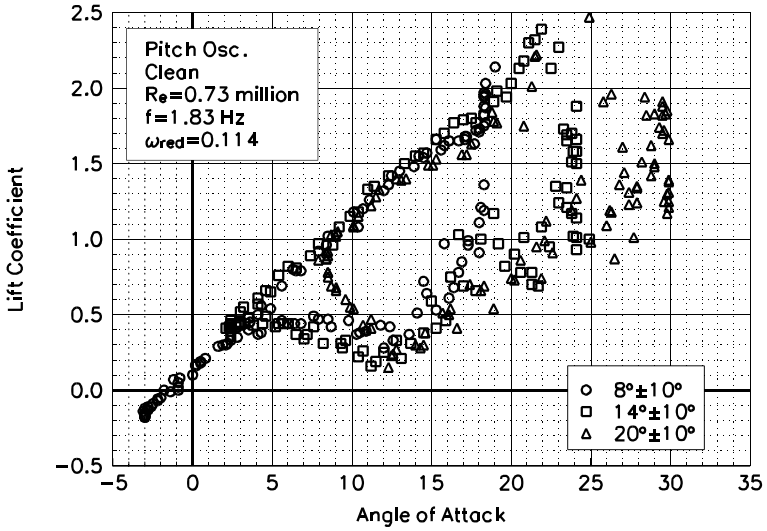

Figure C79. Lift coefficient vs α.

S810
Clean
Re=0.73 million
$\omega_{reduced}$=0.114

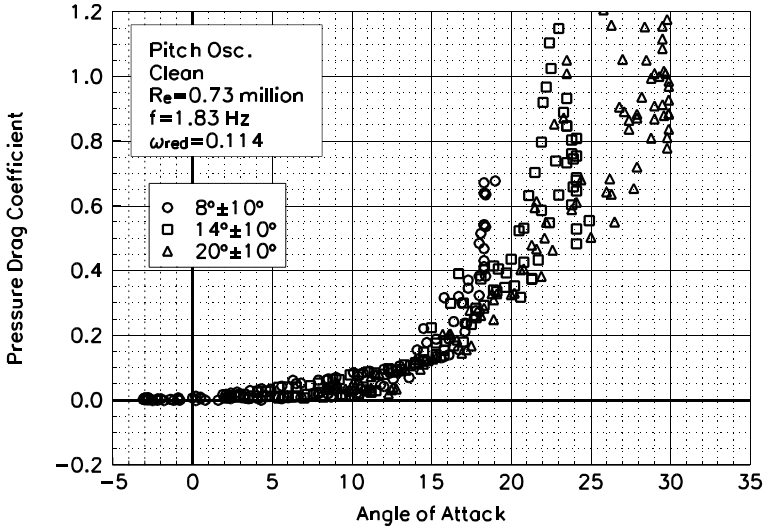

Figure C80. Pressure drag coefficient vs α.

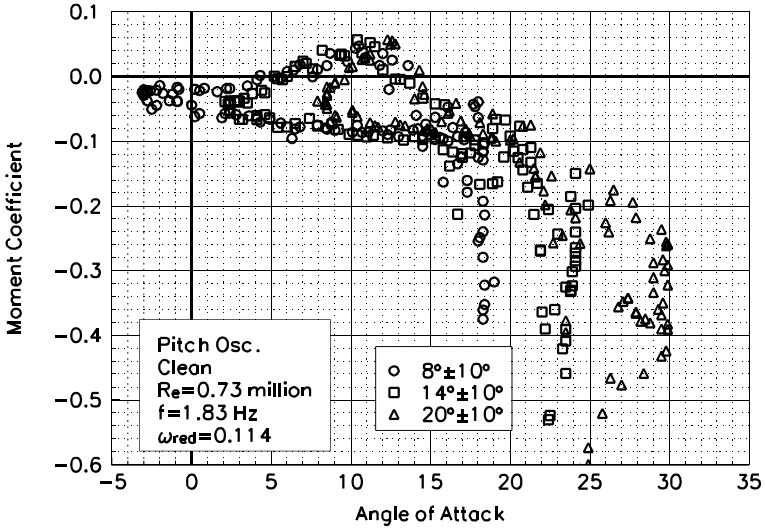

Figure C81. Moment coefficient vs α.

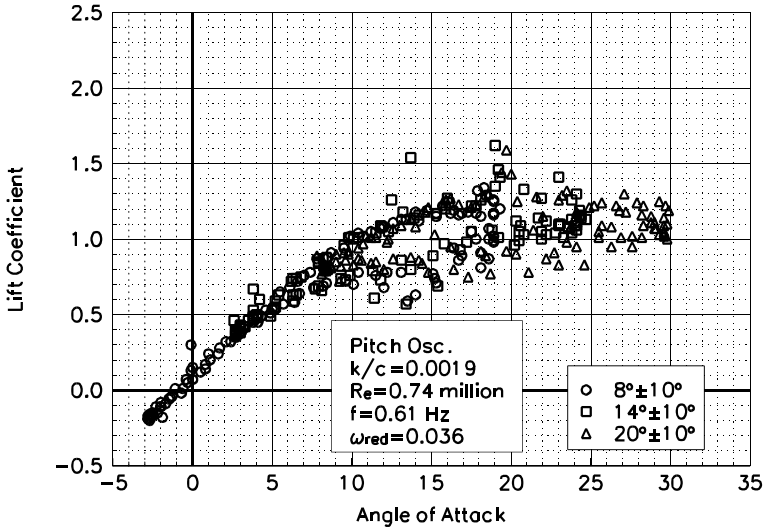

Figure C82. Lift coefficient vs α.

S810
LEGR
Re=0.74 million
$\omega_{reduced}$=0.036

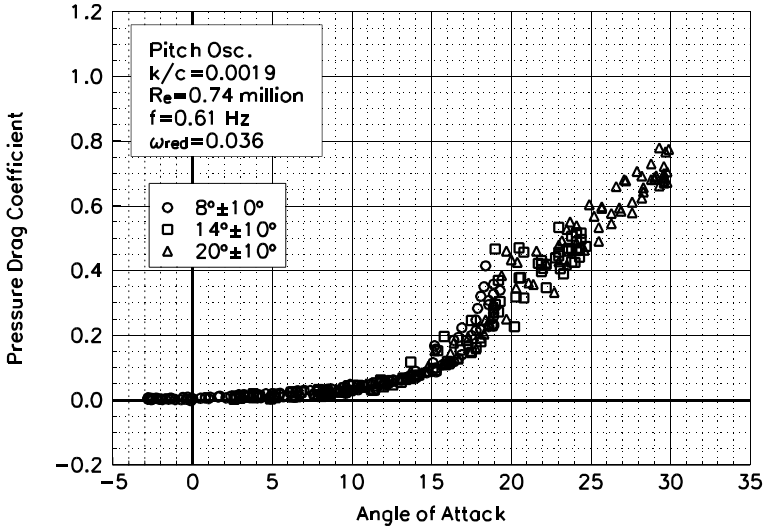

Figure C83. Pressure drag coefficient vs α.

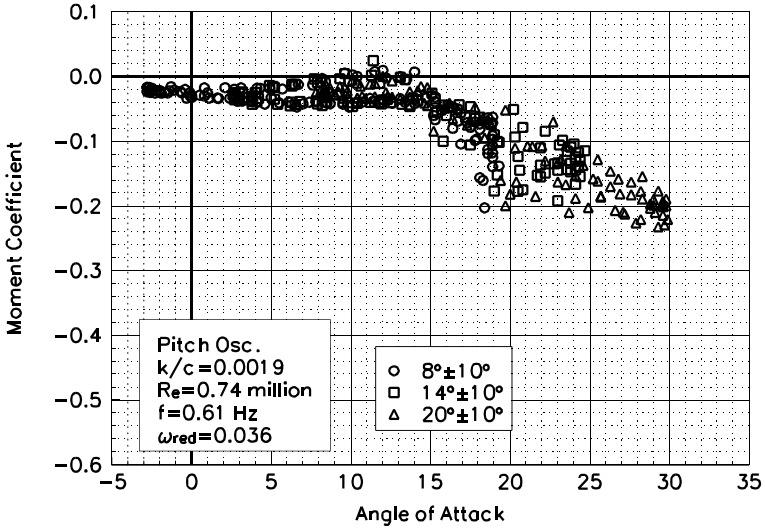

Figure C84. Moment coefficient vs α.

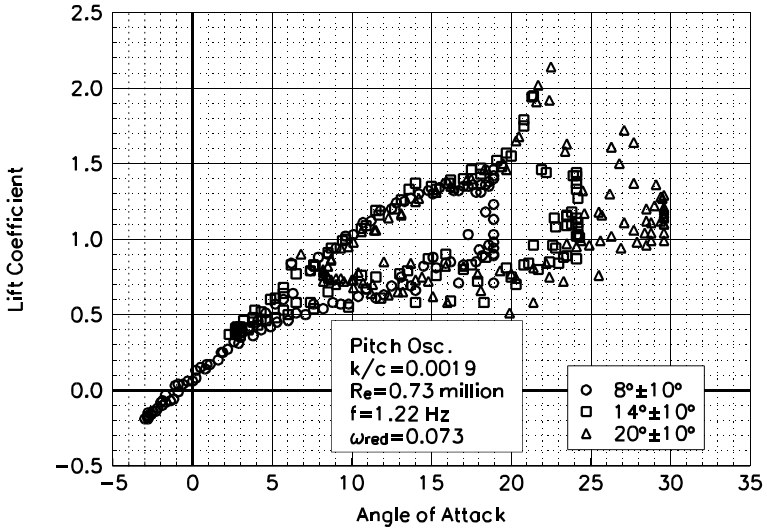

Figure C85. Lift coefficient vs α.

S810
LEGR
Re=0.73 million
$\omega_{reduced}$=0.073

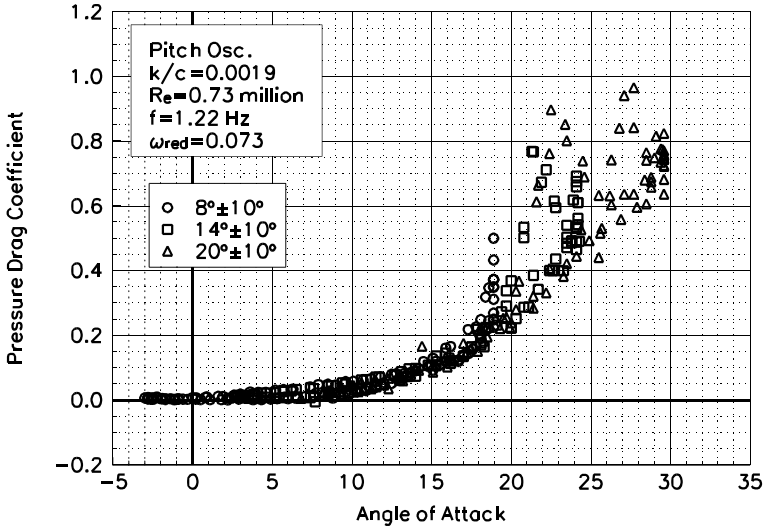

Figure C86. Pressure drag coefficient vs α.

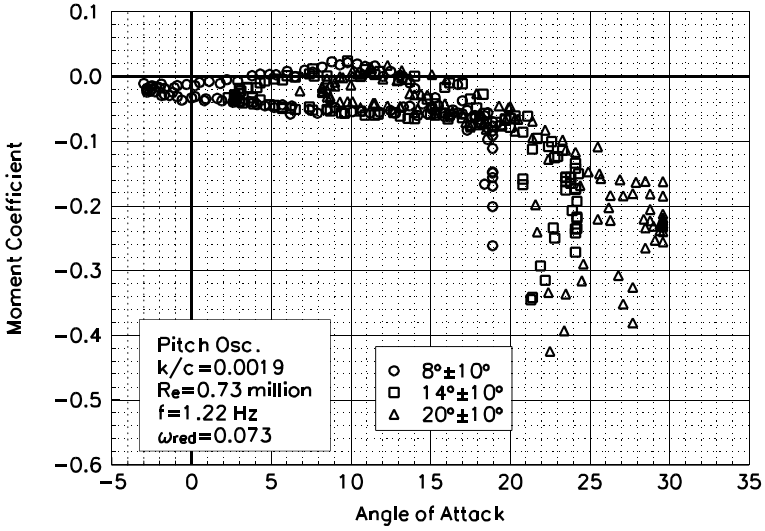

Figure C87. Moment coefficient vs α.

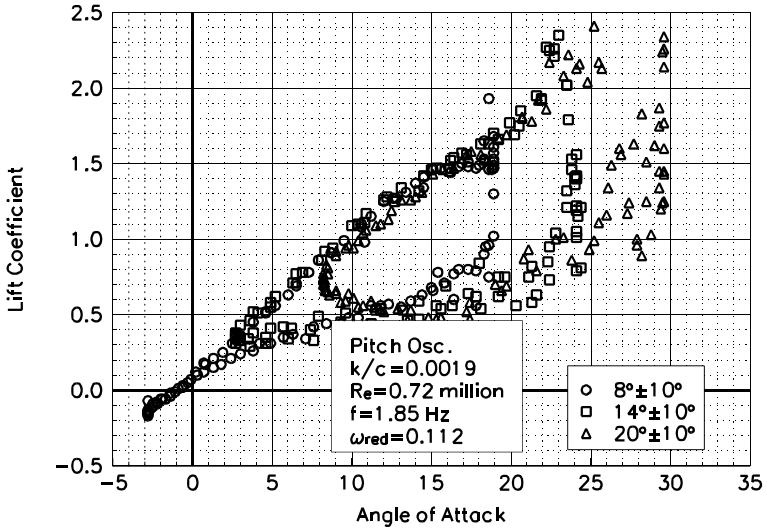

Figure C88. Lift coefficient vs α.

S810
LEGR
Re=0.72 million
$\omega_{reduced}$=0.112

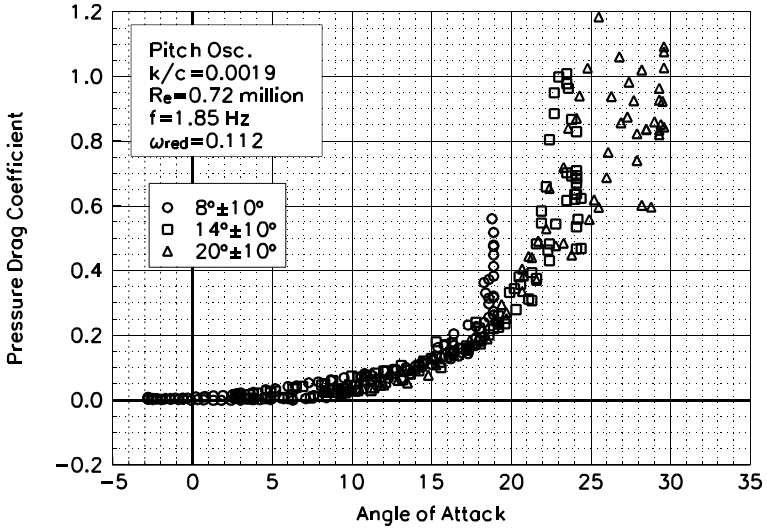

Figure C89. Pressure drag coefficient vs α.

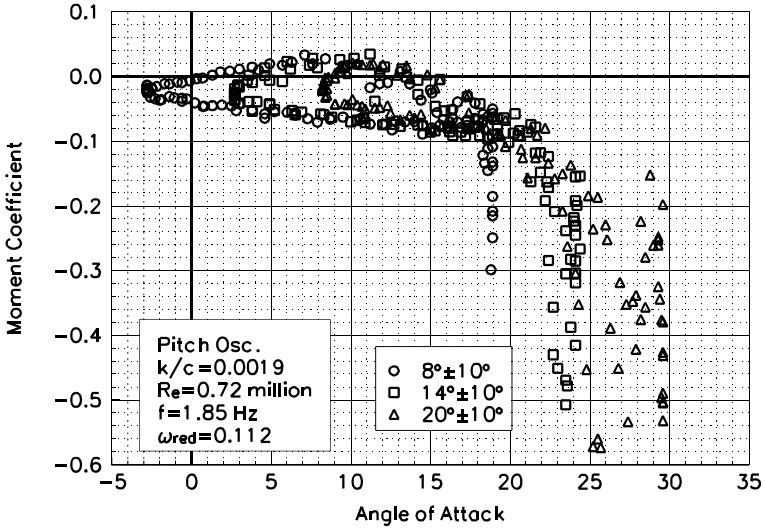

Figure C90. Moment coefficient vs α.

Unsteady Airfoil Characteristics

±10° Sine, Re = 1 million

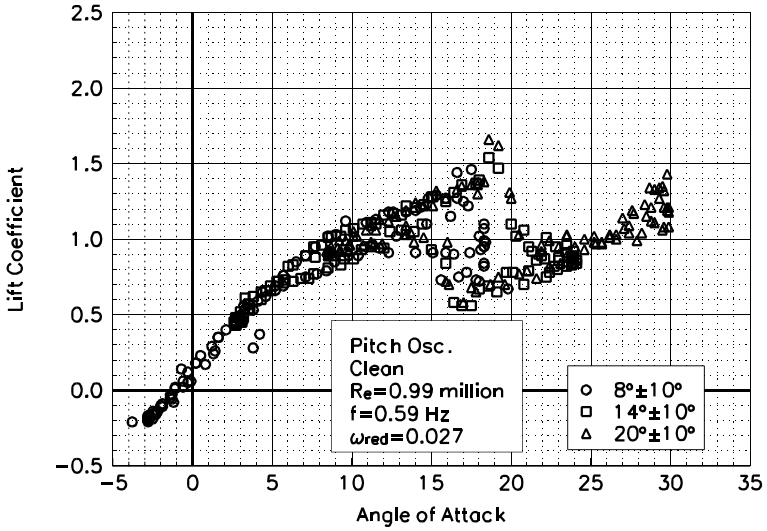

Figure C91. Lift coefficient vs α.

S810
Clean
Re=0.99 million
$\omega_{reduced}$=0.027

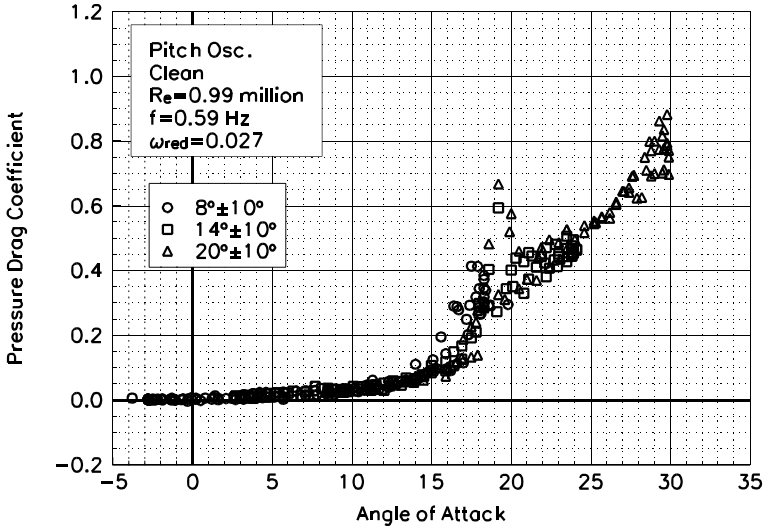

Figure C92. Pressure drag coefficient vs α.

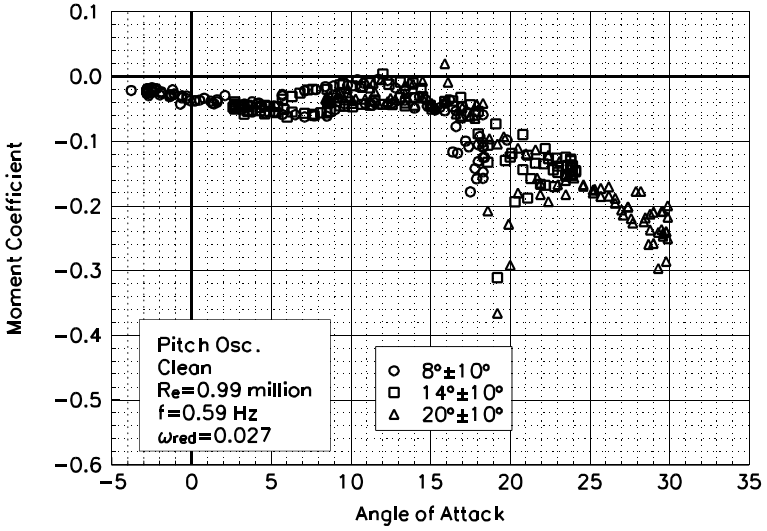

Figure C93. Moment coefficient vs α.

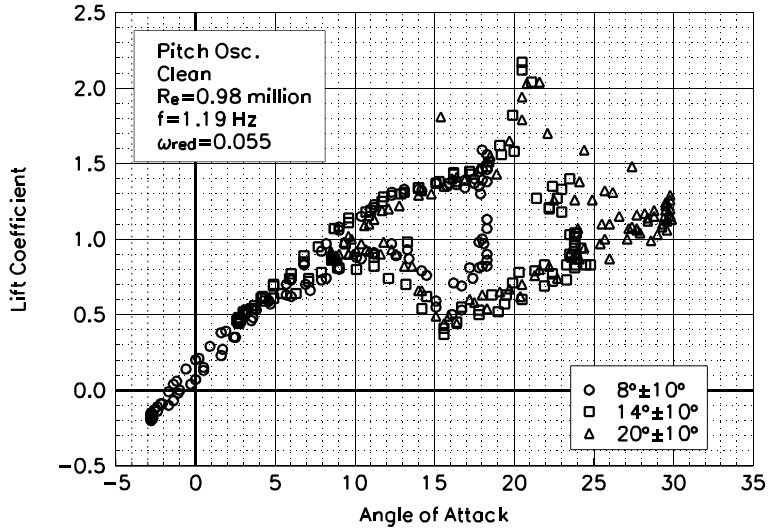

Figure C94. Lift coefficient vs α.

S810
Clean
Re=0.98 million
$\omega_{reduced}$=0.055

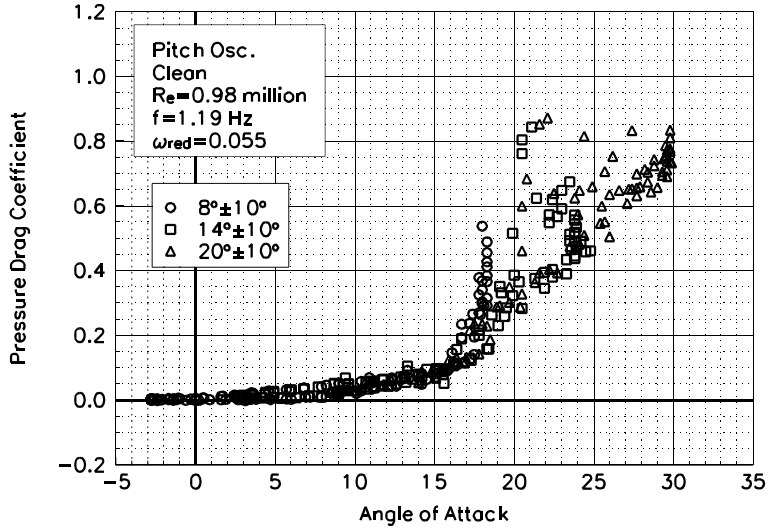

Figure C95. Pressure drag coefficient vs α.

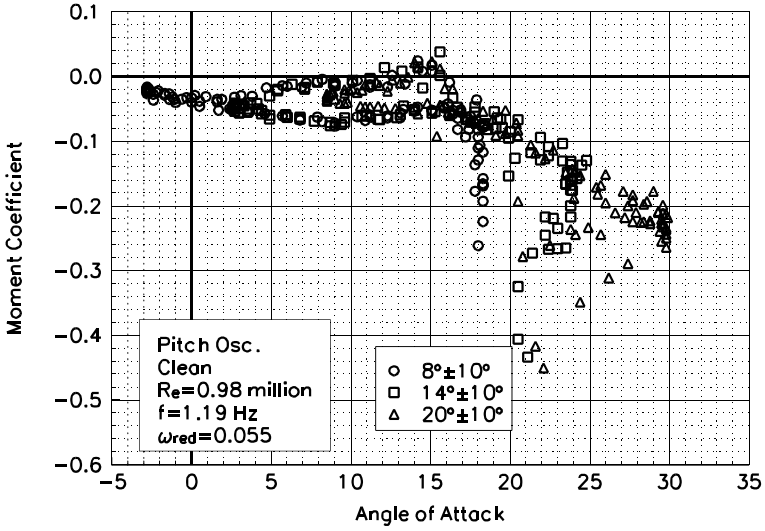

Figure C96. Moment coefficient vs α.

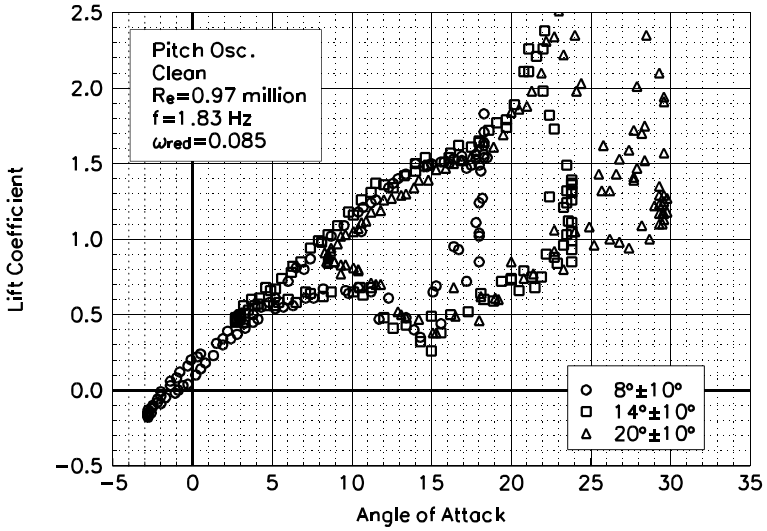

Figure C97. Lift coefficient vs α.

S810
Clean
Re=0.97 million
$\omega_{reduced}$=0.085

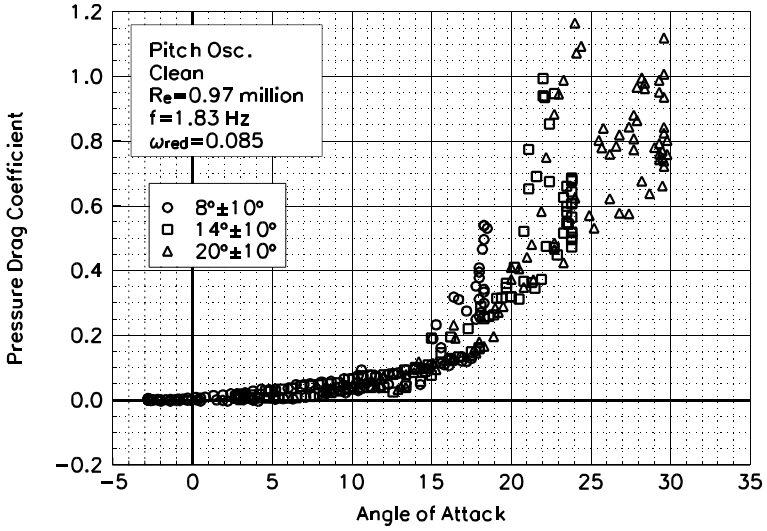

Figure C98. Pressure drag coefficient vs α.

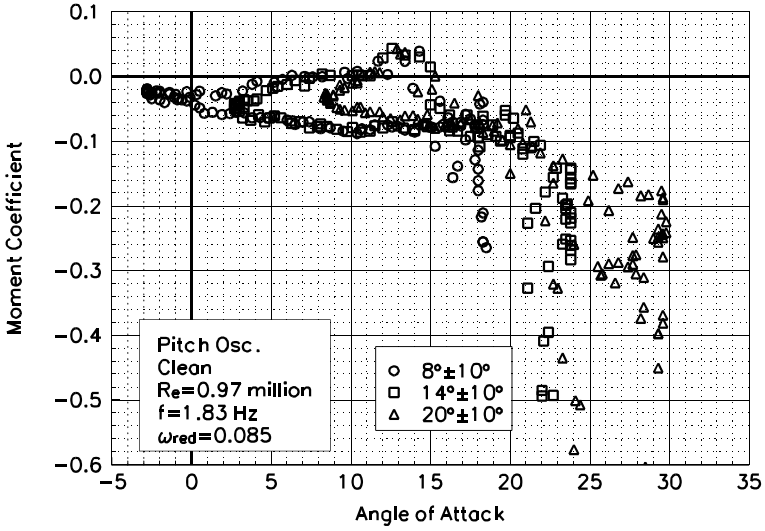

Figure C99. Moment coefficient vs α.

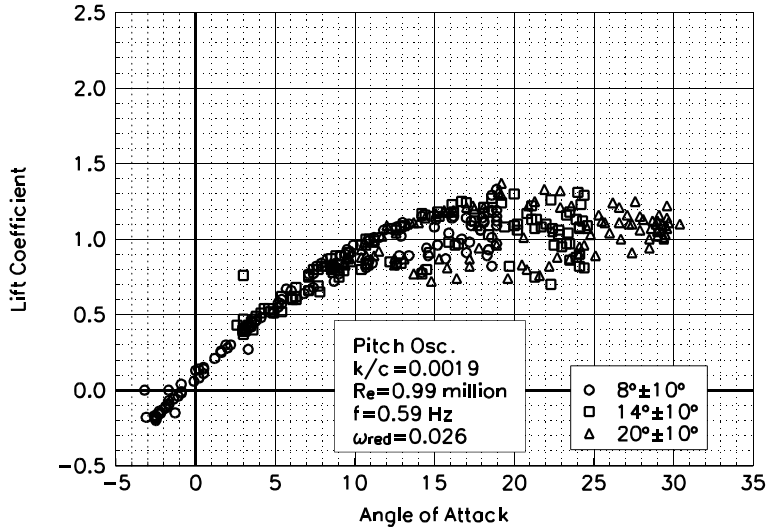

Figure C100. Lift coefficient vs α.

S810
LEGR
Re=0.99 million
$\omega_{reduced}$=0.026

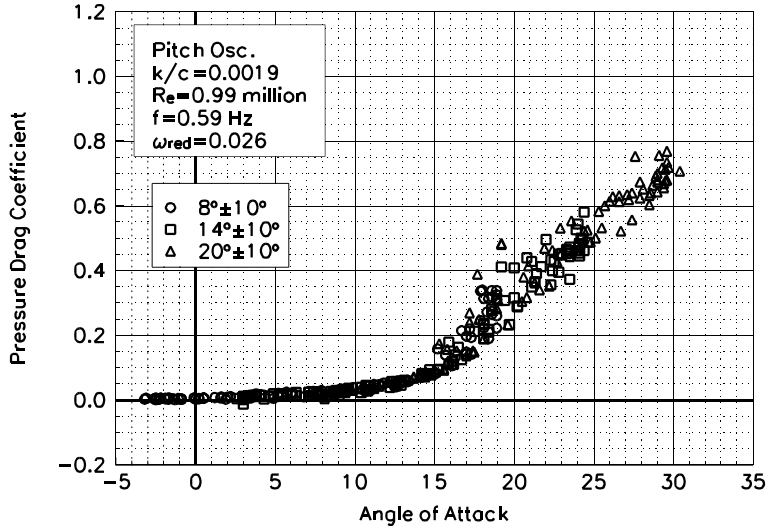

Figure C101. Pressure drag coefficient vs α.

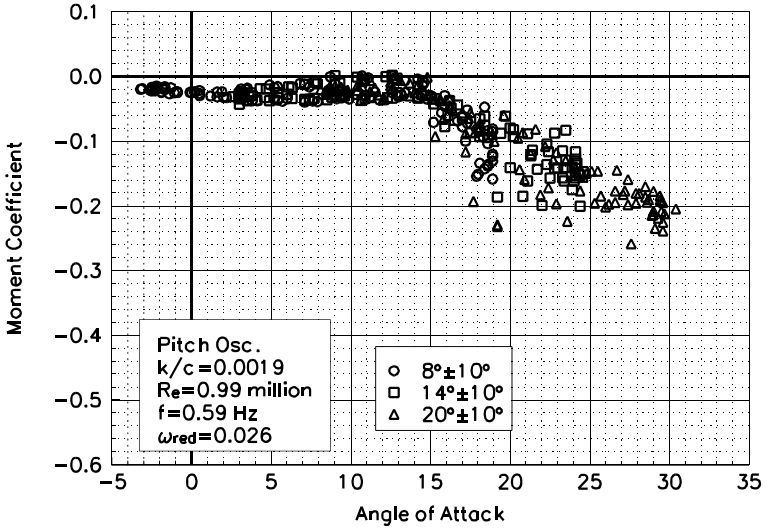

Figure C102. Moment coefficient vs α.

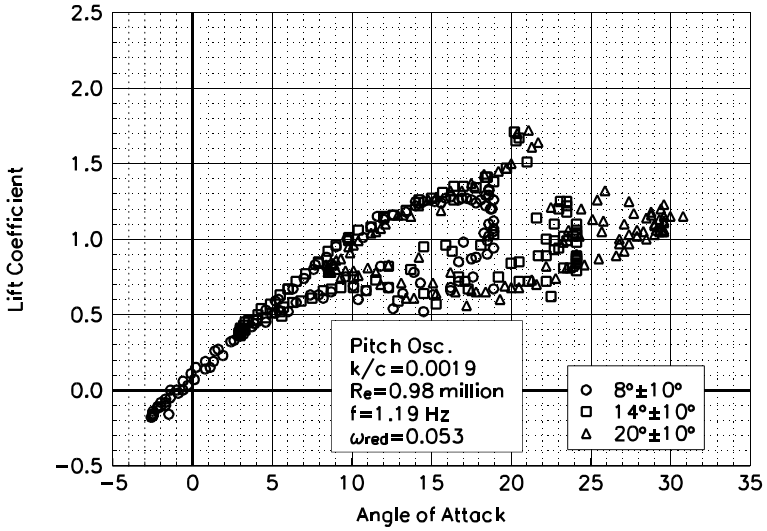

Figure C103. Lift coefficient vs α.

S810
LEGR
Re=0.98 million
$\omega_{reduced}$=0.053

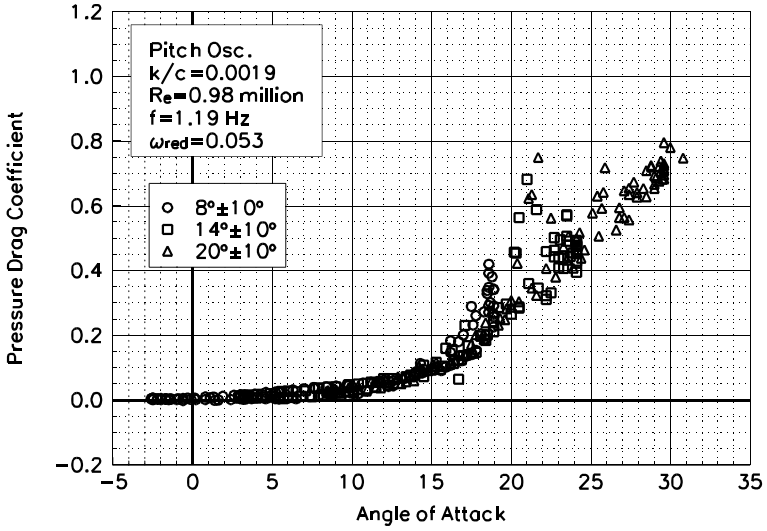

Figure C104. Pressure drag coefficient vs α.

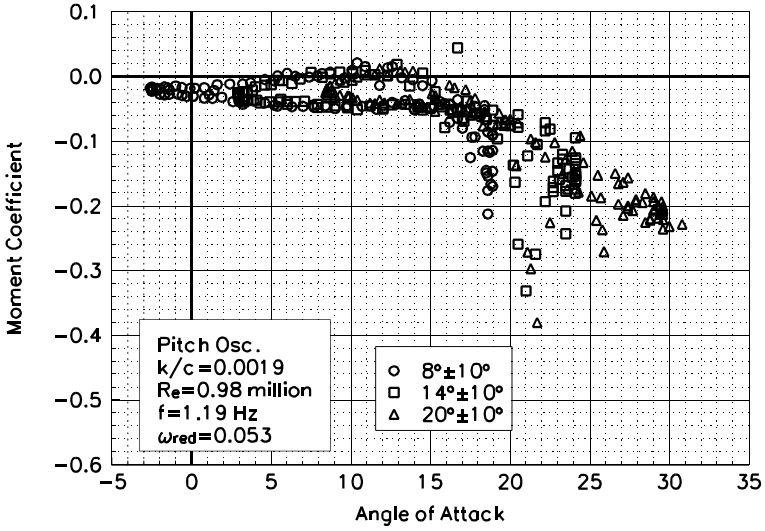

Figure C105. Moment coefficient vs α.

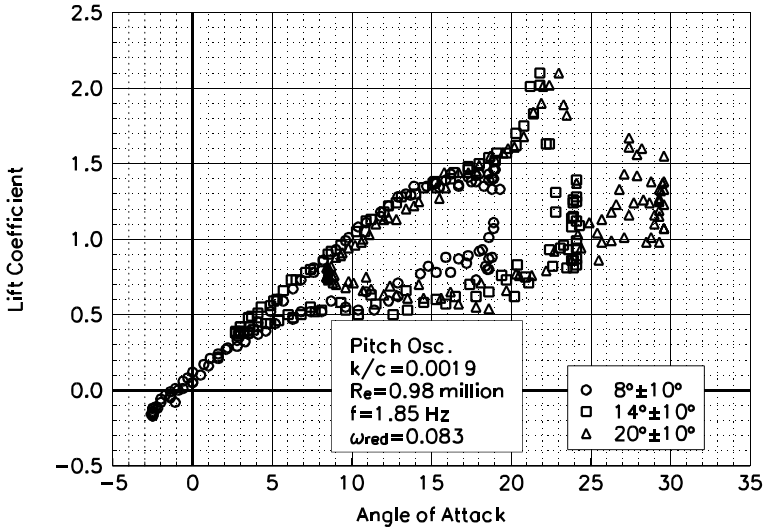

S810
LEGR
Re=0.98 million
$\omega_{reduced}$=0.083

Figure C106. Lift coefficient vs α.

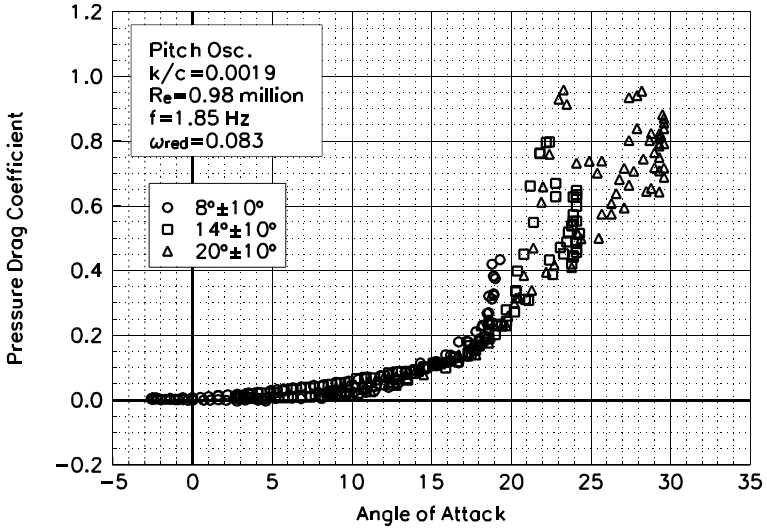

Figure C107. Pressure drag coefficient vs α.

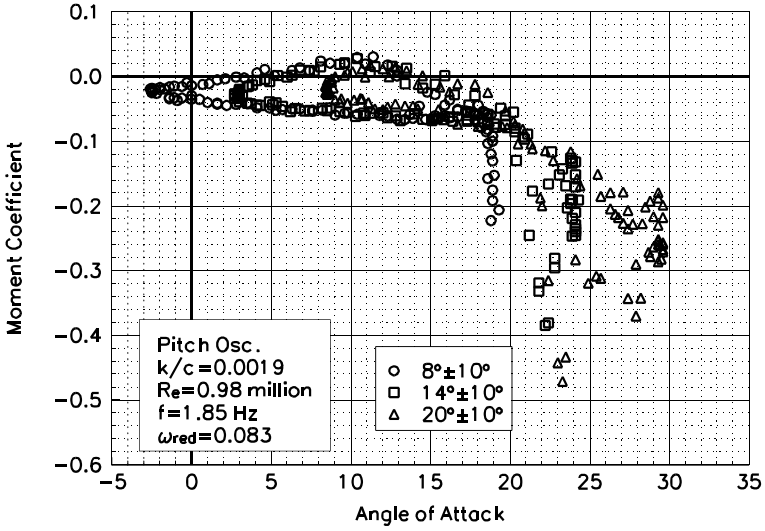

Figure C108. Moment coefficient vs α.

Unsteady Airfoil Characteristics

±10° Sine, Re = 1.25 million

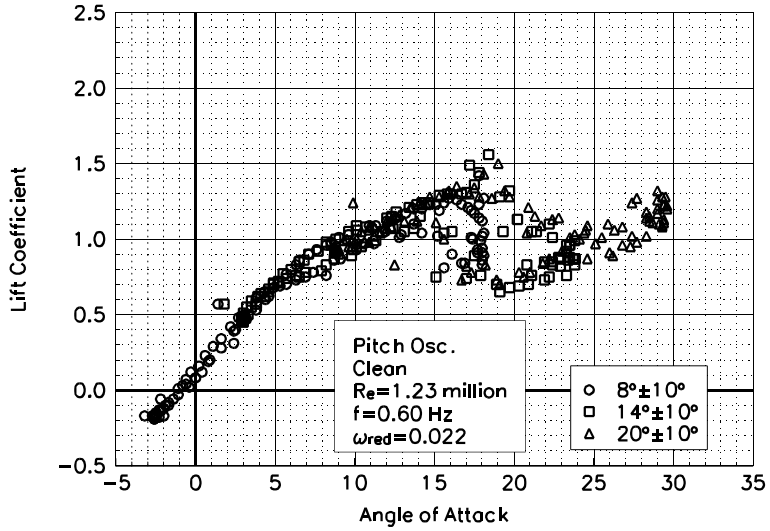

Figure C109. Lift coefficient vs α.

S810
Clean
Re=1.23 million
$\omega_{reduced}$=0.022

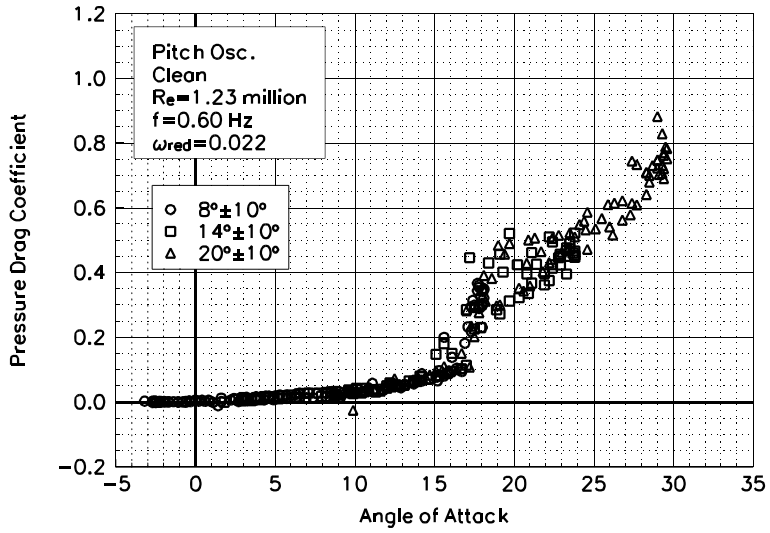

Figure C110. Pressure drag coefficient vs α.

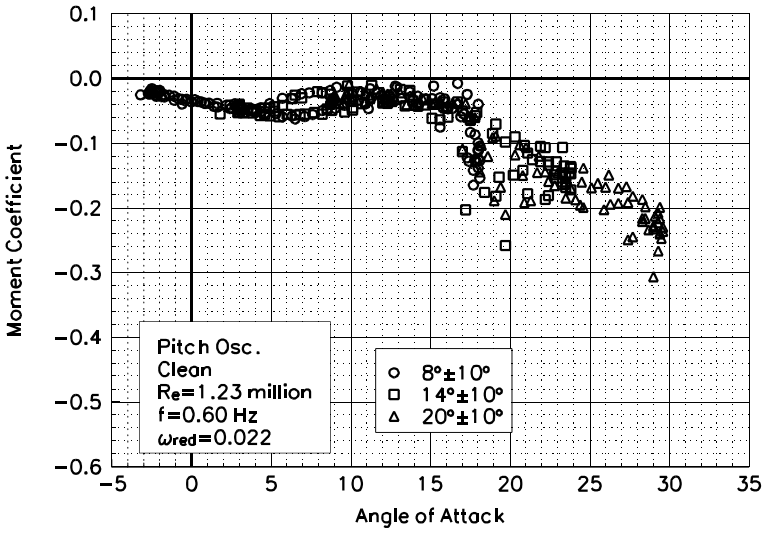

Figure C111. Moment coefficient vs α.

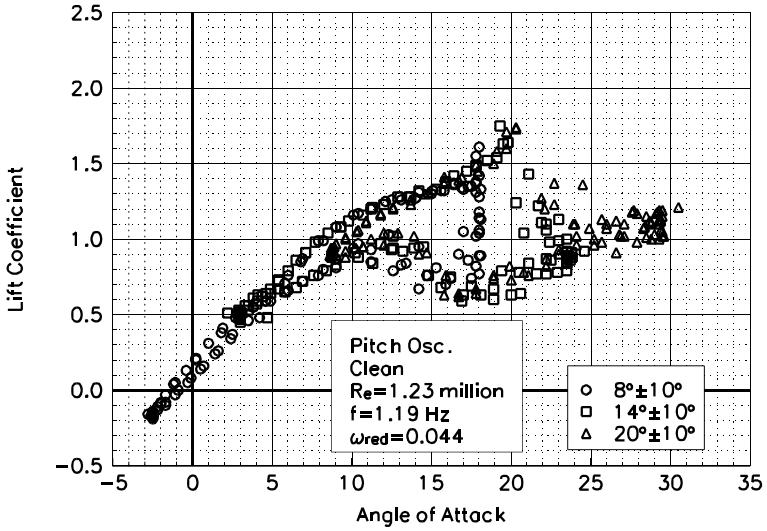

Figure C112. Lift coefficient vs α.

S810
Clean
Re=1.23 million
$\omega_{reduced}$=0.044

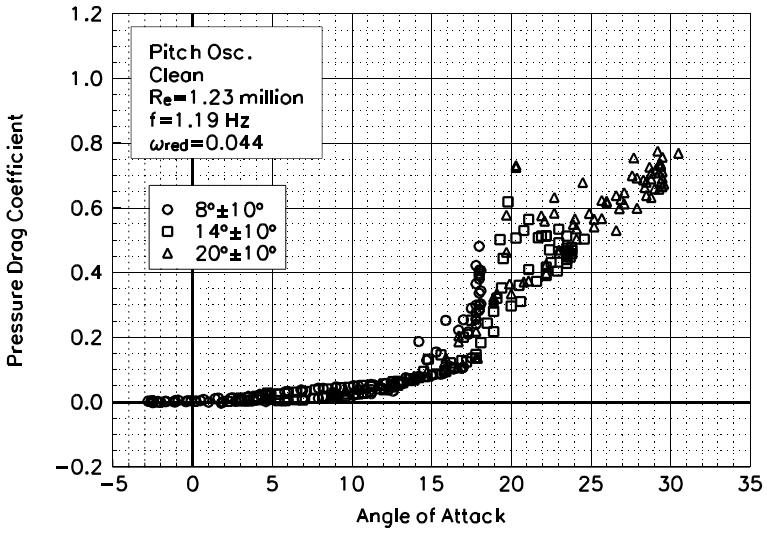

Figure C113. Pressure drag coefficient vs α.

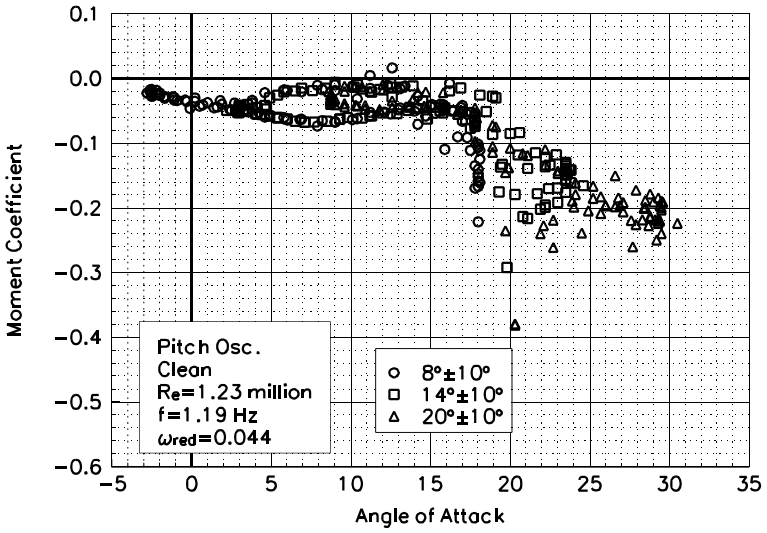

Figure C114. Moment coefficient vs α.

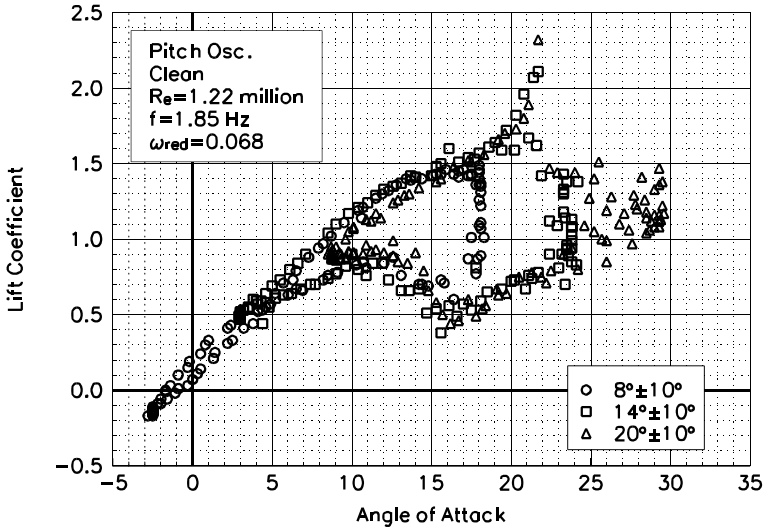

Figure C115. Lift coefficient vs α.

S810
Clean
Re=1.22 million
$\omega_{reduced}$=0.068

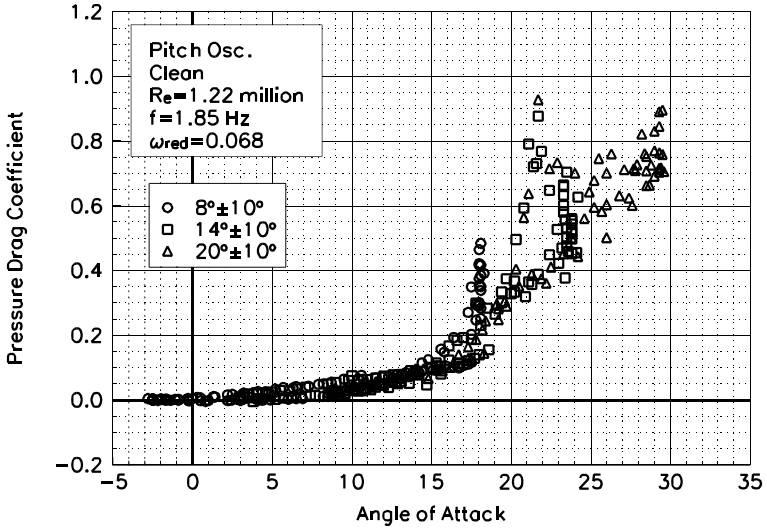

Figure C116. Pressure drag coefficient vs α.

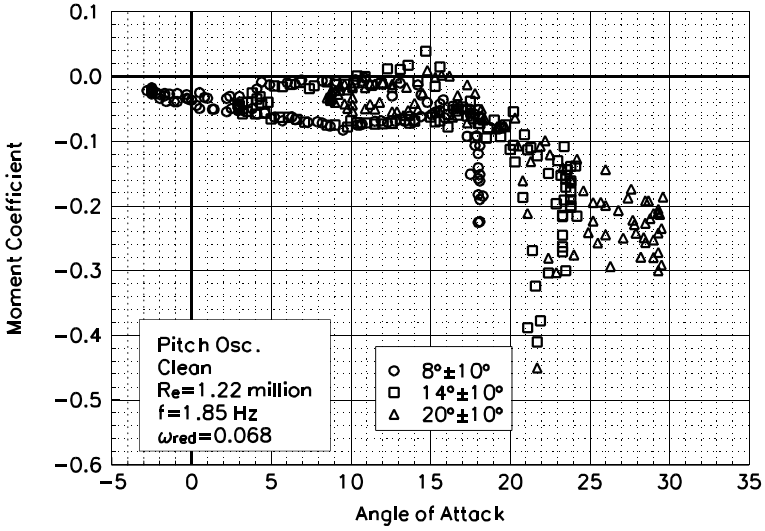

Figure C117. Moment coefficient vs α.

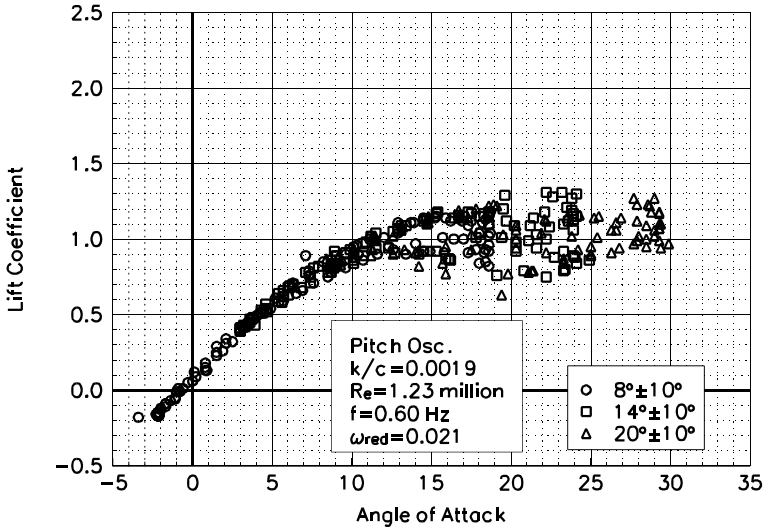

Figure C118. Lift coefficient vs α.

S810
LEGR
Re=1.23 million
$\omega_{reduced}$=0.021

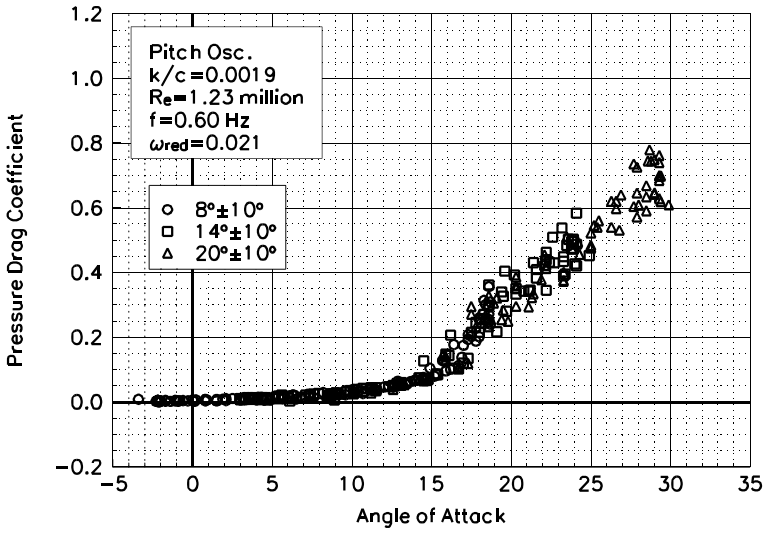

Figure C119. Pressure drag coefficient vs α.

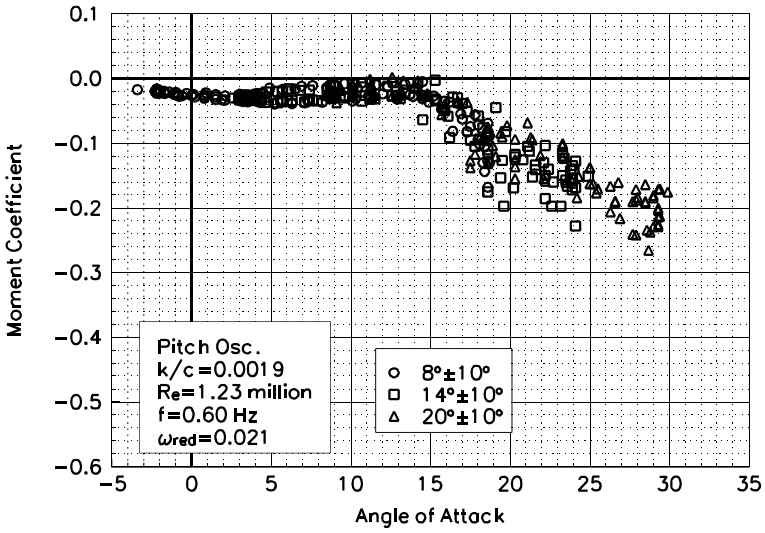

Figure C120. Moment coefficient vs α.

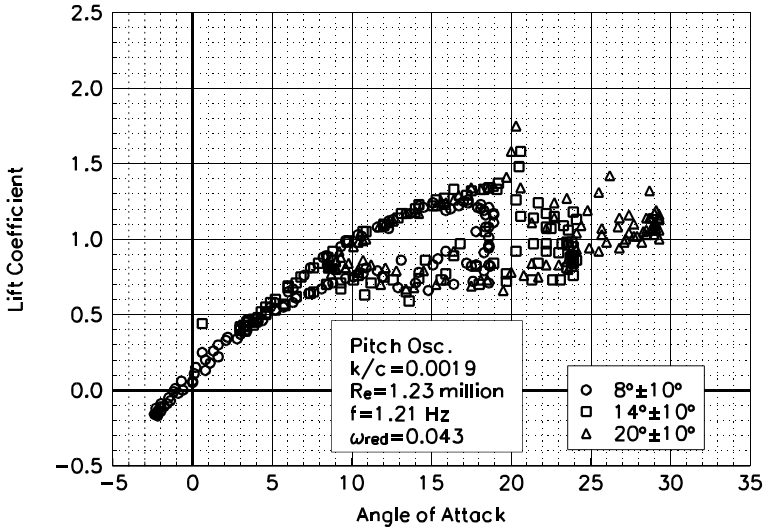

Figure C121. Lift coefficient vs α.

S810
LEGR
Re=1.23 million
$\omega_{reduced}$=0.043

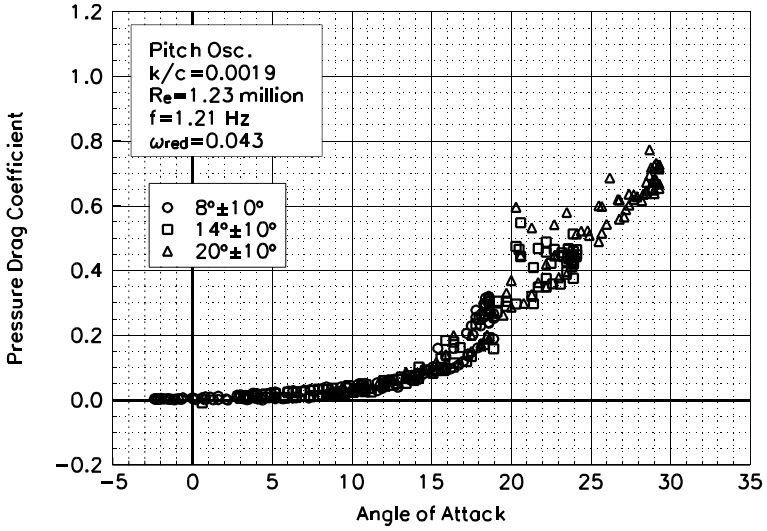

Figure C122. Pressure drag coefficient vs α.

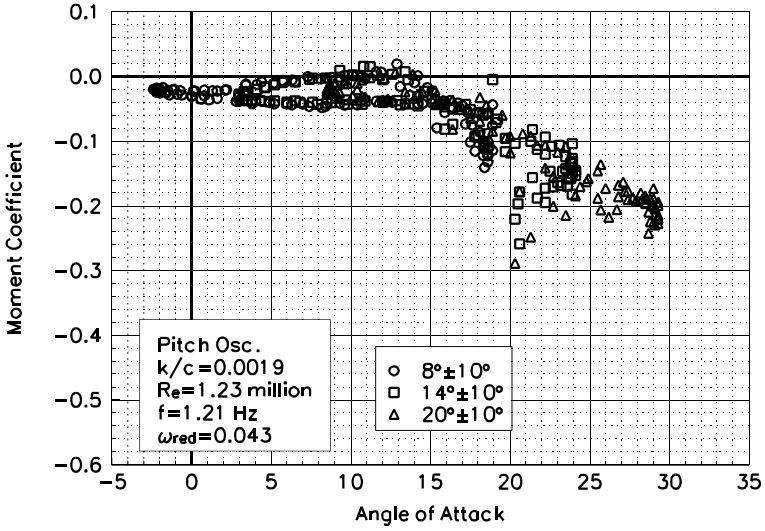

Figure C123. Moment coefficient vs α.

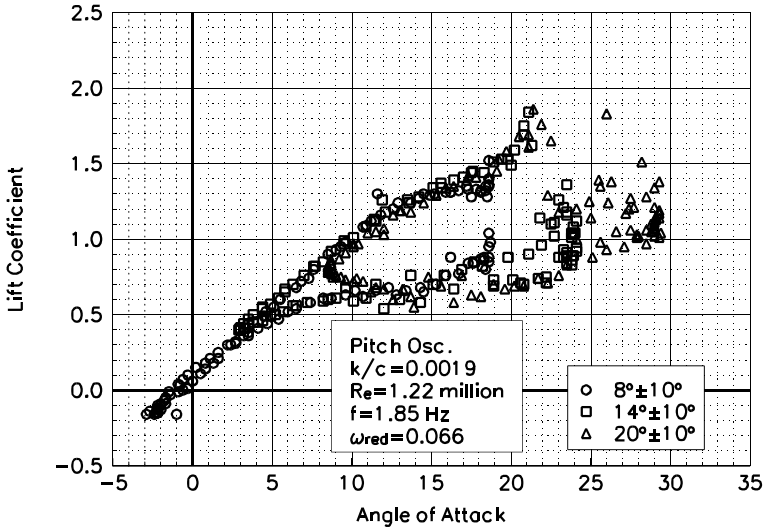

Figure C124. Lift coefficient vs α.

S810
LEGR
Re=1.22 million
$\omega_{reduced}$=0.066

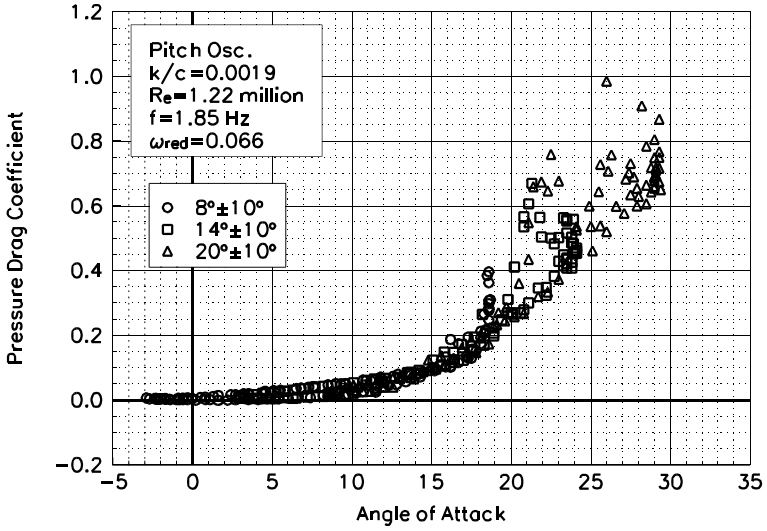

Figure C125. Pressure drag coefficient vs α.

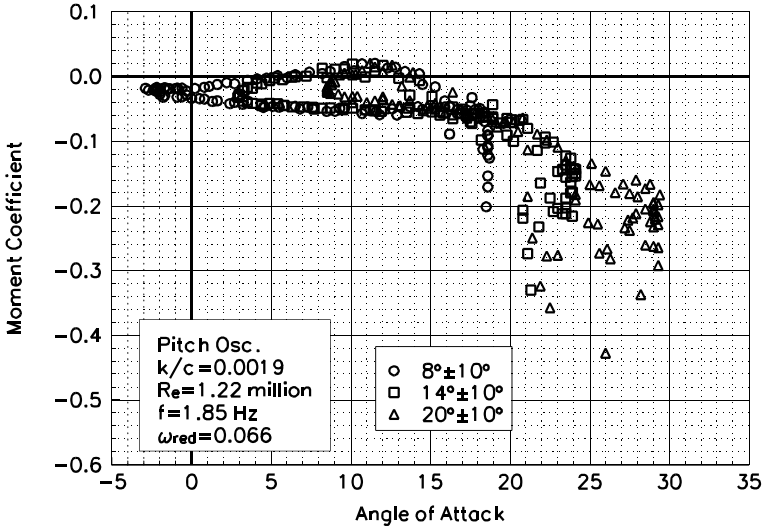

Figure C126. Moment coefficient vs α.

Unsteady Airfoil Characteristics

±10° Sine, Re = 1.5 million

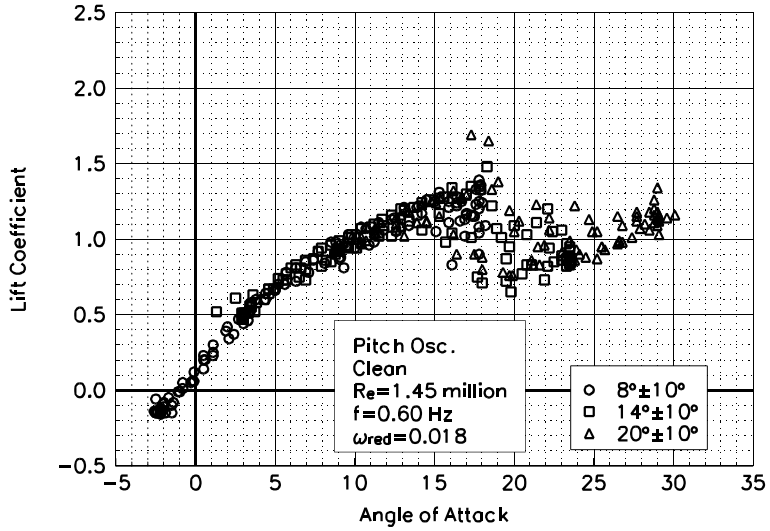

Figure C127. Lift coefficient vs α.

S810
Clean
Re=1.45 million
$\omega_{reduced}$=0.018

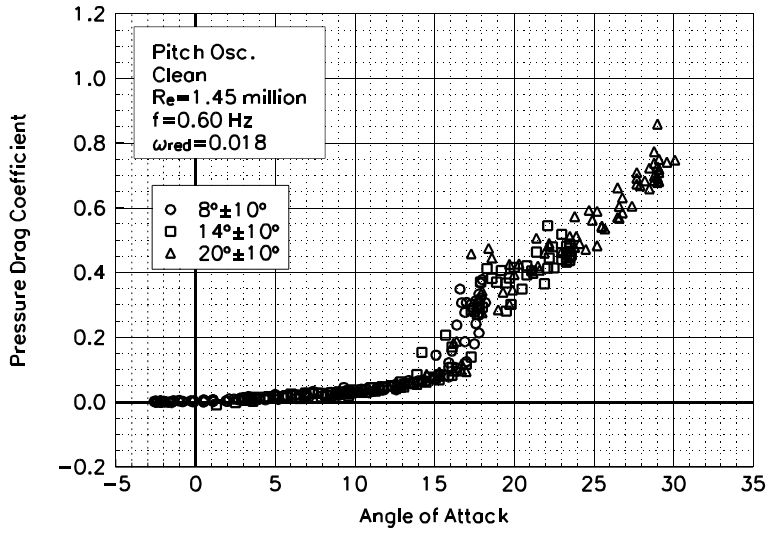

Figure C128. Pressure drag coefficient vs α.

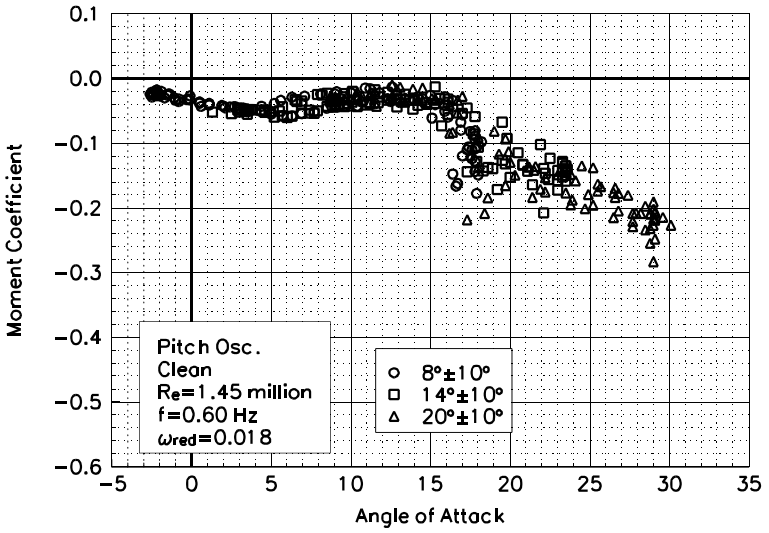

Figure C129. Moment coefficient vs α.

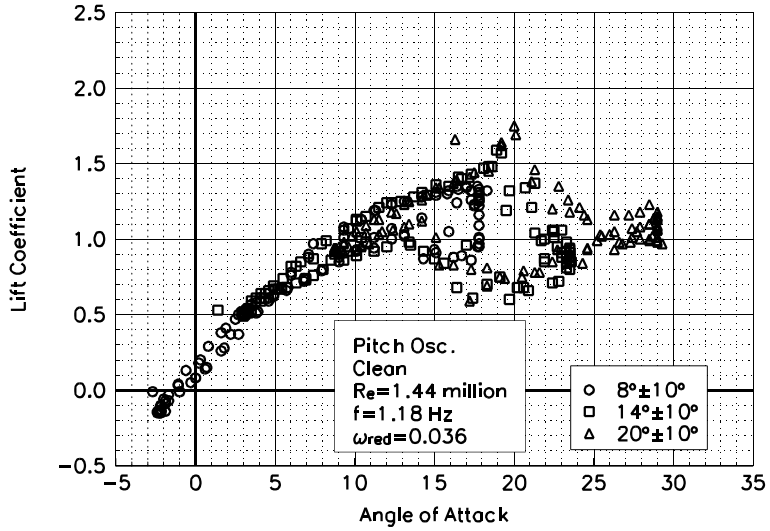

Figure C130. Lift coefficient vs α.

S810
Clean
Re=1.44 million
$\omega_{reduced}$=0.036

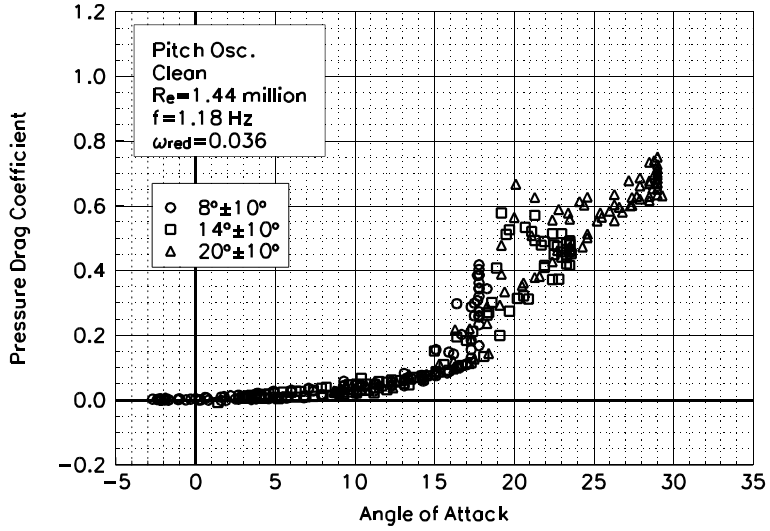

Figure C131. Pressure drag coefficient vs α.

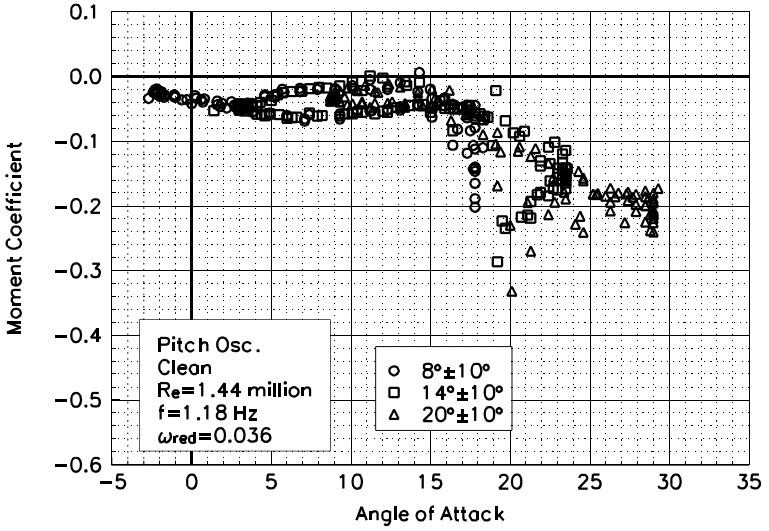

Figure C132. Moment coefficient vs α.

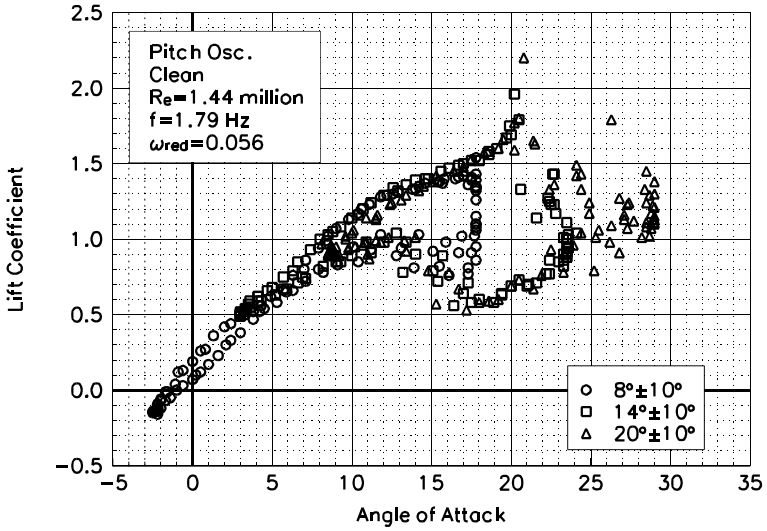

Figure C133. Lift coefficient vs α.

S810
Clean
Re=1.44 million
$\omega_{reduced}$=0.056

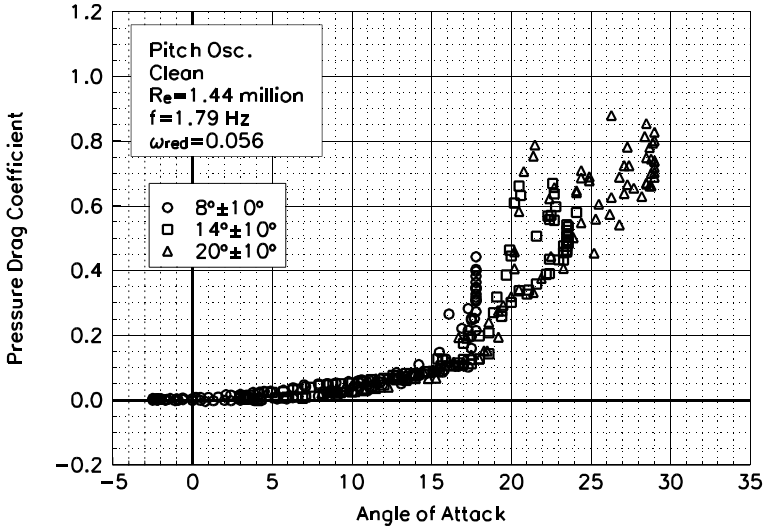

Figure C134. Pressure drag coefficient vs α.

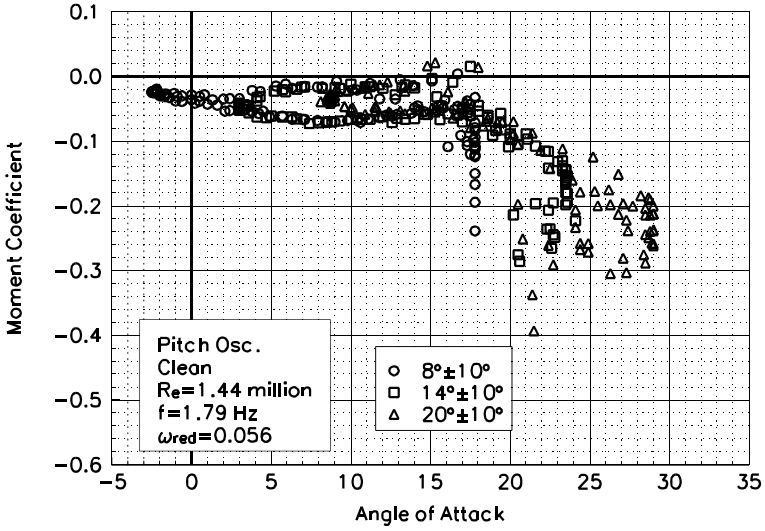

Figure C135. Moment coefficient vs α.

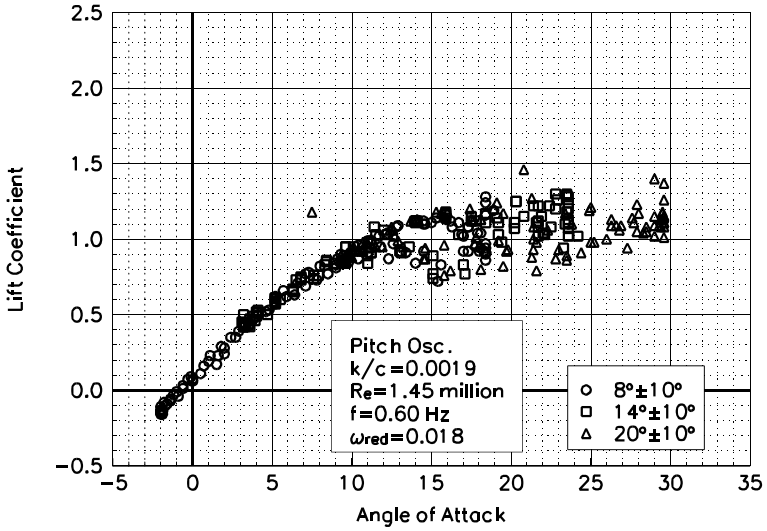

Figure C136. Lift coefficient vs α.

S810
LEGR
Re=1.45 million
$\omega_{reduced}$=0.018

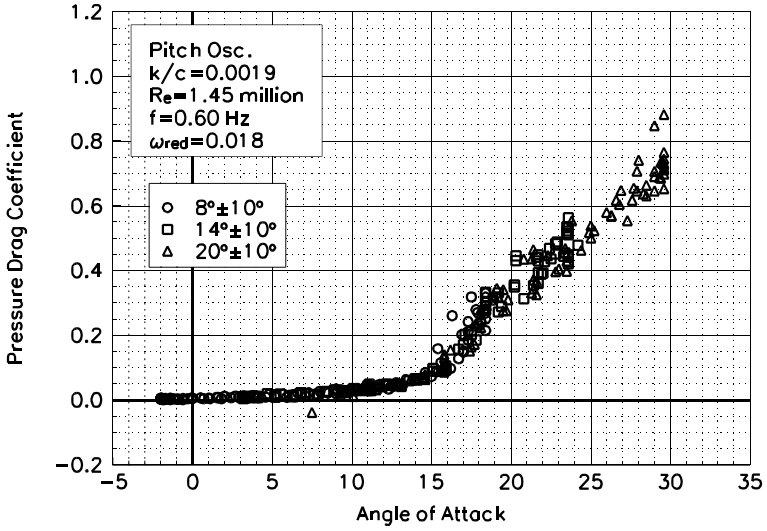

Figure C137. Pressure drag coefficient vs α.

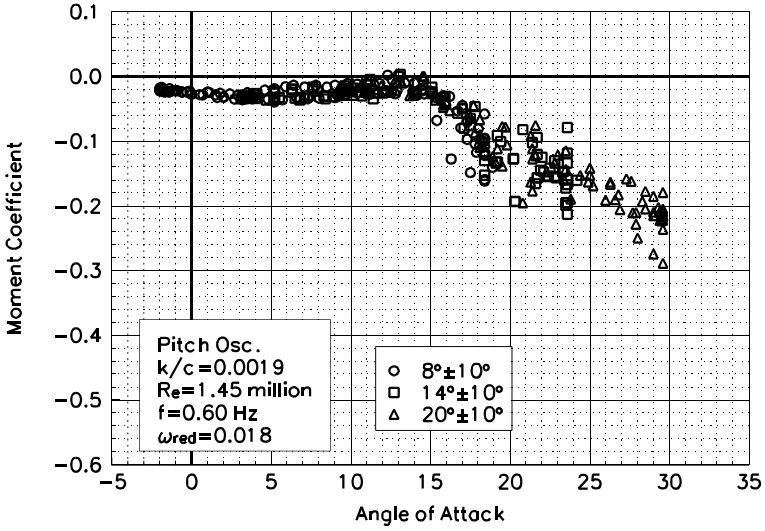

Figure C138. Moment coefficient vs α.

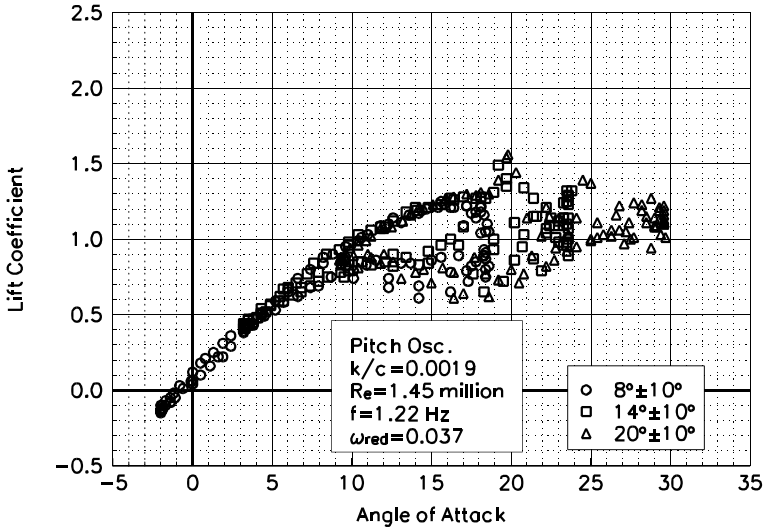

Figure C139. Lift coefficient vs α.

S810
LEGR
Re=1.45 million
$\omega_{reduced}$=0.037

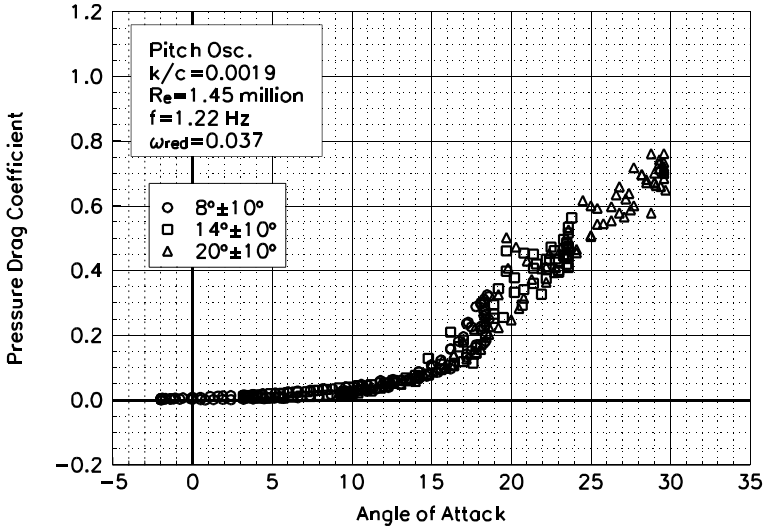

Figure C140. Pressure drag coefficient vs α.

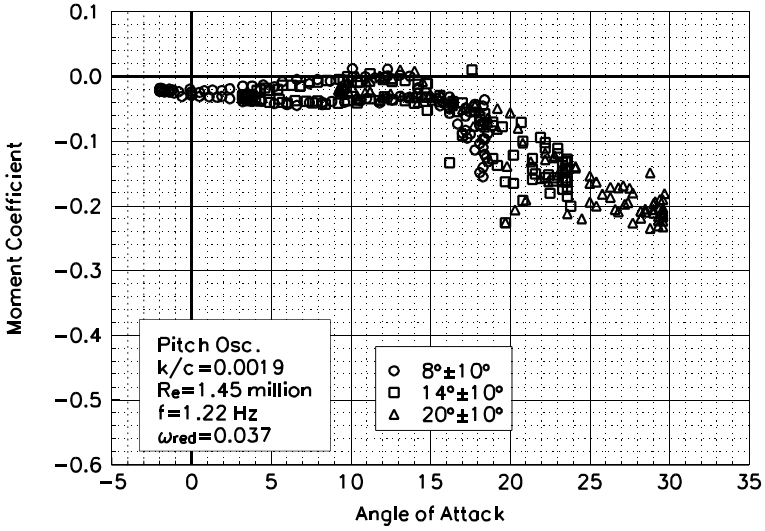

Figure C141. Moment coefficient vs α.

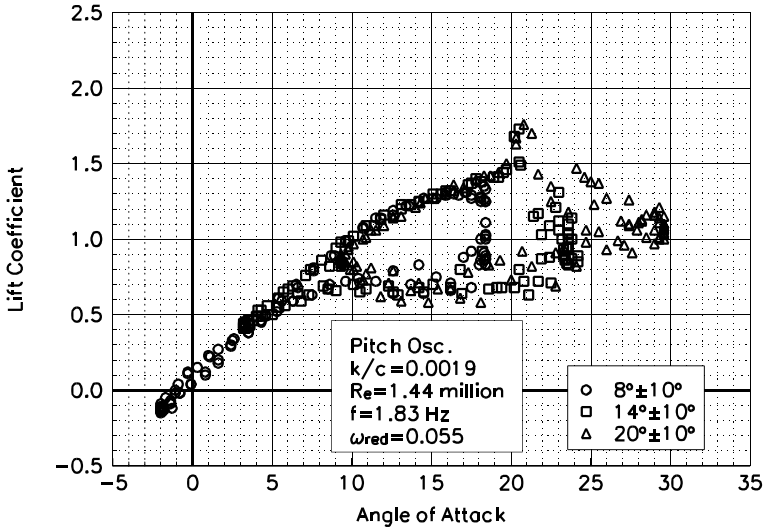

Figure C142. Lift coefficient vs α.

S810
LEGR
Re=1.44 million
$\omega_{reduced}$=0.055

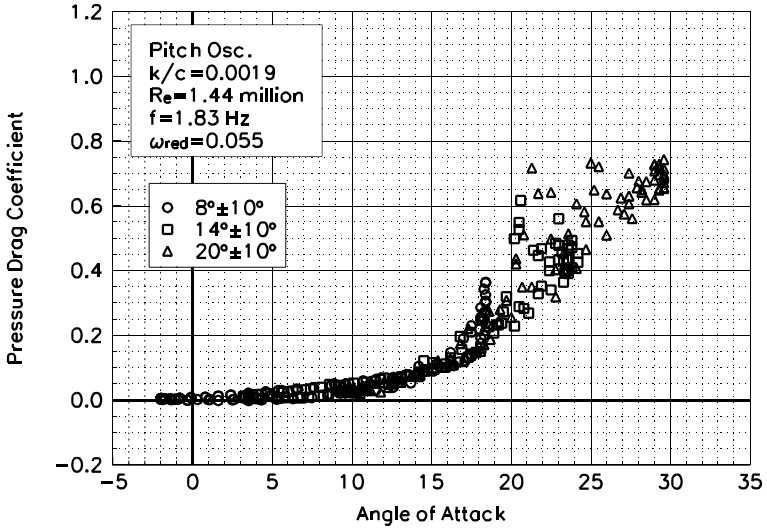

Figure C143. Pressure drag coefficient vs α.

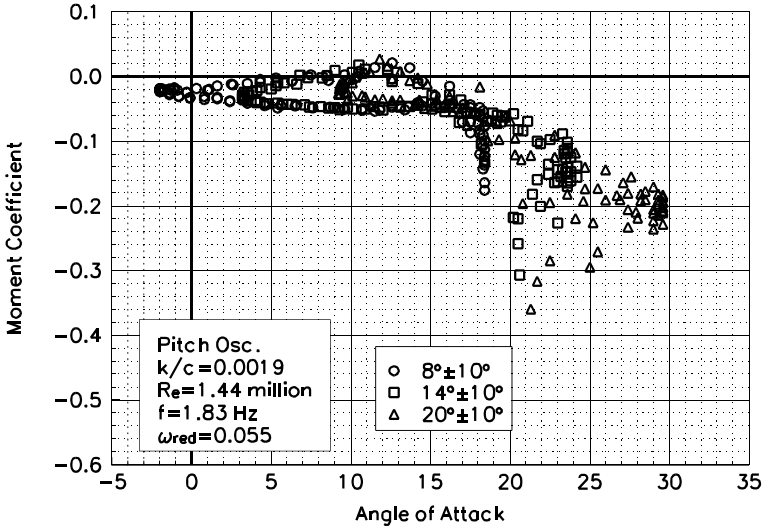

Figure C144. Moment coefficient vs α.